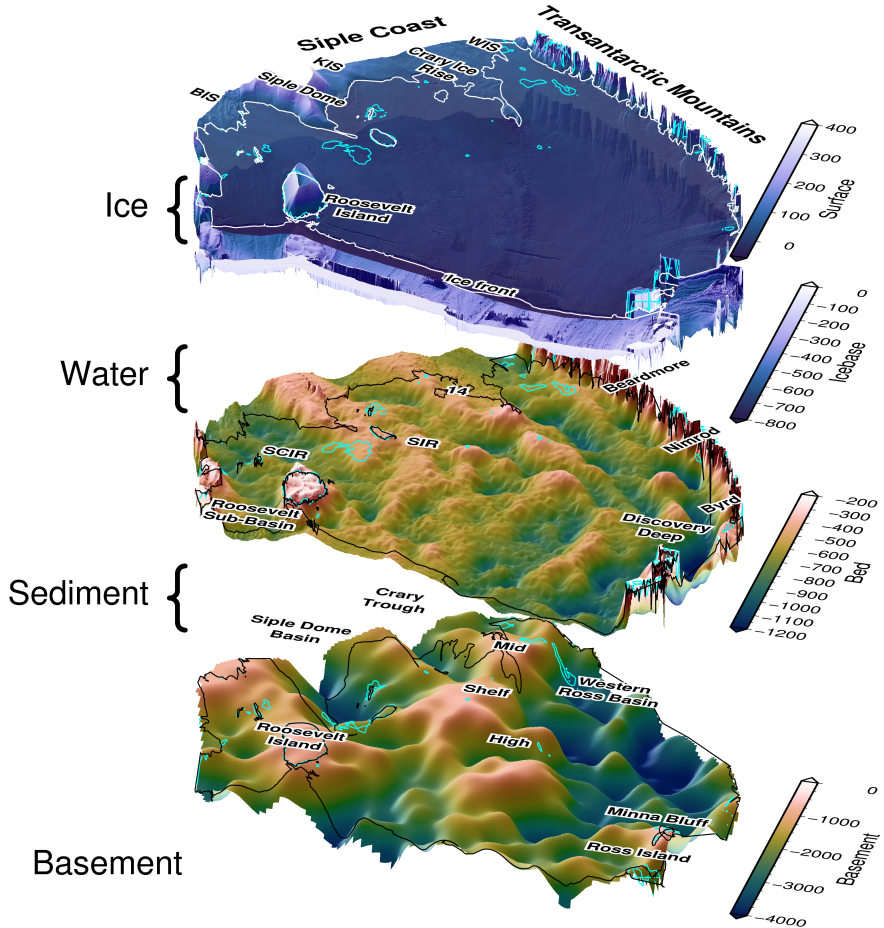


1

# Airborne Geophysical Investigation 2 beneath Antarctica's Ross Ice Shelf



3  
4 A thesis presented for the degree of  
5 Doctor of Philosophy in Geophysics

6 Matthew Tankersley



7  
8 Antarctic Research Centre  
9 Victoria University of Wellington  
10 New Zealand  
11 October 19, 2023



# <sup>12</sup> Abstract

<sup>13</sup> The Ross Ice Shelf controls the flow of ice into the ocean from catchments consisting  
<sup>14</sup> of both the East and West Antarctic Ice Sheets. These catchments hold a volume  
<sup>15</sup> of ice equivalent to  $\sim$ 12 m of global sea level rise. To adequately understand how  
<sup>16</sup> this ice will respond to a warming world requires knowledge of the properties and  
<sup>17</sup> parameters which influence how the ice sheet behaves. These boundary conditions  
<sup>18</sup> include fundamental knowledge of the Earth, such as the shape of the bed beneath  
<sup>19</sup> the ice, the seafloor, and the geologic structures of the upper crust. Knowledge of  
<sup>20</sup> the physiography and sub-surface geology is severely lacking beneath ice shelves due  
<sup>21</sup> to their inaccessibility.

<sup>22</sup> Here, we use airborne geophysical data from an extensive survey over the Ross Ice  
<sup>23</sup> Shelf to better understand these boundary conditions. From the analysis of airborne  
<sup>24</sup> magnetics data, we model the thickness of sediment, the shape of the crystalline  
<sup>25</sup> basement, and the likely locations of faults throughout the crust under the Ross Ice  
<sup>26</sup> Shelf. We find a continuous drape of sediment over the seafloor, including deep and  
<sup>27</sup> narrow fault-bound sedimentary basins beneath the Siple Coast.

<sup>28</sup> Using airborne gravity data, and distributed seismic constraints over the ice  
<sup>29</sup> shelf, we develop and implement a gravity inversion to recover a higher-resolution  
<sup>30</sup> bathymetry model beneath the ice shelf. This bathymetry model and our quantifica-  
<sup>31</sup> tion of spatial uncertainty highlight locations likely important for sub-ice shelf ocean  
<sup>32</sup> circulation and possible recent pinning points. In the process of these geophysical  
<sup>33</sup> investigations, we reveal a wide range of insights relating to how bathymetry and  
<sup>34</sup> geology play a critical role in the past, present, and future dynamics of the ice sheet,  
<sup>35</sup> and how this region has developed over its tectonic history.

## <sup>36</sup> Plain language summary

<sup>37</sup> The Ross Ice Shelf in Antarctica is a vast expanse of floating ice, hundreds of meters  
<sup>38</sup> thick, which is connected to the ice on land. It plays a crucial role in slowing down  
<sup>39</sup> the flow of ice from the Antarctic Ice Sheet into the ocean. Understanding how this  
<sup>40</sup> ice will respond to a warming world requires knowledge of the Earth's properties that  
<sup>41</sup> influence its behaviour. These properties include the depth of the seafloor beneath  
<sup>42</sup> the ice shelf, the topography beneath the ice on land, and geological features like  
<sup>43</sup> faults and rock types. However, accessing and surveying the sub-Ross Ice Shelf is  
<sup>44</sup> challenging, leading to limited knowledge.

<sup>45</sup> In this thesis, we utilized data collected during an airborne survey of the entire  
<sup>46</sup> Ross Ice Shelf to investigate the depths of the seafloor and the underlying geology.  
<sup>47</sup> By analyzing measurements of Earth's magnetic field across the ice shelf, we reveal  
<sup>48</sup> the thickness of sediment beneath the seafloor. This is possible due to variations  
<sup>49</sup> in magnetic properties between sediment and bedrock. The thickness of this layer

---

50 of sediment ranges from tens of meters to several kilometers. Additionally, we de-  
51 termine the shape of the underlying bedrock, which helps identify probable fault  
52 locations.

53 We also utilized measurements of changes in Earth's gravity field across the ice  
54 shelf to estimate the depth of the seafloor, in a process called a gravity inversion.  
55 This method is feasible since variations in the underwater topography (bathymetry)  
56 result in small, measurable changes in Earth's gravity, due to the density difference  
57 between the seafloor and the water. This bathymetry model, along with our as-  
58 sessment of uncertainties, identifies areas beneath the ice shelf that likely influence  
59 ocean currents as well as potential locations where the ice shelf was anchored to the  
60 bedrock in the recent past.

61 Through these geophysical investigations, we gained valuable insights into how  
62 features of the underlying Earth have influenced the behaviour of the overlying ice  
63 in the Ross Ice Shelf region, both historically and in the future. This information  
64 enhances our understanding of the Ross Ice Shelf region and its interaction with the  
65 underlying Earth.

## <sup>66</sup> Acknowledgements

<sup>67</sup> I would like to express my gratitude to the following individuals and organizations  
<sup>68</sup> for their invaluable support and guidance throughout this thesis.

<sup>69</sup>  
<sup>70</sup> First and foremost I would like to thank my advisors, Huw Horgan and Fabio  
<sup>71</sup> Caratori-Tontini for their unwavering support, patience, and mentorship. Huw, I  
<sup>72</sup> will always appreciate your effort to include me in the two field seasons to Antarc-  
<sup>73</sup> tica. Those trips included some of my most valued experiences, which I have you to  
<sup>74</sup> thank for. You have had an immeasurable impact on my development as a scien-  
<sup>75</sup> tist yet gave me space to pursue my own interests and styles. Fabio, through your  
<sup>76</sup> continuous encouragement and belief in my abilities you gave me the confidence to  
<sup>77</sup> explore many challenging aspects of this thesis I would have otherwise omitted.

<sup>78</sup>  
<sup>79</sup> To two of my supporting academics, Christine Siddoway and Kirsty Tinto. With-  
<sup>80</sup> out witnessing your dedication and enthusiasm for Antarctic science I would not have  
<sup>81</sup> pursued this PhD. I hope for years of collaboration to come! To the various members  
<sup>82</sup> of K863; Andrew, Jenny, Hamish, Will, Bob, and Caitlin, there couldn't have been  
<sup>83</sup> a better group to spend so much time with in the deep field. Thank you for making  
<sup>84</sup> those two trips such an incredible part of my PhD. To the open-source coding com-  
<sup>85</sup> munities, including Fatiando, PyGMT and Software Underground, especially Wei Ji  
<sup>86</sup> Leong, Santi Soler and Leo Uieda, thank you for the wonderful tools, tutorials, and  
<sup>87</sup> individual support you have offered me throughout my journey of learning to code.

<sup>88</sup>  
<sup>89</sup> To the various academics and staff on the 5th floor of the Cotton Building, thank  
<sup>90</sup> you for years of great conversations over lunch, beers, or bike rides. Thank you to  
<sup>91</sup> the friends who made living in and exploring NZ so great; Fran, Chris, Alanna,  
<sup>92</sup> Marjo, Knut, Callum, Dina, Flo. Charlotte, thank you for the unconditional sup-  
<sup>93</sup> port throughout this journey, it would not have been possible or as enjoyable without  
<sup>94</sup> you. To my family, thanks for the continuous encouragement and love from afar.  
<sup>95</sup> Knowing I always had you all to count on back home gave me the stability I needed.

<sup>96</sup>  
<sup>97</sup> To the reviewers of this thesis; Andrew Gorman, Simon Lamb, and Paul Win-  
<sup>98</sup> berry, thank you for your time spent thoroughly reading and contemplating on this  
<sup>99</sup> work; your suggestions and discussions with me were much appreciated.

<sup>100</sup> Lastly, to the various funders of this research including several grants I have  
<sup>101</sup> received, thank you for the support; GNS Science, the Antarctic Research Centre  
<sup>102</sup> and Antarctica New Zealand.



# <sup>103</sup> Contents

|                         |   |           |
|-------------------------|---|-----------|
| <sup>104</sup> <b>1</b> | <b>Introduction</b>   | <b>15</b> |
| <sup>105</sup> 1.1      | Motivation . . . . .  | 15        |
| <sup>106</sup> 1.2      | Influences on ice dynamics . . . . .                                      | 15        |
| <sup>107</sup> 1.2.1    | Bedrock topography . . . . .  | 15        |
| <sup>108</sup> 1.2.2    | Geologic structures . . . . .   | 18        |
| <sup>109</sup> 1.2.3    | Basal roughness . . . . .   | 19        |
| <sup>110</sup> 1.3      | Ross Ice Shelf . . . . .  | 20        |
| <sup>111</sup> 1.3.1    | Past investigations . . . . .   | 20        |
| <sup>112</sup> 1.4      | Research questions . . . . .  | 21        |
| <sup>113</sup> 1.5      | Outline . . . . .   | 22        |
| <sup>114</sup> 1.6      | Data and Code . . . . .   | 23        |
| <sup>115</sup> <b>2</b> | <b>Airborne magnetic analysis: Basement depths and sediment thickness</b> | <b>25</b> |
| <sup>116</sup> 2.1      | Introduction . . . . .  | 26        |
| <sup>117</sup> 2.2      | Data and Methods . . . . .  | 28        |
| <sup>118</sup> 2.3      | Results . . . . .   | 29        |
| <sup>119</sup> 2.4      | Discussion . . . . .  | 31        |
| <sup>120</sup> 2.4.1    | West Antarctic Rift System extensional basins . . . . .                   | 31        |
| <sup>121</sup> 2.4.2    | Consequences for ice sheet dynamics . . . . .                             | 33        |
| <sup>122</sup> 2.4.3    | Mid-Shelf High - Central High . . . . .                                   | 33        |
| <sup>123</sup> 2.4.4    | Thermal subsidence and sedimentation . . . . .                            | 34        |
| <sup>124</sup> 2.5      | Conclusions . . . . .   | 35        |
| <sup>125</sup> 2.6      | Open Research . . . . .   | 35        |
| <sup>126</sup> 2.7      | Acknowledgements . . . . .  | 35        |
| <sup>127</sup> <b>3</b> | <b>Gravity inversion: a tool for bathymetry modelling</b>                 | <b>37</b> |
| <sup>128</sup> 3.1      | Introduction . . . . .  | 38        |
| <sup>129</sup> 3.2      | Methods . . . . .   | 40        |
| <sup>130</sup> 3.2.1    | Geophysical inversion . . . . .   | 40        |
| <sup>131</sup> 3.2.1.1  | Non-Linear inversions . . . . .   | 42        |
| <sup>132</sup> 3.2.1.2  | Geometric inversions . . . . .  | 42        |
| <sup>133</sup> 3.2.2    | Forward modelling . . . . .   | 42        |
| <sup>134</sup> 3.2.2.1  | Discretization . . . . .  | 43        |
| <sup>135</sup> 3.2.2.2  | Gravity edge effects . . . . .  | 43        |
| <sup>136</sup> 3.2.3    | Isolating anomalies . . . . .   | 44        |
| <sup>137</sup> 3.2.4    | Regional vs. Residual gravity . . . . .                                   | 45        |
| <sup>138</sup> 3.2.5    | Running the inversion . . . . .   | 46        |
| <sup>139</sup> 3.2.5.1  | Jacobian matrix . . . . .   | 46        |

|     |          |   |           |
|-----|----------|---|-----------|
| 141 | 3.2.5.2  | Least-squares solver . . . . .                  | 48        |
| 142 | 3.2.5.3  | Regularization . . . . .                        | 48        |
| 143 | 3.2.6    | Stopping Criteria . . . . .                     | 50        |
| 144 | 3.2.7    | Software implementation . . . . .               | 51        |
| 145 | 3.3      | Synthetic models . . . . .                      | 51        |
| 146 | 3.3.1    | Simple model . . . . .                          | 52        |
| 147 | 3.3.1.1  | Model setup . . . . .                           | 52        |
| 148 | 3.3.1.2  | Cross validation . . . . .                      | 53        |
| 149 | 3.3.1.3  | Comparing vertical derivative methods . . . . . | 54        |
| 150 | 3.3.1.4  | Added noise . . . . .                           | 55        |
| 151 | 3.3.1.5  | Down-sampled data . . . . .                     | 56        |
| 152 | 3.3.2    | Ensemble of Noise and Sampling values . . . . . | 58        |
| 153 | 3.4      | Adding a regional component . . . . .           | 60        |
| 154 | 3.4.1    | Regional separation methods . . . . .           | 60        |
| 155 | 3.4.2    | Constraint point minimization . . . . .         | 62        |
| 156 | 3.4.2.1  | Tensioned minimum curvature . . . . .           | 63        |
| 157 | 3.4.2.2  | Bi-harmonic splines . . . . .                   | 63        |
| 158 | 3.4.2.3  | Gridding comparison . . . . .                   | 63        |
| 159 | 3.4.3    | Inversion results . . . . .                     | 65        |
| 160 | 3.4.4    | Ensemble of Noise and Sampling values . . . . . | 66        |
| 161 | 3.4.5    | Simple model comparison . . . . .               | 66        |
| 162 | 3.5      | Ross Sea model . . . . .                        | 67        |
| 163 | 3.5.1    | Observed gravity . . . . .                      | 67        |
| 164 | 3.5.2    | Starting bathymetry . . . . .                   | 69        |
| 165 | 3.5.3    | Gravity misfit . . . . .                        | 70        |
| 166 | 3.5.4    | Inversion . . . . .                             | 71        |
| 167 | 3.5.5    | Uncertainty analysis . . . . .                  | 71        |
| 168 | 3.5.6    | Effects of constraint spacing . . . . .         | 73        |
| 169 | 3.5.7    | Effects of gravity data . . . . .               | 75        |
| 170 | 3.6      | Discussion . . . . .                            | 76        |
| 171 | 3.6.1    | Simple synthetic model . . . . .                | 76        |
| 172 | 3.6.1.1  | Inversion results . . . . .                     | 77        |
| 173 | 3.6.1.2  | Ensemble results . . . . .                      | 77        |
| 174 | 3.6.2    | Regional component . . . . .                    | 79        |
| 175 | 3.6.2.1  | Regional separation methods . . . . .           | 79        |
| 176 | 3.6.2.2  | Constraint point minimization . . . . .         | 79        |
| 177 | 3.6.2.3  | Inversion results . . . . .                     | 80        |
| 178 | 3.6.2.4  | Ensemble results . . . . .                      | 80        |
| 179 | 3.6.3    | Ross Sea model . . . . .                        | 81        |
| 180 | 3.6.3.1  | Effects of the gravity data . . . . .           | 82        |
| 181 | 3.6.3.2  | Effects of the constraints . . . . .            | 83        |
| 182 | 3.6.3.3  | Uncertainties . . . . .                         | 84        |
| 183 | 3.7      | Future work . . . . .                           | 85        |
| 184 | 3.8      | Conclusion . . . . .                            | 85        |
| 185 | <b>4</b> | <b>Ross Ice Shelf bathymetry inversion</b>      | <b>89</b> |
| 186 | 4.1      | Introduction . . . . .                          | 90        |
| 187 | 4.2      | Methods . . . . .                               | 92        |
| 188 | 4.2.1    | Gravity reduction . . . . .                     | 92        |

|     |          |  |            |
|-----|----------|--|------------|
| 189 | 4.2.1.1  | Attraction of normal Earth . . . . .             | 93         |
| 190 | 4.2.1.2  | Topographic mass effects . . . . .               | 94         |
| 191 | 4.2.1.3  | Regional separation . . . . .                    | 98         |
| 192 | 4.2.2    | Bathymetry inversion . . . . .                   | 99         |
| 193 | 4.2.3    | Starting bathymetry . . . . .                    | 100        |
| 194 | 4.2.4    | Uncertainty quantification . . . . .             | 100        |
| 195 | 4.3      | Past inversions . . . . .                        | 103        |
| 196 | 4.3.1    | Gravity reduction comparison . . . . .           | 103        |
| 197 | 4.3.1.1  | Regional separation . . . . .                    | 105        |
| 198 | 4.3.2    | Inversion comparison . . . . .                   | 106        |
| 199 | 4.3.3    | Uncertainty comparison . . . . .                 | 107        |
| 200 | 4.4      | Results . . . . .                                | 107        |
| 201 | 4.4.1    | Starting bathymetry . . . . .                    | 108        |
| 202 | 4.4.2    | Gravity processing results . . . . .             | 111        |
| 203 | 4.4.3    | Gravity reduction results . . . . .              | 112        |
| 204 | 4.4.4    | Inversion results . . . . .                      | 114        |
| 205 | 4.4.5    | Uncertainty . . . . .                            | 114        |
| 206 | 4.4.5.1  | Partitioning uncertainty . . . . .               | 119        |
| 207 | 4.5      | Discussion . . . . .                             | 119        |
| 208 | 4.5.1    | Uncertainties and parameter importance . . . . . | 119        |
| 209 | 4.5.1.1  | Gravity component . . . . .                      | 119        |
| 210 | 4.5.1.2  | Constraints component . . . . .                  | 121        |
| 211 | 4.5.1.3  | Density component . . . . .                      | 121        |
| 212 | 4.5.1.4  | Interpolation component . . . . .                | 122        |
| 213 | 4.5.1.5  | Reducing uncertainties . . . . .                 | 123        |
| 214 | 4.5.1.6  | Past estimations of uncertainty . . . . .        | 123        |
| 215 | 4.5.2    | Past bathymetry models . . . . .                 | 124        |
| 216 | 4.5.2.1  | Starting model comparison . . . . .              | 124        |
| 217 | 4.5.2.2  | Inversion result comparisons . . . . .           | 125        |
| 218 | 4.5.2.3  | Ocean cavity comparison . . . . .                | 129        |
| 219 | 4.5.3    | Implications . . . . .                           | 131        |
| 220 | 4.5.3.1  | New potential pinning points . . . . .           | 131        |
| 221 | 4.5.3.2  | Basal melting . . . . .                          | 131        |
| 222 | 4.5.3.3  | Geologic and tectonic significance . . . . .     | 133        |
| 223 | 4.6      | Conclusion . . . . .                             | 134        |
| 224 | <b>5</b> | <b>Synthesis</b>                                 | <b>137</b> |
| 225 | 5.1      | Geologic structures . . . . .                    | 138        |
| 226 | 5.2      | Inversion . . . . .                              | 138        |
| 227 | 5.3      | Ross Ice Shelf bathymetry . . . . .              | 140        |
| 228 | 5.4      | Geologic controls . . . . .                      | 141        |
| 229 | 5.4.1    | Present controls . . . . .                       | 141        |
| 230 | 5.4.1.1  | Basal melt . . . . .                             | 141        |
| 231 | 5.4.1.2  | Modern pinning points . . . . .                  | 142        |
| 232 | 5.4.1.3  | Sediment distribution . . . . .                  | 144        |
| 233 | 5.4.1.4  | Geothermal heat flux at Siple Coast . . . . .    | 144        |
| 234 | 5.4.2    | Past and future implications . . . . .           | 145        |
| 235 | 5.4.2.1  | Retreat dynamics . . . . .                       | 146        |
| 236 | 5.4.2.2  | Glacial initialization . . . . .                 | 147        |

|     |  |            |
|-----|--|------------|
| 237 | 5.5 Future work . . . . .  | 148        |
| 238 | 5.6 Concluding remark . . . . .  | 150        |
| 239 | <b>Appendix A</b>  | <b>151</b> |
| 240 | A.1 Introduction . . . . .   | 151        |
| 241 | A.2 Depth to basement assumptions . . . . .                                  | 151        |
| 242 | A.3 Magnetic data collection, processing, and Werner deconvolution . . . . . | 152        |
| 243 | A.4 Tying magnetic basement to seismic basement . . . . .                    | 153        |
| 244 | A.5 Tying Ross Sea magnetic basement to Ross Ice Shelf magnetic basement     | 154        |
| 245 | A.6 Gridding, merging, and filtering . . . . .                               | 154        |
| 246 | A.7 Sediment thickness and $\beta$ -factor calculations . . . . .            | 155        |
| 247 | A.8 Uncertainties . . . . .  | 156        |
| 248 | <b>Appendix B</b>  | <b>163</b> |
| 249 | B.1 Synthetic inversion with a regional field . . . . .                      | 163        |
| 250 | B.2 Ross Sea synthetic model . . . . .                                       | 164        |
| 251 | <b>Appendix C</b>  | <b>169</b> |
| 252 | C.1 Gravity disturbance vs anomaly . . . . .                                 | 169        |
| 253 | <b>Appendix D Antarctic-Plots</b>  | <b>171</b> |
| 254 | D.1 Fetch . . . . .  | 171        |
| 255 | D.2 Map . . . . .  | 172        |
| 256 | D.3 Profile . . . . .  | 172        |
| 257 | D.4 Regions . . . . .  | 172        |

# <sup>258</sup> List of Figures

|     |      |  |    |
|-----|------|--|----|
| 259 | 1.1  | Past observations and future predictions of sea level rise . . . . .   | 16 |
| 260 | 1.2  | Summary of existing geologic and geophysical data for Antarctica . .   | 17 |
| 261 | 2.1  | Bathymetry, magnetics, and acoustic basement . . . . .                 | 27 |
| 262 | 2.2  | Ross Sea magnetic and seismic basement comparison . . . . .            | 29 |
| 263 | 2.3  | Basement elevation and sediment thickness . . . . .                    | 30 |
| 264 | 2.4  | Tectonic interpretation of the sub-Ross Ice Shelf . . . . .            | 32 |
| 265 | 3.1  | Ice shelves of Antarctica . . . . .                                    | 39 |
| 266 | 3.2  | Equivalent methods of discretizing a density contrast . . . . .        | 44 |
| 267 | 3.3  | Annulus approximation of a vertical prism . . . . .                    | 47 |
| 268 | 3.4  | Training and testing set configuration . . . . .                       | 49 |
| 269 | 3.5  | Weighting grid for the simple synthetic inversion . . . . .            | 50 |
| 270 | 3.6  | Simple synthetic model bathymetry . . . . .                            | 52 |
| 271 | 3.7  | Simple synthetic gravity anomalies . . . . .                           | 53 |
| 272 | 3.8  | Annulus approximation inversion results . . . . .                      | 54 |
| 273 | 3.9  | Annulus approximation inversion cross-validation and profile . . . . . | 54 |
| 274 | 3.10 | Finite differences inversion results . . . . .                         | 55 |
| 275 | 3.11 | Finite differences and annulus approximation convergence curves . .    | 55 |
| 276 | 3.12 | Synthetic inversion with noise . . . . .                               | 56 |
| 277 | 3.13 | Synthetic inversion with noise, CV and profile . . . . .               | 56 |
| 278 | 3.14 | Creating a low-resolution observed gravity survey . . . . .            | 57 |
| 279 | 3.15 | Synthetic inversion with sampled gravity . . . . .                     | 58 |
| 280 | 3.16 | Synthetic inversion with sampled gravity, CV and profile . . . . .     | 59 |
| 281 | 3.17 | Gravity data ensemble for synthetic model . . . . .                    | 59 |
| 282 | 3.18 | Gravity anomalies with a regional field . . . . .                      | 61 |
| 283 | 3.19 | Regional separation methods . . . . .                                  | 62 |
| 284 | 3.20 | Constraint point minimization gridding techniques . . . . .            | 64 |
| 285 | 3.21 | Synthetic inversion with regional component, CV and profile . . . . .  | 65 |
| 286 | 3.22 | Synthetic inversion with regional component results . . . . .          | 65 |
| 287 | 3.23 | Gravity data ensemble with regional component . . . . .                | 66 |
| 288 | 3.24 | Ross Sea semi-synthetic model . . . . .                                | 68 |
| 289 | 3.25 | Ross Sea synthetic airborne survey . . . . .                           | 69 |
| 290 | 3.26 | Ross Sea starting bathymetry . . . . .                                 | 70 |
| 291 | 3.27 | Ross Sea synthetic gravity anomalies . . . . .                         | 71 |
| 292 | 3.28 | Ross Sea inversion, CV and convergence . . . . .                       | 72 |
| 293 | 3.29 | Ross Sea inversion results . . . . .                                   | 72 |
| 294 | 3.30 | Ross Sea Monte Carlo simulation . . . . .                              | 74 |
| 295 | 3.31 | Constraint spacing effects . . . . .                                   | 75 |
| 296 | 3.32 | Ross Sea ensemble of noise levels and gravity spacing . . . . .        | 76 |

|     |   |     |
|-----|---|-----|
| 297 | 3.33 Grouped synthetic inversion ensemble . . . . .                             | 78  |
| 298 | 3.34 Synthetic inversion error and regional error . . . . .                     | 80  |
| 299 | 3.35 Grouped synthetic inversion with regional ensemble . . . . .               | 81  |
| 300 | 3.36 Ross Sea inversion error and regional error . . . . .                      | 82  |
| 301 | 3.37 Grouped Ross Sea inversion with regional ensemble . . . . .                | 83  |
| 302 | 4.1 Ross Ice Shelf inversion inputs . . . . .                                   | 91  |
| 303 | 4.2 Schematic inversion workflow diagram . . . . .                              | 93  |
| 304 | 4.3 Observed gravity data reduction for Antarctica . . . . .                    | 95  |
| 305 | 4.4 Components of the topographic mass effect . . . . .                         | 96  |
| 306 | 4.5 Discretizing the topographic mass effect . . . . .                          | 97  |
| 307 | 4.6 Topographic mass effect for Antarctica . . . . .                            | 98  |
| 308 | 4.7 Schematic Monte Carlo workflow diagram . . . . .                            | 102 |
| 309 | 4.8 Random vs Latin hypercube sampling . . . . .                                | 103 |
| 310 | 4.9 Ross Ice Shelf starting bathymetry . . . . .                                | 109 |
| 311 | 4.10 Ross Ice Shelf weighting grid . . . . .                                    | 110 |
| 312 | 4.11 Re-levelling of the ROSETTA-Ice gravity data . . . . .                     | 111 |
| 313 | 4.12 Gravity reduction results for the Ross Ice Shelf . . . . .                 | 113 |
| 314 | 4.13 Ross Ice Shelf singular bathymetry inversion results . . . . .             | 115 |
| 315 | 4.14 Latin hypercube sampling distributions and correlations . . . . .          | 116 |
| 316 | 4.15 Ross Ice Shelf inverted bathymetry and uncertainty . . . . .               | 117 |
| 317 | 4.16 Monte Carlo results . . . . .  | 118 |
| 318 | 4.17 Inverted bathymetry comparisons . . . . .                                  | 125 |
| 319 | 4.18 Ross Ice Shelf assorted cross-sections . . . . .                           | 128 |
| 320 | 4.19 Water column thickness comparisons . . . . .                               | 130 |
| 321 | 4.20 Basal melt . . . . .   | 132 |
| 322 | 5.1 Ross Embayment geophysical and geologic information . . . . .               | 139 |
| 323 | 5.2 Uncertainty bounds for Ross Ice Shelf bathymetry and ocean cavity .         | 142 |
| 324 | 5.3 3D perspective view of Ross Ice Shelf . . . . .                             | 146 |
| 325 | A.1 Various Ross Ice Shelf grids . . . . .                                      | 157 |
| 326 | A.2 OIB 403.3 magnetic and seismic basement comparison . . . . .                | 158 |
| 327 | A.3 Werner deconvolution solutions for ROSETTA-Ice lines . . . . .              | 159 |
| 328 | A.4 Unfiltered magnetic basement and point solutions . . . . .                  | 160 |
| 329 | A.5 Uncertainty limits of basement and sediment thickness . . . . .             | 161 |
| 330 | A.6 Misfit distributions between magnetic and seismic basement . . . . .        | 162 |
| 331 | B.1 Comparison of four methods of regional separation . . . . .                 | 163 |
| 332 | B.2 Constraint point minimization gridding comparison profiles . . . . .        | 164 |
| 333 | B.3 Synthetic inversion with regional and noise, CV and profile . . . . .       | 165 |
| 334 | B.4 Synthetic inversion with regional and noise, results . . . . .              | 165 |
| 335 | B.5 Inversion and regional error for model with regional and noise . . . . .    | 165 |
| 336 | B.6 Synthetic inversion with regional and re-sampling, CV and profile . . . . . | 166 |
| 337 | B.7 Synthetic inversion with regional and re-sampling, results . . . . .        | 166 |
| 338 | B.8 Inversion and regional error for model with regional and low-res gravity    | 166 |
| 339 | B.9 Inversion and regional error for Ross Sea constraint ensemble . . . . .     | 167 |
| 340 | C.1 Gravity disturbance vs. anomaly . . . . .                                   | 169 |

# <sup>341</sup> List of Tables

|                |   |     |
|----------------|---|-----|
| <sup>342</sup> | 3.1 Simple synthetic model summary . . . . .                            | 67  |
| <sup>343</sup> | 4.1 Bathymetry uncertainties comparison . . . . .                       | 120 |
| <sup>344</sup> | A.1 Previous Ross Ice Shelf seismic sediment thickness measurements . . | 156 |



<sup>345</sup> **Chapter 1**

<sup>346</sup> **Introduction**

<sup>347</sup> **1.1 Motivation**

<sup>348</sup> Improving projections of the rate of global sea level rise in response to a warming  
<sup>349</sup> world is vital for effectively mitigating future environment and socio-economic im-  
<sup>350</sup> pacts (Durand et al., 2022). A large portion of the uncertainties in modern and  
<sup>351</sup> projected sea level rise is related to the contribution from the Antarctic Ice Sheet  
<sup>352</sup> (Figure 1.1b, Bamber et al., 2022; Edwards et al., 2021; Otosaka et al., 2023; Slater  
<sup>353</sup> & Shepherd, 2018). The Antarctic Ice Sheet contains a total volume of ice equivalent  
<sup>354</sup> to 57.2 m of sea level rise (Fretwell et al., 2013). Satellite observations show that  
<sup>355</sup> Antarctica contributed  $\sim$  7.4 mm to mean sea level since 1992 (Otosaka et al., 2023),  
<sup>356</sup> and of the various components of sea level rise, the contribution from Antarctica is  
<sup>357</sup> accelerating the fastest (Figure 1.1a, Nerem et al., 2018). Since the early 1990s, the  
<sup>358</sup> sea level contribution from Antarctica has increased by 25% (Otosaka et al., 2023).  
<sup>359</sup> By the end of the century, Antarctica is projected to contribute between 0.03 and  
<sup>360</sup> 0.28 m to mean sea level (RCP 8.5, Intergovernmental Panel on Climate Change  
<sup>361</sup> (IPCC), 2022). Optimal strategies for preparing coastal communities to best miti-  
<sup>362</sup> gate the impacts of rising sea level depends on where in this range of uncertainties  
<sup>363</sup> the true sea level rise will be. Some of the uncertainty in how the Antarctic Ice  
<sup>364</sup> Sheet will respond to a warming world stems from a lack of understanding of the  
<sup>365</sup> complex interactions between the ice and the underlying earth (e.g. Schlegel et al.,  
<sup>366</sup> 2018; Zhao et al., 2018).

<sup>367</sup> **1.2 Influence of bathymetry, topography, and geol-**  
<sup>368</sup> **ogy on ice dynamics**

<sup>369</sup> The underlying Earth influences ice sheets through several mechanisms, which I  
<sup>370</sup> group as those resulting from bedrock topography, geologic structures, and bedrock  
<sup>371</sup> physical properties. Here I describe each of these categories of influences on the  
<sup>372</sup> Antarctic Ice Sheet, followed by introducing the specific study area, the Ross Ice  
<sup>373</sup> Shelf.

<sup>374</sup> **1.2.1 Bedrock topography**

<sup>375</sup> Offshore bathymetry and onshore bed topography exert several fundamental con-  
<sup>376</sup> trols on how the Antarctic Ice Sheet behaves. Offshore, where the ice is floating, the

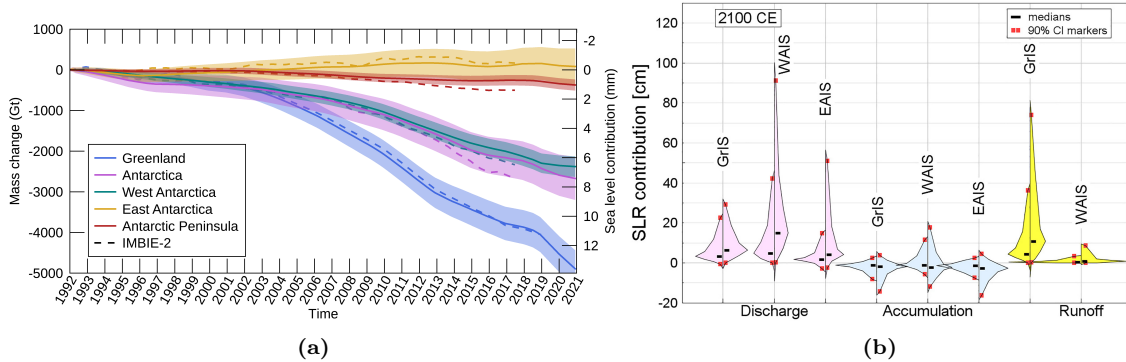


**Figure 1.1:** Past observations and future predictions of sea level rise. **a)** Observed cumulative mass change and sea level contributions from the various ice sheets. Data comes from satellite-altimetry estimates of volume changes, gravimetric estimates of mass changes, and quantification of input-output fluxes. Figure from Otosaka et al. (2023). **b)** Probability distributions for projected global sea level rise contributions for the year 2100 from the Greenland Ice Sheet (GrIS), West Antarctic Ice Sheet (WAIS), and East Antarctic Ice Sheet (EAIS), separated into three processes; discharge, accumulation, and runoff. Left and right sides of each distribution show the +2°C and +5°C global temperature trajectories, respectively. Figure from Bamber et al. (2022).

influence of the bathymetry is limited to the guiding of ocean circulations. Bathymetric ridges have been shown to block, or re-direct, the inflow of melt-inducing waters to the ocean cavity beneath floating ice shelves (De Rydt et al., 2014; Goldberg et al., 2020; Zhao et al., 2019). Approximately 75% of Antarctica's coastline is composed of these floating ice shelves, and 83% of total ice discharged into the Southern Ocean from Antarctica is through these shelves, highlighting their significance to Antarctica's ice budget (Rignot et al., 2013). Of the 83% of total ice loss from Antarctica through ice shelves, basal melt is responsible for approximately half (Greene et al., 2022; Rignot et al., 2013). Some of this melt occurs from surface waters, where bathymetry has little effect, but for many of the largest ice shelves, the majority of basal melt occurs along the deep grounding zone (Adusumilli et al., 2020). Here, the melt-inducing water bodies are dense and flow into the ice shelf cavities along the seafloor (Holland, 2008; Tinto et al., 2015). Therefore, bathymetric features act to guide or block these circulations from reaching the grounding zone where they can melt the ice base. In addition to steering ocean currents, bed topography, in regions of grounded ice, acts to steer the ice flow.

393

As revealed by extensive seismic and swath bathymetry data in Antarctica's Ross Sea (Figure 1.2a), the dynamics of an advancing or retreating ice sheet are predominantly controlled by the physiography of the bed (Anderson et al., 2019; Halberstadt et al., 2016). If large troughs and banks exist, advancing ice is initially confined by these features, while the banks remain ice-free (Anderson et al., 2014). Eventually, after the ice has covered the entire region, the retreat is initially confined to these narrow troughs, while the banks retain grounded ice for much longer (Anderson et al., 2019; Halberstadt et al., 2016). As the ice thins or retreats into regions of deeper bed topography, these banks remain grounded, while the rest of the ice sheet decouples from the bed, begins floating and forms an ice shelf (Shipp et al., 1999). This remaining grounded ice on bathymetric highs forms pinning points.

405

Pinning points are regions of locally grounded ice within a floating ice shelf (Matsuoka et al., 2015). The friction between the bed and ice base at these points

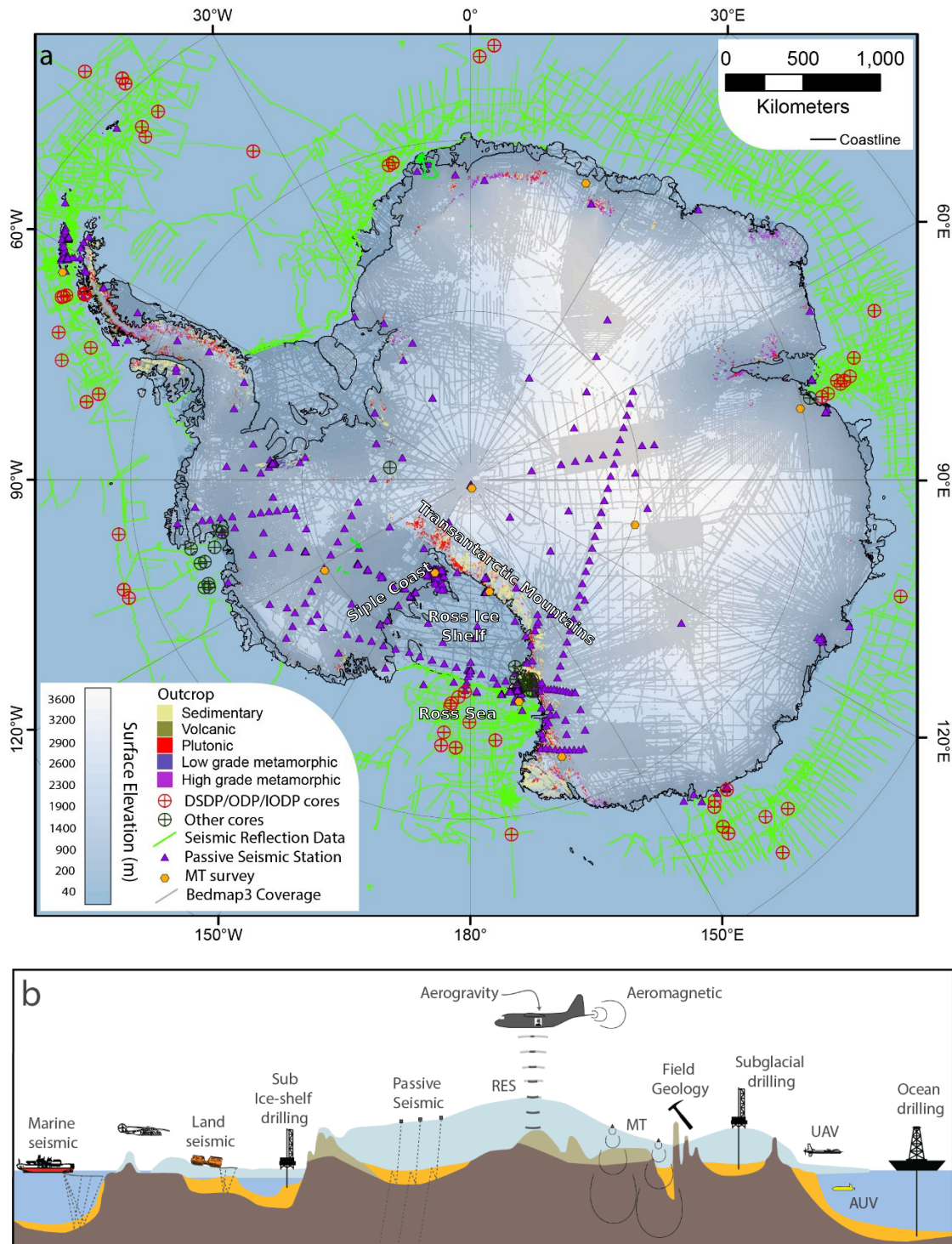


**Figure 1.2:** Summary of existing geologic and geophysical data for Antarctica. **a)** Map of data coverage in Antarctica indicating outcropping regions, drill core sites, seismic and magnetotelluric surveys, and bed elevation data points of Bedmap3, mostly from airborne radio-echo sounding (Frémand et al., 2022). **b)** Various methods of acquiring information sub-surface geology. Figure adapted from Aitken et al. (2023b).

408 impart a critical resisting force to the discharge of upstream ice; an effect known as  
 409 buttressing (Dupont & Alley, 2005; Thomas, 1979). Since the base of ice shelves  
 410 is flat relative to the underlying bathymetry, the morphology of the seafloor is the  
 411 dominant control of the location and geometry of these pinning points. The bedrock  
 412 topography has been thought to be relatively constant over a millennial timescale,

meaning that pinning points' geometries vary mostly by temporal changes in the ice thickness. However, recent studies of glacial isostatic adjustment, the vertical rebound of the Earth following deglaciation, throughout West Antarctica have demonstrated high spatial variability and short (multi-centennial-to-millennial) timescales for these vertical land movements (Barletta et al., 2018; Coulon et al., 2021; Kachuck et al., 2020). As the bedrock beneath portions of West Antarctica continues to rebound, the number and extent of these pinning points will likely increase, possibly providing a stabilizing effect to the ice sheet.

421

All of these above controls on ice dynamics imparted by the physiography of the bed rely on accurate knowledge of bed topography and bathymetry. Due to the inherently challenging nature of Antarctic fieldwork, and the logistical challenge of measuring bed elevations beneath thick ice, 50% of the Antarctic Ice Sheet is more than 5 km from the nearest measurement of bed elevation (Figure 1.2a, Morlighem et al., 2020). This value increases greatly if the floating ice shelves are included. For grounded ice, the dominant techniques for direct measurements of bed elevation data are airborne radio-echo sounding, over-snow radar, and seismic surveying (Figure 1.2b, Fretwell et al., 2013). In the open ocean, bathymetry data are typically collected with ship-borne multibeam echo sounding, seismic surveying (Figure 1.2b), or from satellite-altimetry. Acquiring bathymetry data beneath floating ice shelves presents a particular challenge. The efficient shipborne methods are unavailable since the ice shelves are persistent year-round, unlike the sea ice in the open ocean. Radio-echo sounding, either ground-based or airborne, cannot image through the water column. Direct observations through drilling are possible and exist, but typically require drilling through 100's to 1000's of meters of ice (Figure 1.2, Clough & Hansen, 1979; Patterson et al., 2022). Autonomous underwater vehicles (Figure 1.2b) present another option, but are expensive and have limited range (Dowdeswell et al., 2008; Nicholls et al., 2006). The only feasible method of direct observations of sub-ice shelf bathymetry is over-snow seismic surveying (Figure 1.2b). However, for the vast area of many ice shelves, even sparse coverage ( $\sim 50$  km spacing) of seismic points across the ice shelf takes several field seasons of data acquisition (Bentley, 1984).

### 1.2.2 Geologic structures

Additional influences on the overriding ice include the delivery of geothermal heat and subglacial water to the ice base and the vertical deformation of the bedrock in response to changing ice loads. Geothermal heat influences ice dynamics through several mechanisms; 1) increasing the temperature of the ice which lowers its viscosity, leading to enhanced flow via internal deformation (Llubes et al., 2006), 2) meltwater lubrication of the bed reduces friction, enhancing flow (Pollard et al., 2005), and 3) increasing the ability of the bed to deform via increased pore-fluid pressure, which increases ice flow (Tulaczyk et al., 2000). The latter two effects, while enhanced by geothermal heat through the melting of ice, also occur with simply the presence of liquid water at the ice-bed interface. As briefly mentioned in the above section, glacial isostatic adjustments of the bedrock following changes in ice load can influence the ice by altering the geometry and locations of grounded ice.

458

Each of these effects; geothermal heat flow, subglacial water availability, and

460 glacial isostatic adjustment, are in turn influenced by geologic structures within the  
461 upper crust. A portion of subglacial water comes from either transport along the  
462 ice-bed interface, or from the melting of the ice base. However, an often overlooked  
463 component of the subglacial hydrologic system is groundwater stored in deep sedi-  
464 mentary aquifers. For example, hydrologic modelling of the ice streams of the Siple  
465 Coast (Figure 1.2a) estimated the components of the hydrologic budget to be 8%  
466 from local basal melting, 47% from inflow from the ice sheet interior, and 45% from  
467 groundwater reservoirs (Christoffersen et al., 2014). These modelling observations of  
468 extensive groundwater have been recently verified beneath the Whillans Ice Stream  
469 by a magnetotelluric survey. This survey imaged an extensive groundwater aquifer  
470 within a sedimentary basin, containing at least an order of magnitude more water  
471 than the shallow hydrologic system (Gustafson et al., 2022). The vertical flow of this  
472 basinal groundwater is controlled by the pressure of the overriding ice sheet. As this  
473 overburden pressure decreases with thinning ice, groundwater is discharged to the  
474 ice base (Gooch et al., 2016; Li et al., 2022). This discharge is likely concentrated  
475 along pre-existing weaknesses or impermeable surfaces, such as fault damage zones,  
476 or the margins of crystalline basement (Jolie et al., 2021). During this ice-induced  
477 hydraulic unloading, regional geothermal heat is advected along the fluid pathways,  
478 leading to potentially highly elevated heat flow delivered to the ice base (Li et al.,  
479 2022; Ravier & Buoncristiani, 2018). In addition to concentrating both subglacial  
480 water and geothermal heat, these faults, or more generically, regions of the crust  
481 which have experienced recent faulting, will respond differently to stresses induced  
482 by glacial isostatic adjustment. To a first order, the isostatic response of the solid-  
483 earth to changing ice load is controlled by the rheology of the mantle (Whitehouse  
484 et al., 2019). However, on a more local scale, pre-existing faults are shown to ac-  
485 commodate glacial isostatic rebound-induced stresses (Peltier et al., 2022; Steffen  
486 et al., 2021).

487

488 To be able to understand the above influences on the ice, we must have some  
489 fundamental knowledge of the geologic structures beneath the ice. This includes  
490 knowing where sedimentary basins, and possible aquifers within, are located, where  
491 faults likely intersect the ice base, and the geometry of the crystalline basement.  
492 Each of these components is difficult to image directly. Drilling, seismic surveys,  
493 or geologic analysis of rock outcrops all provide valuable information but are not  
494 feasible to cover wide regions (Figure 1.2). Indirect methods are therefore needed.  
495 These include techniques such as gravity, magnetic, or electromagnetic methods.  
496 Each of these techniques records measurements of the spatial variation of a poten-  
497 tial field, such as the Earth’s gravity, magnetic, or electromagnetic fields. These  
498 fields are all partially dependant on a physical Earth property, such as rock density,  
499 magnetic susceptibility, or resistivity. From these relationships, sub-surface geologic  
500 information can be modelled.

### 501 1.2.3 Basal roughness

502 The last major influence on the ice from the underlying Earth I present is the rough-  
503 ness of the bed which the ice sheet flows over. This bed roughness is important on  
504 both a micro and macro scale. At a micro-scale, roughness is determined by the  
505 material of which the bed is composed. A bed of erosion-resistance crystalline base-  
506 ment, for example, can greatly hinder the flow of ice. This material results in high

friction with the ice base, slowing the sliding of ice (Bell et al., 1998). Conversely, beds composed of fine-grained tills allow fast ice flow. This fast flow is predominantly due to deformation within the till as the ice flows (Alley et al., 1986). In between the end members of crystalline basement and fine grain till are lithified sedimentary rocks, for example. This type of bed may initially lead to high friction with the ice, but due to their high erodability, sedimentary rock will quickly generate till (Anandakrishnan et al., 1998). A macro-scale view of basal roughness is also important for ice dynamics. As observed at the Siple Coast (Figure 1.2a) ice streams, there is a strong inverse relation between bed roughness, from scales of 5 to  $>40$  km, and ice stream velocities (Siegert et al., 2004). The composition of the bed also plays an important role in the total effective resistance imparted on ice flow from pinning points (Still et al., 2019).

519

To best quantify the effect of basal roughness on ice dynamics, information on the material properties of the bed is needed. While sediment samples beneath the ice yield valuable information, they may only represent the bed at the specific location where they were sampled. The most fundamental information needed is the generic rock type of the bed, namely, is the bed loose, unconsolidated sediment, lithified sedimentary rock, or crystalline rock? Aitken et al. (2023b) provide a detailed review of Antarctica's sedimentary basins, and the methods employed to determine both the presence of sediment and the sediment thickness. These methods, as well as the methods described in the above sections, are shown in Figure 1.2, as reproduced from Aitken et al. (2023b).

530

With the dominant influences from the underlying Earth on ice dynamics laid out, I will now introduce the study area of this thesis, Antarctica's Ross Ice Shelf.

## 532 1.3 Ross Ice Shelf

The Ross Ice Shelf is Antarctica's largest ice shelf ( $\sim 480,000$  km $^2$ ), Figure 1.2). It is situated between the Transantarctic Mountains and Marie Byrd Land. It buttresses a catchment of ice that flows from both the East and West Antarctic Ice Sheets. This catchment contains 11.6 m of global sea level equivalent (Fretwell et al., 2013; Rignot et al., 2011; Tinto et al., 2019). Compared to many other ice shelves, the Ross Ice Shelf is currently relatively stable (Moholdt et al., 2014; Rignot et al., 2013). However, geologic evidence from throughout the Ross Sea and the Siple Coast shows that in the past  $\sim 7,000$  years the shelf has experienced rapid destabilization, disintegration, and large-scale grounding line retreat (e.g., Naish et al., 2009; Venturelli et al., 2020). This major Holocene retreat is thought to have been primarily caused by ocean forcings (Lowry et al., 2019), as bathymetric troughs guided in the inflow of melt-inducing ocean circulations (Tinto et al., 2019). Once destabilized, the grounding line retreat from the outer continental shelf to the present-day location was controlled primarily by the physiography and geology of the bed (Anderson et al., 2019; Halberstadt et al., 2016). This shows the importance of the underlying Earth's influence on the dynamics of the Ross Ice Shelf.

### 549 1.3.1 Past investigations

By examining various influences on ice dynamics, I identified some key data needed to understand these influences. These data included onshore bed topography, off-

552 shore bathymetry, the distribution of sediment, and upper crustal structures such  
553 as faults and the topography of the basement. Here, I summarize the history of  
554 data collection in the Ross Ice Shelf region specific to these geologic and physio-  
555 graphic features. Geological and geophysical exploration has occurred in the Ross  
556 Embayment for over a century. The earliest of these include the 1901-1904 *Discovery*  
557 expedition, the 1907-1909 *Nimrod* expedition, and the 1910-1913 *Terra Nova* ex-  
558 pedition. These expeditions laid the groundwork of interest in the Ross Embayment  
559 from a scientific perspective. The first major survey of the Ross Ice Shelf was part  
560 of the 1957-1959 International Geophysical Year traverses. The three over-snow  
561 traverses all included a portion of the ice shelf and collected radar, gravity, and  
562 seismic data to determine ice thickness, surface elevation, and bed elevation (Crary,  
563 1959). These surveys produced early evidence of the extensive below-sea-level bed,  
564 thin crust, and distinct geologic provinces throughout West Antarctica (Bentley et  
565 al., 1960). In the 1970s the Ross Ice Shelf Geophysical and Glaciological Survey  
566 (RIGGS, Bentley, 1984) consisted of a systematic grid of seismic surveys over the  
567 entire ice shelf with an average spacing between survey points of 55 km. After the  
568 RIGGS survey, there were a total of  $\sim$  223 point-source seismic surveys across the  
569 ice shelf, all yielding single-point sub-ice shelf bathymetry depths. Of these, eight  
570 reported sediment thicknesses beneath. Several faults were hypothesized, based on  
571 2D gravity profiles conducted at many of the stations (Greischar et al., 1992). Since  
572 the 1970s, there have been many additional local surveys on the ice shelf, but these  
573 have been focused along the grounding zones (e.g., Horgan et al., 2017; Muto et al.,  
574 2013b; Patterson et al., 2022; Stern et al., 1994; ten Brink et al., 1993; Wannamaker  
575 et al., 2017). The next, and most recent major data-collection campaign on the Ross  
576 Ice Shelf was the ROSETTA-ice project.

577  
578 The Ross Ocean and ice Shelf Environment, and Tectonic setting Through Aero-  
579 geophysical surveys and modelling project (ROSETTA-ice, Tinto et al., 2019), was  
580 a 3-season (2015-2017) airborne geophysical survey of the Ross Ice Shelf. It flew  
581 a regular grid of flight lines, with nominal N-S and E-W line spacings of 10 and  
582 55 km, respectively. During each flight, various geophysical data were collected,  
583 including ice-penetrating radar, gravity, magnetics and laser altimetry. So far, these  
584 ROSETTA-ice data have been used to begin characterizing the geologic nature of  
585 the crust (Tinto et al., 2019), to model the depths to the sea floor (Tinto et al.,  
586 2019), and to quantify basal melt (Das et al., 2020).

587  
588 Following 60 years of surveying and exploration of the Ross Ice Shelf, our fund-  
589 fundamental understanding of the subglacial geology and physiography is still lacking.  
590 For an area almost twice the size of New Zealand, we have approximately 8 locations  
591 of reported sediment thickness, several hypothesized locations of faults, gaps of over  
592 100 km without bathymetric depths, and limited understanding of our uncertainty in  
593 the bathymetry where it has been modelled/interpolated. I propose several research  
594 questions which I aim to answer in this thesis.

## 595 1.4 Research questions

596 The aim of this thesis is to improve our knowledge of boundary conditions beneath  
597 the Ross Ice Shelf in order to better understand the past, present, and future inter-  
598 actions between the ice, ocean, and underlying earth. I aim to accomplish this by

599 answering the following questions:

- 600 1. What is the geologic structure of the upper crust beneath the Ross Ice Shelf?  
601 If there are sediments, what is their thickness and distribution? Where are  
602 the major faults likely located?
- 603 2. How can bathymetry beneath an ice shelf best be modelled? Are there further  
604 improvements that can be made to the currently employed gravity-inversion  
605 process? What are the predominant sources of uncertainty, and how can these  
606 be limited?
- 607 3. How deep is the bathymetry beneath the Ross Ice Shelf and where are we most  
608 and least certain about it?
- 609 4. What are the geologic controls on the Ross Ice Shelf's stability?

## 610 1.5 Outline

611 This thesis is comprised of five chapters.

612  
613 This chapter, Chapter 1, establishes the context behind the research, introduces  
614 the study region, proposes a series of research questions, and contains an outline of  
615 this thesis.

616  
617 Chapter 2 is adapted from a journal article published in Geophysical Research  
618 Letters (Tankersley et al., 2022), reformatted to be included in this thesis. It presents  
619 a model of the basement topography, and overlying sediment distribution, beneath  
620 the Ross Ice Shelf. I use airborne magnetic data from the ROSETTA-ice project,  
621 and a depth-to-magnetic source technique to model the sediment-basement contact.  
622 This reveals large-scale, fault-controlled extensional basins throughout the sub-Ross  
623 Ice Shelf crust. From this, I am able to draw a wide range of inferences on the likely  
624 influence of this basement topography on the past, present, and future ice sheet, as  
625 well as some tectonic implications. These results provide the first holistic view of  
626 the upper crust beneath the Ross Ice Shelf.

627  
628 Chapter 3 details my development of a method to model the depth to the sea floor  
629 beneath a floating ice shelf. This method is a gravity inversion, where observations  
630 of Earth's gravitational field are used to model bathymetry beneath an ice shelf. I  
631 develop open-source Python code with the aim for other researchers to utilize the  
632 inversion. I test the inversion against a suite of synthetic and semi-realistic data.  
633 This confirms the feasibility of using gravity data to attain bathymetry depths in an  
634 Antarctic setting. Additionally, these synthetic tests reveal the relative importance  
635 of various aspects of a gravity inversion. These include the importance of *a priori*  
636 constraints on the bathymetry, the large errors which can be introduced during the  
637 removal of the regional component of gravity, and several suggestions for optimal  
638 survey design to minimize error in the resulting bathymetry model. The use of  
639 Monte Carlo simulation provides both a spatially variable estimation of uncertainty  
640 in the resulting bathymetry and an estimate of the various sources of this uncertainty.

641

642 Chapter 4 uses the inversion algorithm developed in Chapter 3 to create a new  
643 bathymetry model and associated uncertainties beneath the Ross Ice Shelf. The  
644 model shows some major differences with past bathymetry models, highlighting ar-  
645 eas of the ice shelf that should be carefully considered in future surveys. These  
646 include a deeper bathymetric trench along the Transantarctic Mountains, a thicker  
647 ocean cavity along a portion of the ice front which may allow the incursion of warm  
648 ocean waters and a thicker ocean cavity proximal to the Siple Coast grounding  
649 line. My uncertainty analysis shows the region of highest uncertainties is along the  
650 Transantarctic Mountain Front. Within this chapter, we perform a comprehensive  
651 review of past bathymetry-gravity inversions, for all Antarctic studies, and several  
652 Greenland studies. This highlighted some key differences, which I believe I have  
653 improved on.

654  
655 Chapter 5 presents a synthesis of the 3 research chapters, and provides a dis-  
656 cussion of the research questions. Various future works are suggested and the main  
657 conclusions of this thesis are presented. The research chapters in this thesis were  
658 written with the intent to publish, including Chapter 2 which is already published.  
659 Therefore, I have chosen to keep the style of writing consistent throughout the thesis,  
660 with the use of plural possessive pronouns ("we") instead of singular ("I").

## 661 1.6 Data and Code Availability Statement

662 In an effort to adhere to the principles of FAIR scientific investigations, Findability,  
663 Accessibility, Interoperability, and Reusability (Wilkinson et al., 2016), we have  
664 used only open-access data and published all code<sup>1</sup> used in this thesis. Here we  
665 describe where this code and data can be found. All data used from other studies  
666 has been cited within each chapter and can be accessed through their respective  
667 DOIs. However, most of these datasets were downloaded using the Python package  
668 Antarctic-Plots (Tankersley, 2023). I developed this package during this PhD to help  
669 with several aspects of conducting research related to Antarctica. See Appendix D  
670 for an overview of the capabilities of Antarctic-Plots. Analysis in this study was  
671 executed on a computer with an x86\_64 processor with a maximum clock frequency  
672 of 2600 MHz with 56 physical cores, 112 logical cores, and 1TB of RAM, using the  
673 Operating System Linux-Ubuntu.

### 674 Chapter 2

675 All of the Python code used to perform the analysis and create the figures of Chapter  
676 2 is available from the following GitHub repository; <https://github.com/mdtanker/>  
677 RIS\_basement\_sediment, and the version of the repository used in the published  
678 paper is archived at <https://doi.org/10.5281/zenodo.6499863> (Tankersley, 2022).

### 679 Chapters 3 & 4

680 The gravity inversion Python code, the workflow conducted within Jupyter Note-  
681 books, and the creation of all the figures is available from the following GitHub repos-  
682 itory; [https://github.com/mdtanker/RIS\\_gravity\\_inversion](https://github.com/mdtanker/RIS_gravity_inversion) and the version of the  
683 repository used in this thesis is archived at <https://doi.org/10.5281/zenodo.8084469>  
684 (Tankersley et al., 2023).

---

<sup>1</sup>This excludes one component of Chapter 2 which was performed with proprietary software.

685        The code for creating the figures in the remainder of this thesis, and the latex  
686        files of the thesis itself are available at the following GitHub repository; <https://github.com/mdtanker/phdthesis> and is citable with the following DOI; <https://doi.org/10.5281/zenodo.8084606>.  
687  
688

# <sup>689</sup> Chapter 2

## <sup>690</sup> Airborne magnetic analysis: <sup>691</sup> Basement depths and sediment <sup>692</sup> thickness

### <sup>693</sup> Abstract

<sup>694</sup> New geophysical data from Antarctica's Ross Embayment reveal the structure and  
<sup>695</sup> subglacial geology of extended continental crust beneath the Ross Ice Shelf. We use  
<sup>696</sup> airborne magnetic data from the ROSETTA-Ice Project to locate the contact be-  
<sup>697</sup>tween magnetic basement and overlying sediments. We delineate a broad, segmented  
<sup>698</sup> basement high with thin (0-500 m) non-magnetic sedimentary cover which trends  
<sup>699</sup> northward into the Ross Sea's Central High. Before subsiding in the Oligocene, this  
<sup>700</sup> feature likely facilitated early glaciation in the region and subsequently acted as a  
<sup>701</sup> pinning point and ice flow divide. Flanking the high are wide sedimentary basins,  
<sup>702</sup> up to 3700 m deep, which parallel the Ross Sea basins and likely formed during  
<sup>703</sup> Cretaceous-Neogene intracontinental extension. NW-SE basins beneath the Siple  
<sup>704</sup> Coast grounding zone, by contrast, are narrow, deep, and elongate. They suggest  
<sup>705</sup> tectonic divergence upon active faults that may localize geothermal heat and/or  
<sup>706</sup> groundwater flow, both important components of the subglacial system.

### <sup>707</sup> Plain Language Summary

<sup>708</sup> The bedrock geology of Antarctica's southern Ross Embayment is concealed by  
<sup>709</sup> 100s-1000s of meters of sedimentary deposits, seawater, and the floating Ross Ice  
<sup>710</sup> Shelf (RIS). Our research strips away those layers to discover the shape of the  
<sup>711</sup> consolidated bedrock below, which we refer to as the basement. To do this, we use  
<sup>712</sup> the contrast between non-magnetic sediments and magnetic basement rocks to map  
<sup>713</sup> out the depth of the basement surface under the RIS. Our primary data source is  
<sup>714</sup> airborne measurements of the variation in Earth's magnetic field across the ice shelf,  
<sup>715</sup> from flight lines spaced 10 km apart. We use the resulting basement topography  
<sup>716</sup> to highlight sites of possible influence upon the Antarctic Ice Sheet and to further  
<sup>717</sup> understand the tectonic history of the region. We discover contrasting basement  
<sup>718</sup> characteristics on either side of the ice shelf, separated by an N-S trending basement  
<sup>719</sup> high. The West Antarctic side displays evidence of active faults, which may localize  
<sup>720</sup> geothermal heat, accommodate movements of the solid earth caused by changes in

721 the size of the Antarctic Ice Sheet, and control the flow of groundwater between the  
722 ice base and aquifers. This work addresses critical interactions between ice and the  
723 solid earth.

724 **Key Points:**

- 725 1. Aeromagnetic analysis reveals basement surface and evidence of fault-controlled  
726 extensional basins beneath Antarctica's Ross Ice Shelf (RIS).
- 727 2. Active faults at Siple Coast likely influence ice streams through control of  
728 geothermal heat, groundwater, and glacioisostatic adjustments.
- 729 3. A basement high beneath RIS spatially coincides with a lithospheric boundary,  
730 with contrasting sedimentary basins on either side.

731 

## 2.1 Introduction

732 The southern sector of Antarctica's Ross Embayment beneath the Ross Ice Shelf  
733 (RIS; area  $\sim$ 480,000 km $^2$ ) is poorly resolved because the region is not accessible  
734 to conventional seismic or geophysical surveying. Rock exposures on land sug-  
735 gest that Ross Ice Shelf (RIS) crust consists of early Paleozoic post-orogenic sed-  
736 iments, intruded in places by mid-Paleozoic and Cretaceous granitoids (Goodge,  
737 2020; Luyendyk et al., 2003). Following the onset of extension in the mid-Cretaceous,  
738 grabens formed and filled with terrestrial and marine deposits, continuing into the  
739 Cenozoic (e.g. Coenen et al., 2019; Sorlien et al., 2007), as the Ross Embayment  
740 underwent thermal subsidence (Karner et al., 2005; Wilson & Luyendyk, 2009).  
741 The physiography of this region then responded to the onset of glaciation in the  
742 Oligocene (Paxman et al., 2019), coinciding with localized extension in the west-  
743 ern Ross Sea until 11 Ma (Granot & Dyment, 2018). The Oligocene-early-Miocene  
744 paleo-landscape of the Ross Sea sector was revealed by marine seismic data (e.g.  
745 Brancolini et al., 1995; Pérez et al., 2021) and offshore drilling that penetrated crys-  
746 talline basement (DSDP Site 270; Ford & Barrett, 1975) (Figure 2.1). Recognition  
747 of the role of elevated topography in Oligocene formation of the Antarctic Ice Sheet  
748 (DeConto & Pollard, 2003; Wilson et al., 2013) and the likely influence of subglacial  
749 topography upon ice sheet processes during some climate states (Austermann et al.,  
750 2015; Colleoni et al., 2018) motivated our effort to determine basement topography  
751 beneath the Ross Ice Shelf.

752

753 Ice sheet dynamics are of high interest in the RIS region because its grounding  
754 zone (GZ) and pinning points (Still et al., 2019) buttress Antarctica's second-largest  
755 drainage basin (Tinto et al., 2019). Our work in this sensitive region seeks to delimit  
756 the extent and geometry of competent basement because the margins of basement  
757 highs are sites of strong contrasts in permeability that influence the circulation of  
758 subglacial waters. A spectacular example of the confinement of subglacial water  
759 between the ice sheet and basement exists in ice radar profiles for the continental  
760 interior (Bell et al., 2011), but little is known about the subglacial hydrology of  
761 deep groundwater reservoirs within sediment-filled marine basins that receive ter-  
762 restrial freshwater influx (Gustafson et al., 2022; Siegert et al., 2018). These basins  
763 may contain up to 50% of total subglacial freshwater (Christoffersen et al., 2014),  
764 where the discharge and recharge along fault-damage zones (Jolie et al., 2021) is

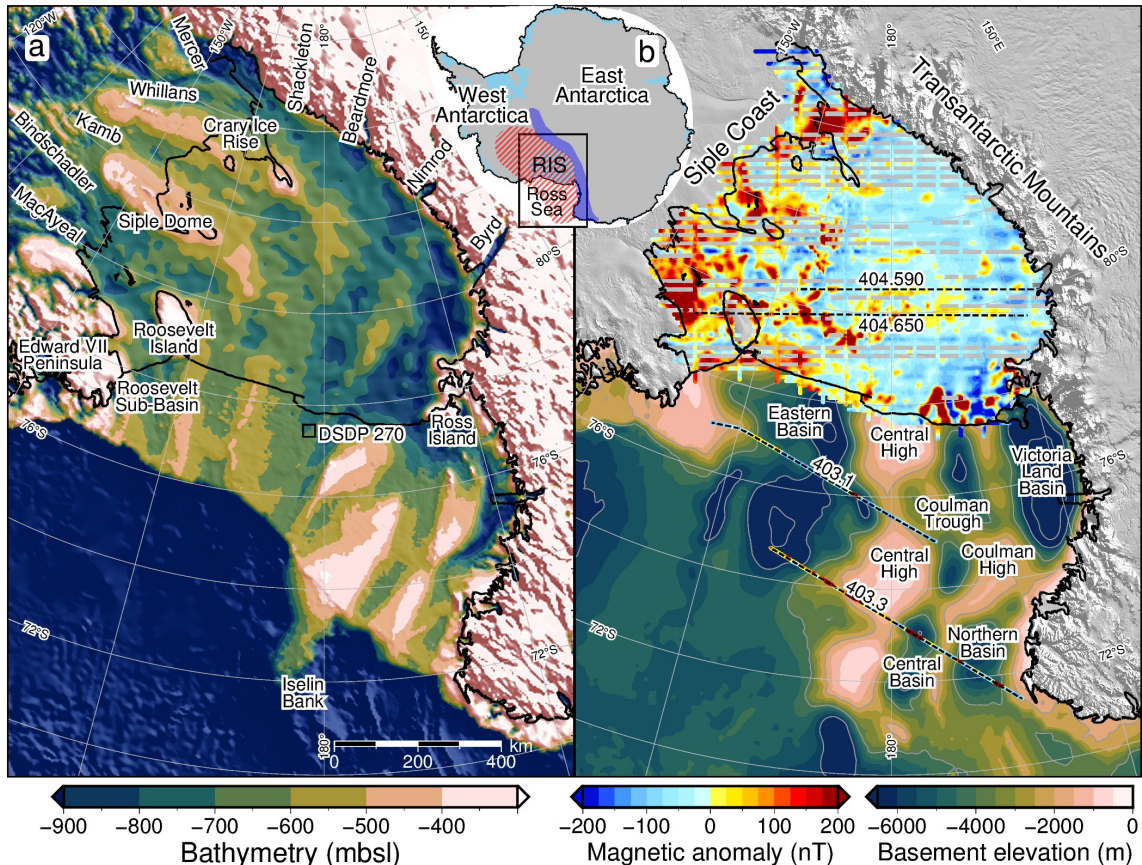


**Figure 2.1:** (a) Bathymetry and sub-ice bed elevations (Morlighem et al., 2020) including ROSETTA-Ice gravity-derived bathymetry (Tinto et al., 2019) beneath the Ross Ice Shelf (RIS). Labels include ice streams and outlet glaciers. (b) Basement elevation from Antarctic Offshore Stratigraphy project marine seismic compilation in the Ross Sea Brancolini et al. (1995) and air-borne magnetic data from ROSETTA-Ice (over RIS) and Operation IceBridge (black dashed lines). Inset map shows figure location, West Antarctic Rift System (hatched red), Transantarctic Mountains (dark blue), and ice shelves (light blue). Shelf edge, grounding line, and coastlines in black (Rignot et al., 2013). MODIS imagery from Scambos et al. (2007).

765 controlled by pressure from the overriding ice sheet (Gooch et al., 2016). Possible  
766 evidence that RIS basement margins localize basinal waters, causing the advection  
767 of geothermal heat, comes from elevated values and significant spatial variability of  
768 measured geothermal heat flux (GHF) at points around the Ross Embayment (Bege-  
769 man et al., 2017). Here we present the first map of magnetic basement topography  
770 and thickness of overlying non-magnetic sediments for the southern Ross Embay-  
771 ment, developed using ROSETTA-Ice (2015-2019) airborne magnetic data (Figure  
772 2.1b, Tinto et al., 2019). Our work reveals three major sedimentary basins and a  
773 broad basement ridge that separates crust of contrasting basement characteristics.

## 774 2.2 Data and Methods

775 We use ROSETTA-Ice aeromagnetic data to image the shallowest magnetic signals  
776 in the crust. Assuming that the overlying sediments and sedimentary rocks produce  
777 smaller magnetic anomalies than the crystalline basement, we treat the resulting  
778 solutions as the depth to the magnetic basement (Section A.2). To do this, we  
779 implemented Werner deconvolution (Werner, 1953) on 2D moving and expanding  
780 windows of line data, isolating anomalies and solving for their source parameters  
781 (Section A.3, location, depth, susceptibility, body type). The resulting solutions are  
782 non-unique; each observed magnetic anomaly can be solved by bodies at multiple  
783 locations and depths by varying the source's magnetic susceptibility and width. The  
784 result is a depth scatter of solutions (Figures 2.2 & A.2), which tend to vertically  
785 cluster beneath the true source. This magnetic basement approach has been used  
786 to map sedimentary basins throughout Antarctica (i.e. Bell et al., 2006; Frederick  
787 et al., 2016; Karner et al., 2005; Studinger et al., 2004a) where typically, the tops  
788 of solution clusters are manually selected to represent the basement depth. Our ap-  
789 proach expands on this method by utilizing a reliable, automated method of draping  
790 a surface over these depth-scattered solutions to produce a continuous basement sur-  
791 face (Section A.4 & A.5).

792

793 We implemented a 2-step tuning process that ties our RIS magnetic basement  
794 to well-constrained seismic basement in the Ross Sea, from the Antarctic Off-  
795 shore Stratigraphy project (ANTOSTRAT) (Figure 2.1b, Brancolini et al., 1995).  
796 This involved using Operation IceBridge (OIB) airborne magnetic data (Cochran  
797 et al., 2014a) collected over the RIS and Ross Sea. Minimizing misfits between  
798 OIB magnetic basement and ANTOSTRAT basement, as well as between OIB and  
799 ROSETTA-Ice magnetic basements, enabled tuning of our method to optimal base-  
800 ment depths (Figures 2.2, A.2, A.3e&f, Section A.4 & A.5).

801

802 Our RIS results (Figure A.4) were merged with offshore ANTOSTRAT data  
803 (Brancolini et al., 1995) and smoothed with an 80 km Gaussian filter to match the  
804 characteristic wavelengths of the Ross Sea basement (Section A.6). The combined  
805 grid (Figure 2.3a) was then subtracted from BedMachine bathymetry (Figure 2.1a,  
806 Section A.7, Morlighem et al., 2020), to obtain the sediment thickness distribution  
807 for the Ross Embayment (Figure 2.3b).

808

809 These sub-RIS results together with free-air gravity data allowed us to infer the  
810 locations of regional scale faults beneath the RIS. Criteria used to locate faults in-  
811 clude 1) high relief on the magnetic basement surface, 2) linear trends that cross

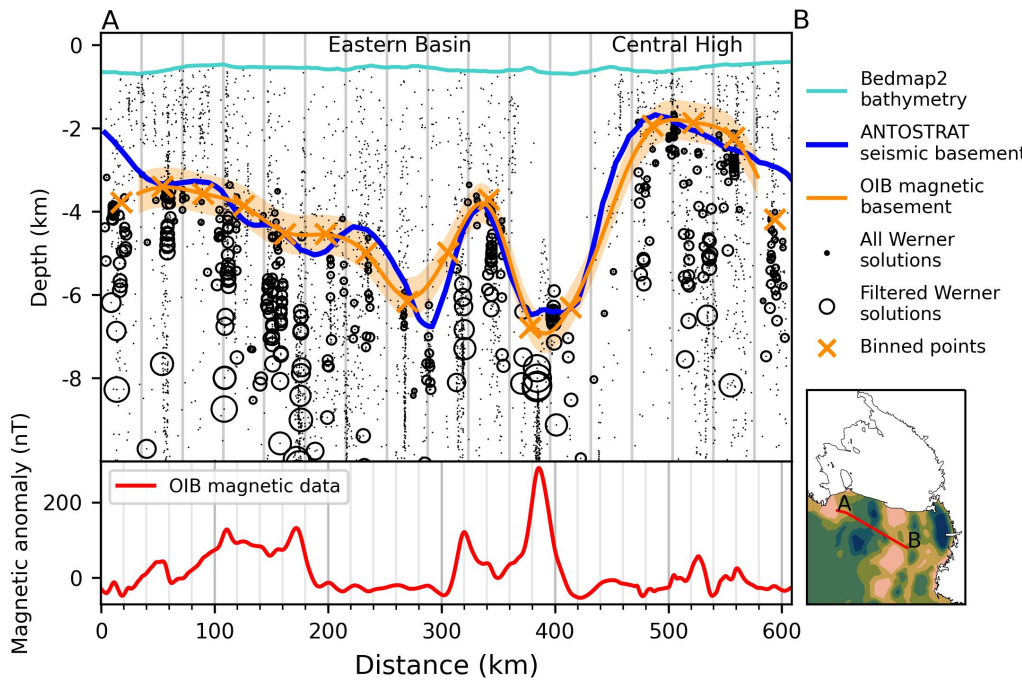


**Figure 2.2:** Ross Sea magnetic and seismic basement comparison. Operation IceBridge airborne magnetic data (lower panel) from segment 403.1 used in Werner deconvolution to produce magnetic anomaly source solutions (black dots). Filtering removed shallow solutions, and remaining solutions (circles scaled to magnetic susceptibility) were binned and interpolated to produce the magnetic basement (orange line with uncertainty band).

812 zones of shallow basement, 3) high gradient gravity anomalies (Figure A.1a, ROSETTA-  
 813 Ice) and 4) large contrasts in sediment thickness. Narrow, deep, linear basins are  
 814 likely to be controlled by active faults (e.g. Drenth et al., 2019; Finn, 2002). We  
 815 display the inferred faults upon a base map of crustal stretching factors ( $\beta$ -factor;  
 816 the ratio of crustal thickness before and after extension, Figure 2.4a), using an initial  
 817 crustal thickness of 38 km (Müller et al., 2007), a continent-wide Moho model (An  
 818 et al., 2015), and our basement surface as the top of the crust (Section A.7).

## 819 2.3 Results

820 We find that an almost continuous drape of sediment covers the RIS region (Figure  
 821 2.3b), with only  $\sim$ 3% of the area having  $<$ 200 m of sedimentary cover. Prominent  
 822 beneath the midline of the RIS is a broad NNW-SSE trending basement ridge  
 823 (Figure 2.3a, Mid-Shelf High; MSH), which comprises most of the shallowest ( $<$ 700  
 824 meters below sea level (mbsl)) sub-RIS basement, with several regions with as little  
 825 as 100 m of sedimentary cover. Basement is deeper on the East Antarctic side of the  
 826 MSH, where it averages  $\sim$ 2400 mbsl, compared to an average depth of  $\sim$ 1900 mbsl  
 827 on the West Antarctic side (Figure 2.3a histogram). Sedimentary fill is  $\sim$ 400 m  
 828 greater and more uniformly distributed on the East Antarctic side than the West  
 829 Antarctic side (Figure 2.3b histogram).

830 To estimate our uncertainty (Section A.8), we examined the misfit between OIB  
 831 and ANTOSTRAT basement (Figures 2.2 & A.2) and between our basement and

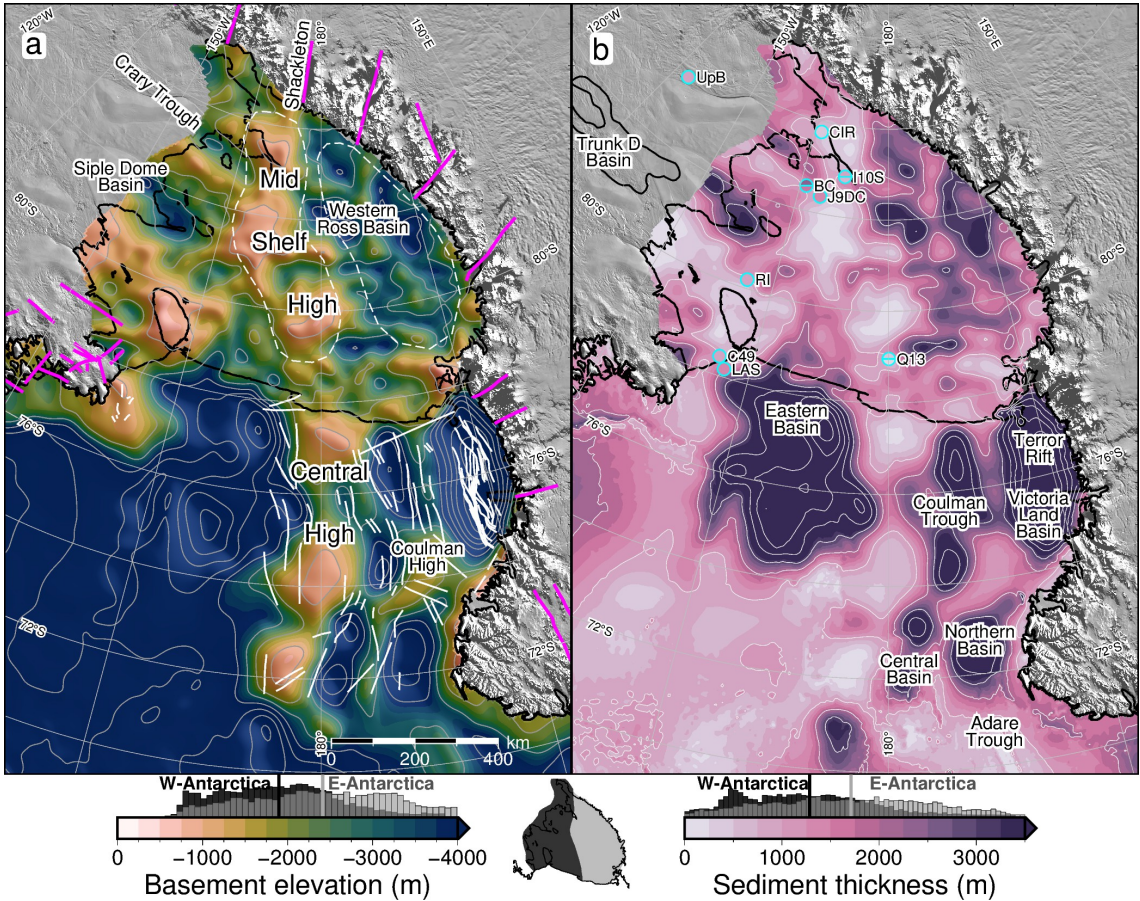


**Figure 2.3:** (a) Basement elevation (magnetic for Ross Ice Shelf (RIS), seismic elsewhere) contoured at 1 km intervals. Pink lines are onshore mapped and inferred faults (Ferraccioli et al., 2002; Goodge, 2020; Siddoway, 2008). White lines are offshore faults (Chiappini et al., 2002; Luyendyk et al., 2001; Salvini et al., 1997; Sauli et al., 2021). Dashed white lines show Mid Shelf High and Western Ross Basin extents. (b) Sediment thickness contoured at 1 km intervals. Previous basement-imaging RIS seismic surveys (cyan circles, Table A.1) are plotted on same color scale, with upper and lower uncertainty ranges as circle halves, where reported. Trunk D Basin outlined in West Antarctica (Bell et al., 2006). Color scales for both a) and b) are set to sub-RIS data range. Colorbar histograms show data distribution for East vs West Antarctic sides of the sub-RIS, separated by the Mid-Shelf High. Inset map shows East vs West divide. Vertical lines on histograms denote average values of each side.

OIB basement (Figures A.3e&f). There is a median misfit of 480 m (22% of average RIS depth) for basement (Figures A.5 & A.6). A similar 470 m median basement misfit is estimated by comparing our results to eight active source seismic surveys (Figure 2.3b, Table A.1). Incorporating the ~70 m uncertainty in the bathymetry model (Tinto et al., 2019), our representative sediment thickness uncertainty is 550 m (37% of average RIS thickness, Figure A.5).

A single broad and deep basin (300 x 600 km) separates the MSH and the Transantarctic Mountains (TAM) (Figure 2.3a, Western Ross Basin). The Western Ross Basin parallels the TAM and has the deepest-observed sub-RIS basement depths of 4500 mbsl, accommodating sediments up to 3800 m thick (Figure 2.3b). It contains a long, narrow NW-SE trending ridge with ~1500 m structural relief above the basement sub-basins on either side. Bordering the MSH on the east, an elongate NW-SE trending basin runs from the RIS calving front to the Siple Coast GZ (Figure 2.3a), where beneath Siple Dome we discover a 100 x 200 km depocenter reaching basement depths up to 4000 mbsl, with sediments up to 3700 m thick. We

refer to this depocenter as Siple Dome Basin, a feature bounded on the east by a basement high that trends southward from Roosevelt Island. This high rises to its shallowest point at the GZ, where its sedimentary cover is less than 100 m. A second deep, narrow basin (50 x 200 km in dimension) is found along the north margin of Crary Ice Rise, separated from the Siple Dome Basin by an NW-SE ridge underlying Kamb Ice Stream. The basin, labelled Crary Trough in Figure 2.3a, reaches basement depths of 3200 mbsl, with sediments 1800-2700 m thick. The southernmost RIS has an additional depocenter with up to 2000 m of fill beneath Whillans Ice Stream (location in Figure 2.1a).

Inferred active sub-RIS faults (Figures 2.4a & A.1) correspond to narrow, linear basement basins with high-gradient gravity anomalies, prevalent on the West Antarctic side (Figure A.1a). Inactive normal and strike-slip faults are inferred along lineaments that segment the shallow MSH into blocks and are oriented parallel to TAM outlet glacier faults.  $\beta$ -factors are indicative of thinned crust and are different on either side of the MSH. The TAM side shows higher  $\beta$ -factors (average 1.99) with low variability. The West Antarctic side has lower  $\beta$ -factors overall (average 1.82), but with some higher values up to 2.1 (Figure 2.4a).

## 2.4 Discussion

Sub-RIS sedimentary basins align with and show lateral continuity with the Ross Sea's Roosevelt Sub-Basin, Eastern Basin, Coulman Trough, and Victoria Land Basin (Figure 2.3, e.g. Cooper et al., 1995). The MSH passes northward into the Ross Sea's prominent Central High (CH). At the southern RIS margin, the narrow Siple Dome Basin has continuity with the previously identified Trunk D Basin (Figure 2.3a, Bell et al., 2006). The throughgoing trends imply regional continuity of crustal structure and a common tectonic development of the Ross Sea and RIS regions. Our sediment thicknesses are compatible with those determined by a) eight active-source seismic surveys (Figure 2.3b), for which the median misfit is 470 m (Table A.1), and b) surface wave dispersion indicating 2-4 km of sediment under the RIS, similar to our range, with the maximum beneath Crary Ice Rise (Zhou et al., 2022). Three additional western RIS seismic profiles report up to several kilometers of sediment, in general accordance with our results (Beaudoin et al., 1992; Stern et al., 1991; ten Brink et al., 1993). Additionally, machine learning applied to geophysical datasets predicts a high likelihood of sedimentary basins at the locations of Siple Dome Basin and Crary Trough (Li et al., 2022).

### 2.4.1 West Antarctic Rift System extensional basins

The Western Ross Basin has a configuration similar to the western Ross Sea rift basins (e.g. Salvini et al., 1997) with a broad and deep basin, separated into distinct depocenters by a linear, low relief ridge. The deeper of the depocenters, on the TAM side of the ridge, coincides with alternating high and low free-air gravity anomalies (Figure A.1a). These similarities suggest the sub-RIS continuations of Coulman Trough and Victoria Land Basin (Figure 2.3b) likely share a common tectonic origin as fault-controlled basins (Figures 2.3a & 2.4a) formed through Cretaceous distributed continental extension across the WARS (Jordan et al., 2020a). These sub-RIS basins terminate against the southern segment of the MSH (Figure

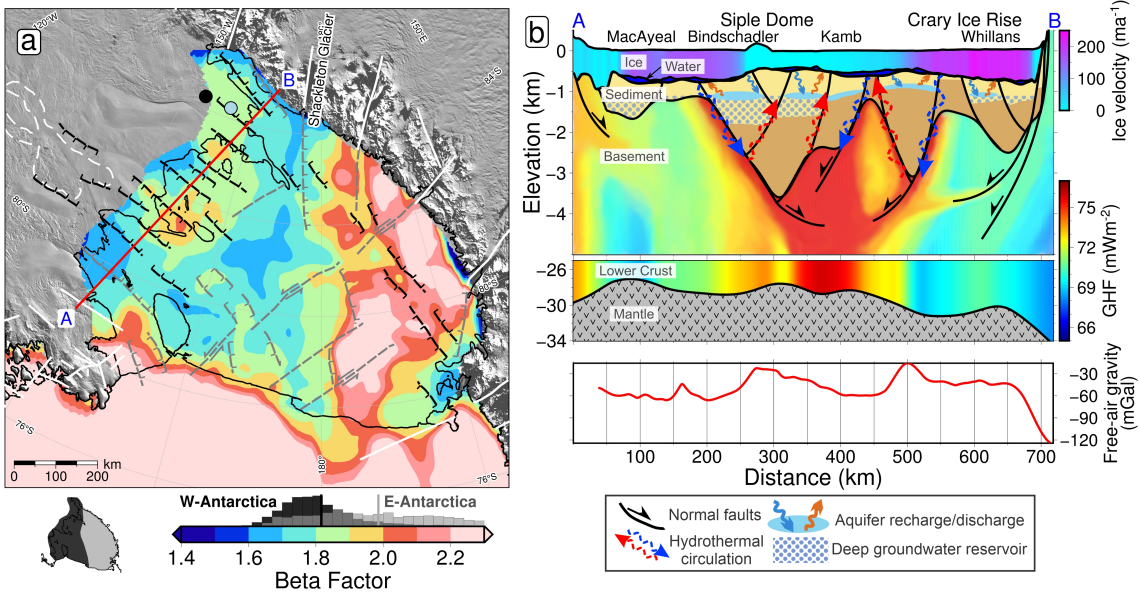


**Figure 2.4:** Tectonic interpretation of the sub-Ross Ice Shelf (RIS). (a)  $\beta$  stretching factors (Section A.7). Colorbar histogram shows data distribution of West vs. East Antarctic sides, same as Figure 2.3. Black and grey lines indicate inferred active and inactive faults, respectively, with kinematics shown with half-arrows (strike or oblique-slip) and hachures (normal-sense). White lines show previously reported faults, same as Figure 2.3a. Dashed-white outline is Trunk D Basin (Bell et al., 2006). Black and blue dots show Subglacial Lake Whillans and sedimentary basin from Gustafson et al. (2022), respectively. Cross-section A-B in red. (b) Siple Coast cross-section from A-B, showing basin sediments bounded by faults, with geothermal heat flux (GHF) through the crust (lower panel from Burton-Johnson et al. (2020), upper panel interpreted). Ice surface, ice base, and bathymetry from Morlighem et al. (2020). Ice streams coloured by velocity (Mouginot et al., 2019; Venturelli et al., 2020). Moho is from Shen et al. (2018a). Lower panel shows ROSETTA-Ice gravity. Named features are labelled on top.

893 2.3a).

894

895 The linear ridge within the Western Ross Basin (Figure 2.3a) may be an ex-  
 896 pression of normal or oblique faults linked to the southward-narrowing Terror Rift  
 897 (Sauli et al., 2021), formed due to Cenozoic oceanic spreading in the Adare Trough  
 898 (Figure 2.3b, Granot & Dyment, 2018). The Western Ross Basin, with up to 3800 m  
 899 of fill, terminates along the prominent edge of the MSH that lines up with the fault-  
 900 controlled trough and crustal boundary that passes southward beneath Shackleton  
 901 Glacier (Borg et al., 1990). We interpret the basement lineament (Figure 2.4a) as a  
 902 transfer fault separating sectors of crust extended to different degrees.

903

904 The southeastern RIS margin is distinguished by linear ridges and narrow, deep  
 905 basins. The prominent NW-SE basement trends coincide with high-gradient gravity  
 906 anomalies (Figure A.1a, Tinto et al., 2019) and thick sediments, suggesting normal  
 907 fault control and active divergent tectonics beneath the GZ. Our Siple Coast cross-  
 908 section (Figure 2.4b) displays dramatic basement relief, exceeding 2 km, in the Siple  
 909 Dome Basin and Crary Trough, which we attribute to displacement upon high angle  
 910 faults. Portions of basin-bounding faults were previously detected by ground-based  
 911 gravity surveys upon the Whillans Ice Stream flank (Figure 2.4a, Muto et al., 2013b)  
 912 and site J9DC (Figure 2.3b), where large variations in sediment thickness indicate  
 913 up to 600 m of fault throw (Grieschar et al., 1992). The continuity between the  
 914 narrow Siple Dome Basin (this study) and the Trunk D Basin (Figure 2.3a, Bell et

al., 2006) suggests that the active tectonic domain continues southward past the GZ. The fault-controlled tectonic basins may reflect a crustal response to the lithospheric foundering hypothesized beneath the South Pole region (Shen et al., 2018b) or be a broader regional expression of Neogene extension that formed the Bentley Subglacial Trench (Lloyd et al., 2015).

### 2.4.2 Consequences for ice sheet dynamics

Our basement topography and suggested crustal faults likely exert a strong influence on the overriding ice, especially along the Siple Coast. Here, we show deep and thick sedimentary basins which likely contain voluminous basinal aquifers (Figure 2.4b; cf. Gustafson et al., 2022). Where these aquifers discharge along fault-damage zones, they can enhance GHF and promote basal melting (Gooch et al., 2016), as depicted in Figure 2.4a. The elevated GHF seen at Subglacial Lake Whillans (285 mW/m<sup>2</sup>, Fisher et al., 2015) may arise from fault localization (Figure 2.4a). Confinement of the aquifers between the ice bed and low-permeability basement may promote fluid overpressure, enabling ice streaming (e.g. Ravier & Buoncristiani, 2018). Additionally, the Siple Coast faults likely accommodate the solid Earth's response to fluctuating ice volume. A matter receiving considerable debate (Lowry et al., 2019; Neuhaus et al., 2021; Venturelli et al., 2020), is Kingslake et al.'s 2018 finding of rapid re-advance of the Siple Coast GZ following Holocene deglaciation. The re-advance was in part due to swift glacioisostatic rebound (cf. Coulon et al., 2021; Lowry et al., 2020), a process aided by the region's low-viscosity mantle (Whitehouse et al., 2019) and likely to be accommodated upon pre-existing crustal faults, as observed in the Lambert Graben (Phillips & Läufer, 2009). Our proposed graben-bounding faults would provide a tectonic control on the glacioisostatic adjustment of the Siple Coast region.

### 2.4.3 Mid-Shelf High - Central High

The 650-km-long Mid-Shelf High features three shallow, blocky segments >150 km in breadth, which have only thin sediment cover (<200 m). At their shallowest points, the top of basement lies within ~300 m of the ice shelf base, at a depth comparable to the basement high at Roosevelt Island. Roosevelt Island is a modern pinning point (Still et al., 2019) owing to the thicker sediment, there (Figure 2.3b). We introduce the MSH as a prominent pinning point at times of advance and greater extent of the Antarctic Ice Sheet, in keeping with evidence from subglacial sediment records that indicate a major ice flow divide between East and West Antarctic ice during and since Last Glacial Maximum (Coenen et al., 2019; Li et al., 2020; Licht et al., 2014).

The prominence of the MSH is due in part to the contrasting geologic properties of the East versus West Antarctic type crust and their respective responses to WARS extension. We distinguished  $\beta$ -factors on the TAM-side that are high and uniform, indicating distributed crustal extension. The West Antarctic side displays lower  $\beta$ -factors overall, but with localized extreme thinning beneath Siple Coast (Figure 2.4a). The greater amount of extension on the East Antarctic side coincides with the deeper bathymetry (Figure 2.1a), deeper basement, and thicker sediments (Figure 2.3). The contrasting properties are also evident in ROSETTA-Ice magnetic

and gravity anomalies, used by Tinto et al. (2019) to identify a north-south trending tectonic boundary along the midline of Ross Embayment. The MSH in the magnetic basement coincides with and spans this boundary, which has been further substantiated by passive-seismic studies that show a lithospheric-scale boundary (Cheng et al., 2021; White-Gaynor et al., 2019). To the north, the features continue into the Ross Sea’s Central High. Southward, the MSH basement feature trends into the TAM, where its western edge aligns with Shackleton Glacier, occupying a major fault separating the distinct geologic domains of the central and southern TAM (Borg et al., 1990; Paulsen et al., 2004), which also parallels a prominent magnetic lineament at the South Pole (Studinger et al., 2006). The structure may be an expression of the East Antarctic craton margin or a major intracontinental transform (Figure 2.4a, Studinger et al., 2006).

972

At the time of Oligocene initiation of the Antarctic Ice sheet, paleotopographic reconstructions of the proto-Ross Embayment depict a long, broad range, emergent above sea level (Paxman et al., 2019; Wilson et al., 2012), that we equate to the MSH-CH that divides the Embayment. The CH hosted small ice caps with alpine glaciers formed during the initial glacial stage in the region (De Santis et al., 1995), and continental ice expanded to the outer Ross Sea continental shelf from those centres (Bart & De Santis, 2012). Between the late Oligocene and mid-Miocene, the CH subsided by up to 500 m (Kulhanek et al., 2019; Leckie, 1983), receiving 100’s of meters of sediment cover ( $\sim$ 400 m at DSDP 270; De Santis et al., 1995). The geophysical similarities and continuity between the Ross Sea’s CH and the RIS’s MSH imply a similar glaciation and subsidence history for the MSH. A terrestrial/alpine stage for the MSH helps to explain the region’s potential to hold the late Oligocene’s larger-than-modern ice volumes (Pekar et al., 2006; Wilson et al., 2013), with the MSH-CH having a central role in Oligocene ice sheet development and the subsequent evolution of the ice sheet and ice shelf, as is documented in the Ross Sea (Halberstadt et al., 2016).

#### 2.4.4 Thermal subsidence and sedimentation

Incorporating the updated basement basin extents and geometries into post-rift thermal subsidence modelling will enable better-constrained paleotopographic reconstructions. For the sub-RIS, these reconstructions (Paxman et al., 2019; Wilson et al., 2012) use a post-Eocene subsidence model based on gravity-derived basin geometries and uniform  $\beta$ -factors (Wilson & Luyendyk, 2009). This model predicts uniform stretching of the eastern sub-RIS from the ice front to the Siple Coast, while our  $\beta$ -factors show increasing stretching from the ice front to the Siple Coast. This observed additional thinning likely has resulted in more subsidence for Siple Dome and the north flank of Crary Ice Rise, which can now be accounted for in reconstructions. Our sediment thickness comparison with past models (Section A.7, Wilson & Luyendyk, 2009) shows the majority of the sub-RIS, especially the Siple Coast, contains more total sediment than previously estimated (Figure A.1f). Depending on the age of this sediment, reconstructions may need to account for the additional sediment deposition and loading.

## 2.5 Conclusions

1004 Here we present a depth to magnetic basement map for the Ross Ice Shelf (RIS) from Werner deconvolution of airborne magnetic data. The RIS magnetic basement is tied to Ross Sea seismic basement, providing the first synthetic view of Ross Embayment crustal structure. Using a bathymetry model, we obtain the sediment thickness distribution and calculate crustal extension factors for the sub-RIS. The extensional features we image, resulting from West Antarctic Rift System extension, have continuity with Ross Sea basement structures to the north, and the prominent Mid-Shelf High trends northward into the Ross Sea's Central High. This combined high separates East and West Antarctic type crust, affected by different degrees of continental extension. The Mid-Shelf High was likely subaerial in the Oligocene, able to support alpine ice caps in early Antarctic glaciation. Subsequently, it formed a prominent pinning point and ice flow divide between the East and West Antarctic Ice Sheets.

1018  
 1019 Newly identified narrow, linear, deep sedimentary basins provide evidence of active faults beneath the Siple Coast grounding zone, where thinned crust overlying anomalous mantle (Shen et al., 2018a) likely experiences elevated geothermal heat flow promoting the formation of subglacial water. Faults that control basement margins may accommodate motion caused by the glacioisostatic response to ice sheet volume changes. Subglacial sedimentary basins in this setting likely contain confined aquifers within permeable basin fill. Here, ice overburden pressure would control flow both between and within the subglacial and groundwater systems, possibly localizing geothermal heat. Updated sediment thickness and basin extents should be incorporated into new paleotopographic reconstructions of time intervals of interest for paleo-ice sheet modelling. Our work contributes critical information about Ross Embayment basement topography and subglacial boundary conditions that arise from an interplay of geology, tectonics, and glaciation.

## 2.6 Open Research

1032 ROSETTA-Ice and Operation IceBridge magnetics data are available through <https://www.usap-dc.org/view/project/p0010035> and <https://nsidc.org/data/IMCS31b>, respectively. Results from this study are available to download from <https://doi.pangaea.de/10.1594/PANGAEA.941238> and a Jupyter notebook documenting our workflow and figure creation is available at <https://zenodo.org/badge/latestdoi/470814953>.

## 2.7 Acknowledgements

1040 Funding support from the New Zealand Ministry of Business and Innovation and Employment through the Antarctic Science Platform contract (ANTA1801) Antarctic Ice Dynamics Project (ASP-021-01) and the National Science Foundation (1443497 and 1443534), and Antarctica New Zealand. We are grateful to Robin Bell, Isabel Cordero, Alec Lockett, Joel Wilner, Zoe Krauss, and the entire ROSETTA-Ice team for undertaking the ambitious data acquisition and processing effort. We thank

1046 Katharina Hochmuth and Guy Paxman for thoughtful reviews which greatly im-  
1047 proved the manuscript, as well as Chris Sorlien, Tim Stern, Simon Lamb, Lara  
1048 Pérez, Ryan Venturelli, Wei Ji Leong, and Dan Lowry for valuable input. Figures  
1049 used GMT6/PyGMT (Uieda et al., 2021; Wessel et al., 2019), with a script adapted  
1050 from Venturelli et al. (2020). Geosoft Oasis Montaj™ was used for magnetics pro-  
1051 cessing and Werner deconvolution. Open access publishing facilitated by Victoria  
1052 University of Wellington, as part of the Wiley - Victoria University of Wellington  
1053 agreement via the Council of Australian University Librarians.

1054

1055 Chapter 2, in full, is a reprint of material as it appears in *Geophysical Re-*  
1056 *search Letters*: Tankersley, M. D., Horgan, H. J., Siddoway, C. S., Caratori Tontini,  
1057 F., & Tinto, K. J. (2022). Basement topography and sediment thickness beneath  
1058 Antarctica's Ross Ice Shelf. *Geophysical Research Letters*, 49, e2021GL097371.  
1059 <https://doi.org/10.1029/2021GL097371>. The only changes made from the published  
1060 version include formatting and replacing preprint citations with accepted paper cita-  
1061 tions. I conceived the study with my co-authors, undertook the study and analysis,  
1062 and wrote the manuscript myself.

# <sup>1063</sup> Chapter 3

## <sup>1064</sup> Gravity inversion: a tool for <sup>1065</sup> bathymetry modelling

### <sup>1066</sup> Abstract

<sup>1067</sup> Sub-ice-shelf bathymetry exerts a primary control on the stability of many Antarctic  
<sup>1068</sup> ice shelves through the geometry of pinning points and the guiding of melt-inducing  
<sup>1069</sup> water masses. Collecting sub-ice-shelf bathymetry data using typical polar sur-  
<sup>1070</sup> veying methods (e.g. seismic surveying or direct observations) can be inefficient,  
<sup>1071</sup> expensive or unfeasible. Gravity inversions provide a more practical alternative,  
<sup>1072</sup> in which observed variations in Earth's gravitational field are used to predict the  
<sup>1073</sup> bathymetry. This chapter describes a gravity inversion algorithm developed specifi-  
<sup>1074</sup> cally for modelling bathymetry. The inversion is tested on a suite of models, created  
<sup>1075</sup> with a combination of synthetic and real bathymetric data. These tests provide the  
<sup>1076</sup> ability to 1) determine the best practices for conducting bathymetric inversions, 2)  
<sup>1077</sup> recognize the limitations of the inversions, and 3) identify where community efforts  
<sup>1078</sup> should be focused for the future of modelling Antarctica's sub-ice-shelf bathymetry.  
<sup>1079</sup> We find that estimating and removing the regional component of gravity prior to  
<sup>1080</sup> the inversion is the largest source of error in the resulting bathymetry model. To  
<sup>1081</sup> address this, we propose procedures to limit this error and provide recommendations  
<sup>1082</sup> on the minimum spatial density of bathymetry constraint points. Additionally, for  
<sup>1083</sup> common airborne gravity survey designs, we find minimizing noise in the data is  
<sup>1084</sup> more important than collecting closer-spaced data.

### <sup>1085</sup> Plain Language Summary

<sup>1086</sup> The shape of the seafloor beneath the floating extensions of the Antarctic Ice Sheet  
<sup>1087</sup> exerts important controls on the ice. Controls include how the seafloor topography  
<sup>1088</sup> (bathymetry) directs the flow of warm water masses which causes melting at the  
<sup>1089</sup> base of the ice, and determines where ice is anchored to the bedrock. Conventional  
<sup>1090</sup> methods of collecting data on bathymetry are ineffective, impractical, or expensive  
<sup>1091</sup> when applied to ice shelves. One alternative method of acquiring sea floor depths  
<sup>1092</sup> is a method called gravity inversion. Variations in bathymetry can be detected by  
<sup>1093</sup> measurements of Earth's gravity over an ice shelf as a result of the difference in  
<sup>1094</sup> density between seawater and the seafloor. Here, we develop a refined technique for  
<sup>1095</sup> performing a gravity inversion and test the method on artificial data to examine its

effectiveness and learn which parts of the inversion are most prone to errors. We find that removing the portion of the gravity data that results from deep geologic structures is the largest source of error. To limit the impact of this and other sources of error in the inversion, we suggest researchers focus on collecting as many point measurements of bathymetry depth (from seismic surveys) and attempt to limit the noise in the gravity data as much as possible.

**Key Points:**

1. We present a new constrained geometric gravity inversion algorithm for recovering density contrasts.
2. Synthetic models show the regional-residual separation of the gravity data prior to inversion is the dominant source of error.
3. Quality over quantity for gravity data; efforts should be focused on reducing noise not increasing coverage.

## 3.1 Introduction

In the last two decades, the Antarctic Ice Sheet has experienced significant ice mass loss, averaging 118 billion tons per year, contributing 5.2 mm to sea-level rise (Smith et al., 2020a). This mass loss has been concentrated along the coast, where ocean currents are able to bring warm waters in contact with the ice (Rignot et al., 2019). Much of Antarctica is fringed with floating extensions of the ice sheet, known as ice shelves (Figure 3.1). These ice shelves provide a critical buttressing effect on the upstream ice, slowing the flow of ice from the continent into the oceans (Dupont & Alley, 2005). This buttressing results from lateral drag along the margins of the ice shelf and friction between the ice and the bed at pinning points. Thinning of the ice shelves lowers these resistive forces. Due to the cold climate and lack of surface melt, the majority of Antarctic ice shelves' thinning occurs as basal melt. This basal melt (Figure 3.1b) occurs from contact with relatively warm ocean waters, such as circumpolar deep water and high-salinity shelf water (CDW and HSSW) (Jenkins et al., 2010; Rignot et al., 2019).

These deep-lying warm masses of water originate offshore from the ice shelves and thus can only induce basal melting if they circulate under the shelves. A large enough ocean draft, the distance between the ice base and the bathymetry (Figure 3.1a), is required for this circulation to be possible. This connection between ocean draft and basal melting is shown by generally low ice shelf basal melt rates for shelves, or sections of shelves, with shallow ocean drafts (e.g. Pritchard et al., 2012; Tinto et al., 2019). Additionally, deep bathymetric troughs in regions of otherwise thin drafts, or conversely, bathymetry ridges in regions of thick drafts, can control the incursion of these water masses (St-Laurent et al., 2013; Yang et al., 2021).

While the elevation of the ice base for many of Antarctica's ice shelves is relatively well-constrained, the water depth is poorly known. The relatively good understanding of the ice base comes from a combination of airborne radar surveys (e.g. Das et al., 2020) and satellite altimetry measurements (e.g. Griggs & Bamber, 2011), in conjunction with the hydrostatic equilibrium assumption (Bamber & Bentley, 1994). Conversely, there is no equivalent fast and cheap technique to directly survey the bathymetry beneath floating ice shelves. Radar (ground or airborne)

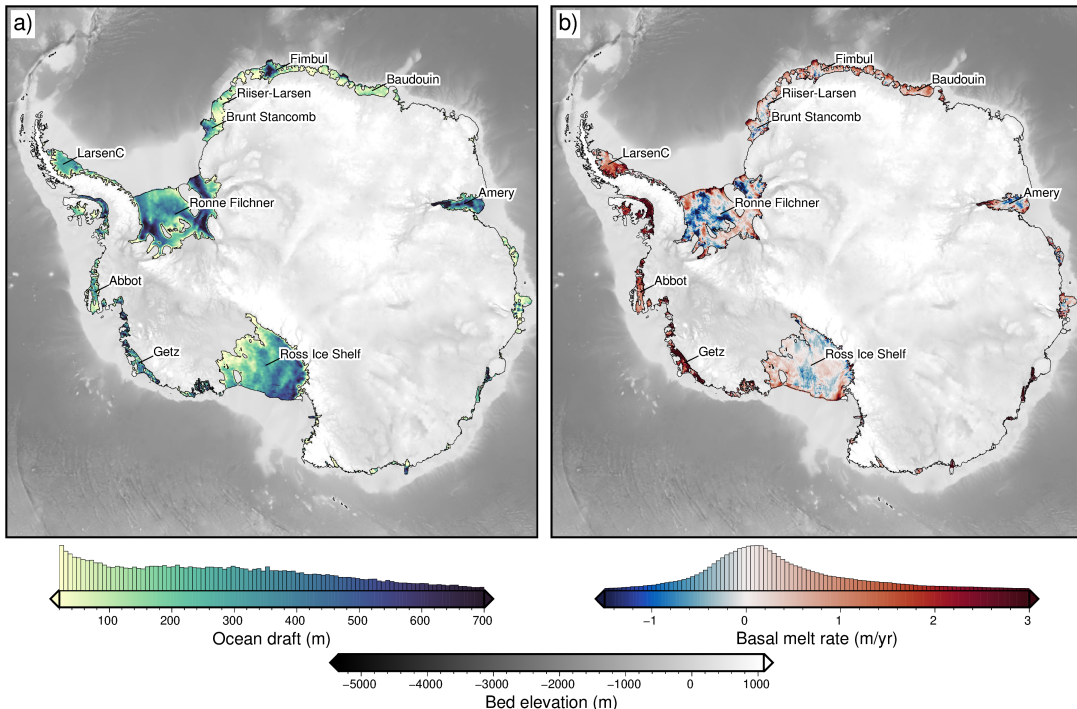


**Figure 3.1:** Ice shelves of Antarctica. **a)** Water column thickness beneath the ice shelves from Bedmachine data (Morlighem, 2022; Morlighem et al., 2020). **b)** Basal melt rate for the ice shelves from Adusumilli et al. (2020). Both plots show bed elevations in the gray colormap. The 10 largest ice shelves are labelled.

cannot image through the thick water, over-ice seismic surveys are slow and expensive, and numerous direct observations through drill holes are impractical. Due to the density contrast between the water and the sediment, the bathymetry surface produces a measurable gravity signal. This signal can be observed from airborne or ground-based gravity surveys, which provides a method, if used correctly, to model sub-shelf bathymetry. This method is a gravity inversion; a geophysical technique to take measurements of an energy source and estimate the physical properties responsible for these measurements (e.g., Menke, 2012; Oldenburg & Li, 2005; Tarantola, 2005). In this case, the energy source is Earth's gravitational field and the physical Earth property is the depth of the density contrast between the ocean and seafloor. This chapter will first introduce the gravity inversion technique in general, followed by the specific style of gravity inversion, a geometric inversion, which is used here. Next, a suite of synthetic models will be used to assess the performance and limitations of the inversion. The suite of models includes:

1. a simple synthetic topography.
2. a synthetic topography with a regional component of the gravity signal.
3. a semi-realistic model, using real Antarctic bathymetry and basement topographies to create the synthetic observed gravity.

With this suite of models, we will test the effects of various levels of noise, the data spacing of the observed gravity, the number of prior constraints, and various inversion methods and parameters. Finally, we will discuss the general limitations of using gravity inversions to recover bathymetry and will provide guidance for conducting gravity inversion for sub-ice-shelf bathymetry.

## <sup>1163</sup> 3.2 Methods

<sup>1164</sup> There are two fundamental types of geophysical modelling, forward modelling, and  
<sup>1165</sup> inverse modelling. Forward modelling is the process of simulating observed data  
<sup>1166</sup> from a model of physical properties. For a gravity application, this may be calcu-  
<sup>1167</sup> lating the gravitational field resulting from a sedimentary basin of a given geometry  
<sup>1168</sup> and/or density model. In general, forward problems are well-posed, meaning there  
<sup>1169</sup> is a unique answer (Oldenburg & Li, 2005). In contrast, inverse modelling, or in-  
<sup>1170</sup> version, is the process of determining physical properties from observed data. For  
<sup>1171</sup> the previous example, this would entail using observed gravity data to predict the  
<sup>1172</sup> sediment thickness of a basin. Inverse problems are generally ill-posed. For a given  
<sup>1173</sup> set of gravity observations, there is a multitude of sedimentary basin configurations  
<sup>1174</sup> which reproduce the observed data with the same degree of accuracy. This is re-  
<sup>1175</sup> ferred to as non-uniqueness and makes geophysical inversions a difficult procedure  
<sup>1176</sup> compared to forward modelling.

### <sup>1177</sup> 3.2.1 Geophysical inversion

<sup>1178</sup> In general, inversions consist of three components;

- <sup>1179</sup> 1. Forward operator ( $f$ ): This is a mathematical means of linking a physical  
<sup>1180</sup> Earth property to the expected geophysical response. It accomplishes the task  
<sup>1181</sup> of forward modelling, as described above.
- <sup>1182</sup> 2. Physical property model ( $p$ ): This is a representation of the physical Earth  
<sup>1183</sup> property of interest. While real-world properties are continuous (i.e. a smoothly  
<sup>1184</sup> varying topography), computation often necessitates discretization (i.e. a  
<sup>1185</sup> DEM (digital elevation model), see section 3.2.2.1). The starting model ( $p_0$ )  
<sup>1186</sup> typically will include the prior geologic knowledge of the region. To discretize  
<sup>1187</sup> the topography we use a layer of adjacent, vertical right-rectangular prisms.
- <sup>1188</sup> 3. Fit function ( $\phi$ ): This function describes the similarity between the observed  
<sup>1189</sup> data and the predicted data (resulting from the forward calculation of the  
<sup>1190</sup> property model ( $f(p)$ )). The goal of the inversion is to minimize this function  
<sup>1191</sup> so that  $f(p)$  is as close to the observed data as possible.

<sup>1192</sup> Here, a mathematical derivation of a generalized discrete inversion problem is  
<sup>1193</sup> shown, following closely to the derivation of Oliveira and Uieda (2014). The inversion  
<sup>1194</sup> problem can be framed as finding the set of physical parameters ( $\vec{p}$ ) which when  
<sup>1195</sup> modelled with the forward operator ( $f$ ) produce predicted data ( $\vec{d}^{pred}$ ) as close  
<sup>1196</sup> to the observed data ( $\vec{d}^{obs}$ ), as possible. This inversion is discrete because the  
<sup>1197</sup> topography is represented with a series of grid cells, instead of a continuous function.  
<sup>1198</sup> The difference between the observed and predicted data gives the misfit  $\vec{m}$ , where

$$\vec{m} = \vec{d}^{obs} - \vec{d}^{pred} = \vec{d}^{obs} - \vec{f}(\vec{p}). \quad (3.1)$$

<sup>1199</sup> Here, the  $\ell^2$ -norm (mean squared error) of the misfit is the metric used to define  
<sup>1200</sup> the *closeness* between the predicted and observed data, where

$$\|\vec{m}\|_2 = \sqrt{\sum_{i=1}^N [d_i^{obs} - f_i(\vec{p})]^2}, \quad (3.2)$$

where  $N$  is the number of observed data points.

This is defined as the *fit function*,  $\phi(\vec{p})$ . The fit function can also be expressed as

$$\phi(\vec{p}) = \vec{m} \cdot \vec{m} = [\vec{d}^{obs} - \vec{f}(\vec{p})] \cdot [\vec{d}^{obs} - \vec{f}(\vec{p})]. \quad (3.3)$$

In this context, the inversion problem is to determine a vector of parameters  $\tilde{\vec{p}}$  of length  $M$  which minimizes  $\phi(\vec{p})$ . This minimum occurs where the gradient of  $\phi(\vec{p})$  at the vector  $\tilde{\vec{p}}$  has zero length. The gradient of  $\phi(\vec{p})$  evaluated at any  $\vec{p}$  is an  $M$ -dimensional vector is defined as

$$\nabla \phi(\vec{p}) = \begin{bmatrix} \frac{\partial \phi(\vec{p})}{\partial p_1} \\ \frac{\partial \phi(\vec{p})}{\partial p_2} \\ \vdots \\ \frac{\partial \phi(\vec{p})}{\partial p_M} \end{bmatrix}. \quad (3.4)$$

Evaluating the gradient at the  $i^{\text{th}}$  element, using Equation 3.3 gives

$$\begin{aligned} \frac{\partial \phi(\vec{p})}{\partial p_i} &= \frac{\partial}{\partial p_i} \sum_j [d_j^{obs} - f_j(\vec{p})] \cdot [d_j^{obs} - f_j(\vec{p})] \\ &= \sum_j \frac{\partial}{\partial p_i} [d_j^{obs} - f_j(\vec{p})] \cdot [d_j^{obs} - f_j(\vec{p})] \\ &= -2 \sum_j \frac{\partial f_j(\vec{p})}{\partial p_i} \cdot [d_j^{obs} - f_j(\vec{p})] \end{aligned} \quad (3.5)$$

Substituting Equation 3.5 into the elements of Equation 3.4 gives

$$\nabla \phi(\vec{p}) = -2 \mathbb{J}(\vec{p}) [\vec{d}^{obs} - \vec{f}(\vec{p})], \quad (3.6)$$

where  $\vec{p}$  is the parameter vector of dimension  $M$ ,  $\vec{d}^{obs}$  is the observed data vector of dimension  $N$  and  $\mathbb{J}$  is the Jacobian matrix of dimension  $M \times N$ , and is given by

$$\mathbb{J}(\vec{p}) = \begin{bmatrix} \frac{\partial f_1(\vec{p})}{\partial p_1} & \cdots & \frac{\partial f_N(\vec{p})}{\partial p_1} \\ \vdots & \ddots & \vdots \\ \frac{\partial f_1(\vec{p})}{\partial p_M} & \cdots & \frac{\partial f_N(\vec{p})}{\partial p_M} \end{bmatrix} \quad (3.7)$$

Each element of the Jacobian matrix is given by

$$\mathbb{J}_{ij} = \frac{\partial f_j(\vec{p})}{\partial p_i}, \quad (3.8)$$

which is the partial derivative of the  $j^{\text{th}}$  predicted data with respect to the  $i^{\text{th}}$  physical parameter. The *Jacobian* ( $\mathbb{J}$ ) is a sensitivity matrix that describes how much the predicted data changes for an infinitesimal change in the physical parameter. For example, let's consider the case of a gravity inversion attempting to recover the density of subsurface cubes. The model consists of 100 cubes, and there are 10 observation points. The Jacobian would be a  $100 \times 10$  matrix where  $\mathbb{J}_{1,1}$  (the first

entry) would be the 1st cube's gravitational derivative with respect to density at the first observation point. The Jacobian, therefore, describes how sensitive each pair of cubes and observations are to a change in density.

Once the Jacobian is created, a matrix equation of the form  $Ax = b$  is set up, where  $A$  is the Jacobian,  $x$  is the unknown variable, and  $b$  is the data misfit.

$$\mathbb{J}\vec{x} = \vec{m} \quad (3.9)$$

A solution to this linear equation can be found directly, by finding the inverse or pseudo-inverse matrix of the Jacobian, or iteratively via a least-squares solver (Jacoby & Smilde, 2009). The solution gives the correction which when applied to the physical parameters of interest minimizes the misfit between the observed data and the starting model.

### 3.2.1.1 Non-Linear inversions

The derivative of the forward operator with respect to the parameter of interest determines the linearity of an inversion. For a gravity inversion attempting to recover rock density, the derivative of gravity with respect to density is constant, and thus the inversion is considered linear (Aster et al., 2018). Conversely, a gravity inversion attempting to recover the depth to a surface, or the thickness of a layer, is non-linear since the vertical derivative of gravity (derivative with respect to depth) is dependent on the depth. Non-linear inversion cannot be solved directly, with matrix inversion (Jacoby & Smilde, 2009). They must be linearized; which is the purpose of the Jacobian matrix. The Jacobian enables a minimum-norm solution to be found with an iterative solver, where at each iteration, the calculated corrections ( $\vec{x}$ ) are applied to the starting model, the residuals ( $\vec{m}$ ) are recalculated, the Jacobian is updated, and Equation 3.9 is solved again, giving a new set of corrections. This is repeated until  $\phi(\vec{p})$  is suitably low.

### 3.2.1.2 Geometric inversions

Most gravity inversions aim to recover the distributions of densities in the subsurface. For this technique, the model domain is discretized into a series of polygons (for 2D) or polyhedrons (for 3D), and the inversion aims to predict the density of each polygon. This is widely used due to its relevance in mineral exploration (Oldenburg & Pratt, 2007). Less commonly used are gravity inversions which aim to recover the depth, shape, or volume of features. This style of gravity inversions are referred to as geometric inversions. They are typically used to estimate relief of the Moho (e.g Borghi, 2022; Uieda & Barbosa, 2017) or the sediment-basement contact (e.g. Barbosa et al., 2007; Santos et al., 2015). In this chapter, geometric inversions are used to recover the bathymetry. This use case of gravity inversion is unique to studying the cryosphere. In locations without ice cover, bathymetry data is typically collected with shipborne multi-beam echo sounding, airborne LiDAR, or satellite altimetry.

### 3.2.2 Forward modelling

To perform a geometric gravity inversion, first, the gravitational field produced by a topographic surface must be able to be calculated. This topography is approxi-

mated as a constant density contrast between the overlying and underlying materials. The topography is often modelled as a series of adjacent vertical right-rectangular prisms. For a certain observation point, the gravitational field produced by this layer of prisms is the sum of the forward gravity of each prism. This forward gravity calculation of a prism is accomplished with the analytical solutions given by Nagy et al. (2000), as implemented in the Python package Harmonica (Fatiando a Terra Project et al., 2023).

### 3.2.2.1 Discretization

There are several options for discretizing a density contrast as a series of prisms (Figure 3.2). The most conceptually simple method is for the prisms to represent the true density and geometry of the material on either side of the surface (Figure 3.2b). In this method, the topography is represented by the base of the upper prisms, and by the tops of the lower prisms. Alternatively, the contrast can be represented by a layer of prisms either above or below the surface, ending at an arbitrary reference, typically the minimum or maximum value of the surface (Figure 3.2c-d). For this, the prism's density values are relative to the medium on the other side of the surface (i.e. if prisms are below the surface, their densities are  $\rho_{below} - \rho_{above}$ ). The last option is to choose a flat reference surface (typically the mean value of the surface or sea level) and create prisms between this and the surface (Figure 3.2e). Prisms above the reference are assigned a positive density contrast ( $\Delta\rho = \rho_{below} - \rho_{above}$ ), and prisms below the surface a negative density contrast ( $\Delta\rho = \rho_{above} - \rho_{below}$ ). All of these methods result in similar forward gravity calculations. Note that the absolute density option (Figure 3.2b) has twice as many prisms as the other options, significantly increasing its computational expense, regardless of whether or not a buffer zone is used.

### 3.2.2.2 Gravity edge effects

Any forward gravity calculation of a surface will include gravitational edge effects. These effects are typically a decay in the gravitational field towards the edges of the prism model due to the void space (density of 0) beyond the edge of the model. The magnitude of decay is dependent on the average thickness and density of prisms near the edge. Larger or denser prisms create a large contrast with the void space, resulting in a greater amount of decay. Therefore, the absolute density method of discretization (Figure 3.2b) produces the largest edge effects due to the high-density values and large total thickness of the prisms. The relative density methods (Figure 3.2c-d) produce a smaller edge effect, since the prisms are only above or below the surface, reducing their total thickness. The density values are also less than in the absolute density method. The reference surface method (Figure 3.2e) produces the smallest edge effects due to both a) the mean prism thickness being smaller, and b) positive and negative density prisms having opposite edge effects, partially cancelling each other out. This is only applicable if the reference level is located within the range of the values of the surface. Note that with a reference level completely above or below the surface, the reference method becomes identical to methods c) and d) of Figure 3.2.

A buffer zone can be used to reduce the impact of these edge effects by calculating forward gravity confined to an inner region, while the prism model extends beyond.

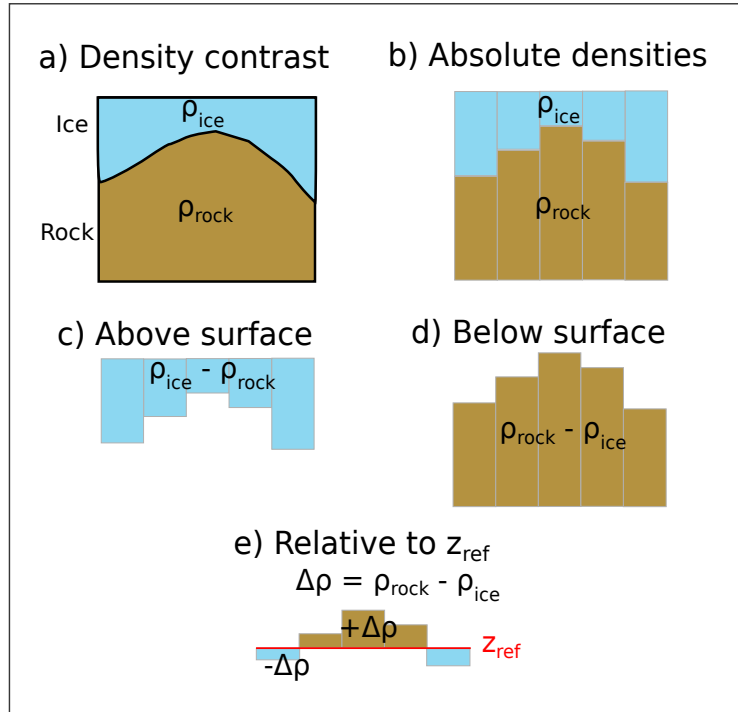


**Figure 3.2:** Equivalent methods of discretizing a density contrast (a) across a surface. b) Use absolute densities of the mediums above and below the reference, with prisms on either side. c-d) Use the density contrast across the surface, with prisms either above or below, and the sign of the density contrast reflecting whether they are above or below. e) Use a reference surface, with prisms above having a positive density contrast and prisms below a negative contrast.

1307 This limits the majority of the edge effects to outside the region of calculation.  
 1308 Too large of a buffer zone will add an unnecessary amount of computation (more  
 1309 prisms), while too small of a zone will introduce unacceptably large edge effects to  
 1310 the calculations.

### 1311 3.2.3 Isolating anomalies

1312 For a successful geometric gravity inversion, the component of the observed gravity  
 1313 field resulting from the density contrast of interest must be isolated from all other  
 1314 gravity signals. This section describes the process of isolating the required anomaly.  
 1315 Since this chapter consists of synthetic gravity, the discussion of correcting raw  
 1316 gravity measurements and deriving the various gravity anomalies is omitted. See  
 1317 Chapter 4 for further discussion of gravity data processing. Here, *synthetic observed*  
 1318 *gravity* is taken to mean the gravity effect resulting solely from deviations between  
 1319 the true synthetic model, and a simple reference model, defined by a flat surface  
 1320 with a constant density above and a constant density below. This is considered a  
 1321 partial topo-corrected gravity disturbance, since the gravity effect of other layers,  
 1322 such as ice and water, if present, is assumed to have been corrected for. The misfit,  
 1323  $\vec{m}$ , in Equation 3.1, is defined as this synthetic observed gravity minus the forward  
 1324 gravity effect of the starting bathymetry.

1325

### 3.2.4 Regional vs. Residual gravity

The topography-free gravity disturbance is often simplified as consisting of two components, the regional and residual fields. The regional field typically dominates the signal and is often the result of deeper and broader structures, such as Moho variations. Superimposed on this signal is the residual field, which is typically the result of shallower structures. The terms residual and regional are relative; here, they are taken to mean the gravity effect of the bathymetry versus that of all deeper structures, respectively. In this inversion, the residual, regional, and misfit are related by

$$\vec{m} = \vec{m}_{res} + \vec{m}_{reg}, \quad (3.10)$$

where  $\vec{m}$  is the overall data misfit, from Equation 3.1. The residual misfit,  $\vec{m}_{res}$ , is the desired input into the inversion, and thus the regional component,  $\vec{m}_{reg}$ , must be removed prior to the inversion. This step proves to be one of the most challenging steps of a bathymetric inversion, especially in areas of limited constraints (Brisbourne et al., 2014). Removing an incorrect regional field, whether it is too much or too little, will directly impact the resulting bathymetry results. Regional-residual separation is also highly non-unique and benefits greatly from *a priori* constraints. Many methods of regional separation rely on the simplifying assumption that the regional field consists of longer-wavelength anomalies, while the residual field dominates the short-wavelength components. Here, four methods of estimating the regional component of gravity are described.

1. Low-pass filter: With the assumption outlined above, a low-pass filter can be used to isolate the regional gravity. For this, a Gaussian wavelength filter is used and the filter width can be varied based on the expected regional anomaly wavelengths. This method requires the data to be gridded over the entire domain, which may be a problem for sparse surveys, or irregularly shaped domains. The choice of wavelength is subjective and needs to be carefully considered. See Eisermann et al. (2020) for a bathymetry inversion utilizing this method of regional separation.
2. Trend removal: Similar to the low-pass filter method, a trend can be fit to the misfit data, representing the regional field. The order of the polynomial trend is subjective and can be varied to suit the data. Again, this parameter choice requires care.
3. Equivalent source prediction: The equivalent sources technique is a method commonly used to grid, smooth, or upward-continue gravity data. It creates a set of point sources with densities, which when forward-modelled, reproduce the measured gravity data. These sources are then used to predict the gravity anomaly at any desired point. The source depths can be varied to achieve the desired regional component. This technique is beneficial over low-pass filter and trend removal in that it does not require the data to be gridded and can thus accommodate sparse surveys, or compilations of surveys at varying altitudes. It is computationally expensive compared to the above methods. Additionally, source depths are a subjective parameter, which needs to be carefully chosen. Past bathymetry inversions have used upward continuation as a means to define the regional field (e.g., Tinto et al., 2015).

1370     4. Constraint point minimization: The last method makes use of constraint points  
 1371     where the bathymetry depths are known. This inversion defines the residual  
 1372     component of the misfit as the gravity effect from deviations of the true  
 1373     bathymetry with respect to the starting bathymetry. At constrained points,  
 1374     there is no deviation between the starting and true bathymetries, and thus  
 1375     the residual component of the misfit should be zero at the constraints. This  
 1376     means the total misfit value at the constrained points is equal to the regional  
 1377     component (Equation 3.10). By sampling the misfit at each constrained point,  
 1378     and fitting a surface to these values, a regional component is estimated. This  
 1379     technique has a few advantages. It imposes a form of smallness regularization,  
 1380     where the inversion won't significantly alter the depth of the constraint points  
 1381     since the input residual at the points is  $\sim 0$  mGal. Additionally, except for  
 1382     the gridding technique, this method doesn't require a subjective parameter,  
 1383     unlike the other methods. Similar to the low-pass filter and trend removal,  
 1384     this method requires gridded data. If this data is sparse, or the constrained  
 1385     points are not located near gravity observation points, some inaccuracies will  
 1386     be introduced. This technique has been used in several bathymetry inversions  
 1387     (An et al., 2019a; Millan et al., 2020; Yang et al., 2021).

1388     Other methods used to approximate the regional component include using high-  
 1389     altitude (satellite) gravity data (Muto et al., 2016; Tinto et al., 2015), the forward  
 1390     modelling of a geologic model, either inferred from 1) other geophysical data (Hodg-  
 1391     son et al., 2019), 2) *a priori* geologic knowledge (Tinto & Bell, 2011), or 3) from an  
 1392     approximated crustal density distribution (Cochran et al., 2020; Tinto et al., 2019).  
 1393     Once estimated, the regional component is then removed from the total misfit, giv-  
 1394     ing the residual misfit. This residual misfit ideally results solely from discrepancies  
 1395     between the starting and true bathymetries.

### 1396     3.2.5 Running the inversion

1397     Here, the necessary steps for running an inversion are explained. First, the Jacobian  
 1398     matrix is calculated (Equation 3.7). Next, the matrix equation (Equation 3.9) is  
 1399     solved, giving the necessary corrections to apply to the bathymetry. Additionally,  
 1400     this solution needs to be constrained to account for the inherent non-uniqueness  
 1401     of the inversion. This is accomplished with various forms of regularization; i.e., a  
 1402     unique solution is determined subject to minimize an additional objective function.

#### 1403     3.2.5.1 Jacobian matrix

1404     The first step of the inversion is to calculate the sensitivity matrix, the Jacobian  
 1405     (Equation 3.7). Each entry of the Jacobian (Equation 3.8) is the vertical derivative  
 1406     of gravity of a prism relative to a single observation point. While a solution exists to  
 1407     the analytical vertical gravity derivative of a prism, we use an approximation to limit  
 1408     the computational expense (Nagy et al., 2000). Here two methods are derived for  
 1409     approximating the vertical gravity derivative resulting from a prism; 1) an annular  
 1410     approximation and 2) a finite differences approach.

#### 1411     Annulus approximation

1412     A vertical prism can be approximated as a sector of an annulus (a cylindrical shell),  
 1413     as in Figure 3.3. This approximation greatly simplifies the calculation of the vertical

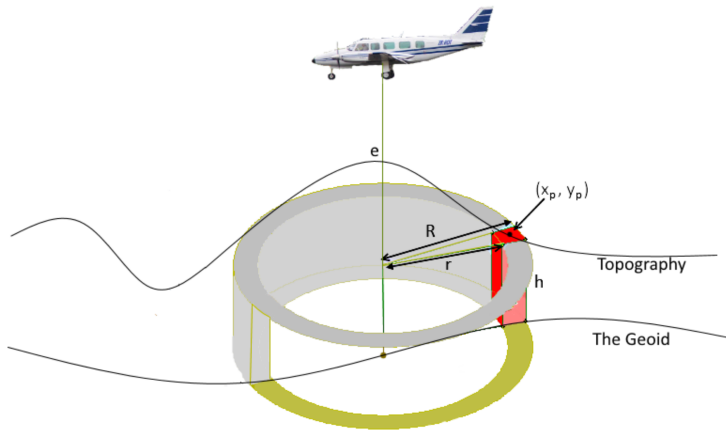


**Figure 3.3:** An illustration of an annulus of topography as an approximation for a vertical prism. From McCubbine (2016).

derivative of the prisms' gravity. The vertical component of gravity of an entire annulus (grey hollow cylinder in Figure 3.3) is defined by

$$\delta g = 2\pi G\rho(R - r + \sqrt{r^2 + h^2} - \sqrt{R^2 + h^2}) \quad (3.11)$$

where  $\rho$  is the density,  $G$  is the gravitational constant,  $r$  and  $R$  are the inner and outer radii, respectively, and  $h$  is the average height of the cylinder (Hammer, 1939).  $r$ ,  $R$ , and  $h$  are relative to the observation point, located in the centre bottom of the annulus. McCubbine (2016) provides an adaption of Equation 3.11 which isolates the gravity of just a portion of this annulus (red section in Figure 3.3). This is accomplished by adding an additional factor  $f$ , relating the area of the annulus to the area of a sector of it:

$$f = \frac{\alpha^2}{\pi(R^2 - r^2)} \quad (3.12)$$

where

$$r = \sqrt{x^2 + y^2} - \sqrt{\frac{\alpha^2}{2}} \quad (3.13)$$

$$R = \sqrt{x^2 + y^2} + \sqrt{\frac{\alpha^2}{2}} \quad (3.14)$$

where  $\alpha$  is the prism width,  $x$ ,  $y$ , and  $z$  are coordinates of the prism centre, relative to the observation point. This factor  $f$  is then multiplied by Equation 3.11 to give the vertical component of gravity for a section of an annulus,  $\delta g_{annulus} = f\delta g$ .

Taking the derivative of this with respect to  $h$  gives

$$\frac{\partial g}{\partial h} = 2f\pi G\rho h \left( \frac{1}{\sqrt{r^2 + h^2}} - \frac{1}{\sqrt{R^2 + h^2}} \right). \quad (3.15)$$

While the approximation of a prism as a section of an annulus introduces some errors, the calculation is efficient and simple to implement.

**1430 Finite differences approximation**

**1431** Another option to calculate the vertical derivative for the Jacobian matrix is with  
**1432** numerical differentiation. For this, a small prism is added above each existing prism,  
**1433** its forward gravity is calculated and the result is divided by the small prism's height.  
**1434** This approximates the vertical derivative of gravity at the surface of the prism, rel-  
**1435** ative to the observation point.

**1436**

**1437** Both methods adequately determine the Jacobian. The annulus method is a  
**1438** more simple calculation and is thus faster, but is likely less accurate and introduces  
**1439** singularities. These singularities occur if the prism is directly beneath the observa-  
**1440** tion point, so that either the inner or outer radii are negative (Figure 3.3). These  
**1441** singularities are resolved by shifting the observation point to a prism edge. Con-  
**1442** versely, the finite differences method, while it is a numerical approximation, uses  
**1443** analytical solutions for calculating the forward gravity (Fatiando a Terra Project  
**1444** et al., 2023; Nagy et al., 2000), and thus is valid in the entire domain, with no sin-  
**1445** gularities. This increased robustness makes the computation slower. Section 3.3.1.3  
**1446** compares the effectiveness and computation time of both of these methods.

**1447 3.2.5.2 Least-squares solver**

**1448** With the Jacobian matrix and the vector of gravity residuals, Equation 3.9 can be  
**1449** solved to find the set of surface correction values that minimize the fit function.  
**1450** Here, the matrix equation  $\mathbb{J}\vec{x} = \vec{r}$  is solved with an iterative damped least squares  
**1451** algorithm (LSQR Paige & Saunders, 1982). The algorithm gives the minimum-norm  
**1452** solution, where for a set of solutions that each fit the data with the same accuracy,  
**1453** the solution with the minimum  $\|p\|^2$  is chosen. LSQR accepts a damping parameter,  
**1454** which helps regularize the problem, preventing the solution from becoming too large.  
**1455** The choice of the damping value is important as it directly affects the inverted  
**1456** results. The optimal value can be chosen with a cross-validation routine following  
**1457** that of Uieda and Barbosa (2017), as described below.

**1458 3.2.5.3 Regularization**

**1459** Regularization is a series of techniques used to help constrain ill-posed inversion  
**1460** problems (Aster et al., 2018). Most potential field inversions, due to their inher-  
**1461** ent non-uniqueness, are ill-posed, containing many solutions which equally satisfy  
**1462** the data. Here regularization is split into *smallness* and *smoothness*. *Smallness*  
**1463** deals with adhering to *a priori* constraints, i.e. having the inverted surface eleva-  
**1464** tion match the previous bathymetry measurements (constraint points). *Smoothness*  
**1465** helps to achieve realistic topographic results, without major jumps or excessively  
**1466** steep slopes.

**1467 Smoothness**

**1468** To achieve a form of smoothness regularization, damping is applied at each iteration  
**1469** to the solver of the matrix equation. One method to choose an optimal damping  
**1470** value is cross-validation of the input gravity data (Uieda & Barbosa, 2017). An  
**1471** effective inversion should produce a topography that, when forward-modelled, accu-  
**1472** rately recreates observed gravity data that weren't included in the inversion. This  
**1473** idea is the basis of the cross-validation routine. The observed gravity data is split

1474 into two sets, a *training* and a *testing* set. For an individual damping value, the  
 1475 inversion is run using only the training set. The final inverted bathymetry is then  
 1476 forward-modelled onto the observation points of the testing set. The difference be-  
 1477 tween the observed and forward gravity at these testing points is calculated. The  
 1478 root mean square (RMS) of the differences provides a metric for the effectiveness  
 1479 of the damping; this is referred to as the *score*. This process is then repeated for a  
 1480 suite of damping values, and the value which produces the lowest score is used as  
 1481 the optimal damping value. In this inversion, the gravity data, whether they are  
 1482 airborne flight lines or scattered ground stations, are interpolated onto a regular grid  
 1483 (see Section 3.3.1.5). To create the testing set of observed gravity data, the original  
 1484 data are interpolated onto a grid at half the desired grid spacing. This leaves the  
 1485 training set with the desired number of points. This grid spacing configuration is  
 1486 shown in Figure 3.4.

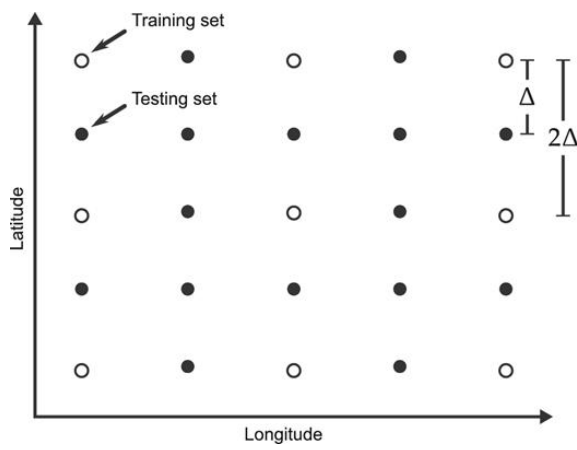


**Figure 3.4:** Configuration of observed gravity data observation points, split into training and testing sets. Reprinted from Uieda and Barbosa (2017).

### 1487 Smallness

1488 A form of smallness regularization is applied here to ensure the inversion results ad-  
 1489 here to any *a priori* bathymetry constraints. A portion of this smallness regulariza-  
 1490 tion is already accounted for when using the constraint point minimization method  
 1491 of regional-residual separation. This method minimizes the residual component of  
 1492 the gravity misfit at the constraint points by assigning the majority of the misfit to  
 1493 the regional component. However, non-zero residual values near the constraints will  
 1494 result in a non-zero correction of the prisms immediately surrounding the constraint.  
 1495 For further smallness regularization, a weighting grid (Figure 3.5) is used to ensure  
 1496 the surface correction values at each iteration are 0 at constraint points. If only  
 1497 the prism immediately at the constraint point is fixed, a *pedestal* effect commonly  
 1498 develops. This is where the nearby prisms' surfaces freely move during the inversion,  
 1499 yet the constrained prism is fixed, resulting in either a pedestal or a hole. To avoid  
 1500 this, the weighting grid smoothly decays from a value of 0 at the constraints, to a  
 1501 value of 1 at a distance. To create this grid, the minimum distance between each  
 1502 grid cell (prism) and the nearest constraint point is calculated. These values are  
 1503 then normalized from 0 to 1 (Figure 3.5). At each iteration, the least squares solver  
 1504 yields a grid of surface correction values. Before being added to the prism layer, the  
 1505 grid is multiplied by this weighting grid. This results in surface corrections of 0 for  
 1506 prisms located at constraint points, unmodified surface correction values far from

1507 constraint points, and a smooth taper between these two endmembers.

1508

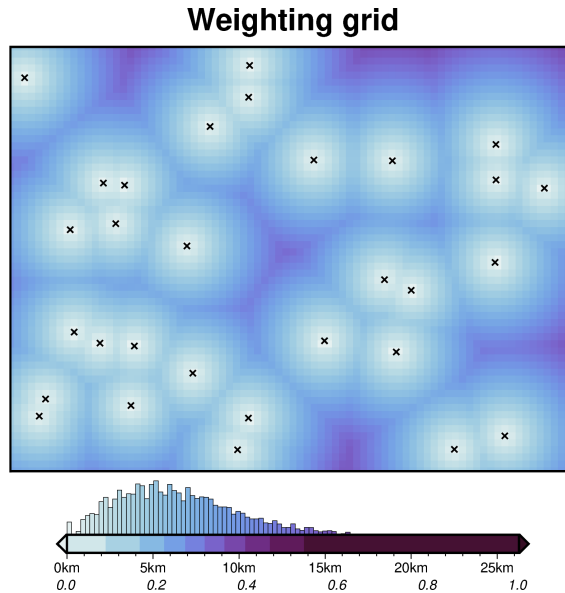


**Figure 3.5:** Weighting grid for the simple synthetic inversion, created from the minimum distance between each grid cell and the nearest constraint (black crosses). Grid values are normalized from 0 to 1 to produce the weighting grid (lower colourmap annotations).

1509 The above sections outline a single iteration of the inversion. Once the surface  
 1510 correction is calculated and the weights are applied, these values are added to the  
 1511 starting bathymetry (or the last iterations inverted bathymetry). This is then re-  
 1512 discretized into prisms. The updated prisms are then forward modelled to create a  
 1513 new predicted gravity,  $\vec{d}^{pred}$ . This is subtracted from the observed gravity,  $\vec{d}^{obs}$ ,  
 1514 to get a new misfit,  $\vec{m}$ . Using the same original regional component, the updated  
 1515 residual gravity misfit,  $\vec{m}_{res}$ , is calculated. This is now the input into the second iter-  
 1516 ation of the inversion. This process is repeated until a user-determined termination.  
 1517 Next, we outline the four criteria for ending the inversion.

### 1518 3.2.6 Stopping Criteria

1519 The inversion is terminated on one of four stopping criteria:

- 1520 1. when the inversion reaches a maximum number of iterations ( $N$ )
- 1521 2. when the  $\ell^2$ -norm of the residual ( $\|\vec{m}\|_2$ , Equation 3.1) is less than a set  $\ell^2$ -  
 1522 norm tolerance
- 1523 3. if there is no significant variation in the  $\ell^2$ -norm between iterations (i.e. the  
 1524  $\Delta\|\vec{m}\|_2$  is less than a set tolerance)
- 1525 4. if the  $\ell^2$ -norm increases above a certain threshold of the starting  $\ell^2$ -norm.

1526 The maximum number of iterations is set as a safety margin to avoid excessively  
 1527 long-running inversions. The  $\ell^2$ -norm tolerance is used to end the inversion before  
 1528 excessive over-fitting of noise in the data. This should be set to the square root  
 1529 of the assumed noise level of the gravity data. The  $\Delta\ell^2$ -norm tolerance is used to

end inversions that have reached their limit of reducing the  $\ell^2$ -norm, Finally, the upper limit of  $\ell^2$ -norm terminates run-away inversions, which occurred during the development of the inversion due to coding errors but is retained here as a fail-safe.

### 3.2.7 Software implementation

The inversion algorithm described here is implemented within the Python programming language. The algorithm uses many open-source scientific libraries. These include Harmonica for the forward gravity modelling of prisms and equivalent sources calculations (Fatiando a Terra Project et al., 2023; Soler & Uieda, 2021), Verde for various spatial operations (Uieda, 2018), PyGMT and Antarctic-Plots for figure creation (Tankersley, 2023; Uieda et al., 2021), Scipy for least squares regression (Virtanen et al., 2020), and Optuna for hyperparameter optimization (Akiba et al., 2019). The majority of the experiments were run in Jupyter notebooks (Pérez & Granger, 2007), which are documented to explain the details of using the software. All source code, results, and figures involved in this chapter are made available in an online GitHub repository ([https://github.com/mdtanker/RIS\\_gravity\\_inversion](https://github.com/mdtanker/RIS_gravity_inversion)). See Section 1.6 for the hardware used in this study.

## 3.3 Synthetic models

To assess the performance of the inversion and showcase its use, it is applied to a suite of synthetic test models. Each model has three components; 1) the ‘true’ bathymetry surface, which the inversion is expected to model, 2) the ‘observed’ gravity data, and 3) the ‘starting’ bathymetry model, which is a low-resolution version of the true surface. The only inputs into the inversions are the observed gravity data and the starting bathymetry. The true bathymetry is only used to evaluate the performance of each inversion. The observed gravity data contains the forward gravity calculated from the true bathymetry, plus, in some cases, additional noise and other gravity signals such as a regional field. The starting bathymetry is created by sampling the true bathymetry at a set of points. These values are then used to re-grid the data for the entire region using a bi-harmonic spline interpolator (Uieda, 2018). This simulates the bathymetric knowledge of many ice shelves, where few direct measurements of bathymetry exist, such as drill holes, or single-point seismic surveys. These points are referred to as the constraints. The models tested here include:

1. A simple model (Section 3.3.1): This model sets a baseline performance expectation of the inversion, with no noise, dense gravity observation points, and no additional components included in the observed gravity. The synthetic bathymetry is created with Gaussian functions of various amplitudes and wavelengths. With this same simple model, the observed gravity data is re-gridded at a lower resolution, and random noise is added, to better simulate a gravity survey.
2. A simple model with a regional field (Section 3.4): Using the same model as above, a ‘regional’ component of the gravity field is added to the observed data.

1572        3. A semi-realistic model (Section 3.5): This last model is created from real  
 1573        bathymetry data from Antarctica's Ross Sea. This model tests the inversion's  
 1574        capabilities with more realistic bathymetric features expected for sub-ice-shelf  
 1575        environments.

1576        **3.3.1 Simple model**

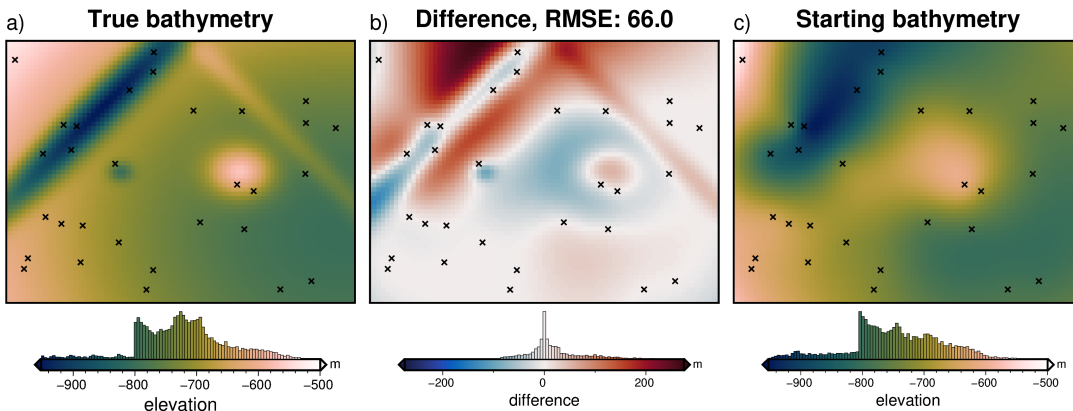


**Figure 3.6:** Simple synthetic model bathymetry. **a)** True bathymetry created from Gaussian functions, **b)** difference between a and c, and **c)** starting bathymetry, created from the sampling and re-gridding of the true bathymetry at 30 points (black crosses).

1577        **3.3.1.1 Model setup**

1578        Simulating typical sub-ice-shelf bathymetry, this model (Figure 3.6a) has an average  
 1579        elevation of  $\sim -700$  m and ranges between  $\sim -400$  m and  $\sim -1000$  m. It contains  
 1580        features of various wavelengths, amplitudes, and shapes; namely two circular fea-  
 1581        tures and two linear features. Overall, the grid is eastward deepening and contains a  
 1582        shallow and wide E-W trough through the centre. The model domain is 80 x 60 km,  
 1583        with 1 km grid cells (4800 cells). A 6 km buffer zone in all directions was included  
 1584        to limit gravitational edge effects. 30 randomly located constraint points were used  
 1585        to create the starting bathymetry (Figure 3.6c). The starting bathymetry has an  
 1586        RMS difference with the true bathymetry of 66 m.

1587

1588        To forward model the gravity of the true bathymetry, a layer of adjacent vertical  
 1589        right-rectangular prisms was created using the reference discretization method (Fig-  
 1590        ure 3.2e) with the mean elevation as the reference level. A density contrast of  $\Delta\rho =$   
 1591         $1276 \text{ kg m}^{-3}$  (contrast between seawater( $1024 \text{ kg m}^{-3}$ ) and sediment ( $2300 \text{ kg m}^{-3}$ )),  
 1592        was used, with  $+\Delta\rho$  for prisms above the reference, and  $-\Delta\rho$  for prisms below  
 1593        the reference. The forward gravity of this prism layer was calculated at a constant  
 1594        height of 1000 m (roughly 1700 m above the bathymetry) on a regular grid at half  
 1595        the grid spacing (500 m) of the bathymetry. This represents the observed gravity  
 1596        data (Figure 3.7a) and consists of both the training and testing data sets used for  
 1597        the cross-validation (Section 3.2.5.3, Figure 3.4).

1598

1599        The low-resolution starting layer was discretized in the same method, and the  
 1600        same density contrast was used. The forward gravity of these starting layer prisms  
 1601        results in the predicted gravity (Figure 3.7c). To account for any offset between

the observed and predicted data, the observed data is DC-shifted to minimize the differences at the constraint points. The difference between the shifted observed and the predicted data gives the gravity misfit (Figure 3.7b). Since there is no regional component in this synthetic model, the input into the inversion, the residual misfit, is equal to this total misfit (Equation 3.10). This residual misfit describes the ability of the starting model to predict the observed data.

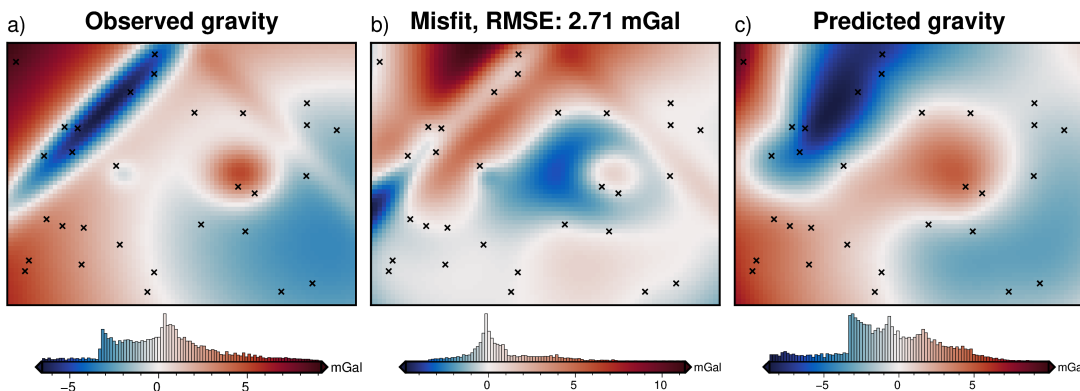


**Figure 3.7:** a) Synthetic gravity data generated from the true bathymetry, b) the residual anomaly, defined as the difference between a and c, and c) the predicted gravity from the starting bathymetry (Figure 3.6c).

### 3.3.1.2 Cross validation

To find the optimal value for the regularization damping parameter, the cross-validation method of Uieda and Barbosa (2017) is used (Section 3.2.5.3). The full set of observed data with a 500 m spacing ( $N = 19481$ ), was separated into the training ( $N = 4941$ ) and testing set ( $N = 14540$ ). With the grid configuration from Figure 3.4, the resulting training data was on a regular 1 km grid, which matches the grid of the bathymetry. This training data set was used as the input to 10 inversions. Each inversion used a different damping value between  $10^{-4}$  and  $10^{-1}$ . The resulting inverted bathymetry of each inversion was then forward-modelled on the observation points of the testing data set (not used in the inversion). The RMS difference between the forward-modelled gravity value and the initial residual misfit values was calculated, giving the cross-validation score (Figure 3.9a). Of the 10 inverted bathymetry models, the model with the lowest score is retained.

This model is shown in Figure 3.8c, and resulted from a damping value of  $10^{-2}$ . This inverted bathymetry has an RMS difference with the true bathymetry of 8 m and an RMS difference at the constraint points of 1 m. Figure 3.9b shows a profile across the model. The overlap of the true (red) and inverted (blue) bathymetry in the first panel shows the effectiveness of the inversion at recovering the true bathymetry. The lower panel shows the inversion's ability to minimize the misfit between the observed gravity (red) and the forward response of the inverted bathymetry (blue). The inversion was able to recover all the features of the true bathymetry, with only minor errors along the edges of the domain, and adjacent to constraint points. For this simple model, the inversion converged in 37 iterations, with a total computation time of 30 seconds and a final RMS residual misfit of 0.022 mGal. It terminated due to the  $\ell^2$ -norm decreasing between the set threshold of 0.15 (0.0225 mGal).

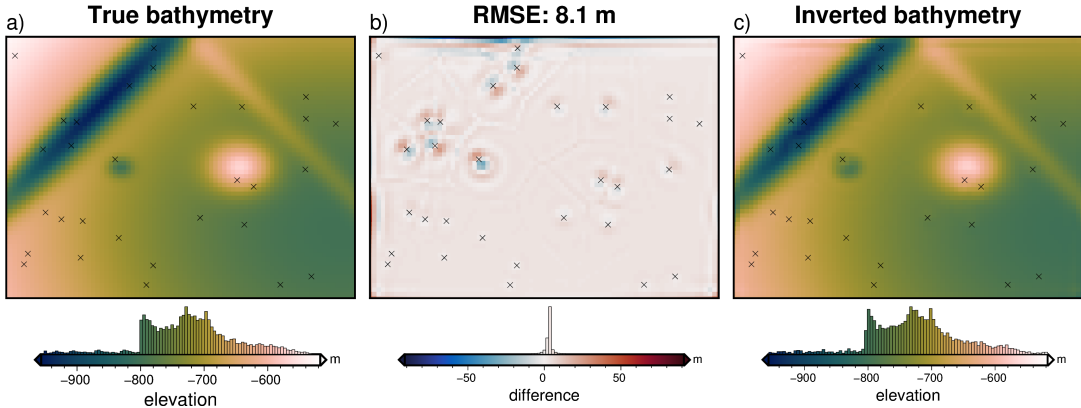


**Figure 3.8:** Inverted results with optimized parameters, using the annulus approximation method of calculating the Jacobian matrix. **a)** True bathymetry, **b)** difference between a and c, and **c)** final inverted bathymetry. Black crosses are constraint points. The RMS difference with the true bathymetry at these constraints is 1 m

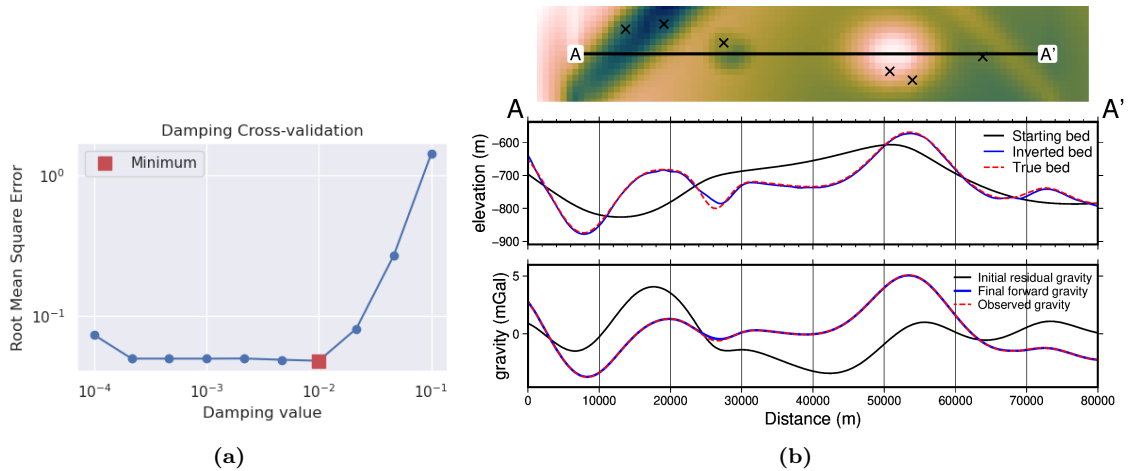


**Figure 3.9:** Cross-validation and profiles for the simple synthetic inversion. **a)** Cross-validation curve showing the optimal damping parameter (red square). Both axes are on a logarithmic scale. **b)** 2D profile of the inversion results. The top panel shows profile location and constraint points (black crosses). The middle panel contains topographic profiles of the starting, inverted, and true bathymetries. The bottom panel contains gravity anomaly profiles.

### 1633 3.3.1.3 Comparing vertical derivative methods

1634 Section 3.2.5.1 presented two methods for calculating the vertical derivative of grav-  
 1635 ity of a prism. This vertical derivative is used to create the Jacobian matrix (Equa-  
 1636 tion 3.9) and needs to be calculated at each iteration of the inversion. The above  
 1637 cross-validation and inversion were performed using the *annulus approximation* of  
 1638 the vertical derivative. Here, this process is repeated with the *finite differences*  
 1639 method of the vertical derivative. Figure 3.10 shows the results of this inversion.  
 1640 The optimal damping parameter was  $10^{-2}$ , and the inversion resulted in an RMS  
 1641 difference with the true bathymetry of 9 m, compared to 8 m for the annulus ap-  
 1642 proximation. Figure 3.11 shows the inversion convergence curves for the inversion of  
 1643 the annulus approximation and the finite differences methods. The inversion with  
 1644 the annulus approximation was  $\sim 500\%$  faster to converge than the finite differences  
 1645 method (30 sec vs 169 sec). Because these vertical derivatives need to be recalcul-  
 1646 ated at each iteration, a large portion of the inversion time is spent performing  
 1647 these calculations. This comparison shows the annulus approximation is not only

significantly faster, but results in comparable, or slightly more accurate, inversion results. For the remainder of this chapter, only the annulus approximation will be used.

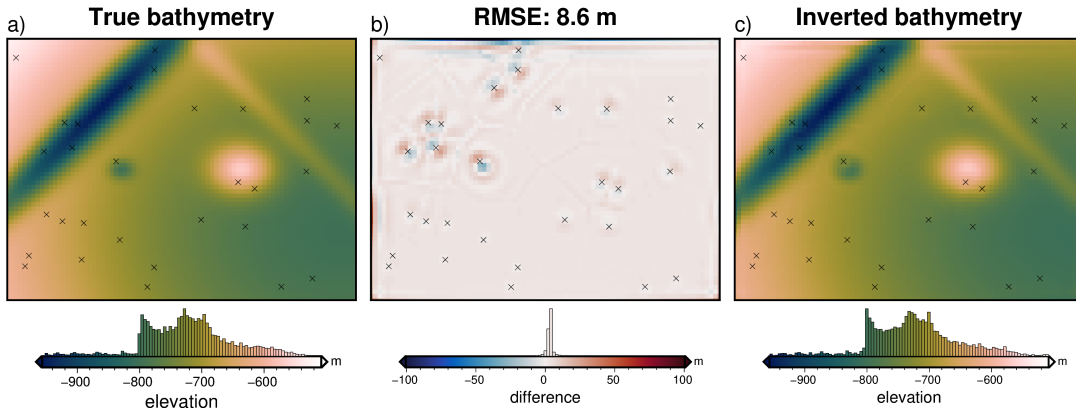


**Figure 3.10:** Inversion results with optimized parameters using the finite differences method. **a)** True bathymetry, **b)** difference between a and c, and **c)** final inverted bathymetry. Black crosses are constraint points. The RMS difference with the true bathymetry at these constraints is 1 m

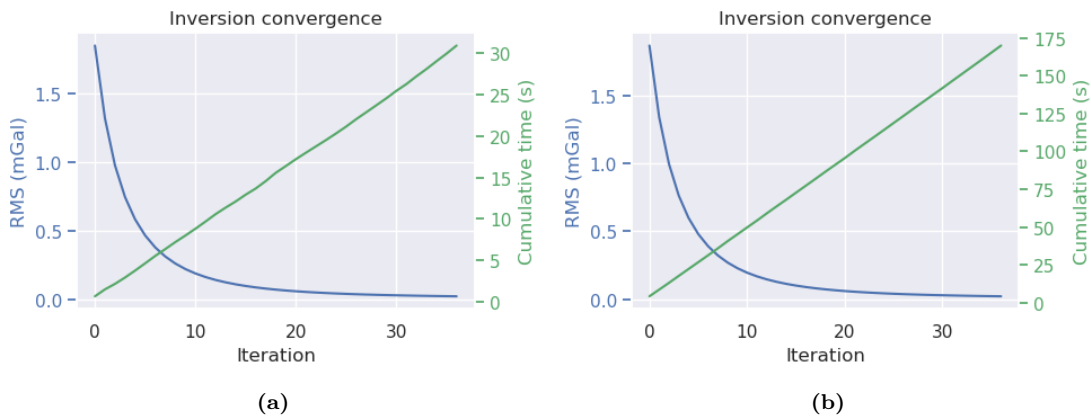


**Figure 3.11:** Inversion convergence curves for the two methods of creating the Jacobian matrix. Blue line (left y-axis) shows the RMS of the residual misfit at each iteration of the inversion. Green line (right y-axis) shows the cumulative time to complete the inversion. **a)** Results for the annulus approximation method of finding the vertical derivative. **b)** Results for the finite differences method.

### 1651 3.3.1.4 Added noise

To test the effect of noise in the gravity data, which is inevitable in data collection, especially so in airborne surveying, the observed gravity was contaminated with noise. The noise has a Gaussian distribution with a mean of 0 mGal and a standard deviation of 2% of the max absolute value of the data ( $\sim .16$  mGal). Similarly, Rashidifard et al. (2021) used 5% noise in their synthetic gravity inversion while Uieda and Barbosa (2017) use 5 mGal of noise, which for their synthetic application equated to  $\sim 1\%$  of the max absolute value. Using this noise-corrupted gravity data, the same damping parameter cross-validation was run as previously (Figure 3.13a), and the lowest score was achieved with a damping value of  $10^{-2}$ . Figure 3.12 shows the inversion results of this noise-contaminated model. The inversion converged in 18 iterations, with a total computation time of 13 seconds and a final RMS residual

misfit of 0.16 mGal. It terminated after the  $\ell^2$ -norm became lower than the set tolerance of 0.4 (0.16 mGal). This tolerance was set to match the known level of noise. The inverted bathymetry had an RMS difference of 12 m with the true bathymetry and an RMS difference of < 1 m at the constraint points. Figure 3.13b shows the inversion is still able to reproduce the observed gravity (lower panel), but a component of the noise was introduced into the final bathymetry (upper panel). All major features of the true bathymetry are recovered, albeit not as accurately as the no-noise model (Figure 3.8).

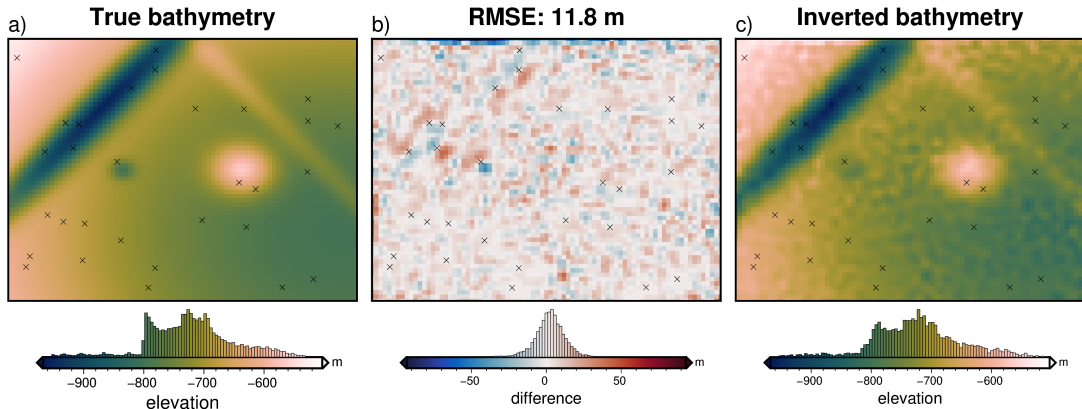


**Figure 3.12:** Simple synthetic model inversion results with 2% added noise (0.16 mGal). **a)** True bathymetry, **b)** difference between a and c, **c)** final inverted bathymetry. Black crosses are constraint points. The RMS difference with the true bathymetry at these constraints is < 1 m.

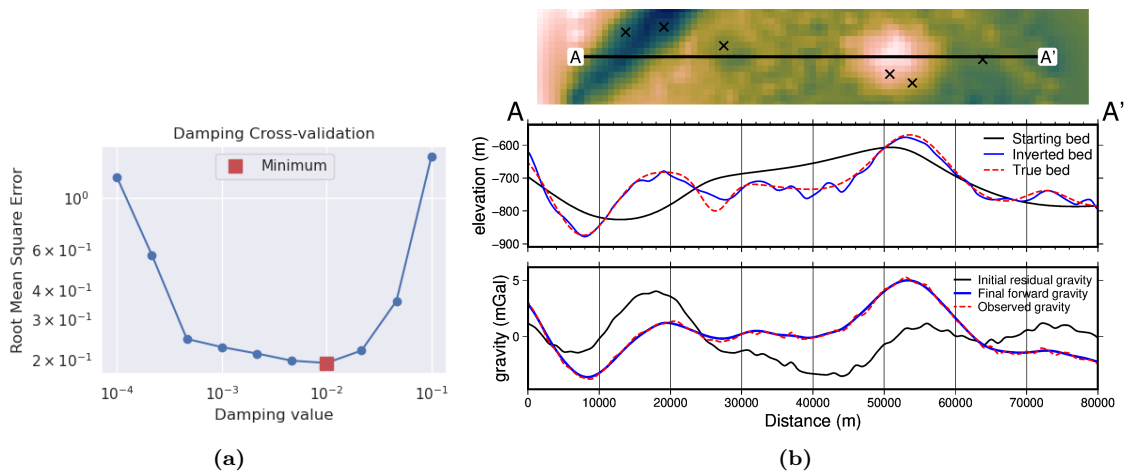


**Figure 3.13:** Cross-validation and profiles for the inversion with noise. **a)** Cross-validation curve showing the optimal damping parameter (red square). **b)** 2D profile of the inversion results. The top panel shows profile location and constraint points (black crosses). The middle panel contains topographic profiles of the starting, inverted, and true bathymetries. The bottom panel contains gravity anomaly profiles.

### 3.3.1.5 Down-sampled data

The previous two models used observed gravity data collected on a grid of observation points at the same grid spacing as the prism layer (1 km). This represents a very dense gravity survey. Gravity surveys are often relatively sparse compared to the resolution of the surface they are attempting to recover in an inversion. This section tests the effect of changing the resolution of the gravity data, to simulate

a coarser gravity survey. Simply sampling the gravity data at a coarser resolution leads to a checker-boarding effect, where the inversion alters prisms nearby the gravity observations, but not prisms further away. For this reason, it is recommended here to re-grid the observed gravity data at a similar grid spacing to the prism layer. This can be accomplished with standard gridding techniques, such as minimum curvature or bi-harmonic splines (see section 3.4.2). However, these techniques aren't well suited for potential field data since they don't account for the variation in observation heights (Soler & Uieda, 2021). An alternative method of interpolating the gravity data onto a finer resolution grid is the equivalent sources technique (Dampney, 1969)<sup>1</sup>.

1687

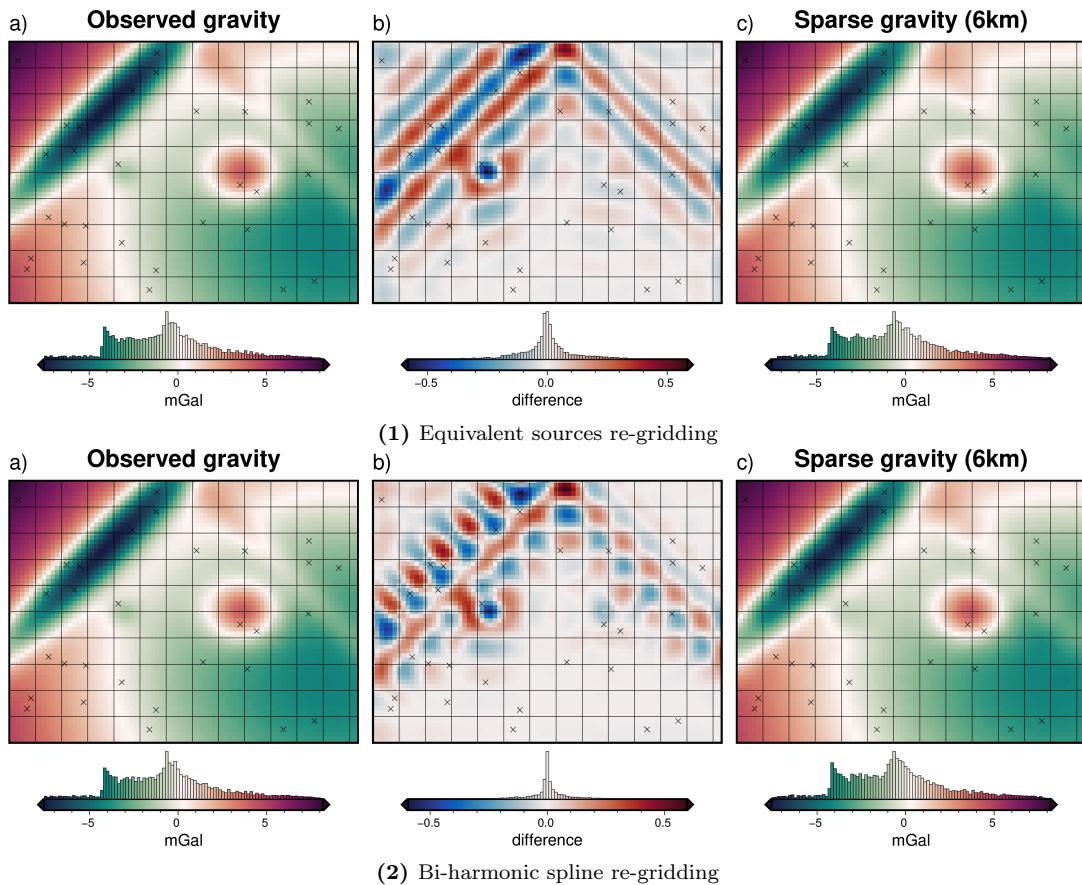


**Figure 3.14:** Creating a low-resolution observed gravity survey. **Top panel** shows results using the equivalent source technique of gridding gravity data. **Bottom panel** shows simple gridding using a bi-harmonic spline. **a)** Original observed data on a 1 km grid, **b)** gravity signal lost due to sampling and re-gridding, **c)** the low-resolution observed gravity (6 km spacing) re-gridded at 1 km with either equivalent sources (top) or a regular gridding algorithm (bottom). Black crosses show constraint points and black lines show 6 km grid.

1688 Here, the original gravity data, on a 1 km grid, is sampled at a 6 km spaced grid  
 1689 to represent a low-resolution survey with observations every 6 km. A series of point  
 1690 sources are created at depth, and their densities are altered to best reproduce the  
 1691 observed gravity data. Once this process of fitting the source parameters to the data  
 1692 is accomplished, the gravity field can be predicted anywhere. For this application,  
 1693 the equivalent sources are predicted onto an even 1 km grid, to match the spacing

<sup>1</sup>The equivalent sources technique is also used in this study as a means of regional separation (see section 3.2.4, this is a similar application but for different purposes).

of the bathymetry. Figure 3.14 shows the results of this process (top panel) and the results using simple gridding without equivalent sources (bottom panel). *Subplot a* shows the original observed gravity data (just training points) on a 1 km grid. This grid is sampled onto a 6 km grid (black grid lines) and re-gridded at 1 km (*subplot c*). *Subplot b* shows the difference, which represents the lost data resulting from the sparse survey. Typically the equivalent sources gridding technique is most beneficial to account for variations in observation heights. Here, even with constant elevations, there are noticeable differences between equivalent source gridding and simple gridding with bi-harmonic splines.

The equivalent-source resampled grid is used, with no added noise, in the same inversion procedure as the previous sections. The cross-validation (Figure 3.16a) resulted in an optimal damping value of  $10^{-2}$ . The inverted bathymetry with this damping value is shown in Figure 3.15. The inversion was completed in 29 seconds and 38 iterations with a final RMS residual misfit of 0.019 mGal. The inversion was terminated due to the  $\ell^2$ -norm decreasing below the set threshold of 0.15 mGal $^{1/2}$ . The inverted bathymetry had an RMS difference of 11 m with the true bathymetry and an RMS difference of 1 m at the constraint points. While the overall difference from the true bathymetry is low, this inversion failed to fully recover the small circular depression. Figure 3.14 shows that the nearest observation point (intersection of gridlines) was on either side of this anomaly, and thus the sparse gravity survey used here failed to image the true magnitude of the feature. Figure 3.15b shows the absence of this feature in the inverted bathymetry.

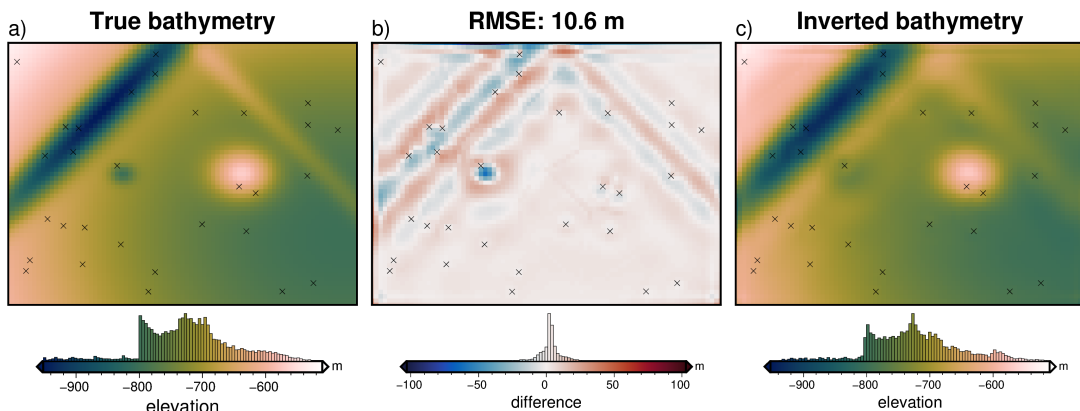


**Figure 3.15:** Simple synthetic model inversion results with input data resampled at 6x the bathymetry grid spacing (6 km). **a)** True bathymetry, **b)** difference between a and c, and **c)** final inverted bathymetry. Black crosses show constraint points. The RMS difference with the true bathymetry at these constraints is 1 m.

### 3.3.2 Ensemble of Noise and Sampling values

To test the relative importance of the level of noise and the resolution of the gravity data (i.e. station/flight line spacing), an ensemble of 100 inversions was run, with 10 noise levels between 0 and 9%, and 10 gravity resolutions between 1 and 10 km. The noise level percentages are of the maximum absolute value of the data, equating to 10 levels between 0 and 0.85 mGal. The differing gravity resolutions were created with the sampling and re-gridding of equivalent sources outlined in the above section. For each set of noise and spacing values, the cross-validation routine was used to

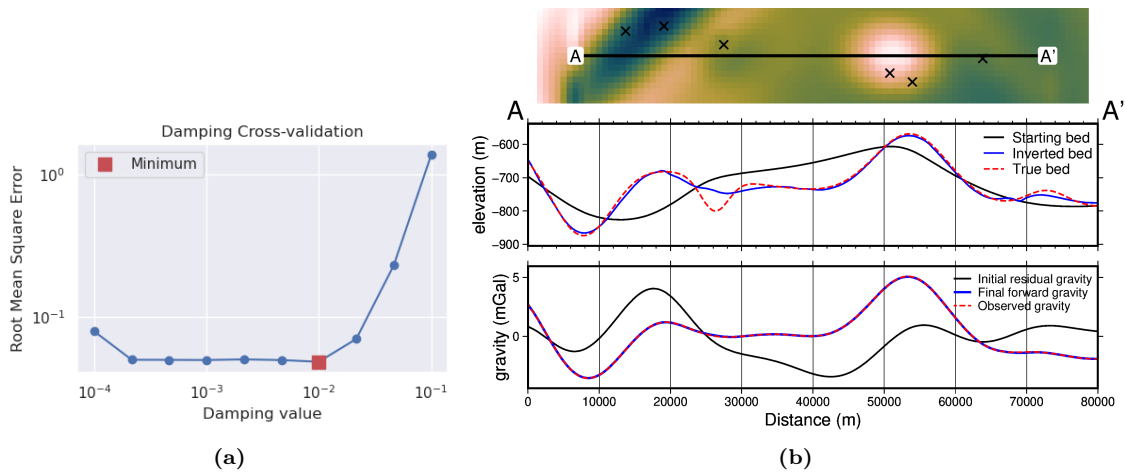


**Figure 3.16:** Cross-validation and profiles for the 6 km resampled inversion. **a)** Cross-validation curve showing the optimal damping parameter. **b)** 2D profile of the inversion results. The top panel shows profile location and constraint points (black crosses). The middle panel contains topographic profiles of the starting, inverted, and true bathymetries. The bottom panel contains gravity anomaly profiles.

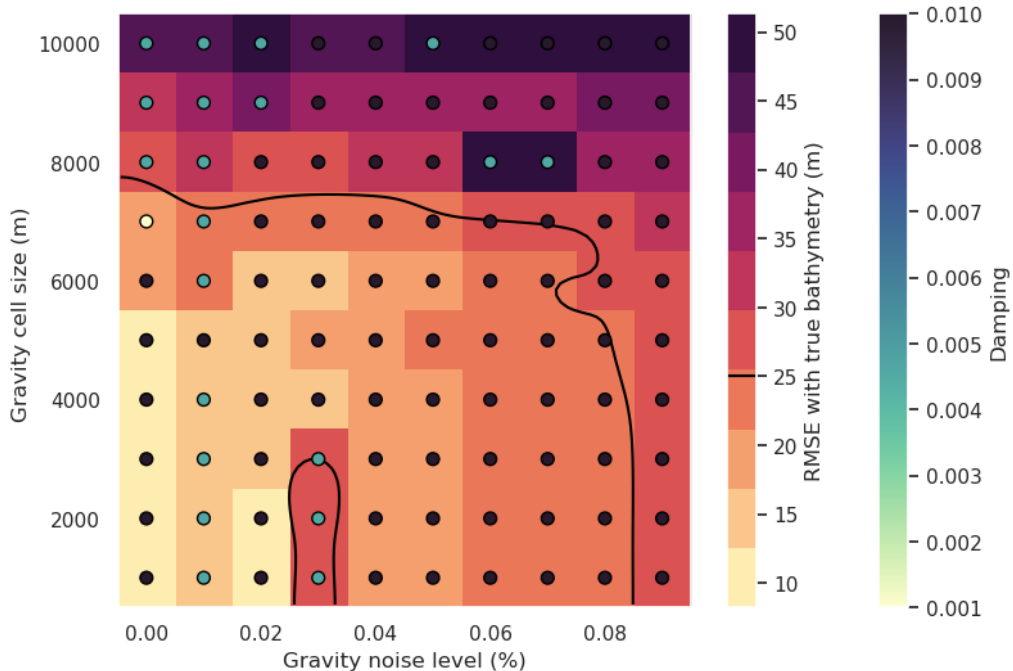


**Figure 3.17:** Ensemble of noise levels and gravity spacing for the simple synthetic model. Grid cell colour indicates each inversion's RMS difference with the true bathymetry. The circles' colour indicates the optimal damping value found for each inversion's cross-validation. Black line shows the 25 m RMSE contour, indicative of the amplitude of the smallest amplitude features.

1725 find the optimal damping parameters and associated inverted bathymetries. Each  
1726 of these 100 inversions were then compared to the true bathymetry yielding an RMS  
1727 difference for each.

1728 Figure 3.17 shows the results of this ensemble of inversion. Each grid cell  
1729 represents a single inversion, with the level of noise and gravity resolution for  
1730 the inversion indicated by the x and y axis, respectively. The background colour  
1731 (warm colours) indicates each inversion's resulting RMS difference with the true  
1732 bathymetry. Coloured circles show the optimal damping value for each inversion

1733 found through cross-validation. This shows a general decrease in the inversion's ac-  
 1734 curacy with either more noise or lower-resolution gravity data. The smallest bathy-  
 1735 metric features which this inversion ideally should recover have amplitudes of tens  
 1736 of meters (small circular depression and narrow ridge). The RMSE here indicates a  
 1737 base-level of error in the inversions, while the error in the vicinity of the short wave-  
 1738 length bathymetry features is likely higher (Figure 3.15b). Inversions with RMSEs  
 1739 of 10's of meters will likely fail to resolve these small features. For this inversion, an  
 1740 RMSE of 25 m (black contour in Figure 3.17) approximately equates to a gravity  
 1741 observation spacing greater than 8 times the prism layer spacing, and a noise level  
 1742 higher than 8% of the survey's max absolute value.

## 1743 3.4 Adding a regional component

1744 Now that the inversion has been demonstrated to adequately recover bathymetry  
 1745 with various levels of noise and resolutions of the input gravity data, an additional  
 1746 complexity is added. This complexity is a regional component of the observed  
 1747 gravity field. To account for this, the inversion remains the same, but the regional  
 1748 component of the gravity misfit must be removed beforehand (Equation 3.10). In  
 1749 this section, first, the four methods of regional separation laid out in 3.2.4 are  
 1750 compared. Next, one of these methods, constraint point minimization, is further  
 1751 investigated. Lastly, the effects of noise and gravity survey spacing are explored.

1752 This model uses the same starting bathymetry (Figure 3.6) as the previous sec-  
 1753 tion, but the observed gravity includes a regional field, which represents the portion  
 1754 of observed gravity signal resulting from unknown crustal sources, such as anomalous  
 1755 bodies or crustal thickness variations. This component (Figure 3.18b) is calculated  
 1756 from a synthetic topography with a median elevation of -4300 m and a density con-  
 1757 trast of  $700 \text{ kg m}^{-3}$ . Its range of gravity values is set to be the dominant signal in the  
 1758 observed gravity, but not large enough to fully mask the signal of the bathymetry  
 1759 signal. Figure 3.18 shows the various components of the gravity and resulting misfit  
 1760 for this model.

### 1761 3.4.1 Regional separation methods

1762 The four methods of regional separation discussed in section 3.2.4 each have at least  
 1763 one hyper-parameter which affects their calculation of the regional field. For each  
 1764 method these include

- 1765 1. Low-pass filter: the distance width of the Gaussian filter.
- 1766 2. Trend removal: the degree of the polynomial trend fit to the misfit.
- 1767 3. Equivalent source prediction: the depth and damping parameters of fitting  
 1768 sources to the data (Soler & Uieda, 2021).
- 1769 4. Constraint point minimization: parameters for the associated gridding method,  
 1770 such as the tension factor for minimum curvature gridding (Smith & Wessel,  
 1771 1990) or the minimum distance and damping parameter for bi-harmonic spline  
 1772 gridding (Uieda, 2018).

1773 Since for this synthetic model, the true regional field is known (Figure 3.18b), the  
 1774 effect of the parameters associated with each of the four methods can be explored.

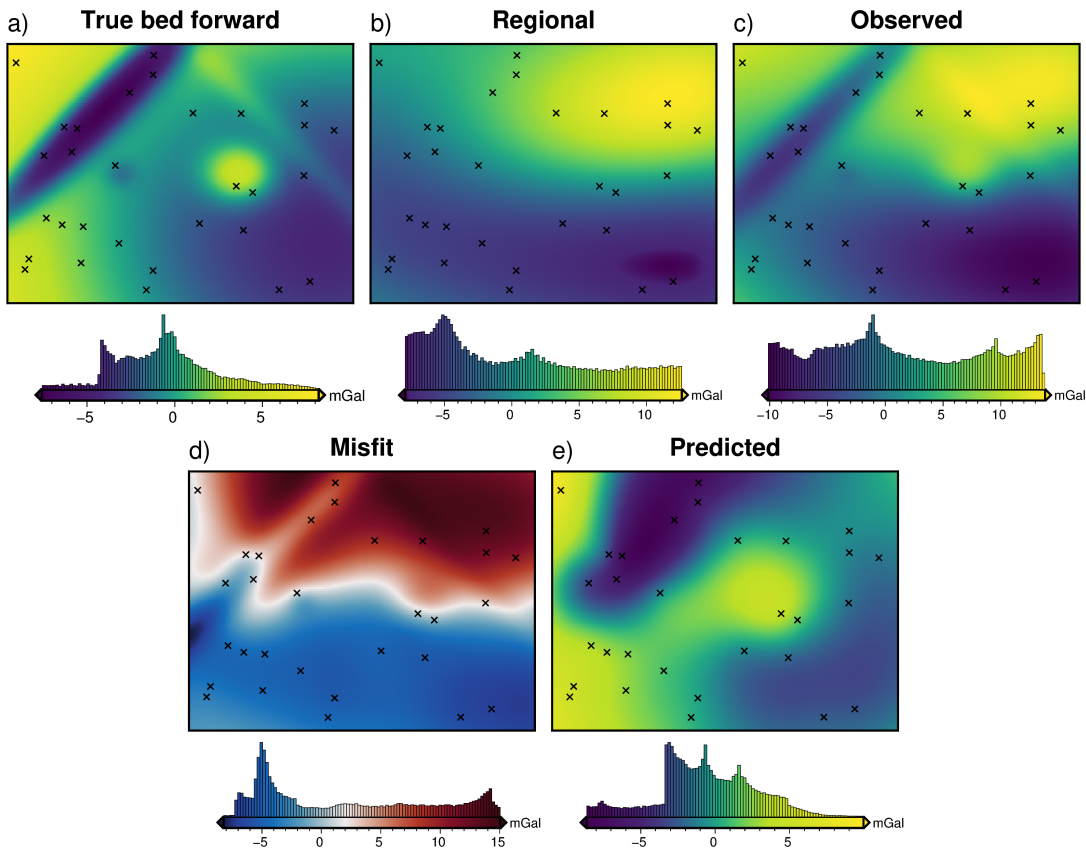


**Figure 3.18:** Gravity components and anomalies for the simple synthetic model with the addition of a regional field. **a)** the forward gravity of the true bathymetry, **b)** the regional component of gravity, **c)** the observed gravity from the combination of a and b, **d)** the gravity misfit from the difference between c and e, and **e)** the predicted gravity from the forward calculation of the starting bathymetry.

Excluding the constraint point minimization method, an optimization is run for each method, with the goal of finding the parameter values which minimize the RMS difference between the true and calculated regional gravity. Each optimization has 20 trials. The constraint point minimization doesn't require optimization because the various gridding parameters won't significantly affect the RMS difference between the resulting regional field and the true field. However, the gridding parameters will affect the inversion itself; this is explored in the next section. For this comparison of the regional removal method, the constraint point minimization method uses bi-harmonic spline gridding, and the gridding damping parameter is chosen with a cross-validation (Uieda, 2018). The best regional field (lowest RMS with the true regional field) of each method was found with the following parameters:

1. a 30 km filter width for the low pass filter method
2. a 3<sup>rd</sup> order trend for the trend removal method
3. source depth of 89 km and a damping value of 1.72 for the equivalent source technique
4. an interpolator damping of  $1.27 \times 10^{-8}$  for the bi-harmonic spline interpolator of the constraint point minimization method.

Each of these regional fields was then removed from the gravity misfit, producing the residual anomalies (Figure 3.19a-d). These resulting residuals were then input

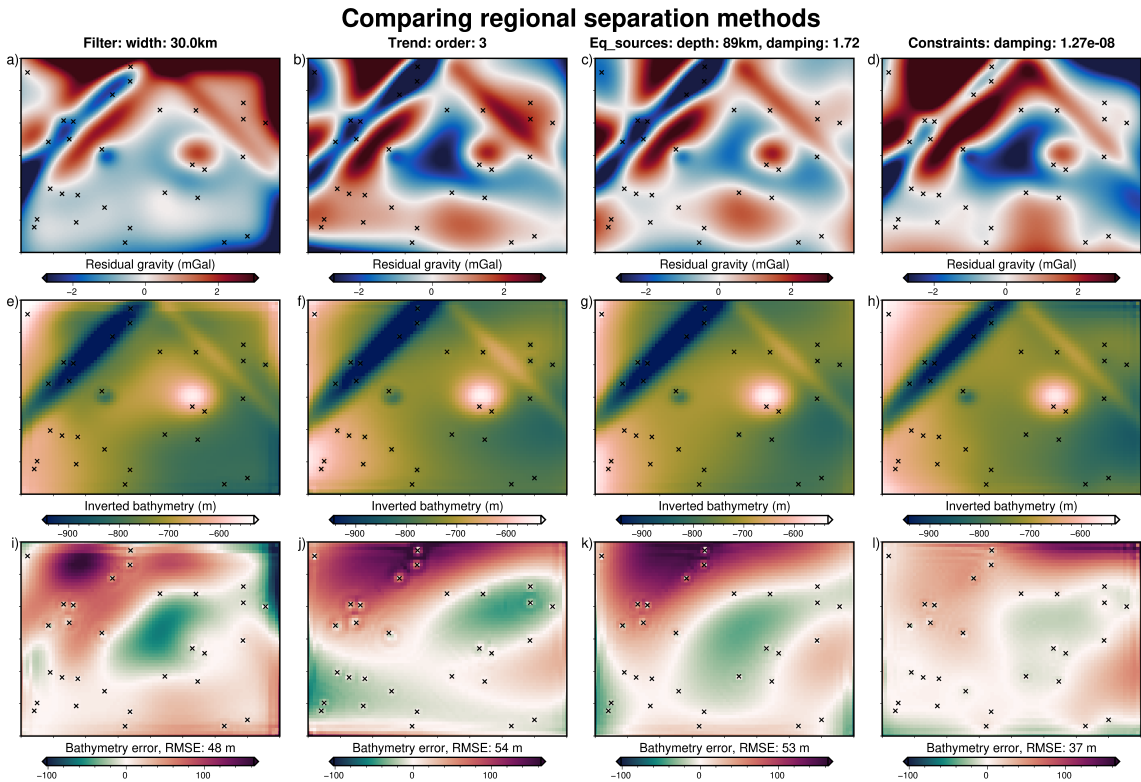


**Figure 3.19:** Comparison of inversions with 4 regional separation methods. First row (**a-d**) shows residual gravity misfit after regional separation. Second row (**e-h**) shows the inverted bathymetry for each method. Third row (**i-l**) shows the error of the inverted bathymetries with the true bathymetry. Constraint points are shown as black crosses. Colourmaps are identical for each row. Profiles of these data are shown in Figure B.1 of Appendix B.

1794 into an inversion, resulting in the inverted bathymetries of d-h of Figure 3.19, and the  
 1795 bathymetry error relative to the true bathymetry was found (Figure 3.19i-l). For  
 1796 these inversions, the same damping parameter cross-validation was conducted, as  
 1797 described in Section 3.3.1.2. This comparison of regional separation methods shows  
 1798 that the constraint point minimization method (Figure 3.19l) produces the best  
 1799 inverted bathymetry, both visually (Figure 3.19h), and based on the RMS difference  
 1800 with the true bathymetry (37 m). Figure B.1 in Appendix B shows a profile of  
 1801 the resulting regional fields and inverted bathymetries of these various methods of  
 1802 regional separation. The remainder of this section further examines the constraint  
 1803 point minimization method of regional separation.

### 1804 3.4.2 Constraint point minimization

1805 The constraint point minimization method assumes that at locations of known  
 1806 bathymetry, there is no residual component of gravity misfit, and the regional com-  
 1807 ponent entirely equals the misfit. To implement this, misfit values at the constraints  
 1808 are sampled and used to create a region-wide grid of regional values. This grid is  
 1809 then removed from the misfit to get the residual misfit (Equation 3.10). This grid-  
 1810 ding can be accomplished by many techniques, which at an initial inspection appear  
 1811 to produce similar results. Here, two methods of gridding and their gridding param-  
 1812 eters are compared, and the impact on the inverted bathymetry are shown. These  
 1813 gridding methods are tensioned minimum curvature (Smith & Wessel, 1990) and  
 1814 bi-harmonic splines (Sandwell, 1987).

**1815 3.4.2.1 Tensioned minimum curvature**

1816 Tensioned minimum curvature gridding is a commonly used technique for gridding  
1817 sparse data which fits the smoothest possible surface while still matching the data  
1818 (Wessel & Bercovici, 1998). It allows variation in the location of maximum cur-  
1819 vature through the tension factor parameter. A tension factor of 0 results in the  
1820 minimum curvature solution (maxima and minima allowed anywhere), while a value  
1821 of 1 localizes the curvature at the data points (maxima or minima only allowed at  
1822 the data points) (Smith & Wessel, 1990). A tension of 0.25 is suggested for poten-  
1823 tial field data (Wessel et al., 2019). Tensioned minimum curvature has been used in  
1824 several bathymetric inversions for constraint point minimization (An et al., 2019a;  
1825 Millan et al., 2020; Yang et al., 2021).

**1826 3.4.2.2 Bi-harmonic splines**

1827 The second method of gridding the sampled gravity misfit values uses bi-harmonic  
1828 splines. This method uses Green's functions and the least squares fit to the data  
1829 (Sandwell, 1987). Computation time for this technique is approximately propor-  
1830 tional to the cube of the number of data, making it computationally expensive for  
1831 large datasets (Deng & Tang, 2011). There is a damping parameter value that can  
1832 be adjusted, to smooth the resulting interpolation. As implemented in the *SplineCV*  
1833 class of the Python package Verde (Uieda, 2018), automated cross-validation of the  
1834 data can be used to identify the damping value which best predicts the data. Once  
1835 the parameter is determined, and the data is interpolated, the interpolation can be  
1836 predicted at any location, such as on the nodes of a uniform grid.

1837  
1838 Despite its slow run time with large datasets, bi-harmonic spline gridding has  
1839 several advantages over tensioned minimum curvature gridding. It allows the in-  
1840 corporation of data uncertainties into the fitting via a weighting parameter. With  
1841 the use of cross-validation, there are no subjective parameters that can significantly  
1842 alter the results. Lastly, the predicted data don't need to be on a regular grid,  
1843 which is useful for irregularly shaped domains that don't adhere to a rectangular  
1844 region. In their bathymetry inversion, Millan et al. (2020) point out features in their  
1845 inverted bathymetry which likely result from the minimum curvature gridding tech-  
1846 nique. Apart from this, there appears to be little work related the how the gridding  
1847 procedure affects this aspect of a bathymetry inversion.

**1848 3.4.2.3 Gridding comparison**

1849 In this section, the effect which the gridding process has on the inverted bathymetry  
1850 is analyzed. Four sets of regional separations were conducted, three using the ten-  
1851 sioned minimum curvature technique, and one using the bi-harmonic spline tech-  
1852 nique. For the three minimum curvature separations, the tension factors used were  
1853 the end members, 0 and 1, and the suggested value for geopotential data, 0.25.  
1854 For the bi-harmonic spline, a cross-validation with 20 varying damping values was  
1855 conducted, and the best resulting damping value was used. For each of the four  
1856 calculated regional fields, the resulting residual fields (Figure 3.20a-d) were used as  
1857 inputs to an inversion. All four residual anomaly data were included in an inversion  
1858 damping parameter cross-validation, as described in Section 3.3.1.2. The difference  
1859 between the resulting inverted bathymetry and the true bathymetry of each model

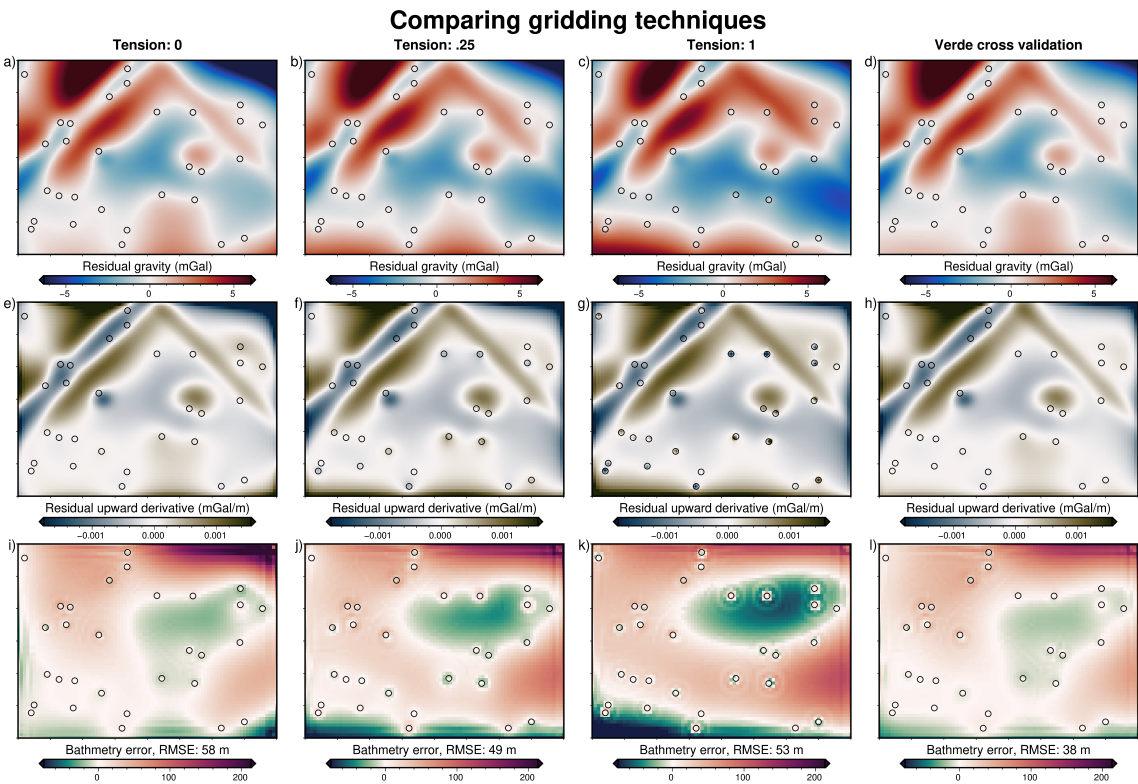


**Figure 3.20:** Comparison of gridding techniques for the constraint point minimization method of regional-residual separation. By sampling the misfit at constraints, and re-gridding over the entire domain, the regional component of the misfit is estimated. Gridding methods include minimum curvature gridding with tension factors of 0 (**column 1**), 0.25 (**column 2**), 1 (**column 3**), and cross-validated bi-harmonic spline gridding (**column 4**). Resulting gridded regional components were removed from the misfit grids to produce the residual grids (**a-d**). Second row (**e-h**) shows the vertical derivative of the residual, to highlight the gridding variations. Third row (**i-l**) shows the error of the inverted bathymetries with the true bathymetry. Constraint points are shown as open circles. Colourmaps are identical across all columns. Profiles of these data are shown in Figure B.2 of Appendix B.

is shown in Figure 3.20i-l. To help visualize the difference in the resulting residual grids, 3.20e-h shows the vertical derivative of the residual fields. This highlights that while the residual values at the constraints are all similar, the slope of the residual in the vicinity of the grids is strongly dependent on the gridding method <sup>2</sup>. Additionally, the minimum curvature gridding is shown, in subplots a-c, to create large artificial anomalies away from constraint points (low values in upper right corners). These gridding artifacts result in large errors in the resulting bathymetry 3.20i-k. The bi-harmonic spline interpolator (last column in 3.20) is shown to produce a residual field that adheres to the constraints, has smooth curvature near constraints, and doesn't create large artificial anomalies. The effectiveness of this interpolator is confirmed by the low RMS difference between the inverted and true bathymetry (38 m). Figure B.2 in Appendix B shows a profile of the resulting regional fields and inverted bathymetries of these various gridding methods. With the bi-harmonic spline gridding techniques shown to be the most effective, the remainder of this chapter uses this gridding technique for the constraint point minimization method of regional separation.

<sup>2</sup>Note that the gridding process creates the regional field (not shown in Figure 3.20), which when subtracted from the total misfit gives the residual field. The residual grid is affected by these gridding effects through the removal of the regional field.

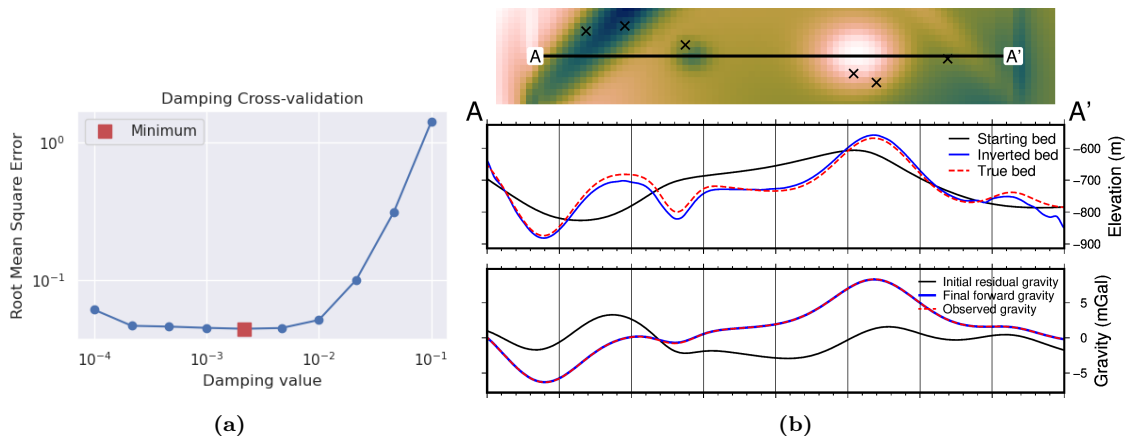


**Figure 3.21:** Cross-validation and profiles for the simple synthetic inversion with a regional component removed. **a)** Cross-validation curve showing the optimal damping parameter (red square). **b)** 2D profile of the inversion results. The top panel shows profile location and constraint points (black crosses). The middle panel contains topographic profiles of the starting, inverted, and true bathymetries. The bottom panel contains gravity anomaly profiles.

### 3.4.3 Inversion results

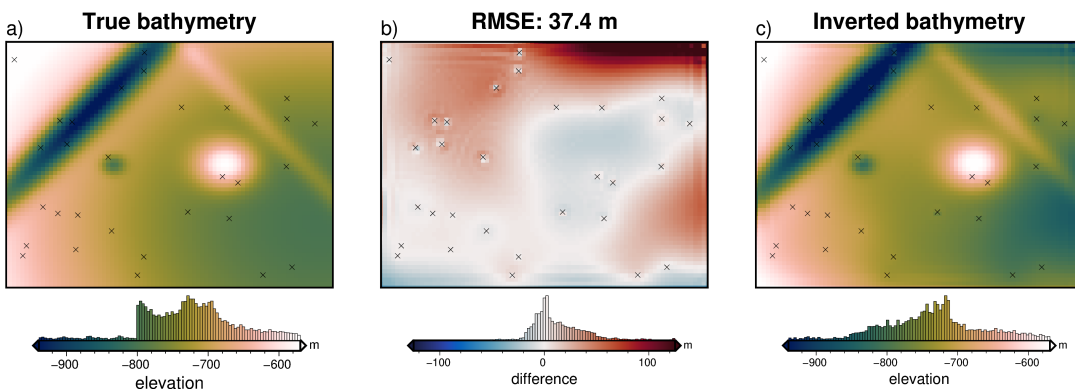


**Figure 3.22:** Simple synthetic model inversion with a removed regional component. **a)** True bathymetry, **b)** difference between a and c, **c)** final inverted bathymetry. Black crosses are constraint points. The RMS difference with the true bathymetry at these constraints is 2 m.

Using the cross-validated bi-harmonic gridding method to separate the regional component of the gravity misfit, the resulting residual misfit was used in an inversion. The same gravity data cross-validation method of determining the optimal damping parameter is used (Figure 3.21). The optimal damping parameter was found to be  $\sim 10^{-2.6}$ . The resulting inversion is shown in Figure 3.22. The inverted bathymetry had an RMS difference with the true bathymetry of 37 m and an RMS difference at the constraints of 2 m. The inversion was completed in 66 seconds, with 39 iterations and a final RMS residual of 0.022 mGal. The inversion was terminated due to the  $\ell^2$ -norm decreasing below the set threshold of  $0.15 \text{ mGal}^{1/2}$ . All four bathymetric features were recovered, but a lack of constraints in a few regions (the upper-right corner) lead to a miscalculation of the regional field and a subsequent over-deepening of the bathymetry.

The regional separation, parameter cross-validation, and inversion were repeated with additive noise and re-sampling of the gravity data to a coarser resolution (Appendix B.1). As in section 3.3.2, this above workflow was also repeated for an ensemble of noise levels and gravity data grid spacings, as discussed next.

### 1893 3.4.4 Ensemble of Noise and Sampling values

1894 Following the method outlined in Section 3.3.2, an ensemble of 100 inversions with  
 1895 varying levels of noise and gravity observation spacings was conducted. The noise  
 1896 and gravity spacing changes were applied to the original observed data, and the  
 1897 forward calculation of the starting model, initial misfit calculation, and regional field  
 1898 removal were all repeated. Each model was then inverted with a cross-validation,  
 1899 and the resulting RMS differences with the true bathymetry are shown in Figure  
 1900 3.23.

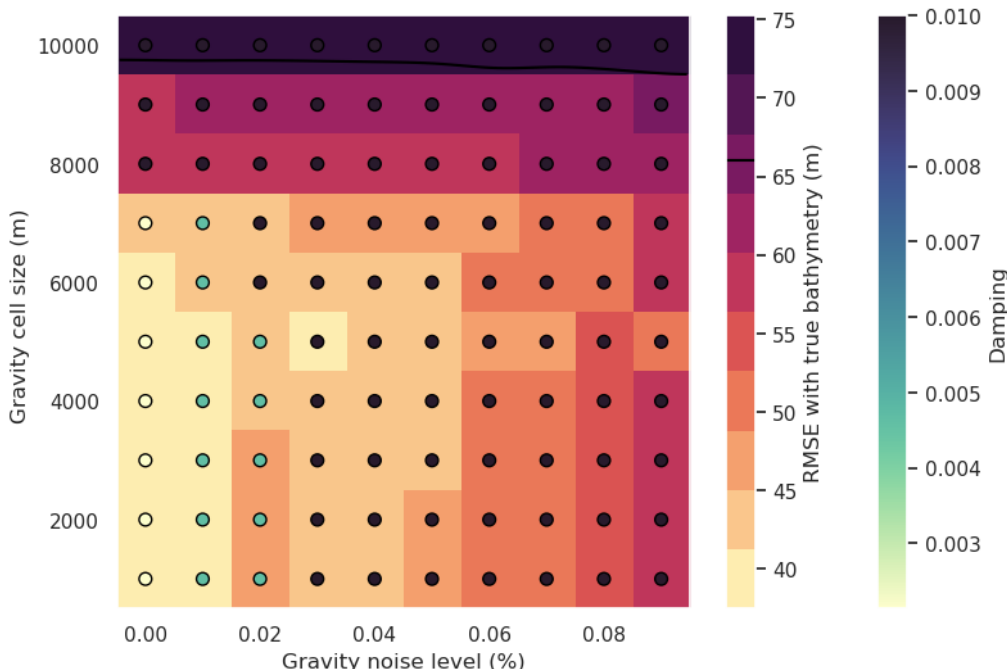


**Figure 3.23:** Ensemble of noise levels and gravity spacing for the simple synthetic model with a regional field. Grid cell colour indicates each inversion's RMSE with the true bathymetry. The circles' colour indicates the optimal damping value found for each inversion's cross-validation. Black line shows the 66 m contour, representing the RMS difference between the true and starting bathymetry.

### 1901 3.4.5 Simple model comparison

1902 Table 3.1 compares the performance of each of the above inversions. The four  
 1903 inversions without a regional component of the gravity data (annulus approximation,  
 1904 prism approximation, with noise, and resampled), all recovered the bathymetry with  
 1905 an RMSE of  $\sim 10$  m. With the regional component, the lowest RMS was raised to  
 1906 37 m. The constraint point minimization method of regional separation produced  
 1907 significantly more accurate bathymetry models than the other methods. With these  
 1908 optimal methods and baseline performance standards, a new synthetic model is  
 1909 introduced which was created to emulate the expected bathymetry features and  
 1910 gravity anomalies associated with a sub-ice-shelf environment.

|                                | RMS<br>(m) | RMS at constraints<br>(m) | Total time<br>(hr:min:sec) | # iterations | Final residual RMS<br>(mGal) |
|--------------------------------|------------|---------------------------|----------------------------|--------------|------------------------------|
| <b>No regional component</b>   |            |                           |                            |              |                              |
| Starting bathymetry            | 66         | 0.04                      | —                          | —            | 2.7                          |
| annulus                        | 8          | 1                         | 00:00:30                   | 37           | 0.022                        |
| finite differences             | 9          | 1                         | 00:02:49                   | 37           | 0.022                        |
| 2% noise                       | 12         | < 1                       | 00:00:13                   | 18           | 0.16                         |
| 6 km re-grid                   | 11         | 1                         | 00:00:29                   | 38           | 0.019                        |
| <b>With regional component</b> |            |                           |                            |              |                              |
| Starting bathymetry            | 66         | 0.04                      | —                          | —            | 7.4                          |
| filter                         | 48         | —                         | —                          | —            | —                            |
| trend                          | 54         | —                         | —                          | —            | —                            |
| equivalent sources             | 53         | —                         | —                          | —            | —                            |
| constraint point minimization  | 37         | 2                         | 00:01:06                   | 39           | 0.022                        |
| 2% noise                       | 45         | 2                         | 00:00:12                   | 13           | 0.23                         |
| 4 km re-grid                   | 38         | 2                         | 00:00:51                   | 38           | 0.022                        |

**Table 3.1:** Summary of the simple synthetic model inversion results.

## 1911 3.5 Ross Sea model

1912 Here a semi-realistic model is introduced. In the past section, two synthetic topographies (bathymetry and a crustal layer) were used in forward modelling to  
 1913 create synthetic gravity data. Here, real topographic data are used to create the  
 1914 synthetic gravity. This model is termed semi-realistic since the gravity is synthetically  
 1915 calculated, but it results from geologically real surfaces. This model uses data  
 1916 from Antarctica's Ross Sea (Figure 3.1, north of Ross Ice Shelf). The bathymetry  
 1917 data are from the IBCSO v2 data compilation (Dorschel et al., 2022), resampled at  
 1918 a 5 km resolution (Figure 3.24a). This data are mostly from shipborne multi-beam  
 1919 echo sounding. To create the regional component of gravity, basement depths from  
 1920 the ANTOSTRAT compilation of shipborne seismic data have been used (Bran-  
 1921 colini et al., 1995), at a 5 km resolution (Figure 3.24b). The inversion domain is  
 1922 320 × 420 km and a buffer zone of 40 km was included in all directions, resulting  
 1923 in 8000 grid cells per surface.  
 1924

1925

### 1926 3.5.1 Observed gravity

1927 The bathymetric and crustal surfaces were discretized with the reference discretization  
 1928 method (Figure 3.2e) with the mean elevation of each surface as its reference level. A density contrast of  $\Delta\rho = 1276 \text{ kg m}^{-3}$  (contrast between seawater( $1024 \text{ kg m}^{-3}$ ) and sediment ( $2300 \text{ kg m}^{-3}$ )), was used, with  $+\Delta\rho$  for prisms  
 1929 above the reference, and  $-\Delta\rho$  for prisms below the reference. For the basement, a  
 1930 density contrast of  $\Delta\rho = 200 \text{ kg m}^{-3}$  was used, representing the contrast between  
 1931 sediment ( $2300 \text{ kg m}^{-3}$ ) and low-density basement rock ( $2500 \text{ kg m}^{-3}$ ). This contrast  
 1932 was set so that the resulting forward gravity of the basement was slightly greater  
 1933 in magnitude than that of the bathymetry. The forward gravity of each layer was  
 1934 calculated at a regular grid of observation points with a 5 km spacing, at a constant  
 1935 elevation of 1 km (Figure 3.24c-d). This created the full-resolution synthetic ob-  
 1936 served gravity dataset. To represent an airborne gravity survey, this grid is sampled  
 1937 along synthetic flight lines.  
 1938

1939

1940 1941 This synthetic survey (Figure 3.25b) consisted of five N-S and 24 E-W flight lines.

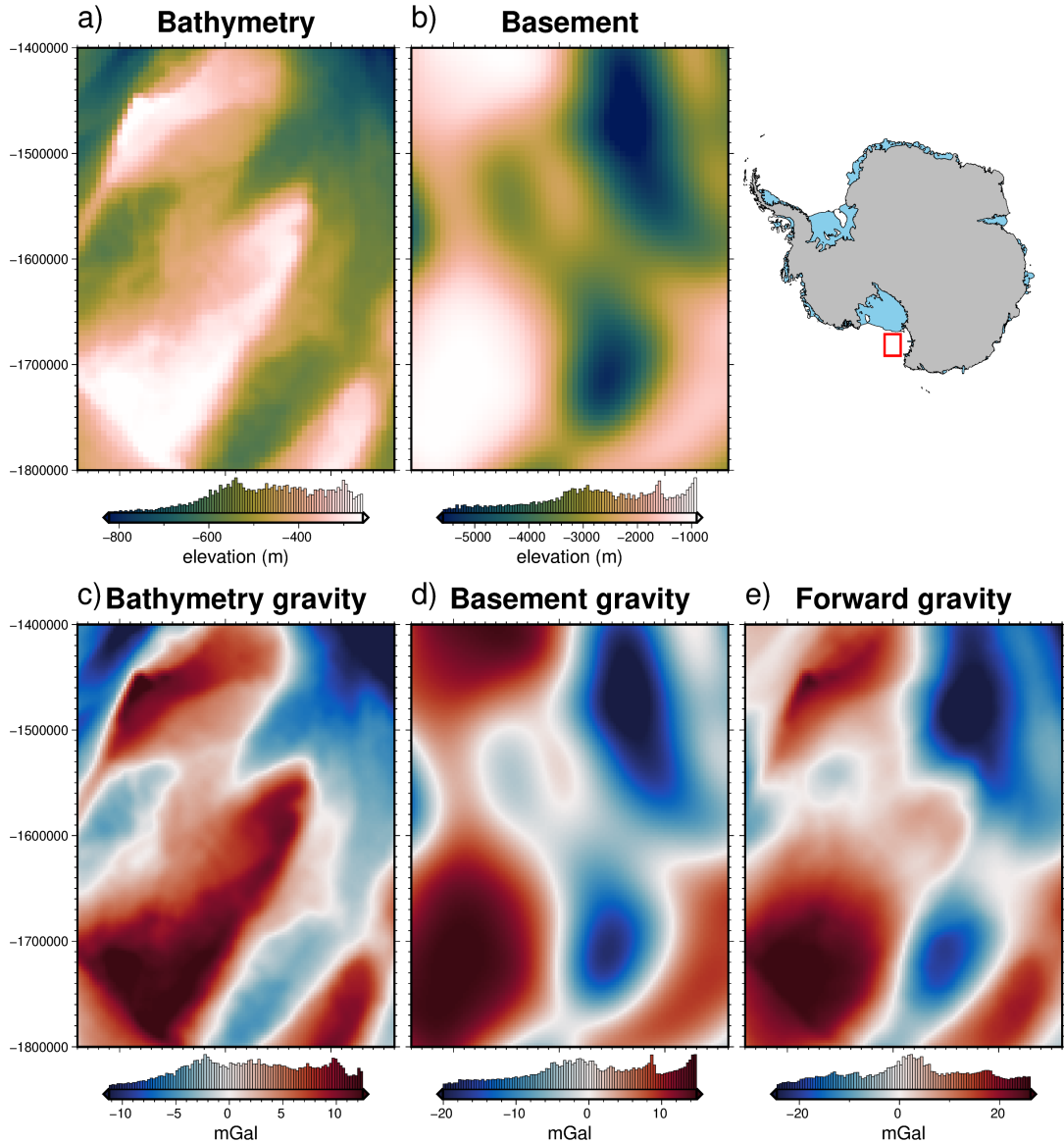


**Figure 3.24:** Ross Sea semi-synthetic model. **a)** Bathymetry data at 5 km resolution from IBCSO v2 (Dorschel et al., 2022), **b)** basement topography from the ANTOSTRAT project at 5 km resolution (Brancolini et al., 1995), **c)** forward gravity calculated at a regular 5 km grid at 1 km altitude for the bathymetry and **d)** for the basement. **e)** Total forward gravity from the combinations of c and d. Location of Ross Sea inversion domain shown as red box.

1942 Spacing between lines was 50 km for the N-S lines and 15 km for the E-W lines. One  
 1943 N-S line and 3 E-W were omitted to represent missed flights. Along line spacing  
 1944 of data was 5 km. This survey configuration is similar to other Antarctic airborne  
 1945 surveys (Tinto et al., 2019). The full resolution gravity (Figure 3.25a) was sampled  
 1946 at these flight line locations, and the resulting values were fitted with equivalent  
 1947 sources. Gravity observations were then predicted from these sources on an even  
 1948 5 km grid<sup>3</sup> over the whole domain (Figure 3.25c). Lastly, the survey data were con-  
 1949 taminated with noise from a Gaussian distribution, with a mean of 0 and a standard  
 1950 deviation of 0.6 mGal (2% of the max absolute value of the full-resolution data).  
 1951 The difference between the true gravity and this noise-contaminated synthetic sur-  
 1952 vey (Figure 3.25b) represents the typical loss of data resulting from a sparse airborne

<sup>3</sup>The gravity observations were actually interpolated onto a 2.5 km grid to account for the testing data.

1953 survey. The RMS difference is 0.75 mGal. The largest differences are located within  
 1954 the flight line data gaps.

1955

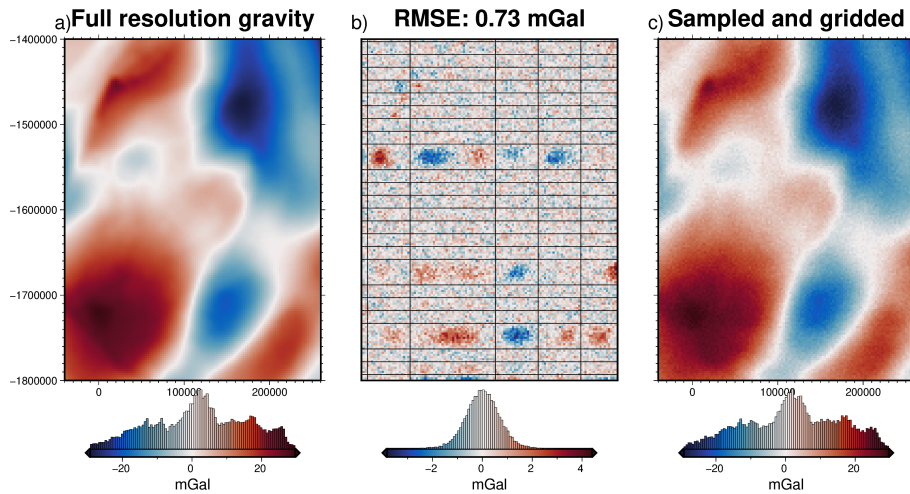


**Figure 3.25:** Ross Sea synthetic airborne survey. **a)** Full-resolution gravity data from the forward calculation of the bathymetry and basement. **b)** Difference between a and b, with black lines showing the synthetic airborne survey points. **c)** Gravity data from sampling along flight lines and re-gridded with equivalent sources.

### 1956 3.5.2 Starting bathymetry

1957 The bed elevations around the borders of ice shelves are generally well-constrained.  
 1958 Bathymetry depths from the open ocean portion of the ice shelf border can be  
 1959 found through satellite altimetry or multi-beam sonar surveys. The remainder of  
 1960 the ice shelf border consists of grounded ice. Bed elevations beneath grounded ice  
 1961 can be efficiently imaged or modelled with methods such as airborne radar or mass-  
 1962 conservation modelling (Morlighem et al., 2020). Many Antarctic ice shelves also  
 1963 contain sparse direct measurements of bathymetry from seismic surveying. This re-  
 1964 sulting configuration for many ice shelves is generalized by a very well-constrained  
 1965 border with sparse constraints located within. Here, this configuration is mimicked  
 1966 for a hypothetical ice shelf in the Ross Sea.

1967

1968 Within the model domain, a polygon is created to represent the ice shelf bor-  
 1969 der (Figure 3.26). Outside this border, constraint points are placed in each grid  
 1970 cell of the model ( $N = 3503$ , small black dots in Figure 3.26). Within the border,  
 1971 constraints are placed on a semi-regular grid. To represent a spatial constraint den-  
 1972 sity similar to other Antarctic ice shelves<sup>4</sup>, 1 constraint per  $2500 \text{ km}^2$  is used. This  
 1973 equates to 39 constraints. In the previous models, the true bathymetry was sampled  
 1974 at the constraints and the resulting values were gridded for the entire domain. Here,  
 1975 to represent measurement uncertainties for attaining the constraint point depths, af-  
 1976 ter each point is sampled, Gaussian noise is added to the values before gridding.

1977

1978 Points outside of the ice shelf are contaminated with noise from a Gaussian  
 1979 distribution with a standard deviation of 5 m. This represents the well-constrained  
 1980 methods associated with bed observations on either grounded ice or in the open

<sup>4</sup>The Ross Ice Shelf has  $\sim 1$  constraint per  $2200 \text{ km}^2$

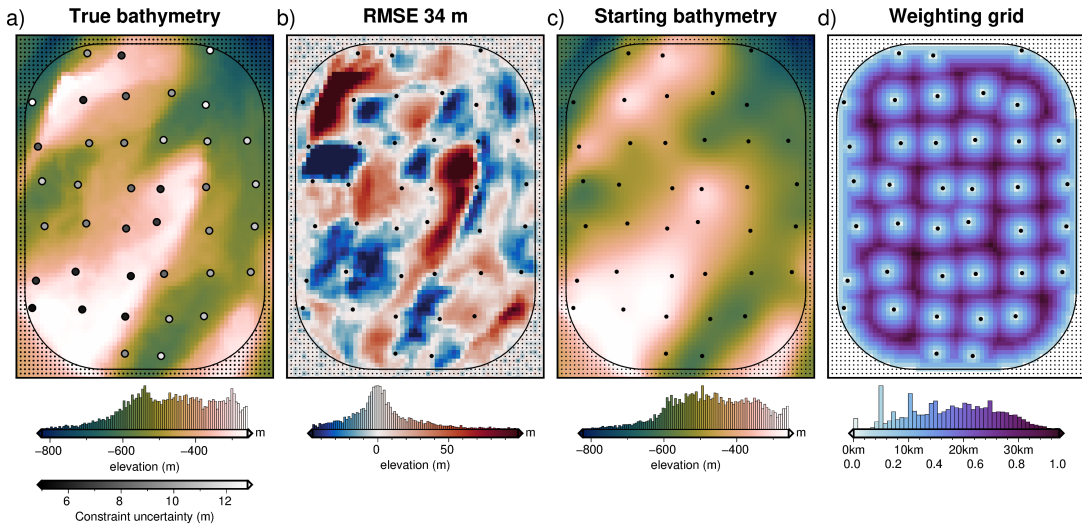


**Figure 3.26:** Gridding of the Ross Sea starting bathymetry. **a)** True bathymetry at 5 km resolution from the IBCSO v2 compilation (Dorschel et al., 2022). Constraint points (coloured dots), show the uncertainty values of each point. These uncertainties were used as the standard deviations of the Gaussian function for contaminating the sampled data with noise before regridding. **b)** Difference between a and b, **c)** starting bathymetry from the sampling and gridding of the constraint points with added noise. **d)** Weighting grid used in the inversion. Grid colours show both the distance between each grid cell and the nearest constraint point and the weight values (0 - 1) from the normalization of these distances. Small black dots and large black dots indicate constraints outside and inside of the ice shelf border, respectively. Semi-rounded black line shows the outline of the synthetic ice shelf.

ocean. Points within the shelf are contaminated with noise based on their depth. The Gaussian distribution used has a standard deviation of 2% of each point's depth. This simulates increasing measurement uncertainty with depth. Brisbourne et al. (2020) provide depth uncertainties for seismically imaged bathymetry beneath the Larsen C ice shelf, which have an average uncertainty as the percentage of depth from the surface of  $\sim 2\%$ . For our points, this equates to an RMS noise value of  $\sim 10$  m for the ice shelf constraints. The uncertainty (the standard deviation of the Gaussian function used, not the actual value of the noise) of each point is shown in Figure 3.26a. This noise-contaminated sparse data is then gridded with a cross-validated bi-harmonic spline yielding the starting bathymetry. This interpolator takes the uncertainties of each point into account so that highly uncertain points don't introduce a bias into the interpolation (Uieda, 2018). The difference between the true and starting bathymetries had an RMS of 34 m over the whole grid, and an RMS at the constraint points of 10 m.

### 3.5.3 Gravity misfit

The starting bathymetry was discretized and forward modelled at the observation points with a density contrast of  $1276 \text{ kg m}^{-3}$ . This forward gravity was then subtracted from the observed gravity to get the gravity misfit (Figure 3.27a). Using the constraint point minimization method, the regional field was estimated with a bi-harmonic spline interpolator (Figure 3.27b), which was subsequently removed, leaving the residual misfit (Figure 3.27c). As in the above section, the interpolator takes the uncertainty of each constraint point into account to avoid overfitting the regional field to highly-uncertain constraint points.

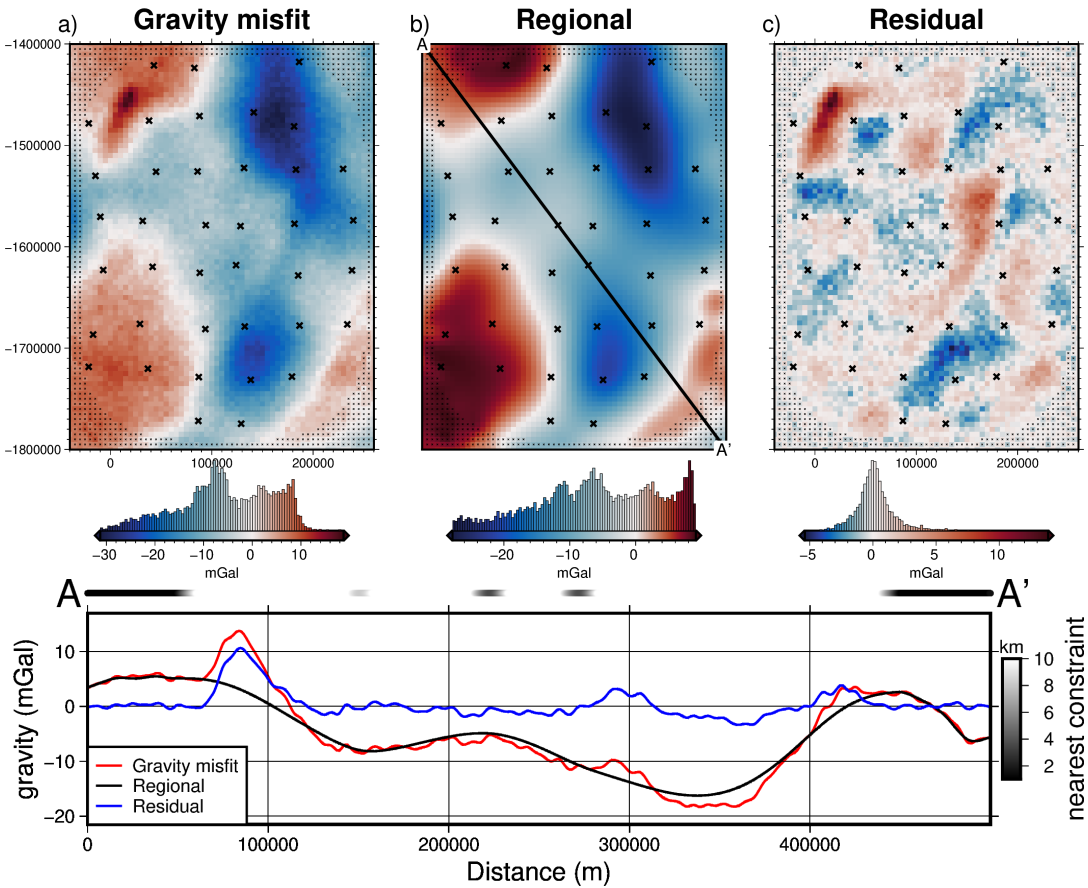


**Figure 3.27:** Ross Sea synthetic gravity anomalies. **a)** total gravity misfit, **b)** the estimated regional component using the constraint point minimization method, and **c)**, the residual misfit, as the difference between the total misfit and the regional component. Black crosses, large and small, show constraints inside and outside the ice shelf, respectively. **Lower panel** shows profile A to A' of gravity misfit and the regional and residual components. Distance to the nearest constraint at each point along the profile shown in black to white colours at top of profile.

### 3.5.4 Inversion

This residual misfit was then used in a cross-validation of 16 damping parameter values (Figure 3.28a). The inversion with the lowest cross-validation score was then chosen as the best model. During the inversions, a weighting grid was used to constrain the bathymetry at the points of known depths (Section 3.2.5.3). This grid (Figure 3.26d) is a normalized (0-1) grid of the minimum distance between each grid cell and the nearest constraint point. The inversion result and the difference from the true bathymetry are shown in Figure 3.29. The inversion had an RMS difference with the true Ross Sea bathymetry of 21 m and an RMS at the constraints of < 1 m. The inversion converged in 12 seconds at 15 iterations and had a final residual misfit of 0.43 mGal (Figure 3.28b).

### 3.5.5 Uncertainty analysis

Since the true Ross Sea bathymetry for this inversion is known, a direct measurement of the spatial uncertainty of the resulting bathymetry is simple to calculate (Figure 3.29b). This spatial uncertainty is useful to provide alongside the bathymetry results. It informs ocean modellers where results can be confidently interpreted and

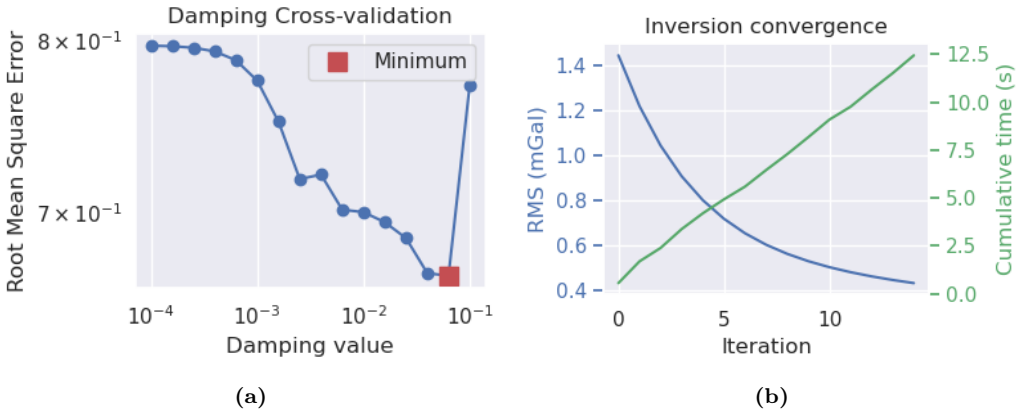


**Figure 3.28:** a) Cross-validation curve showing the optimal damping parameter (red square). b) Convergence of the inversion misfit. Blue line (left y-axis) shows the RMS of the residual misfit at each iteration of the inversion. Green line (right y-axis) shows the cumulative time to complete the inversion.

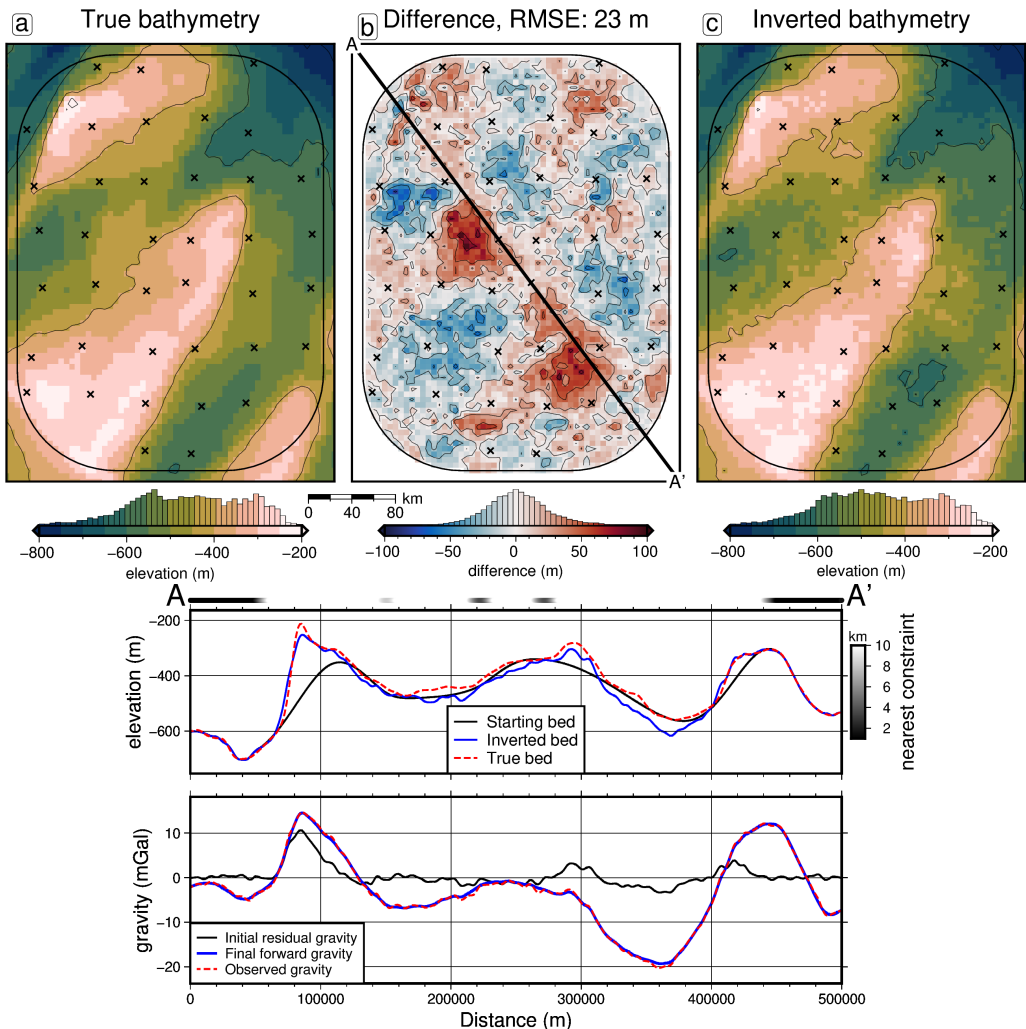


**Figure 3.29:** Ross Sea synthetic model inversion results. a) True bathymetry, b) difference between a and c, and c) final inverted bathymetry. Black crosses are constraint points. The RMS difference with the true bathymetry at these constraints is < 1 m. Lower panel) Profile from A to A'. The top panel contains topographic profiles of the starting, inverted, and true bathymetries. The bottom panel contains gravity anomaly profiles. Distance to the nearest constraint at each point along the profile shown in black to white colours at top of profile.

highlights regions to focus future data collection. Here, a method of uncertainty analysis for this inversion is proposed, and the resulting uncertainty is compared to the inversion error to get a sense of the accuracy of our calculation of uncertainty. This uncertainty analysis is accomplished with Monte Carlo simulations (Helton et al., 2006; Jansen et al., 1994).

Here, 20 inversions are run with the same damping parameter cross-validation as conducted previously. For each inversion, the input parameters are sampled from distributions of their possible values. These prior distributions represent all plausible parameter values and thus the resulting inverted bathymetries should cover the range of plausible inversion outcomes. For each grid cell, the weighted standard deviation of the 20 inverted bathymetry values of that grid cell was calculated. The weighting came from the inverse square of each inversion's RMS difference between the inverted grid values and the constraint point depths. This reduces the bias from inversions with large misfits to the actual constraint points (Schnaadt & Heinson, 2015). Chapter 4 Section 4.2.4 contains a detailed description of this uncertainty analysis methodology.

The parameters included in the Monte Carlo sampling are:

1. the observed gravity data, sampled from a normal distribution with a mean equal to the observed values and a standard deviation of 0.6 mGal (2% of the maximum absolute value).
2. the constraint point depths, sampled from a uniform distribution with a centre as the measured point depth and bounds of  $\pm 5$  m for the points outside the ice shelf, and  $\pm 2\%$  depth for points within the shelf.
3. the bathymetry density contrast. This is defined as the difference between the densities of water and sediment. The mean value was taken to be  $1276 \text{ kg m}^{-3}$  ( $2300 - 1024 \text{ kg m}^{-3}$ ). A standard deviation of  $400 \text{ kg m}^{-3}$  was used.

Four suites of Monte Carlo simulations were run and are shown in 3.30. Each of the above parameters: gravity, constraints, and densities, were included in their own Monte Carlo simulations, and the fourth simulation included all parameters together. Simulations that included the sampling of the constraint depths required the re-calculation of the starting bathymetry, the starting forward gravity, gravity misfit, regional separation, and finally running the inversion. Simulations that included sampling the density values required recalculating the forward gravity, misfit, regional separation, and running the inversion. Simulations that included the sampling of gravity values only required recalculating the regional field and running the inversion. These values were sampled from their respective distributions using Latin hypercube sampling (Jansen et al., 1994). This allows an adequate coverage of the parameter space with only 20 inversions. See Chapter 4 Section 4.2.4 for further details.

### 3.5.6 Effects of constraint spacing

Here we test the effects of the number and spacing of constraint points on the accuracy of the inversion. The constraints outside the ice shelf are kept as they have been in the previous section, at the same grid spacing as the bathymetry (5 km).

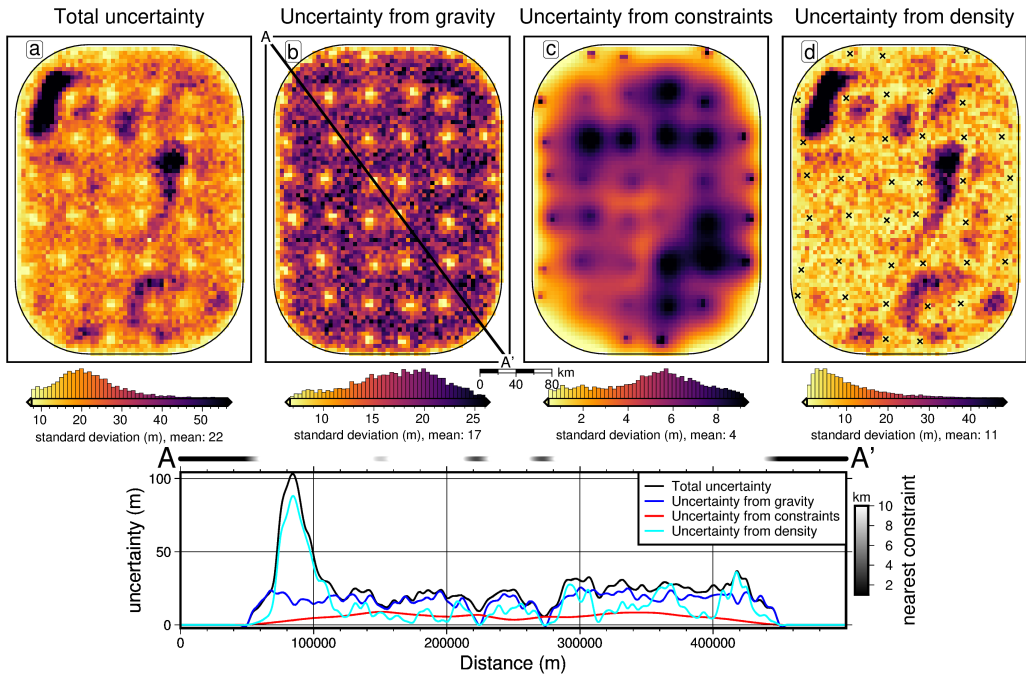


**Figure 3.30:** Monte Carlo simulation results for the Ross Sea synthetic inversion. Cell-wise weighted standard deviations of all inversions in each simulation. **a)** Total uncertainty from the sampling of gravity data, constraint depths, and density contrast value. **b)** Sampling of only the gravity data values. **c)** Sampling of only the constraint point depths. **d)** Sampling of only the density contrast. To aid in interpretation, locations outside of the ice shelf have been masked. Constraints within the ice shelf are shown as black crosses in **d**. **Lower panel**) Profile from A to A' of the total uncertainty and individual components. Distance to the nearest constraint at each point along the profile shown in black to white colours at top of profile.

2067 Constraints within the ice shelf are re-created on a regular grid, where the spacing of  
 2068 the grid, and thus the number of constraints, is varied from 10 km (959 constraints)  
 2069 to 100 km (9 constraints). The depth of the true bathymetry is sampled at each  
 2070 constraint. As in the previous section, points outside the shelf are contaminated with  
 2071 Gaussian noise with a standard deviation of 5 m. Noise for constraints within the  
 2072 ice shelf is relative to each point's depth (to simulate seismic survey uncertainties).  
 2073 These noise-contaminated constraint point depths are used in a bi-harmonic spline  
 2074 gridding to create the starting bed for each of the 10 constraint sets. The RMS  
 2075 difference between each of the starting beds and the true bed is shown as green dots  
 2076 in Figure 3.31a. From these starting beds the inversion workflow was conducted, as  
 2077 below:

- 2078 1. The forward gravity of the starting beds were calculated.
- 2079 2. The misfits with the observed gravity (Figure 3.25a) were calculated<sup>5</sup>.
- 2080 3. The regional component of the misfit was estimated and removed with the  
 2081 constraint point minimization method.
- 2082 4. The residual misfit was inverted with the cross-validation routine.
- 2083 5. The difference between each inverted bed and the true bed was found.

<sup>5</sup>To isolate the effects of changing the constraint density, the full resolution observed gravity with no added noise was used here, instead of the synthetic survey gravity.

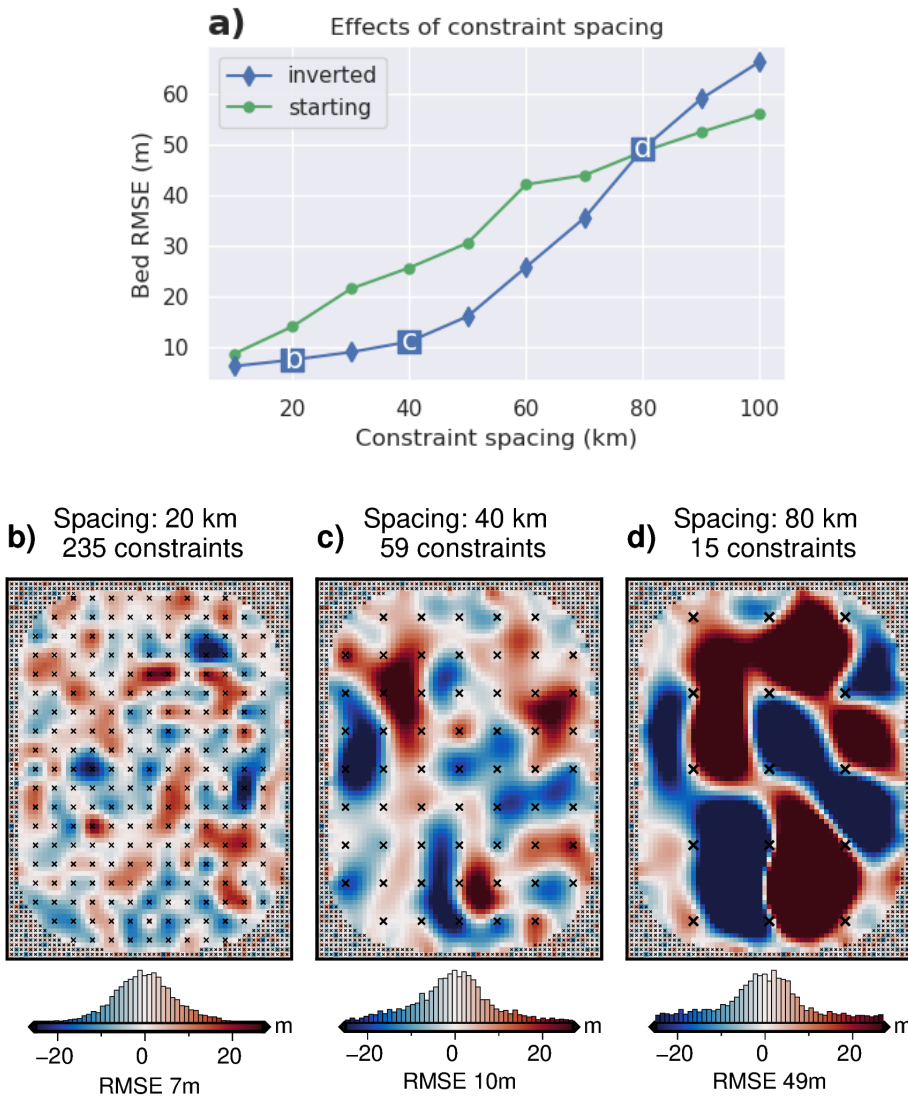


**Figure 3.31:** Effects of constraint spacing on inversion accuracy. **a)** Bathymetry error (RMSE) relative to the true bathymetry for 10 different constraint spacing. Green (circles) shows the starting error and blue (diamonds) shows the error after inversion. Labels b, c, and d refer to the three inversion error results shown as subplots. **b-d)** Inversion error grids for three of the ten configurations of constraints (labelled on a)). Note b-d use the same colour map. Small black crosses show constraints outside the ice shelf, and larger black crosses show inside constraints with the corresponding constraint spacing.

2084     Figure 3.31 shows the results of this analysis. Subplot a) shows the relationship  
 2085     between constraints spacing and the RMSE with the true bed of the starting bed  
 2086     (green circles) and the final inverted bed (blue diamonds). Three of the inverted  
 2087     bed errors are shown in subplots b-d. See Appendix B.2 for plots of the regional  
 2088     separation errors for these three inversions.

### 2089     3.5.7 Effects of gravity data

2090     As the above section analyzed the impact of the number of constraint points on  
 2091     the inversion's accuracy, here we investigate the impact of the quality and quantity  
 2092     of input gravity data. Following the methods of the two ensembles presented in  
 2093     the simple synthetic inversion (Figure 3.3.2 & 3.23), an ensemble of 100 inversions

with varying levels of noise and gravity observation spacing's are conducted with this Ross Sea model. The observed gravity data were contaminated with noise as described in the past sections, with 10 levels between 0 and 9% of the maximum absolute value. To simulate a more sparse gravity survey, the previous two ensembles sampled the full-resolution gravity data onto a coarser evenly spaced grid and then re-gridded the sparse data with equivalent sources back to the full resolution of the bathymetry. Here instead of evenly spaced grids, we use airborne flight lines.

2101

We use a constant along-line observation spacing of 5 km but vary the spacing between flight lines. The N-S and E-W lines both use the same between-line spacing. The full-resolution gravity is then sampled at these points, and the sparse data is re-gridded to the full resolution (5 km) with equivalent sources. The noise and line spacing changes were applied to the original observed data, and the forward calculation of the starting model, initial misfit calculation, and regional field removal were all repeated. Each model was then inverted with a cross-validation, and the resulting RMS differences with the true bathymetry are shown in Figure 3.32.

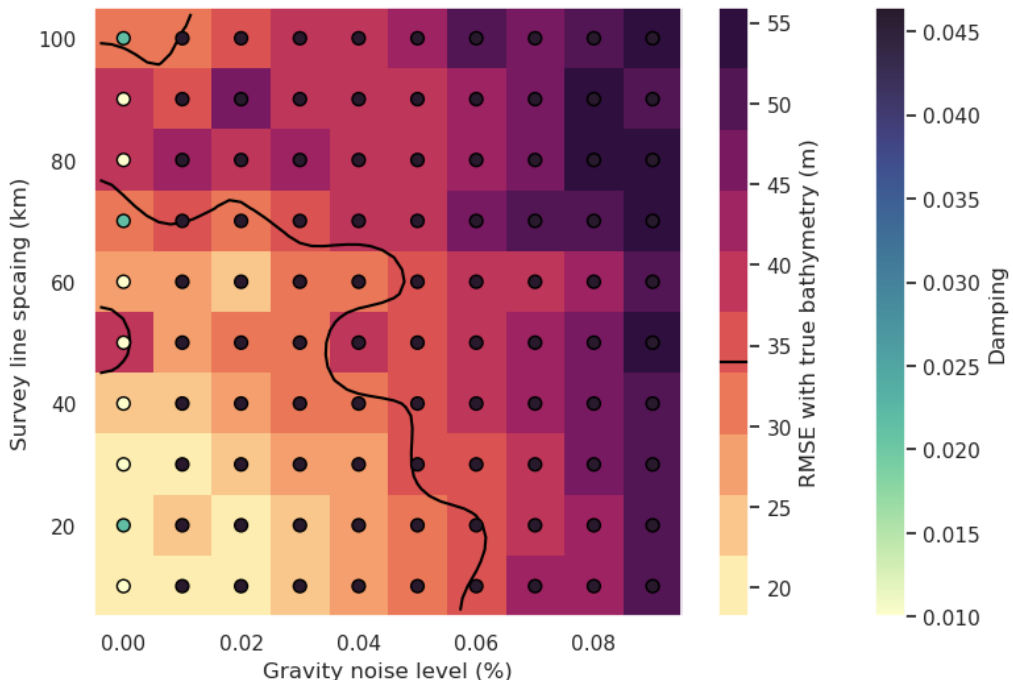


**Figure 3.32:** Ensemble of noise levels and airborne gravity line spacing for the Ross Sea synthetic model. Grid cell colour indicates each inversion's RMSE with the true bathymetry. Circles' colour indicates the optimal damping value found for each inversion's cross-validation. Black line shows the 34 m contour which represents the RMS difference between the true and starting bathymetry (Figure 3.26b).

## 3.6 Discussion

### 3.6.1 Simple synthetic model

The simple synthetic model of Section 3.3.1 was introduced to 1) present the basic workflow of the inversion, 2) determine the best options for various components of the inversion and 3) demonstrate the capabilities and limitations of the inversion.

2115 The starting bathymetry had an RMS difference with the true bathymetry of 66 m  
 2116 (Figure 3.6). This error demonstrates the limitations of gridding sparse data. Even  
 2117 with a very high spatial constraint density (1 constraint per 160 km<sup>2</sup>) compared to  
 2118 most ice shelves (Fretwell et al., 2013), simply gridding the constraints greatly misin-  
 2119 terpreted the true bathymetry. To reduce this bathymetric error, we presented three  
 2120 inversions, a noise-free full-resolution inversion, a noise-contaminated full-resolution  
 2121 inversion, and a noise-free lower-resolution inversion.

### 2122 3.6.1.1 Inversion results

2123 All of these inversions (without a regional component) were able to reduce this  
 2124 RMS difference with the true bathymetry to  $\sim 10$  m and recover all bathymetric  
 2125 features of interest. We demonstrated that the two methods of calculating the verti-  
 2126 cal derivative of gravity produced similar results, but the annulus approximation was  
 2127 significantly faster ( $\sim 5\times$ ). Additionally, for each of these inversions, the weighting  
 2128 grid, based on the distance to the nearest constraints (Figure 3.5), successfully con-  
 2129 strained the resulting inverted bathymetry at the points of prior bathymetry obser-  
 2130 vations. Each inversion's constraint point RMS difference with the true bathymetry  
 2131 was  $<\sim 2$  m, and the technique avoided any pedestal effect around the constraints in  
 2132 the resulting bathymetries. Interestingly, the inversion with low-resolution (6 km)  
 2133 gravity data yielded a very similar RMSE compared to the inversion with the full-  
 2134 resolution (1 km) data. This demonstrates that for recovering bathymetric features  
 2135 of wavelengths similar to those found in our synthetic model, high-resolution gravity  
 2136 surveys may not be necessary to achieve adequate results from an inversion.

### 2137 3.6.1.2 Ensemble results

2138 To test this theory further, we conducted an ensemble of 100 inversions with 10  
 2139 levels of noise contamination and 10 gravity survey resolutions. The resulting RMS  
 2140 difference of each inversion with the true bathymetry is shown in Figure 3.17. All  
 2141 inversions in this ensemble, including the worst-case scenario of 9% noise and a  
 2142 gravity observation grid of  $10\times$  the bathymetry spacing, still resulted in an RMS  
 2143 difference lower than that of the starting bathymetry (66 m). It is worth noting  
 2144 that this metric for the accuracy of the inversion, the root mean squared (RMS)  
 2145 difference with the true bathymetry, is used to give extra weighting to the outlier  
 2146 errors, as opposed to using a mean average error (MAE). These outliers typically  
 2147 include the features of interest in a bathymetry inversion. Figure 3.33a shows these  
 2148 ensemble results grouped by cell size. For each cell size value (colour of lines), the  
 2149 inverted bed RMSE for the range of noise levels is shown. This shows a roughly  
 2150 linear relationship between noise and RMSE, regardless of cell size. This means  
 2151 there is a continuous improvement in the inversion's accuracy with lower levels of  
 2152 noise. Conversely, figure 3.33b shows these ensemble results grouped by the noise  
 2153 level. For each noise level (colour of lines), the inverted bed RMSE for the range of  
 2154 cell sizes is shown. This shows an exponential relationship between gravity survey  
 2155 resolution and RMSE. This exponential relationship is strongest for low noise levels.  
 2156 This means inversion accuracy greatly benefits from increasing the survey resolution  
 2157 (decreasing the cell size), but this benefit diminishes once the survey resolution is at  
 2158 a certain point. Here, surveys at or below  $\sim 6$  km resolutions result in a diminish-  
 2159 ing improvement in RMSE. The linear relationship between noise and RMSE, and  
 2160 the exponential relationship between resolution and RMSE can also be seen by the

spacing of lines in either figure. The close spacing of the low-cell-size lines (purples) in Figure 3.33a show the diminishing improvements at small cell size surveys, while the continuous spacing of lines in Figure 3.33b shows the linear relationship.

2164

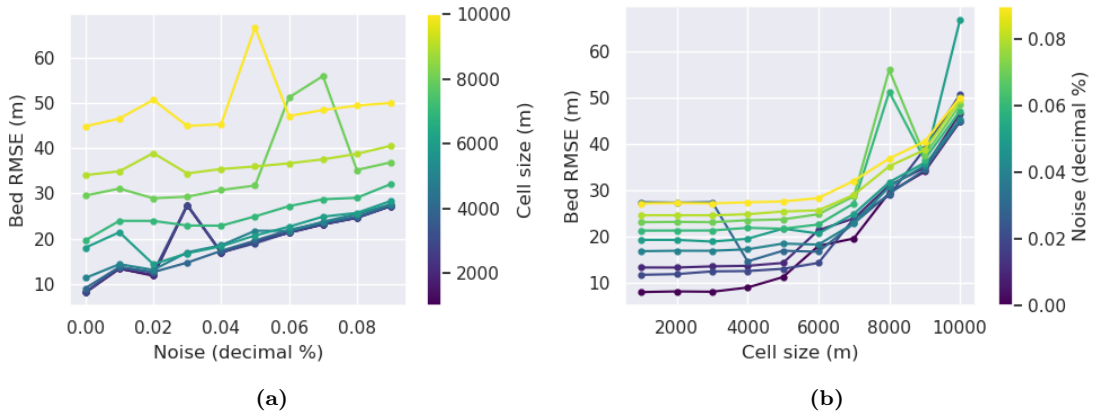


**Figure 3.33:** Ensemble results for the simple synthetic inversion, grouped by **a)** gravity survey cell size, and by **b)** noise level. Each line in a) corresponds to a row of Figure 3.17 and each line in b) corresponds to a column.

2165 In a typical gravity survey, there is often a trade-off between the number of  
 2166 observations made and the quality (noise) of the data. This is due to the time re-  
 2167 strictions of both the total data collection period (i.e. the length of a field season  
 2168 in Antarctica), and the necessity to repeat base-station measurements to account  
 2169 for instrument drift. Collecting more data in the same time period inevitably re-  
 2170 sults in increased noise. At a certain point, this increased noise will have a greater  
 2171 negative effect on the inversion results, than will be counteracted by the increased  
 2172 amount of data. These are important considerations for survey design. Figure 3.33b  
 2173 shows that for a given noise level, there is little benefit in increasing the gravity  
 2174 survey resolution from  $\sim 6$  km to 1 km. For this survey domain ( $60 \times 80$  km),  
 2175 a 6 km resolution results in  $\sim 130$  gravity station, while with a 1 km resolution,  
 2176 this increases to 4800 observation points. Simplistically speaking, if keeping total  
 2177 survey time constant, this means at 6 km spacing as opposed to 1 km spacing, ei-  
 2178 ther  $\sim 36\times$  more area could be surveyed, or higher quality data could be collected,  
 2179 with shorter base station loops, more repeated ties, and more careful measurements.  
 2180

2181 The results from the noise-contaminated inversion (Figure 3.12 & 3.9b) show  
 2182 that this gravity noise is directly reflected in the inversion results. For this reason,  
 2183 data, either the observed data or the residual misfit, is typically low-pass filtered  
 2184 prior to inversion (i.e. Boghosian et al., 2015; Yang et al., 2020a). This is typically  
 2185 done with either a time-based filter for airborne surveys, or a spatial filter (Jordan  
 2186 et al., 2010). With this filtering, there is a trade-off between removing the noise and  
 2187 removing the true signal. Due to this, we have chosen to omit the filtering in these  
 2188 synthetic examples.

**3.6.2 Simple model with a regional component****3.6.2.1 Regional separation methods**

The addition of a regional component to the observed gravity data adds a major complexity to the inversion workflow. The actual inversion remains the same, but this regional component must be estimated and removed beforehand. We tested four methods of regional estimation; 1) a low-pass filter, 2) fitting a polynomial trend to the data, 3) predicting the data with a set of deep point sources, and 4) attributing the entire misfit value to the regional field at constraint points and interpolating between these values. Figure 3.19 compares the inversion results of each of these methods. While each method recovered the short wavelength bathymetry features, the misestimation of the true regional field for each method introduced long-wavelength errors in the inversion results. We show that the constrain point minimization method most accurately estimated the region, and thus produced the best inversion results. For the simple regional field used here, the filter and trend methods achieved reasonable results, but the effectiveness of these methods is expected to be reduced with more complex regional fields associated with real data.

While the constraint point minimization worked best for this model, each of these methods may work better in specific scenarios. All the methods except the equivalent source method require the gravity data to be gridded over the entire region of interest. For sparse gravity surveys the interpolation required may introduce large errors. For this scenario, the equivalent source technique is likely the most appropriate. In scenarios with few bathymetry constraints and where the regional field is expected to be simple, the trend and low-pass filter methods are efficient and can be effective. However, if there are distributed bathymetry constraints, such as in this synthetic scenario, constraint point minimization is likely the best choice. This technique will only effectively remove regional anomalies with a wavelength equal to or greater than the average constraint spacing. If the constraints are sparse relative to the expected regional anomaly wavelengths, this method will underestimate the regional component. Lastly, if the bathymetry contains long-wavelength features which would result in long-wavelength anomalies, the trend, filter, and equivalent source techniques may include these in the regional removal. Therefore, the inverted bathymetry, while recovering the super-imposed short-wavelength bathymetry features, will underestimate the long-wavelength features. It is for these reasons that regional separation is perhaps the most important aspect of a bathymetry inversion.

**3.6.2.2 Constraint point minimization**

This constraint point minimization technique requires the gridding of sparse measurements of the regional field. We explored the impact of this gridding process on the resulting inversion. Figure 3.20 shows the results of four different gridding processes. Minimum curvature gridding without tension (tension of 0, Figure 3.20a) produces a smoothly varying surface at the constraints but introduces artificial minima and maximum at points far from any constraints. This erroneous effect is minimized with a higher tension factor. Using a tension factor of 1, figure 3.20c shows the limited erroneous minima and maxima, but this added tension results in high gradients in the surface immediately near the constraint points (Figure 3.20g). These high gradients in the resulting residual anomalies create a *ringing* effect in

the inverted bathymetry (Figure 3.20k). For these reasons, an intermediate tension factor of 0.25 is suggested for potential field data. While this limits the negative effects of both low and high tension, there are still false minima and maxima (Figure 3.20b), and high gradients at the constraints (Figure 3.20f). The last gridding technique uses bi-harmonic splines. The optimal damping parameter associated with this technique is chosen from a cross-validation of the constraint points. This technique, while being more computationally expensive, solves both issues of tensioned minimum curvature.

### 3.6.2.3 Inversion results

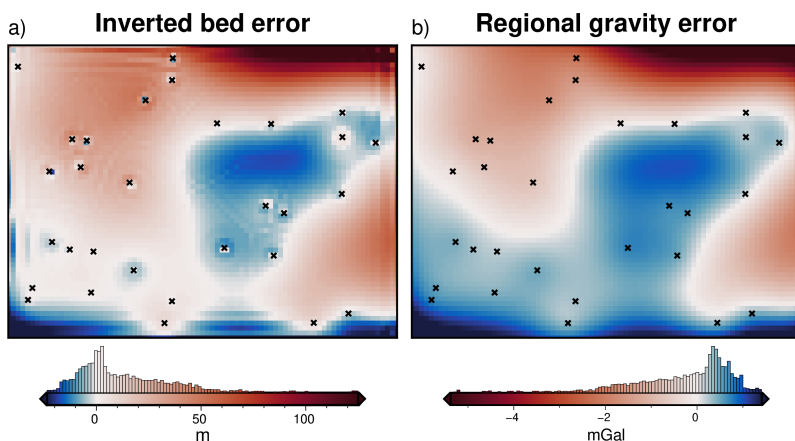


**Figure 3.34:** Source of inverted bathymetry error for the simple synthetic model with a regional field. **a)** Inverted bathymetry error from Figure 3.22b. **b)** Error in the estimation of the regional component of gravity from comparison with the true regional component (Figure 3.18b). Black crosses show constraint points. Colourmaps are inverted to highlight the similarities and the median has been removed from the regional error.

With both the optimal regional separation method and the optimal gridding method determined, we performed a cross-validated inversion with the remaining residual misfit. This inversion was able to recover all the short-wavelength bathymetry features but introduced some long-wavelength errors. Figure 3.34 shows the inverted bathymetry error alongside the error in estimating the regional component of gravity. Comparing these shows that almost all of the inverted bathymetry error is tied to the inaccuracies of determining the regional component. the remaining error is all minor short-wavelength features, mostly around constraint points. They appear to result from the weighting grid implementation of regularization. Since the errors in the regional estimation are the dominant source of error in most inversions, as shown above, and by other Antarctic bathymetry inversions (Brisbourne et al., 2014), we have shown these details of the gridding process are a vital and often overlooked step in many studies.

### 3.6.2.4 Ensemble results

As with the simple model, an ensemble of noise and gravity survey spacing experiments were performed with this model containing a regional component. The lowest resulting RMS difference with the true bathymetry was raised from values of  $\sim 10$  m for the inversion without the regional component, to the lowest value of  $\sim 40$  m with the additional regional component. The black line in Figure 3.23 shows the

66 m contour, which represents the RMS difference between the true and starting bathymetries. Inversions that fall outside (above) this line resulted in a worse bathymetry than the starting model. This shows that for this model, inversion is only worth conducting if the gravity survey has a spacing less than  $\sim 9$  km ( $\sim 9 \times$  the spacing of the desired bathymetry resolution). Figure 3.35 show these ensemble results grouped by cell size and noise level. There is a linear relationship between gravity noise and the resulting bathymetry RMSE, for all gravity survey spacings. There is an approximately exponential relationship between gravity survey resolution (cell size) and resulting bathymetry RMSE. The degree of this exponential relation decreases with increased noise.

2273

For this model, the *elbow* of the exponential curves in Figure 3.35b is at  $\sim 6 - 8$  km survey resolutions ( $6-8 \times$  bathymetry resolution). This suggests that for a survey resolution finer than  $\sim 8$  km, there is little benefit in collecting more data. This is supported by the close spacing of low-cell-size lines (purples) in Figure 3.35a. The effort would be better spent collecting data over a wider region, reducing noise in the data, or if possible collecting more bathymetric constraints.

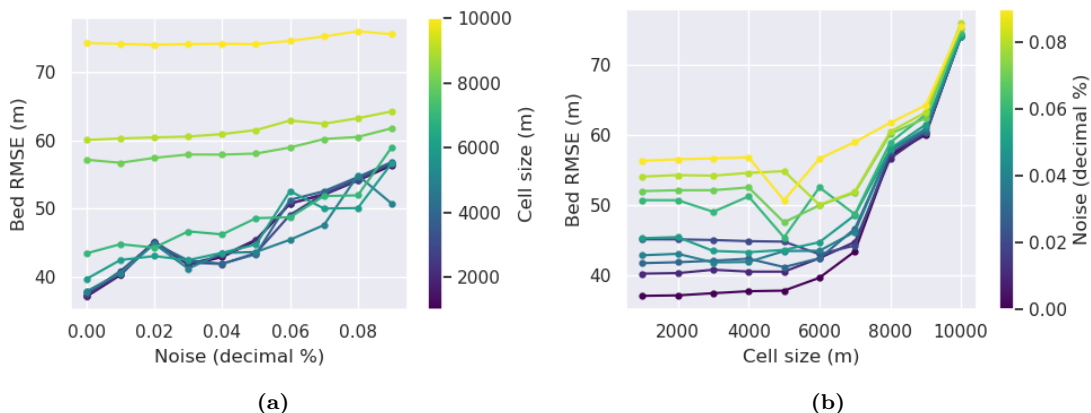


**Figure 3.35:** Ensemble results for the synthetic inversion with a regional component, grouped by a) gravity survey cell size, and by b) noise level. Each line in a) corresponds to a row of Figure 3.23 and each line in b) corresponds to a column.

2280

### 3.6.3 Ross Sea model

The Ross Sea semi-realistic model was created to better emulate the gravity and bathymetries expected for ice shelves. A few extra complexities were added to this model compared to the purely synthetic models. An ice shelf border was included, with a high density of constraints outside of the border, and sparse constraints within. All the constraints had an associated uncertainty, instead of directly sampling the true bathymetry depths. The observed gravity was calculated along the flight paths of a typical airborne survey, instead of along a uniform grid. The main inversion in this section had 2% noise added and had flight lines with 50 km N-S spacing and 15 km E-W spacing. The inversion successfully reduced the starting bathymetry error from an RMSE of 34 m to 23 m. The resulting bathymetry shows a recovery of most of the lost bathymetry features, but some noise from the gravity data has been introduced into the bathymetry. Sharp bathymetry features (upper left corner) and smooth features were both recovered. The constraint points were

2294 relatively evenly distributed (Figure 3.26d), resulting in a relatively even distribution  
 2295 of bathymetry misfits.

2296

2297 Of these errors, the largest were located at the gaps in the synthetic survey  
 2298 where there were missing flight lines (Figure 3.25b). To understand the cause of  
 2299 the remaining errors, we compare the inverted bathymetry error with the regional  
 2300 separation error (Figure 3.36). The strong correlation between these two grids shows  
 2301 that the majority of errors in the inversion are tied to the miscalculation of the  
 2302 regional field, as was seen in the simple synthetic inversion with a regional field.  
 2303 The remaining errors appear to be from the flight line gaps and noise in the gravity  
 2304 data.

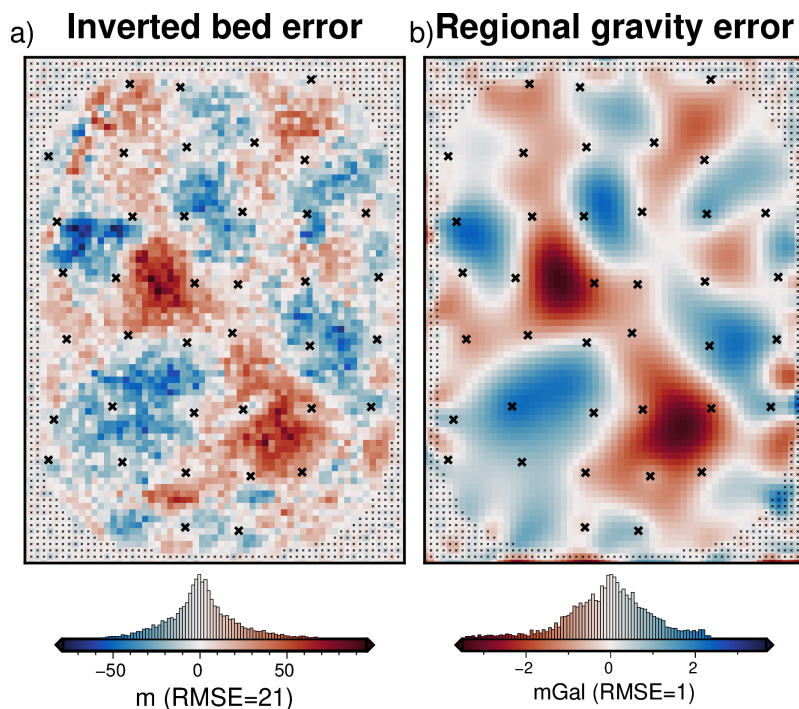


**Figure 3.36:** Comparison of the inverted bathymetry error and the error in the regional field estimation. **a)** Inverted bathymetry error from Figure 3.29b. **b)** Error in the estimation of the regional component of gravity from comparison with the true regional component (Figure 3.24d). Black crosses show constraint points. Colourmaps are opposed to highlight the similarities and the median has been removed from the regional error.

### 2305 3.6.3.1 Effects of the gravity data

2306 The ensemble of gravity data noise levels and flight line spacings from Section 3.5.7  
 2307 shows the relative importance of these two aspects of a gravity survey. As for the  
 2308 previous ensembles, Figure 3.37 shows these results grouped by line spacing and by  
 2309 the noise level. For the Ross Sea model, both factors have a roughly linear relation-  
 2310 ship with inverted bathymetry error. The slopes for the lines of best fit for Figure  
 2311 3.37a and b means the inversion RMSE increases by  $\sim 10$  m for either a 4% increase  
 2312 in the noise level or a 60 km increase in the average flight line spacing. The inversions  
 2313 with a small line-spacing (purple lines) of Figure 3.5.7a are closely grouped, relative  
 2314 to the higher line spacings. This shows that at already low line spacings (40 km)  
 2315 there may be little benefit to reducing the line spacing further. Conversely, there  
 2316 is a larger spread for the low noise inversions (purple lines) in Figure 3.5.7b. This

2317 shows that even at low noise levels, further decreases may still provide important  
 2318 improvements to the inversion outcome. As in the previous ensemble results, for  
 2319 a field application, this demonstrates the important tradeoff between quantity and  
 2320 quality of gravity data.

2321

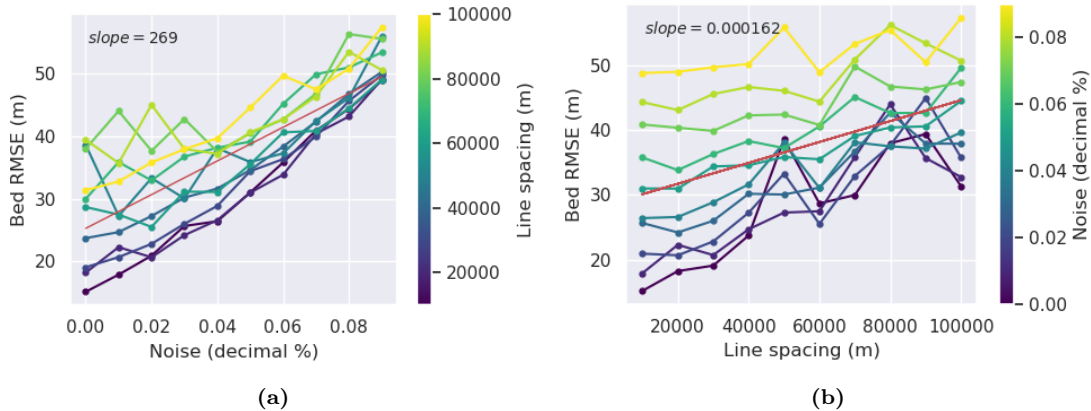


**Figure 3.37:** Ensemble results for the Ross Sea inversion, grouped by **a)** gravity survey line spacing, and by **b)** noise level. Each line in a corresponds to a row of Figure 3.32 and each line in b corresponds to a column. Red lines show the line of best fit, with their slopes shown in the upper left corners.

2322 These specific relationships between noise, line spacing, and inversion error, while  
 2323 not applicable to all survey configurations, show the importance of choosing an  
 2324 appropriate survey design. This analysis with synthetic data could be included in a  
 2325 pre-survey plan, to explore the effects of differing survey configurations.

### 2326 3.6.3.2 Effects of the constraints

2327 These synthetic inversions have shown that the removal of the regional field presents  
 2328 the biggest challenge for gravity inversions for bathymetry. The most robust tech-  
 2329 nique for removing the regional field requires a distribution of points of known  
 2330 bathymetry across the inversion region. Since the largest errors in the inverted  
 2331 bathymetries occur at the largest distance to constraints, an even distribution of  
 2332 constraints will best be able to estimate the regional field. Section 3.5.6 explored  
 2333 the effects of varying the numbers of constraints, while keeping the remaining com-  
 2334 ponents of the inversion constant. Figure 3.31a shows the bathymetry RMSE with  
 2335 the true bathymetry both before (green) and after (blue) the inversion is conducted.

2336

2337 Figure 3.31a shows for this synthetic model that for average constraint spacing's  
 2338 less than  $\sim 20$  km there is little improvement made by running an inversion. This  
 2339 is due to the starting bathymetry model already being relatively accurate, with the  
 2340 inversion only producing minor adjustments between constraint points. At the other  
 2341 end of the spectrum, with constraint densities greater than  $\sim 70$  km, the inverted  
 2342 bathymetry has an error similar to or higher to the un-inverted bathymetry. This is  
 2343 due to the inaccuracies in calculating the regional field with only very sparse con-  
 2344 straints. For these scenarios, the errors introduced by the inversion are greater than  
 2345 the errors of simply interpolating the constraint points. The inverted bathymetry  
 2346 error curve (Figure 3.31a) shows that for this survey, once below a certain constraint  
 2347 spacing ( $\sim 30$  km) there is little benefit to having additional constraints.

2348 **3.6.3.3 Uncertainties**

2349 We have demonstrated that the majority of the inverted bathymetry error is related  
 2350 to the estimation of the regional component of gravity. Without knowing the true  
 2351 regional component, as we do in these synthetic examples, estimating the uncer-  
 2352 tainty in the interpolation between constraint points of the regional field is difficult.  
 2353 The uncertainty of each grid cell is likely strongly dependant on the distance to the  
 2354 nearest constraint, as well as the depth uncertainties of these nearby constraints.  
 2355 While we show this to be true with our synthetic models, a quantitative method  
 2356 of predicting this uncertainty has yet to be implemented here. The field of conven-  
 2357 tional bathymetry surveying has developed uncertainty analysis tools that may be  
 2358 applicable to this (Bourgeois et al., 2016).

2359 These tools are able to account for both the depth uncertainty of each mea-  
 2360 surement, and the distance of each grid cell to the nearest measurement. Future  
 2361 work will benefit from a quantitative assessment of the uncertainty of gridding the  
 2362 regional field from the constraint point values. While the uncertainty of the regional  
 2363 removal accounts for the majority of the uncertainty of the inverted bathymetry,  
 2364 it is technically completed before the inversion and is thus not a component of the  
 2365 inversion uncertainty. To address the uncertainty resulting from the inversion pro-  
 2366 cess, we introduced a suite of Monte-Carlo simulations in Section 3.5.5. The results  
 2367 in figure 3.30 show a mean uncertainty for the entire region of 22 m. The majority  
 2368 of this uncertainty is attributed to the uncertainty in the gravity data, as shown by  
 2369 histograms of Figure 3.30. Here we discuss the significance of each component of the  
 2370 uncertainty analysis:

- 2372 1. **Gravity uncertainty:** The uncertainties in the gravity data result in a rel-  
 2373 atively uniform bathymetry uncertainty across the region of 17 m. A simple cal-  
 2374 culation with the Bouguer slab formula with a density contrast of  $1276 \text{ kg m}^{-3}$   
 2375 and our assumed gravity uncertainty of 0.612 mGal (%2 max absolute value)  
 2376 gives a value of 11.5 m ( $\Delta g_{boug} = 4.18e-5\rho h$ ). This may show the convention-  
 2377 ally used Bouguer slab approximation is underestimating the true uncertainty  
 2378 in inversions resulting from gravity data uncertainty. This uncertainty is lowest  
 2379 at the constraints, due to the use of the weighting grid in the inversion.
- 2380 2. **Constraint depth uncertainty:** The contribution to the bathymetry uncer-  
 2381 tainty from the depth uncertainty of the constraint points is small, with a mean  
 2382 of  $\sim 4$  m. This uncertainty resulting from the constraints is also concentrated  
 2383 around the constraint points. This shows improving the constraint point un-  
 2384 certainties will not greatly improve the inversion, and will only improve it in  
 2385 the immediate vicinity of constraints.
- 2386 3. **Density uncertainty:** The bathymetry uncertainty component resulting  
 2387 from the prism densities is heterogeneous, with some spatially limited, but  
 2388 large values. The mean value is  $\sim 11$  m, but some areas are up to 50 m.  
 2389 These high uncertainties are strongly correlated with the error in the start-  
 2390 ing bathymetry (Figure 3.26b). This is due to the change in density contrast  
 2391 resulting in a change in the total bathymetry correction calculated in the inver-  
 2392 sion. In other words, the residual misfit can be minimized by a large surface  
 2393 correction with a low-density contrast or a small surface correction with a  
 2394 large-density contrast.

The combined Monte-Carlo simulation (Figure 3.30a) shows the expected features of an uncertainty map. It has a base level uncertainty similar to the Bouguer slab thickness from the assumed gravity uncertainty, it is generally lowest at the constraints and highest in the large constraint gaps, and it is high where the inversion has produced a large change from the starting model.

## 3.7 Future work

Running this inversion with the various synthetic models gave us the ability to assess the inversion performance. From this assessment, we have determined several components which would benefit from additional investigation.

1. Implement an additional cross-validation routine to estimate the optimal density contrast, as in Uieda and Barbosa (2017). Here, we have used the same density contrasts for the creation of the observed gravity data and for the inversion itself. In a non-synthetic scenario, this contrast would need to be estimated.
2. Test the effects of flight line orientation relative to the dominant trend of geologic structures.
3. Implement a more robust method of enforcing the constraint points. This may likely be in the form of a bounded least squares solver or some form of manipulation of the Jacobian matrix.
4. Quantify the uncertainty of the regional separation process. This will likely include techniques used in conventional bathymetry surveying (Bourgeois et al., 2016; Calder & Elmore, 2017), or a sequential Gaussian simulation (Perozzi et al., 2021).
5. Testing the effects of pre-filtering the gravity data, either spatially or temporally, to remove the effects of noise (Jordan et al., 2010).

## 3.8 Conclusion

With the goal of modelling the bathymetry beneath a floating ice shelf, we present a geometric gravity inversion method that 1) adheres to prior bathymetry point measurements, within their uncertainties, 2) produces a smooth and realistic bathymetry, 3) accounts for the regional gravity field and 4) is computationally efficient and fully-open source. To demonstrate the effectiveness, as well as the limitations, we conducted a series of inversions using synthetic and semi-realistic data. These inversions showed the importance of accurately estimating and removing the regional component of gravity prior to the inversion. We showed that for the constraint arrangement for many Antarctic ice shelves, the optimal method for estimating this regional field is with a constraint-point minimization. In addition, we further explored this method by testing various gridding (interpolation) techniques and found a clear increase in performance when using a cross-validated bi-harmonic spline instead of the typically used tensioned minimum curvature.

Here we reiterate a few of the key findings from this chapter:

- 2436 1. Estimating and removing the regional component of gravity for typical inver-  
2437 sion scenarios is the most important aspect of the inversion procedure. For  
2438 typical bathymetry inversions, the optimal method for estimating the regional  
2439 field is constraint point minimization.
- 2440 2. When collecting data for an inversion, it is best to aim for quality over quanti-  
2441 ties for the gravity data, and conversely, quantity over quality for bathymetry  
2442 constraint measurements.
- 2443 3. We provide general guidelines on the optimal ranges of constraint density, grav-  
2444 ity survey line spacing, and gravity noise, for which conducting an inversion is  
2445 suitable.

2446 Testing the various models with differing levels of gravity noise and numbers  
2447 of gravity observation points highlights an important factor in planning a grav-  
2448 ity survey. We show for the Ross Sea synthetic model, which likely emulates the  
2449 scenario expected from many Antarctic ice shelves, **there are diminishing re-**  
2450 **turns for average flight line spacings smaller than  $\sim 40$  km if the goal is**  
2451 **to recover bathymetry features typical of the Ross Sea. However, the inverted**  
2452 **bathymetry's accuracy is strongly affected by noise in the gravity data.**  
2453 With this, the typically airborne survey focus on quantity over quality may need to  
2454 be reassessed. If 40 km spaced flight lines produce similar results to 20 km lines,  
2455 flying half the number of lines will save a significant amount of time. This time  
2456 could be used to either expand the area of the survey or reduce the noise in the  
2457 data. Reducing the data noise for an airborne survey may not always be feasible,  
2458 but a few measures may be taken to attempt this, all of which are aided by the  
2459 increased survey time allowed by reducing the number of flight lines. These include  
2460 repeating lines or sections which are noisy, limiting flights to good weather windows,  
2461 increasing the number of tie-lines, making shorter loops for base-station ties, or fly-  
2462 ing at lower altitudes and or ground speeds.

2463

2464 **The previous measurements of bathymetry, referred to as the con-**  
2465 **straints, are a vital part of an inversion for bathymetry.** Due to the non-  
2466 uniqueness of an inversion, there are an infinite number of inverted bathymetry  
2467 models which will equally match the observed data. These constraints provide the  
2468 ground truth necessary to confidently chose a model out of these infinite choices.  
2469 Additionally, if not more importantly, they provide the primary method of account-  
2470 ing for the regional component of gravity. Since this is shown to be the largest  
2471 source of uncertainty, the constraints are the most important aspect of the inver-  
2472 sion. We tested the effects of varying the spatial density of the constraint points.  
2473 The results (Figure 3.31) show the range of constraint point spacings for the Ross  
2474 Sea synthetic model which justifies conducting a gravity inversion if the goal is to  
2475 recover bathymetry with a 5 km resolution.

2476

2477 **The optimal constraint spacing is  $\sim 20\text{-}70$  km.** Smaller spacing values al-  
2478 ready have an adequate amount of information and little is gained over a simple  
2479 interpolation of the data. At spacings larger than  $\sim 70$  km, the errors in estimating  
2480 the regional field are larger than the improvements made by the inversion. These  
2481 values, while specific to the Ross Sea scenario, provide an important context for the  
2482 feasibility of conducting bathymetry inversions. Taken together with the above as-  
2483 sessment of the relative importance of gravity data noise and density, some general

2484 guidelines are provided.

2485

2486 As long as the gravity data is on the order of magnitude of  $2\text{-}4 \times$  the spacing of  
2487 the desired bathymetry resolution, and the noise levels are low, **efforts should be**  
2488 **focused on collecting more bathymetry measurements.** The uncertainty of  
2489 these depth measurements is relatively unimportant (Figure 3.30c), meaning quan-  
2490 tity over quality is acceptable here. The final spatial uncertainty of the inverted  
2491 bathymetry is strongly tied to the distance to the nearest constraint. This suggests  
2492 that an even distribution of the constraints is important. However, if specific re-  
2493 gions of the survey are expected to have larger amplitude regional anomalies, an  
2494 increased spatial density of constraints over this region would be beneficial. With  
2495 these recommendations, future planning for Antarctic fieldwork should be able to  
2496 collect data that prioritizes the accurate assessment of sub-ice-shelf bathymetry.

2497

2498 Chapter 4 applies the inversion presented here to model the bathymetry beneath  
2499 Antarctica's Ross Ice Shelf.



2500 **Chapter 4**

2501 **Ross Ice Shelf bathymetry inversion**

2502 **Abstract**

2503 Antarctica's Ross Ice Shelf buttresses large catchments of ice from both the East and  
2504 West Antarctic Ice Sheets. Changes to the current stability of the ice shelf, likely  
2505 through basal melt of the sensitive grounding zones or pinning points, will reduce this  
2506 buttressing and accelerate the Antarctic Ice Sheet's contribution to global sea level  
2507 rise. The distribution of basal melt is predominantly controlled by the ocean cavity  
2508 thickness and the channelling of ocean waters by bathymetric features. Bathymetry  
2509 is, however, poorly known for the Ross Ice Shelf. Here we use airborne gravity  
2510 data and distributed seismic constraints across the ice shelf to create an updated  
2511 sub-ice shelf bathymetry model. We accomplish this with a non-linear geometric  
2512 gravity inversion, available as open-source Python code. Monte Carlo sampling  
2513 of the inversion inputs provides a robust means of addressing spatial uncertainty  
2514 and the relative significance of each component of the inversion. The resulting  
2515 bathymetry closely matches the seismic constraints and reveals significant changes  
2516 compared to past bathymetry models. We find several likely locations of past pinning  
2517 points, locations where enhanced basal melting is likely, and sites of possible tectonic  
2518 significance.

2519 **Plain Language Summary**

2520 The floating Ross Ice Shelf slows the flow of a large amount of ice into the ocean.  
2521 Melting at the base impacts the ice shelf's ability to slow down this upstream ice.  
2522 The shape of the seafloor beneath the ice shelf (bathymetry), acts to guide ocean cur-  
2523 rents which cause this melting. Our knowledge of the bathymetry beneath the Ross  
2524 Ice Shelf comes from a series of point measurements with an average distance be-  
2525 tween points of over 40 km. Here, we use measurements of Earth's gravity collected  
2526 over the ice shelf to estimate the shape of the bathymetry beneath. This technique  
2527 provides an increased resolution of the bathymetry and informs us about where we  
2528 are most and least confident of the bathymetry depth. With this new model of  
2529 sub-ice-shelf bathymetry, we highlight locations where melt-inducing ocean currents  
2530 are likely directed, and several places with the seafloor is very close to the base of  
2531 the ice. These results will better inform ocean circulation models beneath the ice  
2532 shelf, and therefore the likely future contributions of the Ross Ice Shelf to sea level  
2533 rise.

**2534 Key Points**

- 2535 1. We present a new bathymetry model beneath Antarctica's Ross Ice Shelf from  
2536 a gravity inversion.
- 2537 2. A Monte Carlo simulation provides a detailed spatial uncertainty analysis.
- 2538 3. Results highlight locations where the updated bathymetry may impact ocean  
2539 circulation models or where the shelf may have been recently grounded.

**2540 4.1 Introduction**

2541 Much of Antarctica's coastline is fringed by floating extensions of the Antarctic Ice  
2542 Sheet. These floating masses of ice, referred to as ice shelves, are connected to the  
2543 grounded ice on the continent. Over 80% of Antarctica's grounded ice drains to the  
2544 oceans through these ice shelves (Rignot et al., 2013). While they are floating, and  
2545 thus already displace their mass equivalent of seawater, they are vital to the current  
2546 and future contribution of the Antarctic Ice Sheet to global sea level rise (Fürst et  
2547 al., 2016; Jacobs et al., 1992). The ice shelves slow the flow of upstream ice into the  
2548 ocean by imparting a resistive force, known as buttressing. This buttressing occurs  
2549 from lateral drag along the sides of the ice shelves and resistive stresses incurred  
2550 where they flow over pinning points (localized areas of grounded ice) (Dupont &  
2551 Alley, 2005; Matsuoka et al., 2015). Changes to the geometry of the ice shelves can  
2552 reduce their restraining effect on the flow of grounded ice, leading to an increased  
2553 mass flux of ice across the grounding zone, thus increasing the ice sheet's contribu-  
2554 tion to global sea level rise (e.g., Pritchard et al., 2012; Scambos et al., 2004).

2555  
2556 The largest ice shelf on Earth is the Ross Ice Shelf (Figure 4.1, Fretwell et al.,  
2557 2013). Situated in West Antarctica, along the boundary with East Antarctica, the  
2558 Ross Ice Shelf comprises ice from both the East and West Antarctic Ice Sheets; a  
2559 combined catchment totalling 11.6 meters of potential global sea level rise (Tinto  
2560 et al., 2019). While the Ross Ice Shelf is in approximate steady-state, that is a  
2561 near net-zero mass change (e.g., Moholdt et al., 2014; Rignot et al., 2013), geo-  
2562 logic evidence shows rapid disintegration (Naish et al., 2009; Yokoyama et al., 2016)  
2563 and extensive grounding line retreat (Spector et al., 2017; Venturelli et al., 2020)  
2564 may have occurred as recently as the mid-Holocene ( $\sim 7$  kyr B.P.). Ocean forcing,  
2565 specifically basal melting along the grounding zone, is thought to drive these rapid  
2566 grounding line retreats (Lowry et al., 2019). The current stability of the ice shelf is  
2567 in part attributed to the lack of warm Circumpolar Deep Water penetrating into the  
2568 cavity (Dinniman et al., 2011; Tinto et al., 2019). Ocean waters that do penetrate  
2569 the cavity, such as High Salinity Shelf Water, are dense and relatively cold. Despite  
2570 their temperature, they are responsible for significant melting at the large depths of  
2571 the grounding zone (Adusumilli et al., 2020) due to the pressure suppression of the  
2572 freezing temperature of ice (Tinto et al., 2019).

2573  
2574 This High Salinity Shelf Water is formed on the continental shelf from the cre-  
2575 ation of sea ice. Due to their density and the reverse slope of the continental shelf,  
2576 they flow into the cavity, guided by bathymetric troughs (Jacobs et al., 1992; Tinto  
2577 et al., 2019). There are many examples of bathymetric features controlling the  
2578 routing of these sub-shelf waters (e.g., De Rydt et al., 2014; Dutrieux et al., 2014;

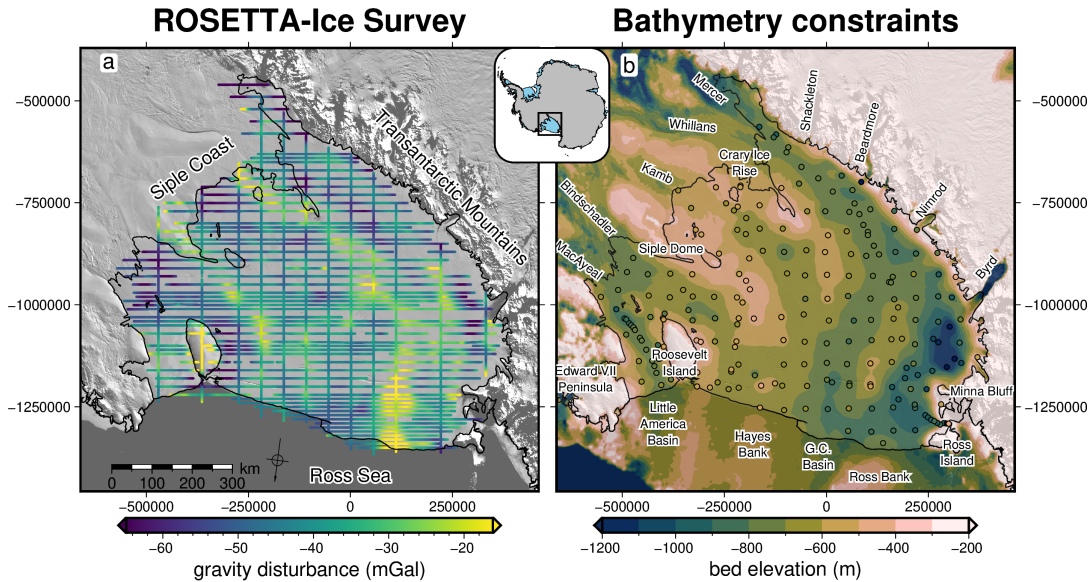


**Figure 4.1:** Input datasets for the Ross Ice Shelf bathymetry inversion. **a)** ROSETTA-Ice airborne gravity disturbance data (cleaned and re-levelled). **b)** Bedmap2 bed elevations in background, with individual constraint points within the ice shelf boundary (dots) on the same colour scale. Black line in both figures shows the grounding line and ice front from Mouginot et al. (2017). Background imagery is from MODIS-MOA (Scambos et al., 2007). Regional names shown in **a** and specific location names shown in **b**, which include ice streams along the Siple Coast, outlet glaciers along the Transantarctic Mountains, and bathymetry features in the Ross Sea. The RMS difference between the constraint point values and the BedMap2 gridded values is 138 m.

2579 Gladish et al., 2015; Zhao et al., 2019). Additionally, ocean modelling sensitivity  
 2580 testing highlights the importance of bathymetric features to sub-shelf circulations  
 2581 and melt (De Rydt et al., 2014; Goldberg et al., 2020). Bathymetry, therefore, plays  
 2582 a key role in the stability of the Ross Ice Shelf through its likely control on the basal  
 2583 melt magnitude and distribution (Goldberg et al., 2019) and through the buttressing  
 2584 effect of bathymetric pinning points (Still et al., 2019).

2585  
 2586 Direct observations of the sea floor beneath the Ross Ice Shelf (excluding along  
 2587 its periphery) are limited to two drill holes. The first was the 1977 J9 drill hole north  
 2588 of Crary Ice Rise as part of the Ross Ice Shelf Project (Clough & Hansen, 1979). The  
 2589 second was the 2017 HWD2 drill hole near the centre of the ice shelf (Stevens et al.,  
 2590 2020). Apart from these two drill holes, all other inferences of sub-shelf bathymetry  
 2591 depths have been from seismic surveying, or the gravity inversion of Tinto et al.  
 2592 (2019). The majority of seismic surveys on the Ross Ice Shelf were accomplished  
 2593 during two projects, the International Geophysics Year traverses of the late 1950s  
 2594 and early 1960s (Crary et al., 1962; Crary, 1959; Crary & Robinson, 1962), and the  
 2595 Ross Ice Shelf Geophysical and Glaciological Survey (RIGGS, 1973-1974 Bentley,  
 2596 1984). These extensive surveys systematically covered the entire ice shelf, collecting  
 2597 223 observations of bathymetry with a mean spacing of approximately 40 km be-  
 2598 tween points (Figure 4.1b).

2599  
 2600 These seismic and drill hole depths have been included in various Antarctic bed  
 2601 and bathymetry products (Fretwell et al., 2013; Le Brocq et al., 2010; Timmermann  
 2602 et al., 2010). As discussed later, Tinto et al. (2019) conducted a gravity inver-  
 2603 sion over the entirety of the ice shelf with data from the Ross Ocean and ice Shelf  
 2604 Environment, and Tectonic setting Through Aerogeophysical surveys and modellng

project (ROSETTA-Ice). This provided a significantly improved resolution over just the interpolation of the sparse seismic data. This gravity-inverted bathymetry was later incorporated in the BedMachine bed compilation (Morlighem, 2022; Morlighem et al., 2020). This chapter focuses on once again improving the sub-Ross Ice Shelf Bathymetry model. Following Tinto et al. (2019), we also use a gravity inversion of the ROSETTA-ice data to model the bathymetry. However, we conduct additional processing of the gravity data, and apply an entirely new gravity inversion algorithm, as described in Chapter 3. Additionally, our method provides an assessment of the spatial uncertainty of the resulting model, a useful component needed for the ocean modelling community (Goldberg et al., 2020).

2615

## 2616 4.2 Methods

2617 Here we describe the three main methodologies of this chapter; 1) the gravity reduction process (Figure 4.2a), 2) the bathymetric inversion process (Figure 4.2b), which  
2618 is explained in detail in Chapter 3 and briefly re-introduced here, and 3) the use of a  
2619 Monte Carlo simulation to quantify spatial uncertainty in the resulting bathymetry.

### 2621 4.2.1 Gravity reduction

2622 A common task in geophysics is the removal of predictable noise to help amplify the  
2623 signal of interest. This is the basis of gravity reduction; the process of isolating the  
2624 desired gravity signal from the raw measurements of the Earth's gravitational field.  
2625 The magnitude of Earth's gravitational acceleration, which we will refer to as *gravity*  
2626 from here-on, ranges from  $\sim 978,000$  to  $\sim 983,000$  mGal, from the equator to the  
2627 poles, respectively (Hofmann-Wellenhof & Moritz, 2006). The range in these values,  
2628 approximately 5000 mGal, vastly outweighs the typical values of gravity anomalies  
2629 resulting from geologic features of interest. These anomalies of interest are typically  
2630 on the order of magnitude of 10's of mGal. This exemplifies the issue of removing  
2631 *noise* which has a significantly greater magnitude than the *signal* of interest.

2632

2633 Here, we start the gravity reduction process with observed gravity. We take ob-  
2634 served gravity to be the signal which is produced by 1) the gravitational attraction  
2635 of all massive bodies in Earth and 2) the rotation of the Earth. This means non-  
2636 geological and time-dependent effects such as machine drift, tidal changes, aircraft  
2637 manoeuvres and the effect of measuring gravity on a moving platform (Eötvös cor-  
2638 rection) have already been removed from the observed gravity (Hinze et al., 2005;  
2639 Hinze et al., 2013). With this, observed gravity is defined as;

$$g_{obs}(p) = \gamma(p) + g_{geology}(p) \quad (4.1)$$

2640 where, for an observation point  $p$ ,  $g_{obs}(p)$  is the observed gravity,  $\gamma(p)$  is the at-  
2641 traction of the *normal* Earth and  $g_{geology}(p)$  encompasses the gravity effects of all  
2642 deviations between the *normal* Earth and the real Earth. This *normal* Earth is  
2643 often taken as a single surface (here the reference ellipsoid) with a constant density  
2644 above ( $\rho_{air}$ ) and a constant density below ( $\rho_{crust}$ ). Therefore, deviations between  
2645 the *normal* and real Earth include 1) any masses above the ellipsoid which don't  
2646 have the uniform density of air or 2) any masses below the ellipsoid which don't

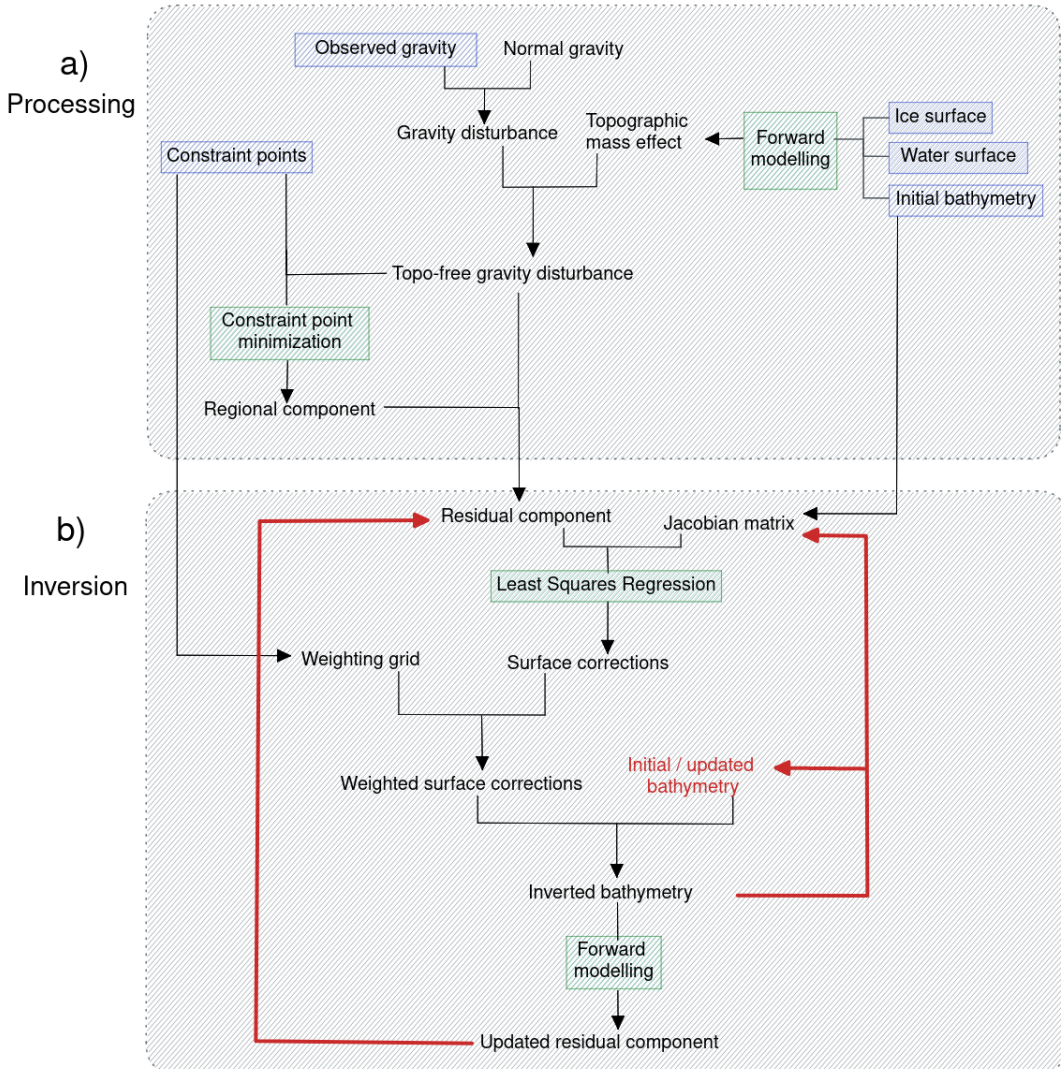


**Figure 4.2:** Schematic workflow diagram for **a)** gravity processing steps and **b)** running the inversion. Blue boxes show the input datasets, green boxes show the key processes and red lines signify iterative components of the inversion.

have the uniform density of crust. For a bathymetry inversion, the gravity signal of interest is a component of  $g_{\text{geology}}$ , which we must separate from  $\gamma$ .

#### 4.2.1.1 Attraction of normal Earth

Observed gravity varies greatly due to the observation point's position, both based on latitude and elevation. Due to the oblate shape of the Earth, gravity is generally lower at low latitudes due to 1) increased distance from the centre of Earth's mass, and 2) more importantly, the increased tangential velocity (Jacoby & Smilde, 2009). Additionally, there is a decay of gravity with increased elevation, due to an increased distance from the centre of Earth's mass. These effects aren't related to the geologic variations of interest and thus should be removed. Historically, these effects of latitude and elevation were approximated separately, using the International Gravity Formula (*Latitude correction*) and the *Free-air correction*, respectively (Hinze et al., 2005). Alternatively, Li and Götze (2001) derived an analytical solution to the

2660 gravity effects of an ellipsoid, at any point on or above its surface<sup>1</sup>. With this,  
 2661 the Latitude and Free-air corrections are combined, and their approximations are  
 2662 replaced with closed-form solutions. By subtracting the normal gravity from the  
 2663 observed gravity at each observation point the gravity disturbance is found, where

$$\delta g(p) = g_{obs}(p) - \gamma(p), \quad (4.2)$$

2664 where for an observation point  $p$ ,  $\delta g(p)$  is the gravity disturbance,  $g_{obs}(p)$  is the  
 2665 observed gravity, and  $\gamma(p)$  is the normal gravity (Pašteka et al., 2017).

2666  
 2667 The observation point,  $p$ , is defined by three coordinates; latitude, longitude, and  
 2668 geometric height (ellipsoidal height). It is a common mistake in geophysical studies  
 2669 for the normal gravity calculation to use the point  $p$ 's orthometric height (geoidal  
 2670 height or mean sea level), instead of its geometric height (Oliveira et al., 2018). This  
 2671 results in the calculation of normal gravity at a different point in 3D space relative  
 2672 to the observation. This calculation, while truly determining the gravity anomaly  
 2673 (a.k.a. free-air anomaly), is not well-suited for geological interests because the grav-  
 2674 ity anomaly contains signal from centrifugal acceleration effects due to the different  
 2675 locations of the points. Conversely, the gravity disturbance is defined as the differ-  
 2676 ence between gravity and normal gravity at the same point, and thus only contains  
 2677 signal resulting from geologic sources (Hofmann-Wellenhof & Moritz, 2006). The dif-  
 2678 ference between the gravity anomaly and the disturbance for Antarctica ranges from  
 2679 -20 to +20 mGal (See Figure C.1 in appendix C for a comparison). It is common  
 2680 for studies to correctly use the gravity disturbance while referring to it as the free-  
 2681 air anomaly to adhere to tradition. Combining Equations 4.1 and 4.2, shows that  
 2682 the gravity disturbance,  $\delta g$ , results solely from deviations between the theoretical  
 2683 model of the Earth (the *normal* Earth) and the true density variations and topog-  
 2684 raphy of the Earth (Vajda et al., 2004). Figure 4.3 compares the observed gravity,  
 2685 the normal gravity, the gravity disturbance, and the gravity anomaly for Antarctica.  
 2686

#### 2687 4.2.1.2 Topographic mass effects

2688 Typically, geophysical studies are interested in interpreting or inverting gravity sig-  
 2689 nals resulting from subsurface features. To accommodate this, all other gravity  
 2690 effects must be computed and removed from the gravity disturbance. These other  
 2691 effects include the gravity resulting from masses bound by known surfaces, referred  
 2692 to as *topographic* or *terrain masses*. These surfaces include, but are not limited to,  
 2693 the rock surface (topography), the ocean surface (geoid), the seafloor (bathymetry),  
 2694 and the ice surface. Together, the gravity resulting from these masses is referred to  
 2695 as the *topographic mass effect*. Correcting the gravity disturbance for these topo-  
 2696 graphic masses yields the *topo-free gravity disturbance*  $\delta g_{TC}$ , where

$$\delta g_{TC}(p) = \delta g(p) - g_{topo}(p). \quad (4.3)$$

---

<sup>1</sup>Note that the normal gravity calculation with this analytical solution is not valid below the ellipsoid. While this is irrelevant for most locations on Earth, West Antarctic has negative geoid elevations, meaning observations near sea level are likely below the reference ellipsoid, invalidating the normal gravity calculation. For these situations, the use of a quasi-ellipsoid is recommended (Pašteka et al., 2017; Vajda et al., 2008b)

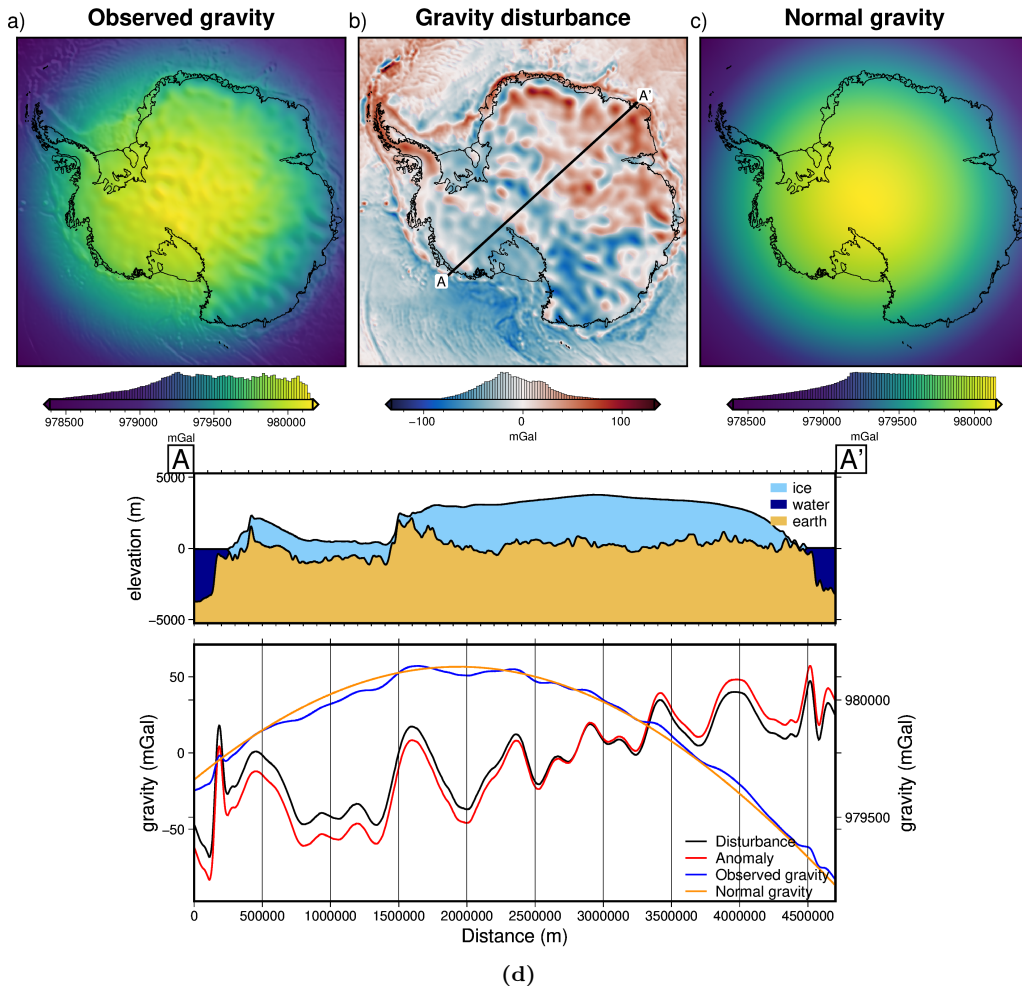


**Figure 4.3:** Observed gravity data reduction for Antarctica. **a)** Observed gravity data from Förste et al. (2014) at a geodetic observation height of 10 km. **b)** The gravity disturbance at 10 km height, defined as **a-c.** **c)** The normal gravity calculated at the same observation points as **a** using the closed-form equations of Li and Götze (2001). **d)** Profile A-B across Antarctica, location shown in **b.** Gravity disturbance (black) and anomaly (red) values are on the left y-axis, while observed (blue) and normal (orange) gravity values are on the right y-axis.

2697      $g_{topo}(p)$  represents the summed topographic mass effect.  $\delta g_{TC}$  is sometimes referred to as the *Bouguer disturbance*, owing to the historic use of the *Bouguer anomaly*. In accordance with Vajda et al. (2007), we refer to it as the *topo-free gravity disturbance* to clarify that the ellipsoid has been used instead of the geoid in all reduction steps. In the past, the topographic mass effect has been split into the Bouguer slab correction and the terrain correction. The Bouguer slab correction approximates the topographic masses as laterally infinite flat slabs, while the terrain correction accounts for the overestimation of the Bouguer slab resulting from the assumption of the flat slab. With modern computing able to efficiently calculate the gravity resulting directly from a topographic surface (Fatiando a Terra Project et al., 2023), there is no need for the separate two-step correction.

2708     The topographic mass effect reflects all topographic deviations (including topography of the ice, water, and seafloor) between the *normal* Earth and the real Earth. 2710     The *normal* Earth model is shown in Figure 4.4a, as defined by air above the ellipsoid 2711     and crust below. A simplified model of the true Earth is shown in Figure 4.4b, and 2712     contains air, ice, water, crust, and various geologic bodies within the crust. These 2713

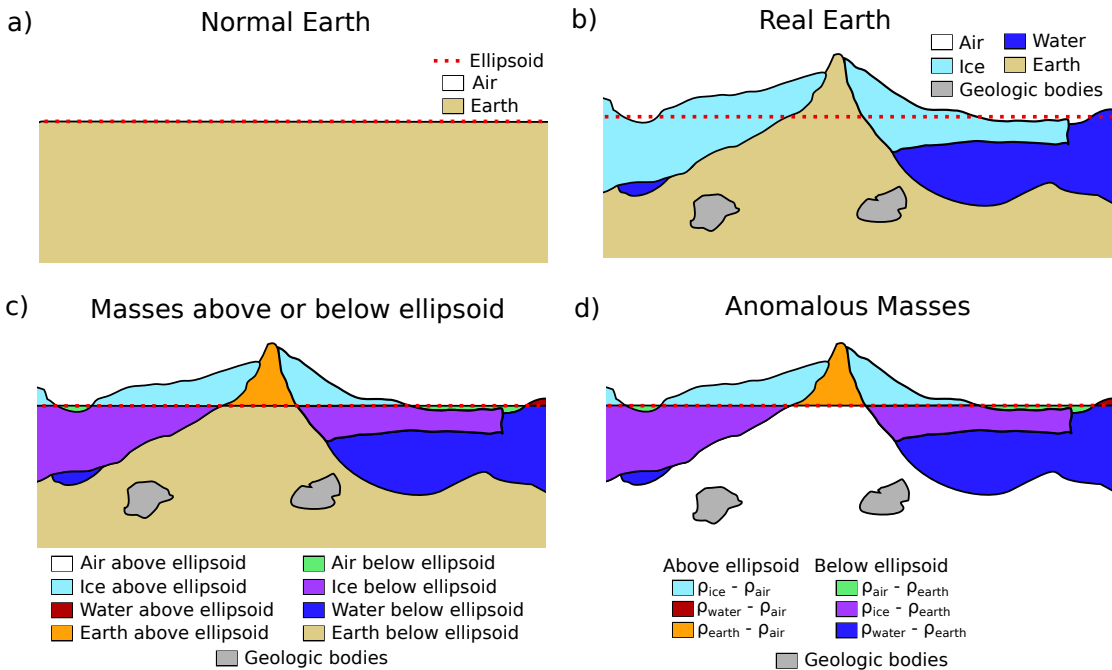


**Figure 4.4:** Components of the topographic mass effect and resulting topo-free gravity disturbance, or Bouguer disturbance. **a)** The normal Earth model, **b)** a simplified real Earth model. **c)** Topographic masses separated into components above and below the ellipsoid. **d)** Real Earth topographic masses which are anomalous with respect to the normal Earth. Note if the reference level (red dashed line) is switched from the ellipsoid to the geoid, this would result in a Bouguer anomaly.

masses are separated in Figure 4.4c into components above and below the ellipsoid. From this, the masses which are anomalous with respect to the *normal* Earth can be distinguished, as shown in Figure 4.4d. These anomalous masses include water, ice, and crust above the ellipsoid, and air, ice, water, and geologic bodies below the ellipsoid. The gravitational effect of these anomalous masses can be approximated by assuming each mass's density and setting it relative to the density of the component of the *normal* Earth which the mass is replacing. These relative densities are shown in the key of Figure 4.4d. Calculating and summing the gravity effect of each of the components of Figure 4.4d (excluding the geologic bodies) gives the topographic mass effect. Subtracting this from the gravity disturbance gives the topo-free gravity disturbance<sup>2</sup>.

To compute the topographic mass effect, the anomalous masses from Figure 4.4d are discretized into a series of vertical right-rectangular prisms. To achieve the geometry and density configuration of Figure 4.4d, three sets of prisms are used, as shown in Figure 4.5c-e.

1. Prisms between the ice surface and the ellipsoid are assigned densities of  $\rho_{\text{ice}} - \rho_{\text{air}}$  for prisms above the ellipsoid, and  $\rho_{\text{air}} - \rho_{\text{ice}}$  for prisms below the ellipsoid.
2. Prisms between the water surface (ice base) and the ellipsoid are assigned densities of  $\rho_{\text{water}} - \rho_{\text{ice}}$  for prisms above the ellipsoid, and  $\rho_{\text{ice}} - \rho_{\text{water}}$  for prisms below the ellipsoid.

<sup>2</sup>The use of the reference ellipsoid as the bounding surface of the topographic mass effect calculations results in a topo-free gravity disturbance while using the geoid as the bounding surface would result in a Bouguer anomaly (Vajda et al., 2006).

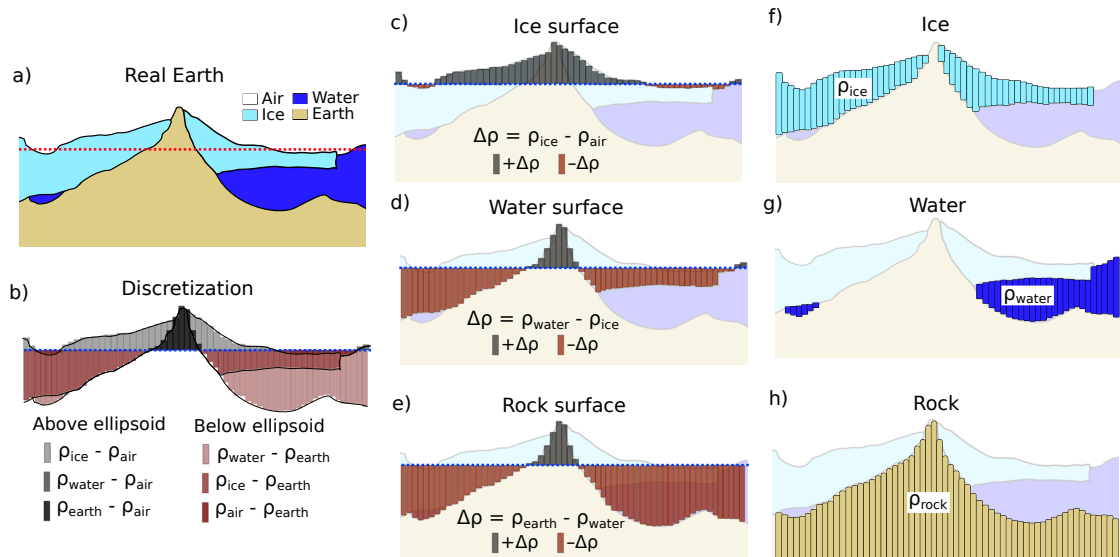


**Figure 4.5:** Discretizing the topographic mass effect. **a)** The simplified real Earth model, with air, ice, water, and earth. **b)** the resulting anomalous masses relative to the *normal* Earth, as shown in Figure 4.4d. **c)** Prisms between the ellipsoid and the ice surface, **d)** prisms between the ellipsoid and the water surface (ice base), and **e)** prisms between the ellipsoid and the rock surface (topography onshore and bathymetry offshore). Overlap of prisms from **c-e** creates the different shades shown in **b**. The alternative discretization approach, commonly used, is shown in **f-h** where the prism layers are bound both above and below by topographic layers, or arbitrary references (bottom of prisms in **h**), instead of by the normal Earth reference surface (ellipsoid). Additionally, density values of the prisms are related to the material they discretize and are not relative to the expected density of the normal Earth.

2735     3. Prisms between the rock surface (topography onshore and bathymetry off-  
2736       shore) and the ellipsoid are assigned densities of  $\rho_{\text{earth}} - \rho_{\text{water}}$  for prisms  
2737       above the ellipsoid, and  $\rho_{\text{water}} - \rho_{\text{earth}}$  for prisms below the ellipsoid.

2738     This configuration of prisms correctly discretizes the topographic mass effect be-  
2739       cause the ice surface is equal to the water surface in areas of no ice thickness, and  
2740       the water surface is equal to the rock surface in areas of no water thickness. Due  
2741       to this, the overlap between the three sets of prisms, shown in Figure 4.5b gives the  
2742       appropriate densities, as defined in Figure 4.4d. From these three sets of prisms, the  
2743       topographic mass effect can be calculated at the gravity observation points using the  
2744       analytical solutions of Nagy et al. (2000). As a demonstration, the topographic mass  
2745       effect for Antarctica is calculated using topographic data from Bedmap2 (Fretwell  
2746       et al., 2013), referenced to the WGS-84 ellipsoid. The observed satellite gravity data  
2747       has a low spatial resolution, so the lower resolution of Bedmap2 over BedMachine  
2748       v3 is insignificant. The calculated topographic mass effect, the gravity disturbance,  
2749       the resulting topo-free gravity disturbance, and the topographic mass effect from  
2750       the alternative method of discretization (Figure 4.5f-h) are shown in Figure 4.6.

2751     The theoretical topo-free gravity disturbance is the gravity effect caused by and  
2752       only by anomalous subsurface bodies, which have a density different from the as-  
2753       sumed constant density of the crust. In reality, there are additional components of  
2754       the topo-free gravity disturbance resulting from 1) noise in the observed data, 2)  
2755       non-uniform densities used in the topographic mass effect calculation, and 3) inac-  
2756       curate topographic data used for the topographic mass effect calculation. In most  
2757       geophysical applications, the uncertainty of the topographic data is small compared

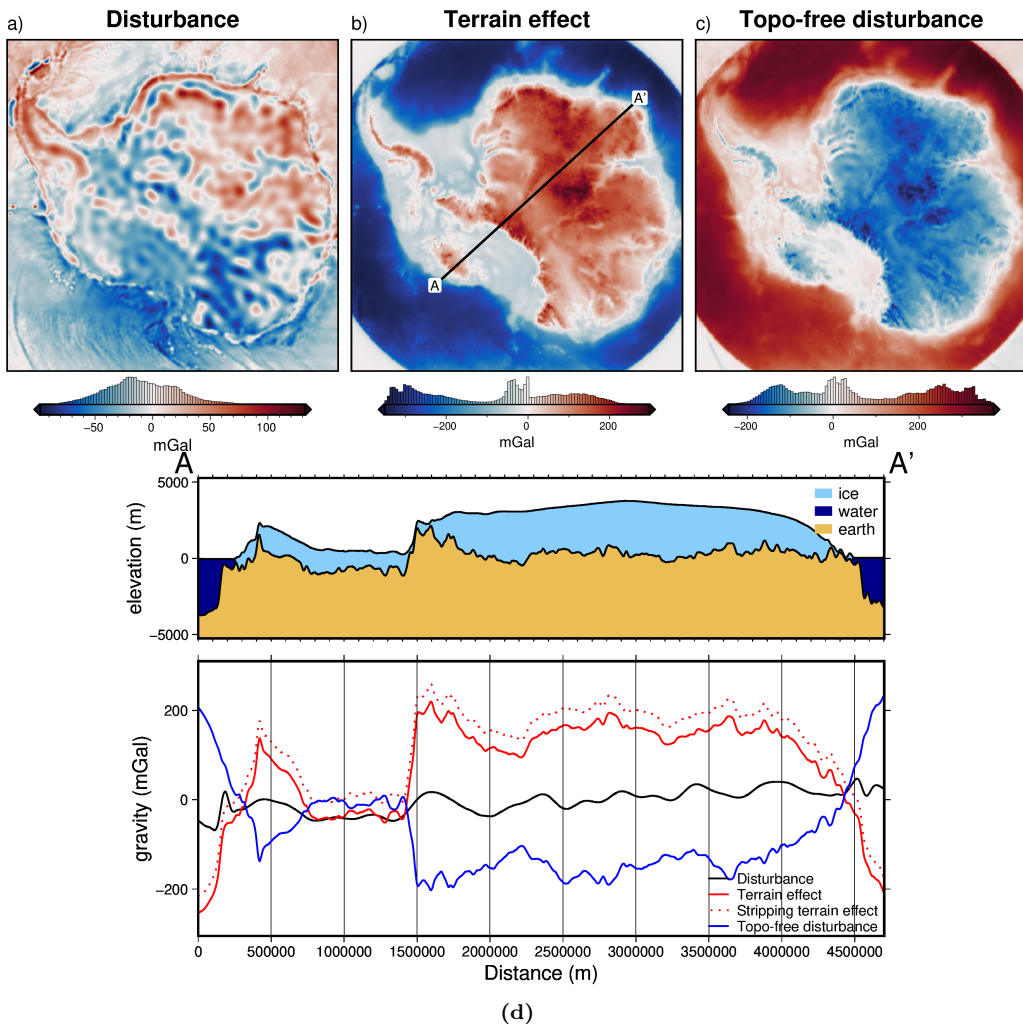


**Figure 4.6:** Topographic mass effect at 10 km height for Antarctica, from Bedmap2 topographic data (Fretwell et al., 2013). **a)** Gravity disturbance at a geodetic observation height of 10 km, from Figure 4.3b. **b)** The combined gravity effect of the anomalous masses defined in Figure 4.4d and discretized following 4.5b. **c)** The topo-free gravity disturbance, calculated as **a** - **b**. **d)** Profile A-A' across Antarctica, location shown in **b**. The dotted red line shows the terrain mass effect results of the alternative discretization method shown in Figure 4.5f-h. A DC shift was applied to attempt to remove the offset.

2759 to other uncertainties in the analysis, and thus component #3 is assumed to be zero.  
 2760 Conversely, for the case of a bathymetry inversion, this component of the topo-free  
 2761 disturbance resulting from the inaccuracies of the topography (bathymetry) data is  
 2762 the signal of interest. Next, we will isolate this component from the remainder of  
 2763 the topo-free gravity disturbance.

2764

#### 2765 4.2.1.3 Regional separation

2766 Here, we separate the topo-free gravity disturbance into components resulting from  
 2767 1) subsurface geologic variations and 2) inaccuracies between the true bathymetry  
 2768 and the low-resolution bathymetry data used for the terrain mass effect. These  
 2769 are referred to as the regional and residual components, respectively. Chapter 3  
 2770 highlighted the importance of accurately estimating and separating this regional  
 2771 component from the residual. The regional estimation was found to be the largest

source of uncertainty in several synthetic bathymetry inversions, as well as other Antarctic bathymetry inversions (Brisbourne et al., 2014). While there are many techniques to estimate the regional component, we will use constraint point minimization due to its demonstrated effectiveness over the other methods (Section 3.2.4). This technique samples the topo-free gravity disturbance at points of known bathymetry depth, referred to as the constraint points. Since the depth is known here, the residual component of gravity should be near zero, and thus the regional component should entirely equal the topo-free gravity disturbance. Using these sampled values, the entire model domain is gridded with an interpolation, using either bi-harmonic splines (Uieda, 2018) or minimum curvature (Smith & Wessel, 1990). The resulting grid makes up the regional component, and when subtracted from the topo-free gravity disturbance gives the residual component. This residual component is the input into the inversion.

2785

## 4.2.2 Bathymetry inversion

Here we start by briefly summarising the bathymetry inversion workflow described in Chapter 3, and shown schematically in Figure 4.2b. Then we compare our method to several other commonly used bathymetry inversion algorithms. The basis of modelling bathymetry with a gravity inversion is that the bathymetry surface, which is a contrast between lower-density material (seawater) and higher-density material (sediment) creates a measurable effect on Earth's gravity. Our inversion begins by computing the Jacobian matrix (Equation 3.7), which is a quantitative means of describing the sensitivity of the residual gravity data to changes in the height of each grid cell of bathymetry. In other words, the Jacobian quantifies the ratio between the amplitude of bathymetric features and the gravity anomaly resulting from them. From this Jacobian matrix, the optimal change to apply to each bathymetry grid cell to minimize the residual gravity data is estimated. This is in the form of a surface correction grid, with a value for each grid cell of bathymetry. Since there are locations of already known bathymetry depths (constraint points), this surface correction grid should be zero at these points. To achieve this, a weighting grid is calculated (Section 3.2.5.3), which is based on the minimum distance between each grid cell and the nearest constraint point. These distance values are then normalized from 0 to 1, with 0 being the cells closest to the constraints, and 1 being the cells furthest. The surface correction grid is multiplied by this weighting grid, to achieve a correction value of 0 m at the constraints, smoothly tapering off to the full estimated correction values at a distance.

2808

With this weighted surface correction grid, the original bathymetry depths are updated. To ensure the updated bathymetry doesn't intersect the ice base, the ice base topography is set as an upper-bounding surface. The forward gravity of this updated bathymetry is then re-calculated, with the prism configuration and densities shown in Figure 4.5e. The updated forward gravity is used to recalculate the topo-free gravity disturbance. Using the same regional component as calculated before the inversion (Section 4.2.1.3), an updated residual gravity is computed. This is then input into the next iteration of the inversion (red lines in Figure 4.2b). Iterations continue until a set of user-defined stopping criteria are met; 1) a maximum number of iterations is reached, 2) a minimum value of the  $\ell^2$ -norm of the residual

2819 is reached, or 3) there is no significant variation in the  $\ell^2$ -norm in two consecutive  
2820 iterations.

2821

2822 This process describes a single *inversion*. The critical step in this inversion, deter-  
2823 mining the surface correction values from the sensitivity matrix, includes a damping  
2824 parameter that controls the smoothness of the resulting inverted bathymetry. This  
2825 damping parameter value directly affects the resulting bathymetry model and needs  
2826 to be carefully chosen. For this, we follow the cross-validation routine described in  
2827 Chapter 3 from Uieda and Barbosa (2017). This involves running the entire inver-  
2828 sion for a suite of different damping parameter values. The input gravity data to  
2829 these inversions is split into a *testing* set and a *training* set. The inversion only  
2830 uses the *training* set. After each inversion, the forward gravity effect of the updated  
2831 bathymetry model is calculated at the points of the *testing* set. The root mean  
2832 squared difference between the testing gravity values and the forward gravity values  
2833 gives the *score* of each cross-validation. The damping parameter which produces  
2834 the lowest score is chosen as the optimal value.

2835

### 2836 4.2.3 Starting bathymetry

2837 An initial bathymetry model for the inversion is needed to compute the topographic  
2838 mass effect and to run the inversion. The weighting grid constrains the inversion  
2839 from changing the starting grid values at the constraint points. For this reason,  
2840 the starting model should be carefully created. As discussed in the previous chap-  
2841 ter (Chapter 3, Section 3.4.2), there are several methods of creating the starting  
2842 model from the sparse measurements at the constraint points. Here, we use and  
2843 compare two techniques for interpolating these constraint point values over the en-  
2844 tire domain; tensioned minimum curvature (Smith & Wessel, 1990) and bi-harmonic  
2845 splines (Sandwell, 1987). See Chapter 3 Section 3.4.2 for the details of these gridding  
2846 techniques.

2847

### 2848 4.2.4 Uncertainty quantification

2849 A major component missing from many bathymetry inversions is assessing the spa-  
2850 tially variable uncertainty in the resulting bathymetry depths. This uncertainty  
2851 arises from a multitude of sources, including uncertainty in 1) the gravity data mea-  
2852 surements, 2) constraint point depths, 3) user-defined variables, such as ice, water,  
2853 or sediment density, and 4) uncertainties associated with the various methodologies  
2854 of the inversion. Here we use a sampling-based approach to estimate the uncertainty,  
2855 where the uncertainty of the *inputs* is used to assess the uncertainty of the *output*,  
2856 in this case, the inverted bathymetry. This general method of uncertainty analysis  
2857 is referred to as Monte Carlo sampling (Jansen et al., 1994).

2858

2859 For a generalized problem of inputs  $\mathbf{x}$  and a function  $\mathbf{y}(\mathbf{x})$ , Monte Carlo sim-  
2860 ulation provides a means to answer the two following questions; 1) what is the  
2861 uncertainty in  $\mathbf{y}(\mathbf{x})$  given the uncertainty in  $\mathbf{x}$ ? and 2) what are the relative im-  
2862 portance of the various components of  $\mathbf{x}$  with respect to  $\mathbf{y}(\mathbf{x})$  (Helton et al., 2006)?  
2863 While there are many components that contribute to the overall inversion uncer-

tainty, here we will examine 1) uncertainty in the gravity data values, 2) depth uncertainty of the constraint points, 3) uncertainty in the chosen density values used for ice, water, and earth, and 4) uncertainties related to user-chosen parameter values in the inversion. Uncertainties that are not covered here are those which relate to processes of the inversion which don't have associated measurable input uncertainties. This includes the use of spatially non-variable density values for ice, water, or earth, or the effects of discretizing a real topographic surface as a series of prisms.

2871

The Monte Carlo simulation consists of sampling the input parameters  $N$  times from their respective distributions (Figure 4.7b) and running the entire inversion workflow for each of the  $N$  parameter sets (Figure 4.7c). For each bathymetry grid cell, the weighted standard deviation of the  $N$  resulting inverted bathymetries is found (Figure 4.7d). This grid of cell-specific standard deviations show where the input parameters have a large effect on the bathymetry results. This grid is used as our estimate of the spatial uncertainty in the inversion. The grid of cell-specific weighted median values is then taken to be the optimal inversion result. These cell-specific statistics are weighted by the inverse square of each inverted bathymetry's RMS difference with the constraint point depths (Figure 4.7d). This reduces the bias of inversions in the ensemble which performed poorly, as defined by not adhering to the constraints (Schnaidt & Heinson, 2015). To assess the relative importance of the input parameters, in addition to the complete Monte Carlo simulation, additional simulations are run where each parameter's effect is isolated. For these, only a singular parameter is sampled from its distribution, so that the resulting spatial standard deviation is due solely to the uncertainty of that parameter.

2888

The parameters included in the Monte Carlo sampling are: 1) the gravity disturbance data, 2) the constraints point depths, 3) the gridding parameters to create the starting bathymetry, 4) the density of ice, 5) the density of water, 6) the density of sediment, and 7) gridding parameters for the constraint point minimization technique of regional gravity estimation (Figure 4.7b). For the full Monte Carlo simulation, with all the above inputs sampled from their respective distributions, the entire inversion workflow needs to be repeated with each of the  $N$  parameter sets. This includes 1) creating the starting bathymetry model from the constraint points (Section 4.2.3), 2) calculating the terrain mass effect to get the topo-free gravity disturbance (Section 4.2.1.2), 3) estimating the regional component of the disturbance and removing it (Section 4.2.1.3), and 4) running the damping parameter value cross-validation (Section 4.2.2) to obtain the inverted bathymetry (Figure 4.7). For the individual Monte Carlo simulations, only portions of this workflow need to be repeated. For example, if only the gravity disturbance is sampled, only the regional field and inversion need to be re-run. The starting bed and topographic mass effect calculated during the baseline inversion are re-used.

2905

Due to the computational demand of a full inversion workflow, the total number of inversions in each Monte Carlo simulation is limited. To ensure the uncertainty distributions of the inputs are adequately sampled with this limited number of possible runs, we have used Latin hypercube sampling where possible (Jansen et al., 1994). This sampling technique is well suited for computationally demanding tasks since it ensures proper coverage of the uncertainty distributions of the sampled values, despite a low number of samples Helton et al., 2006. To accomplish this, for a

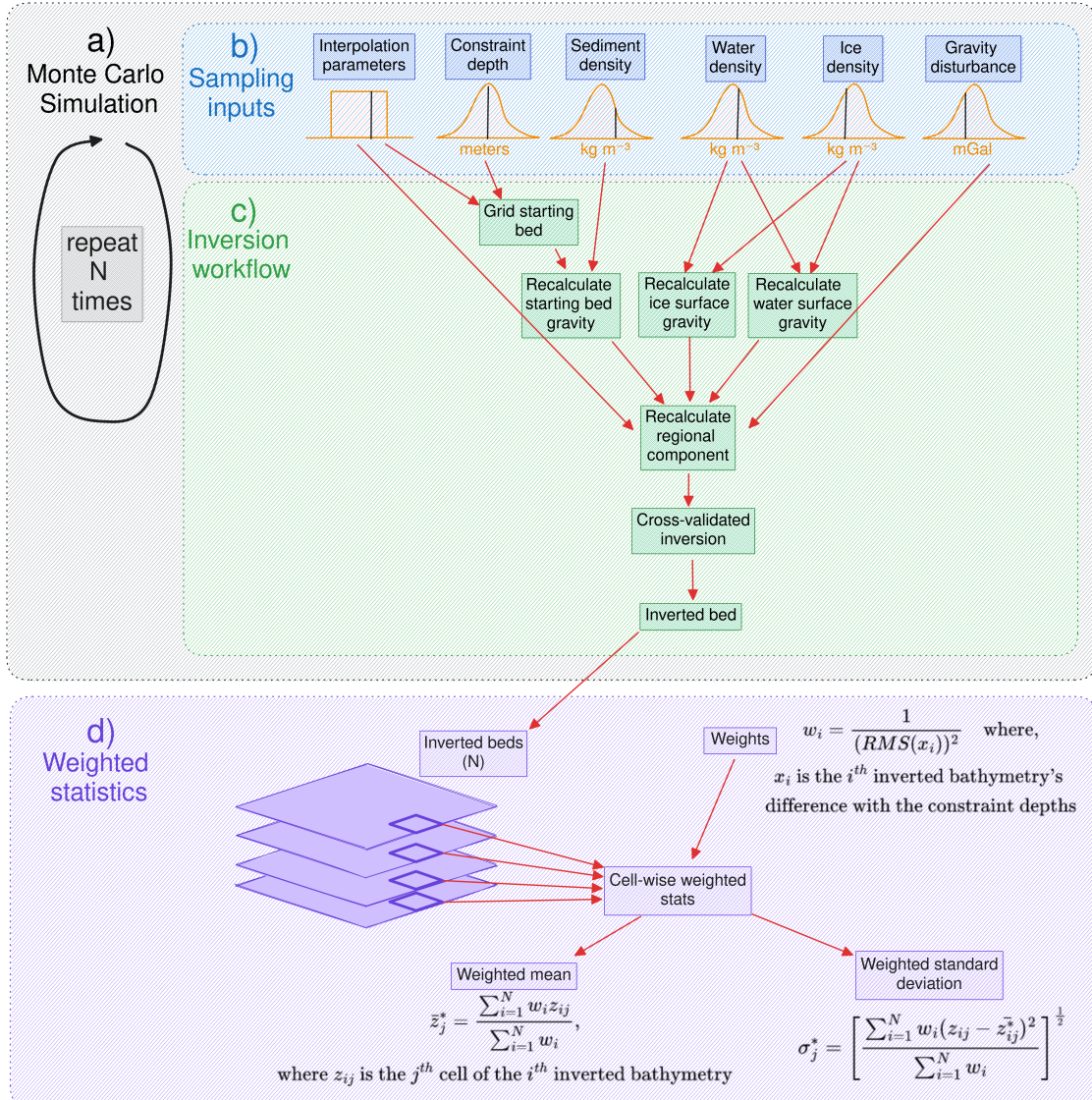


**Figure 4.7:** Schematic workflow diagram for the Monte Carlo uncertainty analysis. **a)** The Monte Carlo simulation, consisting of **b)** sampling the inputs from their respective distributions, and **c)** implementing the various components of the workflow, depending on which inputs have been sampled. This process is repeated  $N$  times, yielding  $N$  inverted bathymetry grids. **d)** Weighted cell-specific statistics are computed. Each inverted bathymetry grid (large purple boxes) is weighted by the respective inversion's constraint depth RMSE. These weights are used to compute the weighted mean and weighted standard deviation of each grid cell (bold purple square).

2913 Monte Carlo simulation of  $N$  runs, the given distributions are split into  $N$  intervals  
 2914 of equal probability and one value is chosen from each interval. The  $N$  values for  
 2915 each parameter are then randomly paired to get  $N$  sets of sampled input parameter  
 2916 values (Helton et al., 2006). Since the gravity data and constraint points are each  
 2917 sampled on a point-by-point basis, Latin hypercube sampling is unnecessary and  
 2918 random sampling is used. Figure 4.8 shows a  $N = 9$  comparison of random sam-  
 2919 pling and Latin hypercube sampling for a two-parameter simulation.

2920

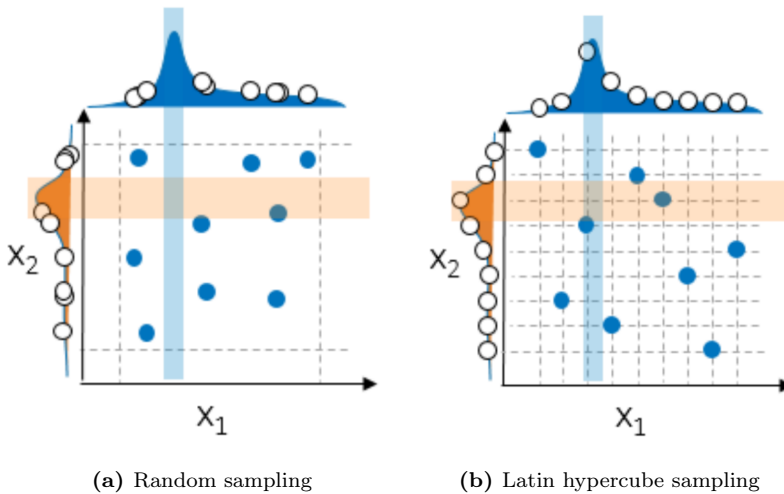


**Figure 4.8:** Comparison of sampling methods for a Monte Carlo simulation of two variables ( $X_1$  and  $X_2$ ) with 9 samples drawn from each. **a)** Random sampling, where values are drawn at random from each variable's distribution, and **b)** Latin hypercube sampling, where values are drawn from equal-probability intervals. Note the effective coverage of the distributions in **b** relative to **a**. The figure is adapted from Koch et al. (2017).

## 2921 4.3 Relation to past bathymetry inversions

2922 The fundamental theory in all bathymetry inversions is based on the fact that the  
 2923 density contrast across the bathymetry surface produces a measurable gravity effect.  
 2924 This phenomenon gives rise to several techniques to convert observed gravity  
 2925 data into bathymetric depths. This by definition is a geophysical inverse problem  
 2926 (Oldenburg & Li, 2005), but the methods chosen to solve it vary from 3D rigorous  
 2927 inversions to iterative 2D forward modelling. Our inversion method follows a clas-  
 2928 sical least-squares approach to solving the inverse problem, while our uncertainty  
 2929 and sensitivity analysis follows a Bayesian approach (Aster et al., 2018). Here, we  
 2930 compare our inversion method and workflow to other bathymetry inversions. We  
 2931 attempt to include all past studies related to Antarctica, as well as several from  
 2932 Greenland. We start by comparing our technique for the gravity reduction process,  
 2933 followed by differences in the actual inversion, and finally by differences in our as-  
 2934 sessment of uncertainty.

2935

### 2936 4.3.1 Gravity reduction comparison

2937 One of the largest differences between our method and past studies is the gravity  
 2938 reduction process. We employ a rigorous terrain mass effect calculation to obtain  
 2939 a topo-free gravity disturbance, often referred to as a Complete Bouguer Anomaly  
 2940 (Vajda et al., 2007). Theoretically, this gravity signal contains only effects due to  
 2941 subsurface density anomalies and inaccuracies in calculating the terrain mass effect.  
 2942 Our method isolates the gravity effect of this inaccuracy since it is due to the de-  
 2943 viations between the starting model of bathymetry and the true bathymetry. This  
 2944 is referred to as our residual component of the topo-free gravity disturbance. While  
 2945 most other bathymetry inversion studies achieve a similar residual anomaly, they  
 2946 complete this procedure in a theoretically different way, which may be introducing  
 2947 unnecessary errors. The differences arise from other studies ignoring the reference

2948 surface (the ellipsoid) for all calculations after the normal gravity correction.

2949

2950 The sign of a gravity disturbance value informs the interpreter as to whether  
2951 the true Earth has either excess or deficient mass at that location with respect to  
2952 the normal Earth. Therefore, the absolute level of gravity disturbance data should  
2953 be retained, even though direct offsets (DC shifts) don't alter the amplitude of  
2954 the gravity anomalies. For this reason, the reference surface used in the normal  
2955 gravity calculation (here the ellipsoid) should be continued to be used in all further  
2956 calculations of topographic masses, including in the forward calculation made during  
2957 the inversion, as shown in Figure 4.5 b. Many studies instead have discretized the  
2958 ice, water, and starting bathymetry surfaces into prism layers which either have  
2959 arbitrary references or density values not relative to the normal Earth model. This  
2960 alternative discretization is shown in Figure 4.5f-h. For example, the gravity effect of  
2961 ice, if not just ignored (e.g., Cochran & Bell, 2012; Jordan et al., 2020b; Millan et al.,  
2962 2017; Yang et al., 2020b), is typically removed via a "stripping" technique (Vajda  
2963 et al., 2008a), (e.g., Greenbaum et al., 2015; Millan et al., 2020; Muto et al., 2013a;  
2964 Yang et al., 2021). This stripping involves calculating the forward gravity of prisms  
2965 with tops defined by the ice surface, bottoms defined by the ice base, and densities  
2966 defined by the assumed density of ice (Figure 4.5f). Additionally, the prisms which  
2967 comprise the starting bathymetry model for many inversions are bound above by  
2968 the starting bathymetry, and below by an arbitrary constant depth (Figure 4.5h)  
2969 (e.g., Muto et al., 2013a; Tinto et al., 2019). The forward gravity calculations of  
2970 this style of discretization can introduce several errors.

- 2971 1. The largest of these errors is an offset in the mean value of the forward gravity  
2972 relative to the observed gravity. This offset needs to be estimated and removed  
2973 prior to comparison with the observed data. The DC-shift used to remove the  
2974 offset is typically estimated by finding a value that minimizes the difference  
2975 between the observed and predicted data at locations of known bathymetry  
2976 (e.g., Boghosian et al., 2015; Cochran et al., 2020; Constantino et al., 2020;  
2977 Eisermann et al., 2020; Millan et al., 2017; Muto et al., 2013a). This additional  
2978 step, referred to as "pinning", is unnecessary in our implementation, due to  
2979 adhering to a rigorous determination of the terrain mass effect. If an incorrect  
2980 DC shift is applied, the significance of the zero level of the topo-free gravity  
2981 disturbance is lost. The value of 0 signifies that the simplified model of the  
2982 Earth (i.e. the starting bathymetry model) is equal to the true Earth density  
2983 distribution. Shifting this zero-level due to errors in estimating the DC-shift  
2984 may lead to a vertical offset in the inverted bathymetry, especially if the in-  
2985 version domain isn't well constrained. The DC-shifted terrain mass effect and  
2986 the rigorous terrain mass effect for Antarctica are compared in Figure 4.6d.
- 2987 2. The forward gravity calculation with this style of discretization results in  
2988 slightly different amplitude anomalies compared to the true terrain mass ef-  
2989 fect. This difference is due to the different densities assigned to the prism layer  
2990 between the two techniques (Figure 4.5). While this difference is likely below  
2991 the range of uncertainties in the gravity error, it is an unnecessary addition of  
2992 error to the gravity reduction process.
- 2993 3. The last drawback to using this alternative discretization is an increased grav-  
2994 itational edge effect. As shown in Figure 4.5, the average densities and prism

heights are larger with this technique. This increases the overall decay of calculated gravity at the edges of the model space, due to the contrast with the void-space beyond the model domain. To account for this, a larger buffer zone is needed, which can significantly increase the computational requirements during forward modelling (see Chapter 3 Section 3.2.2.2).

#### 3000 4.3.1.1 Regional separation

3001 The last step in the gravity reduction process for bathymetry inversion is separating  
3002 the regional and residual signals, where the residual signal should theoretically be  
3003 entirely a result of the bathymetry surface. Some techniques commonly used for  
3004 this are described in Chapter 3 Section 3.2.4. Past bathymetry inversions have used  
3005 a variety of these techniques, as summarized below.

- 3006 1. Zero or uniform adjustment; For small inversion domains the regional field  
3007 is sometimes assumed to be minimal. In these scenarios, past studies have  
3008 either limited the inversion domain to where the regional field is assumed  
3009 small (Boghosian et al., 2015; Cochran & Bell, 2012), used a uniform value  
3010 for the regional component (Muto et al., 2013b), or found a constant density  
3011 value for the starting model which minimize the gravity misfit (An et al., 2017;  
3012 Millan et al., 2018; Millan et al., 2017).
- 3013 2. Low-pass filtering; for inversion domains with an expected regional field slightly  
3014 larger than the above scenario, low-pass filtering of the gravity data can ap-  
3015 proximate the regional component (Eisermann et al., 2020; Hodgson et al.,  
3016 2019).
- 3017 3. Geologic modelling; To account for the regional field, some studies create ge-  
3018 ologic models of varying density to estimate the regional field. These models  
3019 are typically informed from other geophysical data (Greenbaum et al., 2015;  
3020 Hodgson et al., 2019), *a priori* geologic knowledge (Cochran et al., 2014b; Con-  
3021 stantino et al., 2020; Tinto & Bell, 2011), or from an approximated crustal  
3022 density distribution (Cochran et al., 2020; Eisermann et al., 2021; Tinto et al.,  
3023 2019; Wei et al., 2020).
- 3024 4. Upwards continuation / high altitude surveys; This technique estimates the  
3025 long-wavelength regional component by either upward continuing the gravity  
3026 data to large altitudes, using separate gravity data collect from high-altitude  
3027 surveys (Muto et al., 2016), or a combination of both (Tinto et al., 2015)
- 3028 5. Constraint point minimization; the last commonly used technique utilizes the  
3029 assumption that the desired residual component is near-zero at points of known  
3030 bathymetry. From this assumption, the regional component at these constraint  
3031 points is entirely equal to the gravity anomaly value. To estimate the regional  
3032 field, the gravity values are sampled at the constraint points and interpolated  
3033 over the region. This technique has been used in several recent inversions  
3034 where sparse constraint points are available (An et al., 2019a; An et al., 2019b;  
3035 Jordan et al., 2020b; Millan et al., 2020; Vaňková et al., 2023; Yang et al., 2021;  
3036 Yang et al., 2020a). While implemented in a different method, this constraint  
3037 point minimization follows the same concept as several studies which use the  
3038 constrained locations to derive a spatially variable density model, accounting

3039 for the regional field (Eisermann et al., 2021; Tinto et al., 2019; Wei et al.,  
 3040 2020).

3041 Here, we use the constraint point minimization technique for estimating and  
 3042 removing the regional component of the topo-free gravity disturbance.

### 3043 4.3.2 Inversion comparison

3044 We have developed a conventional non-linear geometric gravity inversion algorithm,  
 3045 as often used in modelling density contrasts, such as sedimentary basins (e.g., Mar-  
 3046 tins et al., 2010; Santos et al., 2015), or the Moho (e.g., Pappa et al., 2019; Uieda  
 3047 & Barbosa, 2017). This algorithm is similar in concept to inversions used in other  
 3048 bathymetric studies but differs in its implementation. Past inversion techniques  
 3049 used for bathymetry modelling can be grouped into several categories;

- 3050 1. algorithmic approaches. This method termed the "topographic shift method"  
 3051 (Hodgson et al., 2019; Jordan et al., 2020b), while not a formal inversion,  
 3052 calculates the equivalent rock thickness from the residual component of gravity,  
 3053 adds this to the starting bathymetry model, and constrains the results by the  
 3054 locations of known bathymetry.
- 3055 2. 2D profile inversions. Using the method of Talwani et al. (1959), and often  
 3056 implemented within the commercial software Geosoft Oasis Montaj, these in-  
 3057 verisions retain the 2D nature of the airborne flight lines and invert only along  
 3058 the path of the flight (Boghosian et al., 2015; Cochran et al., 2014b; Cochran  
 3059 et al., 2020; Constantino & Tinto, 2023; Tinto & Bell, 2011; Tinto et al., 2015;  
 3060 Wei et al., 2020).
- 3061 3. 3D frequency-based inversions. This category of inversion uses a Fourier trans-  
 3062 formation to calculate the forward gravity effect of a continuous topographic  
 3063 surface, forgoing the need to discretize the topography into vertical prisms  
 3064 (Oldenburg, 1974; Parker, 1972). This Fourier transform is then iteratively  
 3065 modified to minimize the misfit to the observed gravity. This method, par-  
 3066 ticularly its implementation within the commercial software Geosoft Oasis  
 3067 Montaj, is frequently used for bathymetry inversions (An et al., 2017; An et  
 3068 al., 2019a; An et al., 2019b; Cochran & Bell, 2012; Eisermann et al., 2020;  
 3069 Eisermann et al., 2021; Greenbaum et al., 2015; Millan et al., 2018; Millan  
 3070 et al., 2017; Millan et al., 2020; Studinger et al., 2004b).
- 3071 4. Simulated Annealing. This global optimization technique (Kirkpatrick et al.,  
 3072 1983) performs many forward calculations of possible bathymetry surfaces and  
 3073 slowly converges on a model which minimizes the misfit with the observations.  
 3074 This method, similar to our Monte Carlo uncertainty analysis, has the benefit  
 3075 of providing an uncertainty estimate of the resulting bathymetry based on the  
 3076 uncertainty in the inversion inputs. This has been used in several bathymetric  
 3077 inversions (Filina et al., 2008; Muto et al., 2013a; Muto et al., 2016; Roy et al.,  
 3078 2005; Yang et al., 2021; Yang et al., 2018; Yang et al., 2020a)
- 3079 5. Regularized least-squares inversions. This style of inversion is the conven-  
 3080 tional approach to solving non-unique inverse problems (Aster et al., 2018).  
 3081 While this method is commonly used for other geometric gravity inversions

3082 (e.g., Moho and basement), to our knowledge it is only applied to bathymetry  
 3083 inversions here, and in Vaňková et al. (2023).

### 3084 4.3.3 Uncertainty comparison

3085 Here we compare our uncertainty analysis to those from other bathymetry-gravity  
 3086 inversion studies. Most of these past studies provide an estimation of uncertainty,  
 3087 but only a few provide spatially variable uncertainties (e.g., An et al., 2019a; Muto  
 3088 et al., 2016). Typically, these inversion uncertainties are assumed to result from  
 3089 three sources.

- 3090 1. Uncertainty in the gravity data. The uncertainties resulting from the grav-  
 3091 ity data uncertainty are typically estimated using a Bouguer slab approx-  
 3092 imation, with an assumed density of the contrast between rock and water  
 3093 ( $\sim 1600 \text{ kg m}^{-3}$ ), and a gravity uncertainty approximated from the RMS  
 3094 crossover values of the airborne gravity survey (e.g., Boghosian et al., 2015;  
 3095 Constantino et al., 2020; Tinto et al., 2019). Alternatively, a simple conver-  
 3096 sion factor has been proposed of 100 m of inversion uncertainty per 5 mGal of  
 3097 gravity uncertainty (An et al., 2019a; An et al., 2019b).
- 3098 2. Assumptions of the geologic structure. The uncertainty resulting from as-  
 3099 sumptions of the geologic structure is typically simplified as uncertainties in  
 3100 the choice of the constant density contrast between sediment and seawater.  
 3101 This uncertainty is sometimes approximated as a ratio of change in density to  
 3102 change in inverted relief as a percentage (e.g.,  $\sim 3\%$  relief for  $50 \text{ kg m}^{-3}$  Tinto  
 3103 et al., 2019) or by altering the density and comparing the results (Boghosian  
 3104 et al., 2015).
- 3105 3. Uncertainties in the past measurements of bathymetry (constraints). Lastly,  
 3106 constraint point measurement uncertainties are typically assumed to result in  
 3107 a 1:1 uncertainty in the inverted bathymetry (e.g., Boghosian et al., 2015;  
 3108 Tinto et al., 2019).

3109 Our uncertainty analysis, through Monte Carlo simulation, provides robust spa-  
 3110 tial uncertainty estimates for each of these three sources of uncertainty. Similar to  
 3111 the above methods, Monte Carlo simulation only addresses uncertainties related to  
 3112 the uncertainty of the inputs to the inversion.

## 3113 4.4 Results

3114 Here we apply the above-described methods to recover a higher resolution bathymetry  
 3115 beneath Antarctica's Ross Ice Shelf. First, we show the results from an individ-  
 3116 ual workflow, as depicted in Figure 4.2. This includes the starting bathymetry  
 3117 model, the topo-free gravity disturbance calculations, and the resulting inverted  
 3118 bathymetry. Next, we present the Monte Carlo simulation results, where this entire  
 3119 workflow is repeated many times with varying values of input data and parameters.

### 4.4.1 Starting bathymetry

Existing options for a starting bathymetry model for the sub-Ross Ice Shelf include Bedmap2 (Fretwell et al., 2013) or BedMachine v3 (Morlighem, 2022; Morlighem et al., 2020). BedMachine v3 for the Ross Ice Shelf contains the gravity-inverted bathymetry results from Tinto et al. (2019). To avoid over-interpretation of the gravity data (starting an inversion with the results of a separate inversion) we opted to not use BedMachine for the starting model. Bedmap2 bed elevations for the Ross Ice Shelf were created through the interpolation of the point constraints (Fretwell et al., 2013). These point constraints within the ice shelf (Figure 4.1b) were compiled from several surveys, including the early traverses of the 1950s and 60s (Crary et al., 1962; Crary, 1959; Crary & Robinson, 1962)<sup>3</sup>, and the Ross Ice Shelf Geophysical and Glaciological Survey (RIGGS, 1973-1974 Bentley, 1984) ( $N = 223$ ). However, the gridding algorithm used (ArcGIS Topogrid), while producing smooth results for the Ross Ice Shelf, didn't strictly adhere to the constraint point depths. This can be seen through the comparison of constraint point depths and Bedmap2 grid values at the same location (Figure 4.1b). The RMS difference between the constraint depths and the grid depths within the ice shelf is 138 m. The largest differences are concentrated along the Transantarctic Mountain Front, where Bedmap2 grid values are much shallower than the constraint points. Due to this over-smoothing of the constraints, we have opted to create our own starting bathymetry model.

Our starting model was created from the combination of various seismic survey constraint points on the ice shelf, and bed data from BedMachine v3 (Morlighem, 2022; Morlighem et al., 2020) outside of the ice shelf. To create this, the BedMachine v3 bed elevations, relative to the WGS-84 ellipsoid, were masked within the Ross Ice Shelf, based on the MEASUREs v2 Ross Ice Shelf boundary (Mouginot et al., 2017; Rignot et al., 2013). These data were converted from gridded data into point data and merged with the various bathymetry data within the ice shelf. A continuous grid of bathymetry depths at a 5 km cell size was then interpolated from the combined data inside and outside the shelf. The interpolation can be accomplished with two gridding methods, bi-harmonic splines (Sandwell, 1987), and minimum curvature (Smith & Wessel, 1990). While the bi-harmonic spline method appears to have several advantages over minimum curvature (Chapter 3 Section 3.4.2), such as the ability to apply weights to the data, interpolating the above Ross Ice Shelf data resulted in significant unconstrained minima and maxima. Initial inversion results showed these erroneous features carry through to the final inverted bathymetry. Due to this, we have opted to interpolate the data to create the starting bathymetry model using tensioned minimum curvature. This method resulted in less extreme un-constrained minima and maxima.

To test the importance of the tension value used in the minimum curvature gridding, we performed 6 interpolations, with tension values of 0, 0.2, 0.4, 0.6, 0.8, and 1 (Figure 4.9a-f). From these six resulting bathymetry models, we calculated the standard deviation (Figure 4.9g) and the cell-specific mean (Figure 4.9h). These statistics were weighted, in the same method described in Figure 4.7d. The weight

---

<sup>3</sup>These surveys included the Ross Ice Shelf Traverse (1957-1958), the Little America Station Byrd Trail Traverse (1958), the Victoria Land Traverse (1958-1959), and the Discovery Deep Traverse (1960), see Bennett (1964) for the data and descriptions.

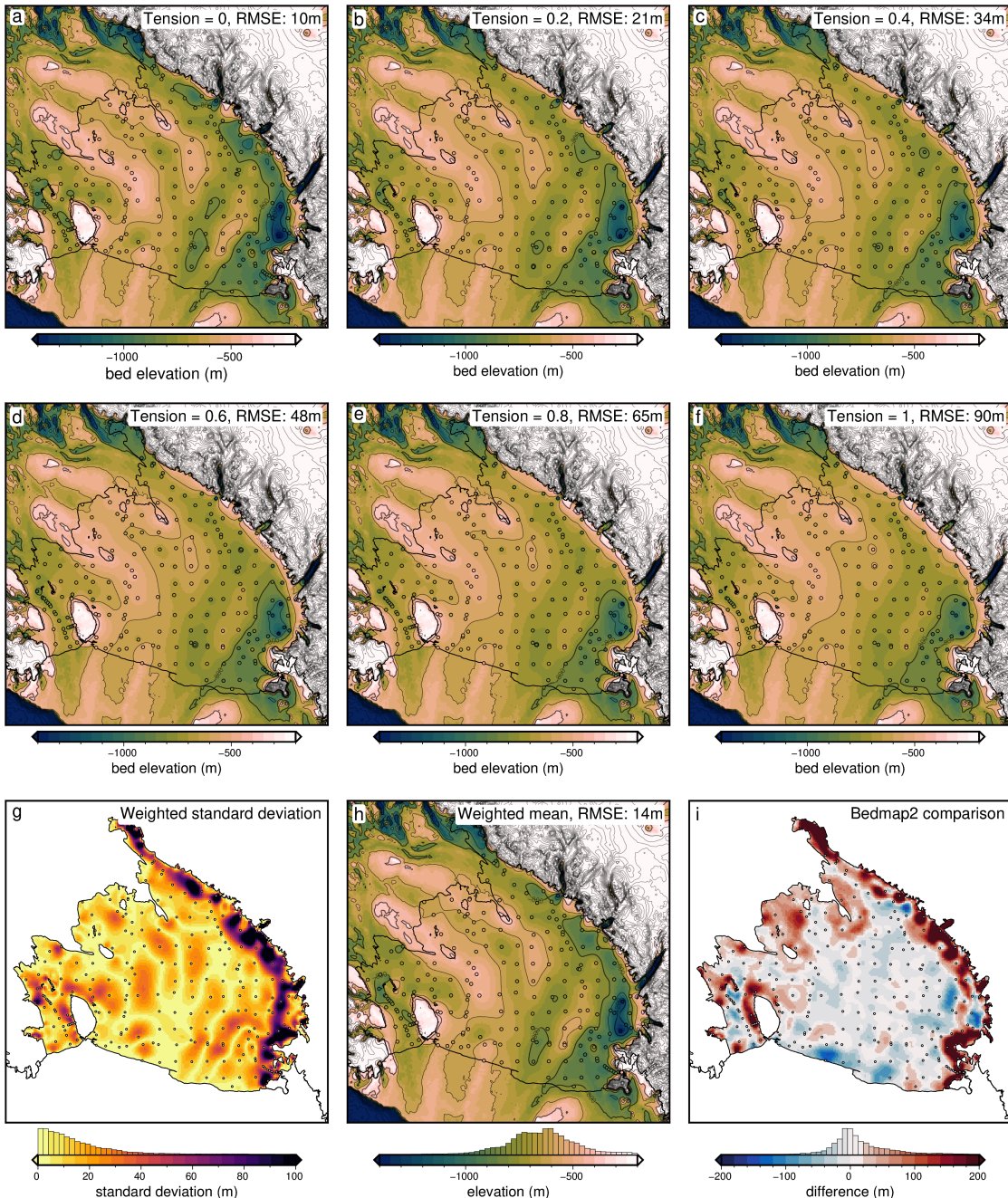


**Figure 4.9:** Starting bathymetry models from the interpolation of constraint points within the ice shelf and BedMachine v3 gridded data outside of the shelf (Morlighem, 2022; Morlighem et al., 2020). The ice shelf border, from Mouginot et al. (2017), is shown as the solid black line, representing the grounding line and the calving front. **a-f)** Bathymetry models resulting from 6 varying tension factor values of minimum curvature interpolation. Contours shown at 400 m intervals. **g)** The cell-specific weighted standard deviation of the six models (**a-f**). **h)** The cell-specific weighted mean bed elevation from the six models. **i)** The difference between Bedmap2 bathymetry and the mean model (**h**). The RMS difference is 95 m. Blues show where the mean model is shallower than Bedmap2, while reds show where the mean model is deeper. Root mean square error (RMSE) values in the plot titles are between the constraint point depths and the values at those points on the interpolated grids.

3166 value used for each grid was the inverse square of the RMS difference between  
 3167 the constraint point depth values and the resulting grid values at the same points.  
 3168 These RMS values are shown in the figure titles of Figure 4.9a-f. This weighted  
 3169 mean starting model is compared to Bedmap2 bathymetry (Figure 4.9i). Note that

3170 while low tension factors result in models that closely match the constraints, they  
 3171 also produce local maxima and minima away from the data, which is not ideal since  
 3172 these features can be seen to carry through the inversion to the final bathymetry,  
 3173 as discussed later. Alternatively, higher tension values produce models that don't  
 3174 match the constraints as well (higher RMS values), but they don't have as many  
 3175 erroneous features. For this reason, we use the cell-specific mean of the six models  
 3176 as our starting bathymetry (Figure 4.9h). This model has an RMS difference from  
 3177 BedMap2 within the ice shelf of 95 m.

3178

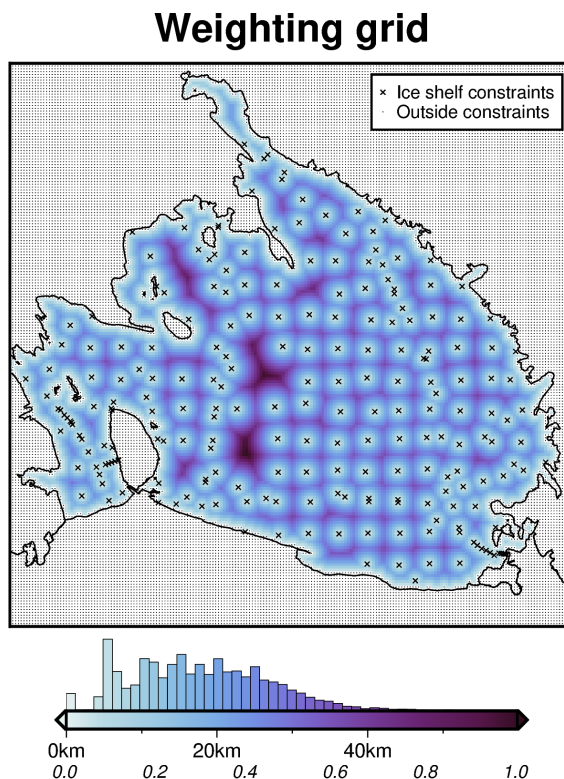


**Figure 4.10:** Weighting grid used in the Ross Ice Shelf bathymetry inversion. Grid colours show both the distance between each grid cell and the nearest constraint point and the weight values (0 - 1) from the normalization of these distances. Constraint points are defined as either direct measurements of bathymetry within the ice shelf (black crosses), or any grid cell outside of the ice shelf (small black dots). The ice shelf border, from Mouginot et al. (2017) is shown as the solid black line, representing the grounding line or the calving front.

3179 From these constraint points used to create the starting bathymetry, a weighting  
 3180 grid was created (Figure 4.10). This grid was calculated from the distance between  
 3181 each grid cell and the nearest constraint point. This minimum constraint distance  
 3182 (top annotations of Figure 4.10 colourbar) was then normalized between 0 and 1 to  
 3183 create the weighting grid (bottom annotations of Figure 4.10 colourbar). As all grid  
 3184 cells outside of the ice shelf border are considered constraint points non-zero weights  
 3185 and minimum constraint distances are confined to within the ice shelf border. The  
 3186 colourbar histogram shows a mean minimum constraint distance within the ice shelf  
 3187 of approximately 20 km, and an upper limit of approximately 60 km. Within the  
 3188 shelf, there are 223 constraint points. Over an area of  $\sim 480,000 \text{ km}^2$  (Mouginot  
 3189 et al., 2017), this equates to a constraint density of  $\sim 1$  constraint per  $46 \times 46 \text{ km}$   
 3190 ( $2154 \text{ km}^2$ ).

3191

### 4.4.2 Gravity processing results

We use airborne gravity data from the Ross Ocean and ice Shelf Environment, and Tectonic setting Through Aerogeophysical surveys and modelling project (ROSETTA-Ice). This project was created with the goal of investigating the interactions between ice, ocean, and earth of Antarctica's Ross Ice Shelf (Tinto et al., 2019). The survey consisted of 3 field seasons (2015-2017) of airborne geophysical surveying with a survey design consisting of E-W flight lines, at a nominal spacing of 10 km, and N-S tie lines with a nominal spacing of 55 km (Figure 4.1a). Flights were flown at an average of 750 m above the ice surface and a speed of 180 knots ( $93 \text{ ms}^{-1}$ ). The survey was designed to maximize the overlap between the flight lines and the past bathymetry constraints across the ice shelf from the RIGGS seismic surveys (Bentley, 1984). The data collection and initial processing were performed by Tinto et al. (2019) and are briefly summarized here. The gravity data were collected with a combination of a LaCoste and Romberg gravimeter upgraded with a ZLS UltraSys control system, an iMAR inertial measurement unit, and a DgS gravimeter. The ZLS data were tied to an absolute gravity reference station at McMurdo Station. Poor-quality data from the ZLS were replaced with the iMAR or DgS values. The accelerations of the aircraft were calculated from GPS data and removed from the gravity signal. The Eötvös correction was applied, to account for measuring gravity on a moving platform (Harlan, 1968). At each observation point, the effects of the normal earth were calculated and removed, giving the gravity disturbance values (See Section 4.2.1.1). Levelling was then performed using the cross-over values between E-W flight lines and N-S tie lines.

3215

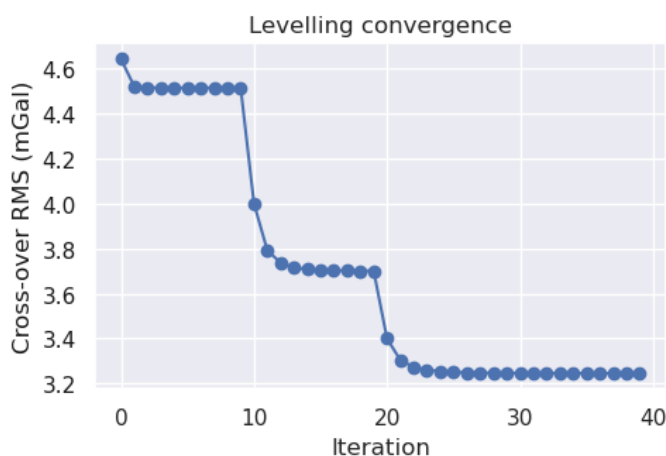


**Figure 4.11:** Re-leveling of the ROSETTA-Ice gravity data. First, flight lines were individually upward continued, then cross-over point misties were found. These were used in 0<sup>th</sup>, 1<sup>st</sup>, and 2<sup>nd</sup> order iterative levelling, alternative between levelling flight lines to tie lines and vice versa at each iteration. The RMS cross-over errors at each iteration are shown. The major steps show the 0<sup>th</sup>, 1<sup>st</sup>, and 2<sup>nd</sup> order stages of levelling.

Since this bathymetry inversion is strongly influenced by noise in the gravity data, as demonstrated in Chapter 3 Section 3.6.3.1, we have performed additional processing to the published ROSETTA-Ice dataset. Erroneous sections of flight line data were manually removed, and the dataset was re-levelled. The levelling procedure utilizes the gravity difference between E-W and N-S flight lines at cross-over points. While the flight paths intersect in 2-D space, their altitudes typically differ,

meaning there is no true cross-over point in 3-D space. To account for this, the flight lines are individually upward continued to a constant elevation of 1 km (ellipsoidal height). The mean elevation of the cleaned data was  $\sim 790$  m, and 1 km was greater than 96% of the data. This limited the amount of downward continuation while retaining a spatial resolution close to the original data. This continuation was calculated using the equivalent source technique (see Section 3.3.1.5 Dampney, 1969; Soler & Uieda, 2021). Since the cross-over points are now true 3-D intersections, the difference between E-W and N-S lines at these points (mis-ties) can be used to re-level the dataset. Here, we alternate between levelling the E-W lines to the N-S lines, and vice versa. We start with a 0<sup>th</sup> order levelling, where only DC shifts are applied. Followed by a 1<sup>st</sup> and 2<sup>nd</sup> order levelling, where 1 and 2-degree polynomials, respectively, are fit to the mis-ties, and used to level the lines. The results of this levelling procedure are shown in Figure 4.11. For each order of levelling several iterations are performed. The step-wise convergence of the RMS mis-tie values shows the 0<sup>th</sup>, 1<sup>st</sup>, and 2<sup>nd</sup> order levelling stages. The re-leveelling procedure brought the RMS mis-tie from  $\sim 4.8$  mGal to  $\sim 3.2$  mGal.

3238

Finally, this re-levelled gravity disturbance line data were gridded onto a regular grid at 2.5 km spacing, using equivalent sources. Since the inversion only affects the bathymetry within the ice shelf border, as implemented with the weighting grid (Figure 4.10), the interpolated gravity grid is masked beyond 10 km outside of the ice shelf border (Figure 4.11b). This 2.5 km gridded data ( $N = 85,914$ ) consists of both the *testing* ( $N = 64,435$ ) and *training* ( $N = 21,479$ ) sets used in the cross-validation. With the grid configuration shown in Chapter 3 Figure 3.4, the *training* data used in the actual inversion are on a regular 5 km grid.

3247

### 4.4.3 Gravity reduction results

The terrain mass effect was calculated at each of the gridded gravity data points. For this calculation, the three layers of prisms shown in Figure 4.5c-e were created from BedMachine v3 (Morlighem, 2022; Morlighem et al., 2020) ice surface and water surface data and the mean starting bathymetry from Figure 4.9h. All data are referenced to the WGS-84 ellipsoid. The ice surface elevations used from BedMachine v3 are in ice equivalent, meaning they have had a firn depth correction applied, making for a slightly lower surface elevation to account for spatially variable firn thickness (Morlighem et al., 2020). An ice equivalent surface is suitable for calculating the terrain mass effect since it gives the estimated thickness of the ice shelf with a density of ice, instead of the true ice shelf thickness, with a layer of low-density firn above. Comparing the forward gravity calculated from the true geometry of ice shelf thickness, the ice equivalent thickness, and a 2-layer model with firn and ice, show minimal differences, and thus we use the ice equivalent thickness in the terrain mass effect. The densities used in the terrain mass effect calculations were 1 kg m<sup>-3</sup> for air, 915 kg m<sup>-3</sup> for ice, 1024 kg m<sup>-3</sup> for seawater (Griggs & Bamber, 2011), and 2300 kg m<sup>-3</sup> for seafloor. Since we use a single value for the density of the seafloor, it should represent the expected average density of the seafloor over the entire region. Chapter 2 showed a continuous drape of sediment over the seafloor. We chose 2300 kg m<sup>-3</sup> to be in the middle between unconsolidated sediment ( $\sim 1900$  kg m<sup>-3</sup>) and low-density crystalline rock ( $\sim 2700$  kg m<sup>-3</sup>) (Schön, 2015). The inversion domain

3269 was 1 million km<sup>2</sup> (1000 km × 1000 km). To avoid gravitational edge effects in the  
 3270 forward calculations, the prism layers were extended in all directions by a 40 km  
 3271 buffer zone, resulting in 120,000 prisms. The resulting terrain mass effect was sub-  
 3272 tracted from the gravity disturbance to get the topo-free gravity disturbance. These  
 3273 data are shown in Figure 4.12.

3274

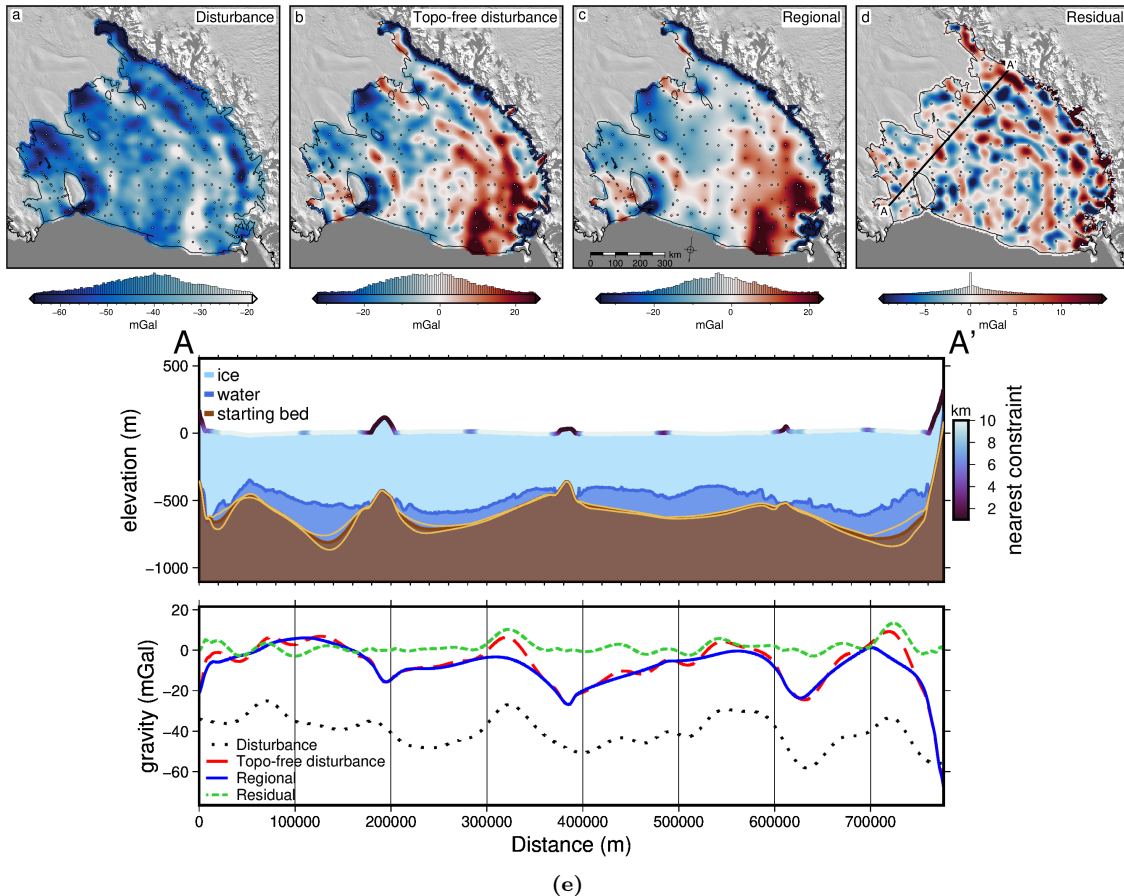


**Figure 4.12:** Gravity reduction results for the Ross Ice Shelf. **a)** Gravity disturbance, **b)** topo-free gravity disturbance, after the removal of the terrain mass effect, **c)** regional component of the topo-free disturbance, estimated with constraint point minimization, and **d)** residual component of the topo-free disturbance, as the difference between **b** and **c**. Background imagery is from MODIS-MOA (Scambos et al., 2007) and grounding line and coastlines are from (Morlighem, 2022). Constraint points within the ice shelf are shown as dots. **e)** Profile from A to A', location shown in **d**. **Upper panel** shows cross-section, with ice surface and ice base from BedMachine v3 (Morlighem, 2022; Morlighem et al., 2020). Brown layer shows the mean starting bed model with bounding uncertainty (light brown lines) from the standard deviation of the various starting bed models in Figure 4.9. The colour of ice surface shows the distance to the nearest constraint point. **Lower panel** shows data from **a-d** along the profile.

3275 The topo-free gravity disturbance was subsequently separated into the regional  
 3276 and residual components. This was accomplished with constraint point minimization  
 3277 (Chapter 3 Section 3.2.4). While the synthetic data of the past chapter showed  
 3278 a clear benefit of using a bi-harmonic spline interpolation over a minimum curvature  
 3279 interpolation, we use minimum curvature here. As with the interpolation for the  
 3280 starting bathymetry model, bi-harmonic spline interpolation led to excessive uncon-  
 3281 strained maximum or minima. The resulting regional and residual components are  
 3282 shown in Figure 4.12.

3283

### 3284 4.4.4 Inversion results

3285 With the residual component of the topo-free gravity disturbance as the inversion  
 3286 input (Figure 4.12d), we ran 10 inversions with varying levels of damping. Each in-  
 3287 version used a density of  $1024 \text{ kg m}^{-3}$  for ocean water and  $2300 \text{ kg m}^{-3}$  for the density  
 3288 of the seafloor. For each value of the damping parameter, the cross-validation score  
 3289 was calculated by forward modelling the gravity effect of the resulting bathymetry  
 3290 model onto the locations of the testing gravity data. The RMS difference between the  
 3291 residual component of the topo-free gravity disturbance and the forward-modelled  
 3292 results at these testing points gave the score. These scores are shown in Figure  
 3293 4.13a. The lowest score was achieved with a damping value of  $10^{-2}$ .

3294

3295 This inversion took 8 iterations and 135 seconds<sup>4</sup> and converged due to a lack of  
 3296 change in the  $\ell^2$ -norm between subsequent iterations (Figure 4.13b). The RMS of  
 3297 the residual gravity started at 6.1 mGal prior to the inversion and was reduced to  
 3298 4.0 mGal (Fig 4.13b).

3299

3300 The inverted bathymetry model for the sub-Ross Ice Shelf, at a 5 km resolution,  
 3301 is shown in Figure 4.13c. Note that this is just the result of a single inversion. Our  
 3302 final inverted bathymetry model is achieved through the Monte Carlo simulation, as  
 3303 described below. The RMS difference between the inversion results and the starting  
 3304 model at the constraints is 16 m. The thickness of the water column, defined as the  
 3305 difference between BedMachine v3 ice base and the inverted bathymetry, is shown  
 3306 in Figure 4.13d.

3307

### 3308 4.4.5 Uncertainty

3309 We used a series of Monte Carlo simulations (Figure 4.7) to assess both the spatial  
 3310 uncertainty of the resulting inverted bathymetry and the importance of the various  
 3311 components and parameters of the inversion. By varying the inputs of the inversion  
 3312 within their ranges of uncertainties, we can gather a range of the possible bathymetry  
 3313 results, which when compared shows where the inversion results are more or less  
 3314 certain. The inputs and their respective uncertainty distributions included in the  
 3315 sampling are:

- 3316 1. Gravity disturbance data; sampled from a normal distribution with a mean of  
 3317 the data point, and a standard deviation of the RMS mis-tie of the line data  
 3318 after levelling (3.3 mGal).
- 3319 2. Constraint point depths; sampled from a normal distribution with a mean of  
 3320 the measured depth, and a standard deviation of 10 m for points outside of  
 3321 the ice shelf, and 5% of depth from the ice surface for points within the ice  
 3322 shelf (mean of 36 m).
- 3323 3. The density of ice, water, and sediment; all sampled from normal distributions  
 3324 with means of  $915 \text{ kg m}^{-3}$ ,  $1024 \text{ kg m}^{-3}$ , and  $2300 \text{ kg m}^{-3}$  respectively, and stan-  
 3325 dard deviations of  $5 \text{ kg m}^{-3}$ ,  $5 \text{ kg m}^{-3}$ , and  $400 \text{ kg m}^{-3}$ . The small standard  
 3326 deviations of ice and water compared to sediment reflects the relative certainty

---

<sup>4</sup>See Appendix 1.6 for a description of the hardware used.

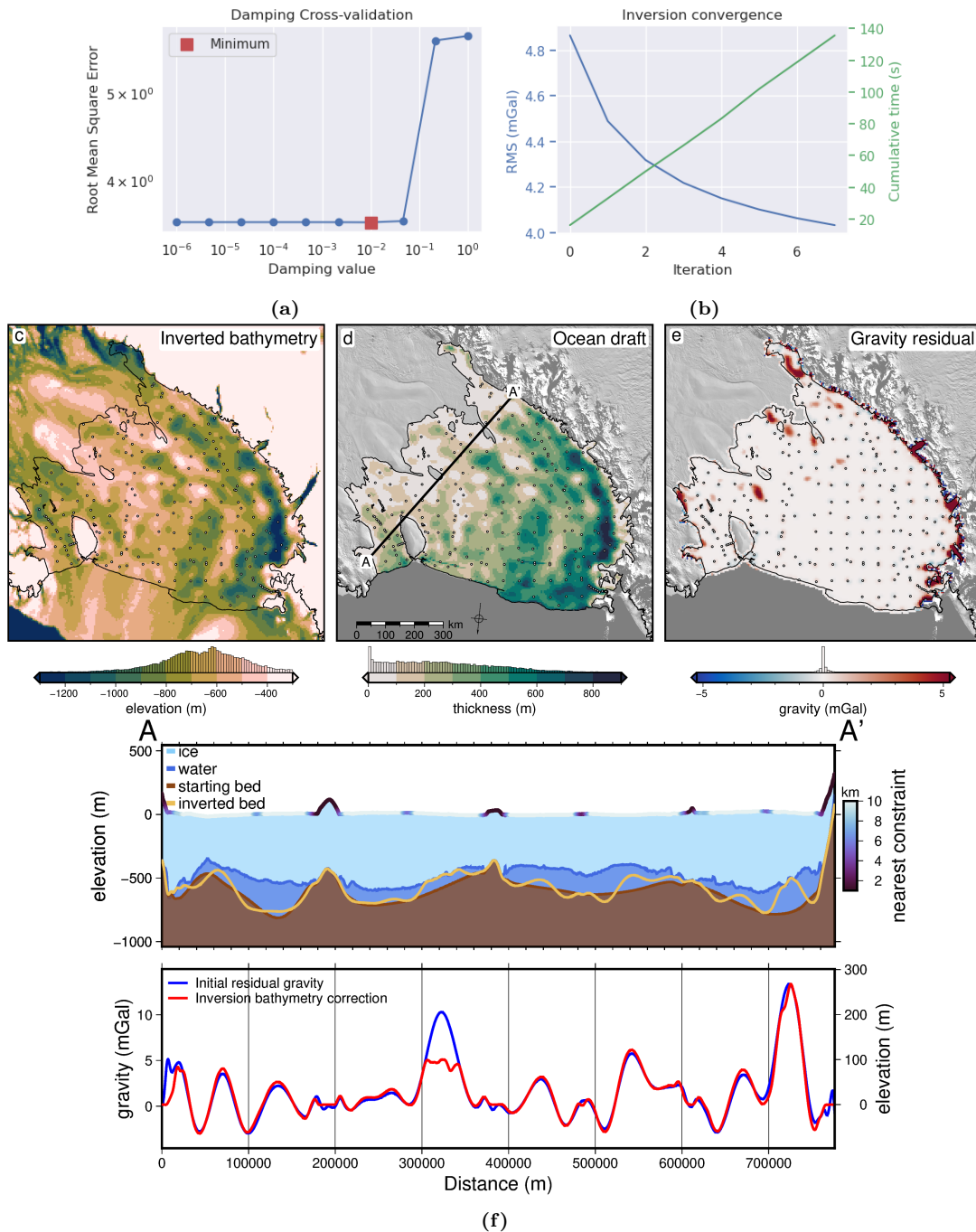


**Figure 4.13:** Ross Ice Shelf singular bathymetry inversion results. **a)** Damping parameter cross-validation with the lowest score shown in red. **b)** Convergence curve and cumulative inversion time for the optimal inversion. Blue line (left y-axis) shows consecutive iteration's RMS residual component of the topo-free gravity disturbance. Green line (right y-axis) shows cumulative time to run the inversion. **c)** Inverted bathymetry, **d)** water column thickness between the inverted bathymetry and Bedmachine v3 icebase (Morlighem, 2022; Morlighem et al., 2020), **e)** final residual component of the topo-free gravity disturbance. **f)** **Profile A to A'**. **Upper panel** shows ice surface and icebase from BedMachine v3, both the starting bathymetry (dark brown) and the inverted bathymetry (light brown). The colour of the ice surface shows the distance to the nearest constraint point. **Lower panel** shows the initial residual gravity used as input to the inversion (blue line, left y-axis), and the total correction (red line, right y-axis) applied to the starting bathymetry surface during the inversion to get the inverted bathymetry.

3329 the entire region is likely to be draped is at least 10's of meters of sediment  
 3330 (Chapter 2, Tankersley et al., 2022). With a mean of  $2300 \text{ kg m}^{-3}$  and a stan-  
 3331 dard deviation of  $400 \text{ kg m}^{-3}$ , these values span the range from unconsolidated  
 3332 sediment to low-density crystalline rock (Schön, 2015).

3333 4. The tension factor used in minimum curvature gridding for interpolating both  
 3334 the starting bathymetry model and the regional component of gravity. The  
 3335 tension factor values were sampled from a uniform distribution between 0 and  
 3336 1.

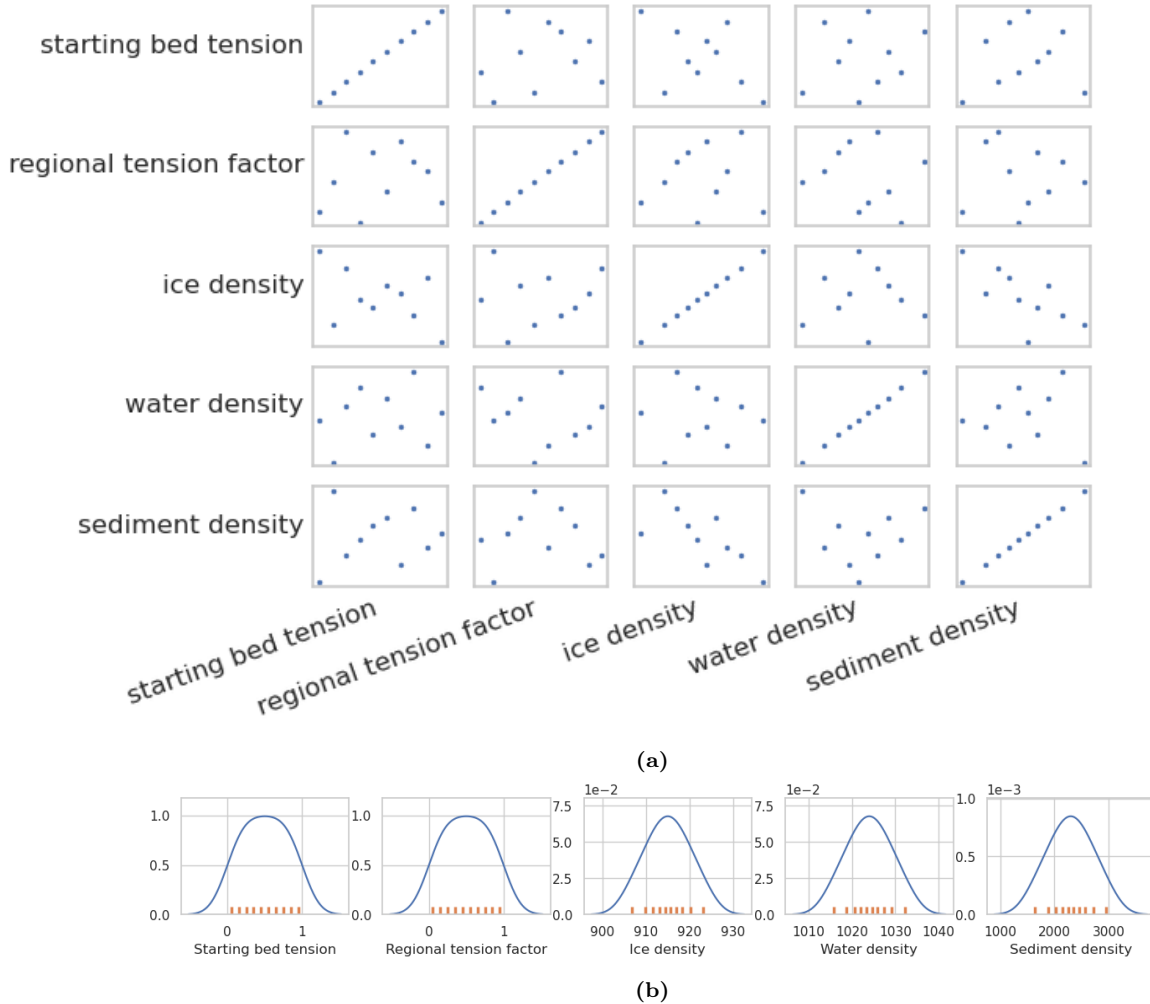


**Figure 4.14:** Latin hypercube sampling results for the 10 inversions of the full Monte Carlo simulation. **a)** Correlations between each pair of the 5 sampled input parameters. **b)** Resulting distributions of the 10 sampled values of each parameter. Blue line shows kernel density estimates fit to each set of sampled values, which are shown as orange ticks.

3337 Figure 4.14 shows the results of the Latin hypercube sampling of the 5 input  
 3338 variables (not including the gravity and constraints data). The correlations between  
 3339 each set of variables show that pairwise correlation was minimal. This is ideal since  
 3340 these inputs are unrelated, and therefore their sampled values should be uncorre-  
 3341 lated (Helton et al., 2006). This also shows that with only 10 samplings, the Latin  
 3342 hypercube sampling was able to provide adequate spatial coverage of the individual  
 3343 distributions (4.14b) as well as all the pairwise distributions combinations (4.14a).

3344 Each simulation consisted of 10 runs. We performed a *full* simulation, where  
 3345 each of the above inputs were sampled (Figure 4.15). We performed five additional

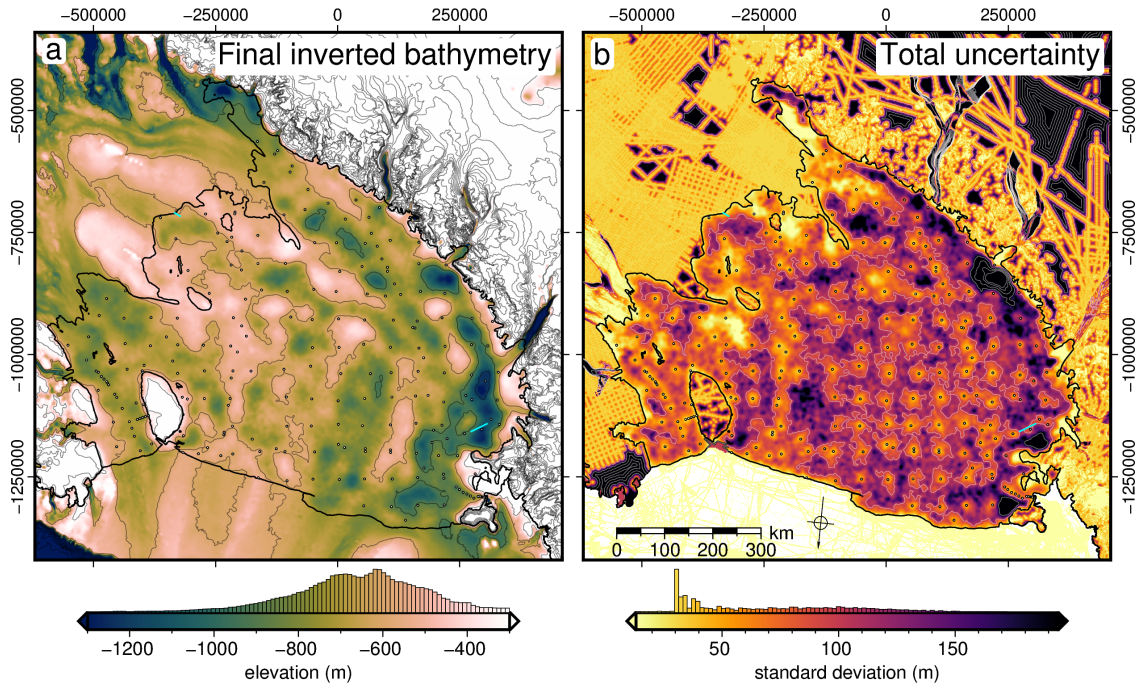


**Figure 4.15:** Final bathymetry depths and uncertainties from the full Monte Carlo simulation, merged with 500m resolution elevation and uncertainty data outside of the shelf from BedMachine v3 (Morlighem, 2022; Morlighem et al., 2020). **a)** Final inverted bathymetry model, calculated as the weighted mean of the full Monte Carlo simulation. Shown with 300 m contours. **b)** Uncertainty estimation of the inverted bathymetry from the cell-specific weighted standard deviation of the inverted bathymetry results from the full Monte Carlo simulation. Shown with 100 m contours. Constraints within the ice shelf are shown as dots in **a**. Grounding line and coastline are shown in black (Morlighem, 2022). Background imagery is from Scambos et al. (2007). Cyan lines show Discovery Deep and Kamb Ice Stream seismic surveys.

3346 simulations (Figure 4.16) where 1) only the gravity data were sampled, 2) only the  
 3347 constraint point depths were sampled, 3) only the density values of ice, water, and  
 3348 sediment were sampled, 4) only the tension factor for interpolating the starting  
 3349 bathymetry model was sampled, and finally 5) only the tension factor for interpo-  
 3350 lating the regional component of gravity was sampled. Each simulation results in a  
 3351 series of inverted bathymetries. Finding the cell-specific weighted standard deviation  
 3352 of the bathymetry depths for each of these simulations gives an estimation of the  
 3353 uncertainty resulting from the associated parameter. The cell-specific statistics of  
 3354 these simulations were low-pass filtered to remove high-frequency noise induced by  
 3355 the random sampling. For the full simulation (Figure 4.15b) the weighted mean of  
 3356 the resulting bathymetries gives the final inverted bathymetry results of this study  
 3357 (Figure 4.15a). Note that this final bathymetry model resulting from the Monte  
 3358 Carlo simulation is similar, but distinct from the inverted bathymetry resulting  
 3359 from a single inversion without the Monte Carlo simulation, shown in Figure 4.13c.  
 3360

3361 The final bathymetry and uncertainty grids were resampled to a resolution of  
 3362 500 m, from their original 5 km resolutions, masked outside of the ice shelf, and  
 3363 merged to the 500 m resolution bed and uncertainty data of BedMachine v3. This  
 3364 final bathymetry has a mean elevation of  $\sim 700$  m within the ice shelf. The deepest  
 3365 point is  $\sim -1370 \pm 187$  m, located near the Byrd Glacier outlet (Figure 4.1b).  
 3366 Bathymetric features appear to have continuity with features from BedMachine v3  
 3367 data outside of the ice shelf. The RMS difference between the bathymetry and the

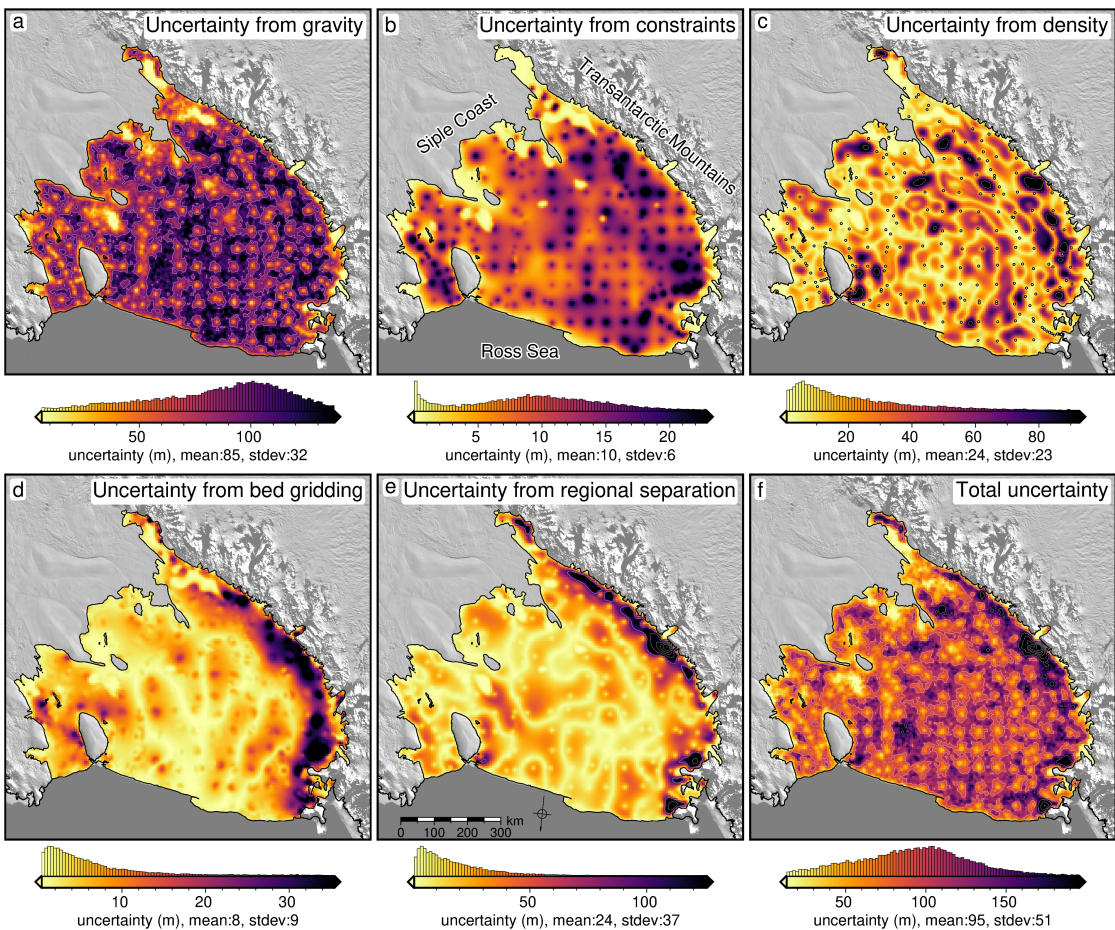


**Figure 4.16:** Sensitivity analysis for the inversion input data and parameters. Cell-specific weighted standard deviations of the inverted bathymetry results from Monte Carlo simulations with sampling the uncertainties of the **a)** gravity data, **b)** constraint points depths, **c)** ice, water, and sediment density values, **d)** starting bed interpolation tension factor, and **e)** tension factor for interpolating the regional gravity component. **f)** The total uncertainty from the full simulation. 100 m contours in white. Constraints within the ice shelf are shown as dots in **c)**. Grounding line and coastline shown in black (Morlighem, 2022). Background imagery is from Scambos et al. (2007).

original constraint point depths is 44 m. Subtracting the bathymetry from the ice base elevations of BedMachine v3 (Morlighem, 2022; Morlighem et al., 2020) gives the water column thickness, as shown in Figure 4.18b. Without ice base uncertainty estimates from BedMachine v3, we use the bathymetry uncertainty as our uncertainty for the water column thickness, acknowledging that this is a minimum uncertainty. Within the ice shelf boundary, this water column thickness has a mean value of 260 m and a maximum of 1000 m, located near the Nimrod Glacier outlet. Here, the bathymetry has an uncertainty of  $\pm 800$  m. Outside of this region, the thickest ocean cavity is  $\sim 940 \pm 180$  m, located at the Byrd Glacier outlet. The similarity between the bathymetry depth and the water column thickness shows that the ocean cavity is predominantly controlled by bathymetry and that the ice base topography is smooth compared to the bed. The uncertainty in the bed elevation ranges from  $\sim 10 - 850$  m, with a mean of 95 m (Figure 4.13b). It has an approximately normal distribution, with a slight skew to the higher values. In general, the uncertainty is lowest at the constraint points and highest far from constraints. There are elevated uncertainties in several spots, with the largest being along the Transantarctic mountain front.

3385

3386 **4.4.5.1 Partitioning uncertainty**

3387 The uncertainty in the inverted bathymetry which arises from the uncertainty in  
 3388 gravity data (Figure 4.16a) is relatively spatially uniform, with a mean of 85 m.  
 3389 It is lowest immediately at the constraint points, and generally highest far from  
 3390 constraint points. The uncertainty from the constraint point depths (Figure 4.16b)  
 3391 is also generally spatially uniform, with a mean of 10 m. Conversely, it is highest  
 3392 at the constraint points, and lowest far from constraint points. The uncertainty  
 3393 resulting from the choice of density values (Figure 4.16c) displays a more heteroge-  
 3394 neous spatial distribution than the previous two uncertainties. It is lowest at the  
 3395 constraint points and has a mean of 24 m. The largest values are located at the gaps  
 3396 between constraint points. The uncertainty resulting from the interpolation of the  
 3397 starting bed (Figure 4.16d) has a distinct spatial distribution. It is highest along  
 3398 the Transantarctic Mountain front, with values up to 40 m, but it has an overall  
 3399 mean of 7 m. Lastly, the uncertainty resulting from the estimation and removal of  
 3400 the regional component of gravity, prior to the inversion, (Figure 4.16e), also shows  
 3401 highest values along the mountain front, with values over 200 m (up to 700 m at the  
 3402 Nimrod Glacier outlet). The mean value is 24 m. The reported uncertainties and  
 3403 their components from a wide range of past studies are shown in Table 4.1.

3404

3405 **4.5 Discussion**

3406 Here we discuss the results of our Ross Ice Shelf bathymetry model from the in-  
 3407 version of airborne gravity data. First, we describe the results of the uncertainty  
 3408 and parameter sensitivity analysis. Then we compare our results with two past  
 3409 bathymetry models beneath the Ross Ice Shelf and discuss the differences. Lastly,  
 3410 we discuss various implications of this updated bathymetry model, including how  
 3411 the findings relate to geology, tectonics, and ice sheet dynamics.

3412 **4.5.1 Uncertainties and parameter importance**

3413 The results of our Monte Carlo simulations provide answers to several important  
 3414 questions. 1) How confident are we in the inverted bathymetry depths? 2) Where  
 3415 are we most and least confident about the bathymetry depth? 3) What are the  
 3416 specific sources of this uncertainty? and finally, 4) What can be done to limit the  
 3417 uncertainty? Figures 4.15b and 4.16f show the resulting spatial uncertainty of the  
 3418 inverted bathymetry, providing an answer to the first two questions. To determine  
 3419 the sources of this uncertainty, the individual inputs to the inversion were isolated  
 3420 and their effects on the estimated uncertainty were found (Figure 4.16).

3421

3422 **4.5.1.1 Gravity component**

3423 The largest contributor to the overall uncertainty of the inversion is the uncertainty  
 3424 of the gravity data (Figure 4.16a). This uncertainty resulting from the gravity data  
 3425 results in a base-level bathymetry uncertainty of  $\sim 85$  m and is relatively spatially

| Study  | Inverted bathymetry uncertainty (m) |              |              |                  |
|--|-------------------------------------|--------------|--------------|------------------|
|  | total                               | from gravity | from geology | from constraints |
| <b>This study (<math>\bar{x} \pm 1\sigma</math>)</b> | 95±51                               | 85±32        | 48±30        | 10±6             |
| Eisermann et al. (2021)                              | 220                                 | 84           | 116          | 20               |
| Tinto et al. (2015)                                  | 160                                 | 26           | 124          | 10               |
| Constantino et al. (2020)                            | 133                                 | 34           | 90           | 5-10             |
| Boghosian et al. (2015)                              | 110                                 | 10-28        | 50-70        | 10               |
| Tinto and Bell (2011)                                | 70                                  | 34           | 10-15        | 20               |
| Constantino and Tinto (2023)                         | 69-123                              | 32-39        | 27-74        | 10               |
| Tinto et al. (2019)                                  | 68                                  | 48           | 10           | 10               |
| Eisermann et al. (2020)                              | 175-225                             | -            | -            | 10               |
| Jordan et al. (2020b)                                | 100                                 | 23           | -            | -                |
| An et al. (2019a)                                    | 60                                  | 60           | -            | -                |
| Studinger et al. (2004b)                             | 250                                 | -            | -            | -                |
| Wei et al. (2020)                                    | 246                                 | -            | -            | -                |
| Greenbaum et al. (2015)                              | 190                                 | -            | -            | -                |
| Brisbourne et al. (2014)                             | 160                                 | -            | -            | -                |
| Hodgson et al. (2019)                                | 100                                 | -            | -            | -                |
| Yang et al. (2021)                                   | 68                                  | -            | -            | -                |
| An et al. (2017)                                     | 60                                  | -            | -            | -                |
| Millan et al. (2017)                                 | 50-65                               | -            | -            | -                |
| Millan et al. (2018)                                 | 30-50                               | -            | -            | -                |
| Millan et al. (2020)                                 | 45                                  | -            | -            | -                |
| Filina et al. (2008)                                 | -                                   | 19           | -            | -                |
| <b>Mean</b>  | 117 (N=25)                          | 40 (N=13)    | 57 (N=11)    | 12 (N=10)        |

**Table 4.1:** Reported inverted bathymetry uncertainties and the various components. Our reported geologic uncertainty is the combination of uncertainties resulting from the density values and the tension factor used in grinding the regional field.

uniform. This is because each gridded gravity data point is contaminated with independent noise of varying levels during the Monte Carlo sampling. It is this point-by-point random noise that creates the noisy component in the final inverted bathymetry. In reality, the uncertainty of nearby gravity data is likely correlated, where entire lines, or sections of lines have similar uncertainty values, due to changing data collection conditions, like turbulence, or mis-levelling, causing values of entire lines to be offset, or tilted. Here our estimate of gravity uncertainty is entirely dependent on cross-over misties; likely an oversimplified estimation of uncertainty for an entire survey. This suggests that the true uncertainty resulting from the gravity data likely has a different spatial distribution and may be larger than we report; a finding which is not surprising, since the entire method depends on these data.

3437

#### 3438 4.5.1.2 Constraints component

3439 The uncertainty in the other data input to the inversion, the constraint point depths,  
 3440 has only a small effect on the results (Figure 4.16b). It is worth noting that while  
 3441 the uncertainty resulting from the constraint point measurement uncertainty is low,  
 3442 the constraints themselves are fundamental to the inversion. These constraints feed  
 3443 into all the components of the inversion and thus affect the uncertainty of each  
 3444 component, including the uncertainty from the gravity data. This is shown by the  
 3445 correlation between uncertainty and the distance to the nearest constraint (Figure  
 3446 4.10) of all the components of Figure 4.16. Our Monte Carlo sensitivity analysis  
 3447 only tests the effects of estimated noise in the inputs, and not their overall impor-  
 3448 tance for the inversion. Since the uncertainty in the constraints only impacts the  
 3449 inversion in the immediate vicinity of the constraint, for constraint data collection,  
 3450 efforts should be focused on quantity over quality, assuming the uncertainty can  
 3451 be limited to a reasonable amount. In practice, for over-ice seismic surveying, this  
 3452 may lead to the choice of fast and efficient systems as opposed to high-resolution  
 3453 systems, if the main goal of the survey is to collect bathymetry constraints. For  
 3454 example, towable snow streamers and sources such as surface detonations or vibro-  
 3455 seis (e.g., Hofstede et al., 2021; Smith et al., 2020b) can collect data very efficiently  
 3456 ( $\sim 20$  km/day), compared to higher-resolution surveys with buried geophone arrays  
 3457 and drill-emplaced explosives (e.g., Horgan et al., 2013). The remaining sources of  
 3458 uncertainty are related to user-defined inversion parameters.

3459

#### 3460 4.5.1.3 Density component

3461 The choice of density values for the ice, water, and sediment results in a mean un-  
 3462 certainty in the bathymetry model of 24 m (Figure 4.16c). The ranges of densities  
 3463 tested in the Monte Carlo simulation were  $\sim 905 - 925 \text{ kg m}^{-3}$  for ice<sup>5</sup>,  $\sim 1015 -$   
 3464  $1035 \text{ kg m}^{-3}$  for seawater, and  $\sim 1600 - 3000 \text{ kg m}^{-3}$  for the seafloor. We only test  
 3465 homogeneous changes in the density values.

3466

3467 The uncertainty arising from the choice in density values has a strong spatial cor-  
 3468 relation with the absolute value of the inversion's input gravity, the residual gravity

---

<sup>5</sup>We note that the maximum density of meteoric ice is  $917 \text{ kg m}^{-3}$ , however; the inclusion of marine ice may raise this value (Fricker et al., 2001)

(Figure 4.12d). This correlation can be explained by the inverse relation between the amplitude of the corrections applied to the bathymetry during the inversion, and the density contrasts used in the inversion. For the same gravity anomaly, a smaller density contrast results in a larger amplitude correction while a larger density contrast results in a smaller correction. This means that changes in the density values just affect the amplitude of the correction applied to the bathymetry. Often, spatially variable density is used as a means to account for the regional component of gravity (e.g., Constantino et al., 2020; Tinto et al., 2019). We note that there is an additional benefit to incorporating spatially variable densities. If adequate *a priori* information is known to justify a density distribution, this can be used to allow differing amplitudes of corrections across the inversion domain. In other words, if the seafloor truly is denser in one region of the inversion compared to the seafloor elsewhere, for a similar gravity anomaly, the inversion correction should be of smaller amplitude in the high-density region. However, due to a lack of geologic knowledge beneath the ice shelf, we use constant density values. We propose Monte Carlo sampling of a wide range of possible density values as a robust and feasible method to avoid biasing the resulting bathymetry model to either too high or too low correction amplitudes, to achieve both the most realistic results and an estimation of the uncertainty.

3488

#### 3489 4.5.1.4 Interpolation component

3490 The final components of the overall uncertainty are related to interpolation con-  
3491 ducted during two stages of the inversion; 1) the interpolation of the starting model  
3492 from the sparse constraint point depths, and 2) the estimation of the regional field  
3493 from the interpolation of gravity values at the constraint points. Here, we have used  
3494 a minimum curvature gridding algorithm (Smith & Wessel, 1990), which accepts a  
3495 tension factor for the interpolation which can range from 0 to 1. Figure 4.9 shows  
3496 the results of six different values of this tension factor for creating the starting bed  
3497 model. These figures show that low values of tension are able to accurately reproduce  
3498 the data with a smooth interpolation, but can result in unconstrained local maxima  
3499 or minima. Conversely, high tension values produce smooth surfaces without false  
3500 oscillations but don't adhere to the data as well. For these issues associated with  
3501 the two end members, intermediate values of 0.25 and 0.35 are often suggested for  
3502 potential field data and topographic data, respectively. We suggest a more robust  
3503 alternative to using these suggested values is the Monte Carlo sampling approach  
3504 we have used. This runs the inversion with a variety of tension factors and uses  
3505 the standard deviation of the resulting bathymetry models as a means to estimate  
3506 the uncertainty associated with the choice of the tension factor. While tensioned  
3507 minimum curvature gridding has been used in several past inversions (e.g., An et al.,  
3508 2019a; Millan et al., 2020; Yang et al., 2021), the choice of the tension values has  
3509 not been discussed for these applications.

3510

3511 The uncertainties arising from the choice of tension factors are shown in Figure  
3512 4.16d and e. The tension factor for gridding the starting bed model results in a  
3513 relatively low uncertainty with a mean of 7 m. The resulting uncertainty for the  
3514 regional separation is comparatively high, with a mean of 24 m. Both of these re-  
3515 sults show large spatial heterogeneity, with significantly larger uncertainties along  
3516 the Transantarctic Mountain front. This is likely related to the poor performance

3517 of this gridding algorithm for high-gradient data. This region along the mountain  
3518 front has both steep topography and high amplitude gravity anomalies.

3519

#### 3520 4.5.1.5 Reducing uncertainties

3521 Of the various components of the uncertainty analysis, only some can feasibly be  
3522 reduced. Reducing the uncertainty resulting from the interpolation parameters may  
3523 be possible with future method development, but this is beyond the discussion of this  
3524 research. To our knowledge, there is no robust method of determining a spatially  
3525 variable density distribution to be used in the inversion, without the collection of in-  
3526 situ data. This leaves the data inputs, gravity and constraints, as viable components  
3527 of a bathymetry inversion where further reductions of uncertainties can occur. We  
3528 propose a favourability of quantity over quality for constraint data since typical bed  
3529 elevation uncertainty is already relatively low, and therefore more data of mediocre  
3530 quality should be prioritized over high-quality but spatially limited data. In order  
3531 to reduce the uncertainty component resulting from the gravity data, first we must  
3532 be able to estimate the realistic spatial uncertainty of the gravity data itself. A  
3533 simple cross-over analysis is too simple to cover the effects of turbulence, chang-  
3534 ing flight speed and altitude, and errors in processing steps, such as base station  
3535 ties and levelling. The areas of largest uncertainty are generally a function of 1)  
3536 distance to the nearest constraint point (Figure 4.10) and 2) proximity to steep gra-  
3537 dients of topography and/or gravity (Figure 4.16d and e). This highlights the entire  
3538 Transantarctic Mountain front of the Ross Ice Shelf and the two major constraint  
3539 gaps in the central-east portion of the ice shelf (Figure 4.10) as locations that would  
3540 greatly benefit from additional seismic surveying.

#### 3541 4.5.1.6 Past estimations of uncertainty

3542 Our comprehensive uncertainty and sensitivity analysis is shown to be similar to the  
3543 approximated uncertainties reported for other ice shelves (Table 4.1). Some differ-  
3544 ences include; our reported uncertainty resulting from the gravity data uncertainty  
3545 is the highest reported, while our values resulting from other sources, and the total  
3546 uncertainty, were similar to those of other studies. Our larger reported uncertainty  
3547 resulting from the gravity data likely shows that the simple Bouguer slab approx-  
3548 imation used by the other studies underestimates the component of uncertainty  
3549 resulting from the gravity data uncertainty. We take the uncertainties resulting  
3550 from geologic variations to be the combination of our reported uncertainties from  
3551 the chosen density values (Figure 4.16c) and from the regional separation gridding  
3552 (Figure 4.16e) since these both affect the estimation of the regional component. The  
3553 uncertainty resulting from the constraint point measurement uncertainty was very  
3554 similar across all studies.

3555

3556 From this, we propose future bathymetry inversions undertake similar uncer-  
3557 tainty analysis through the Monte Carlo sampling of the input parameters. This  
3558 technique not only provides similar uncertainty estimates to past studies, but it ac-  
3559 complishes it in a systematic and reproducible method. Additionally, this technique  
3560 provides a spatial distribution of the uncertainties, instead of a single value. Once  
3561 the inversion workflow is set up, the sampling and re-running of the inversion is a  
3562 simple procedure, and with the use of Latin hypercube sampling, we have shown

3563 that with only 10 runs, the parameter space of all the inputs is adequately sampled  
3564 (Figure 4.8).

3565

### 3566 4.5.2 Past bathymetry models

3567 Our gravity-inverted bathymetry model for the sub-Ross Ice Shelf reveals significant  
3568 differences with previous bathymetry models. However, a portion of these differences  
3569 are not related to the inversion, but to the creation of the starting model. First,  
3570 we will discuss the differences between our starting bathymetry model and another  
3571 interpolation-based bathymetry model, then we will compare our inversion results  
3572 with two past models. These past models include Bedmap2 (Fretwell et al., 2013)  
3573 and BedMachine v3 (Morlighem, 2022; Morlighem et al., 2020). The Bedmap2  
3574 model for the Ross Ice Shelf region is created from the interpolation of the same  
3575 constraint points within the ice shelf as used in this study, as well as grounded ice  
3576 thickness measurements and limited rock outcrop elevation data (Fretwell et al.,  
3577 2013; Le Brocq et al., 2010; Timmermann et al., 2010). BedMachine v3 used these  
3578 point measurements and applied additional methods to increase the resolution of  
3579 the bed. For outside of the ice shelf, this included mass conservation for areas of  
3580 fast-moving ice (outlet glaciers and ice streams), streamline diffusion for regions of  
3581 slow-moving ice, as well as minimum curvature gridding to interpolate the remaining  
3582 gaps (Morlighem et al., 2020). Within the ice shelf, BedMachine used the gravity  
3583 inversion results of Tinto et al. (2019).

3584

#### 3585 4.5.2.1 Starting model comparison

3586 Figure 4.9 shows the series of six starting bed models we created from the interpolation  
3587 of the sparse constraints. These were created with six levels of tension applied  
3588 to a minimum curvature interpolation. The cell-specific standard deviation of these  
3589 six models shows the uncertainty associated with this interpolation (Figure 4.9g),  
3590 and the mean of the six grids is our chosen starting model (Figure 4.9h). This is  
3591 compared with the Bedmap2 model in (Figure 4.9i). The RMS difference between  
3592 the two grids, within the ice shelf, is 95 m. Our starting bed is deeper proximal to  
3593 the entire grounding zone, while it is shallower along the ice front and throughout  
3594 the centre of the ice shelf. However, these differences of up to 200 m do not suggest  
3595 our starting model is inaccurate. Sampling the grid values at the constraint points  
3596 and comparing them with the constraint depths shows that our model was signif-  
3597 icantly better at adhering to these constraints, compared to Bedmap2. The RMS  
3598 of the difference with our model was 14 m, while the RMS of Bedmap2 was 138 m  
3599 (Figure 4.1).

3600

3601 These large differences for Bedmap2 are concentrated along the Transantarctic  
3602 Mountain front, where the interpolation algorithm used in Bedmap2 resulted in ex-  
3603 cessively shallow bathymetry. This interpolation appears to have favoured smooth-  
3604 ness over accuracy for this location of steep terrain. This has resulted in a "leakage"  
3605 of the high elevations within the mountains into the bathymetry interpolation, as  
3606 pointed out in this region (Le Brocq et al., 2010), as well as for other ice shelves  
3607 (Brisbourne et al., 2020). This over-smoothing and "leakage", while strongest along  
3608 the mountain front, can be seen along the entire grounding zone. This is the reason

3609 why Bedmap2 was shallower than our starting model along the grounding line. This  
 3610 shows that care needs to be taken when picking or creating a starting model for an  
 3611 inversion, especially in regions of steep topography. The re-creation of the starting  
 3612 model from the point data allows the choice of interpolation techniques better suited  
 3613 for the region of interest, compared to techniques determined most suitable for a  
 3614 continent-wide study.

3615

### 3616 4.5.2.2 Inversion result comparisons

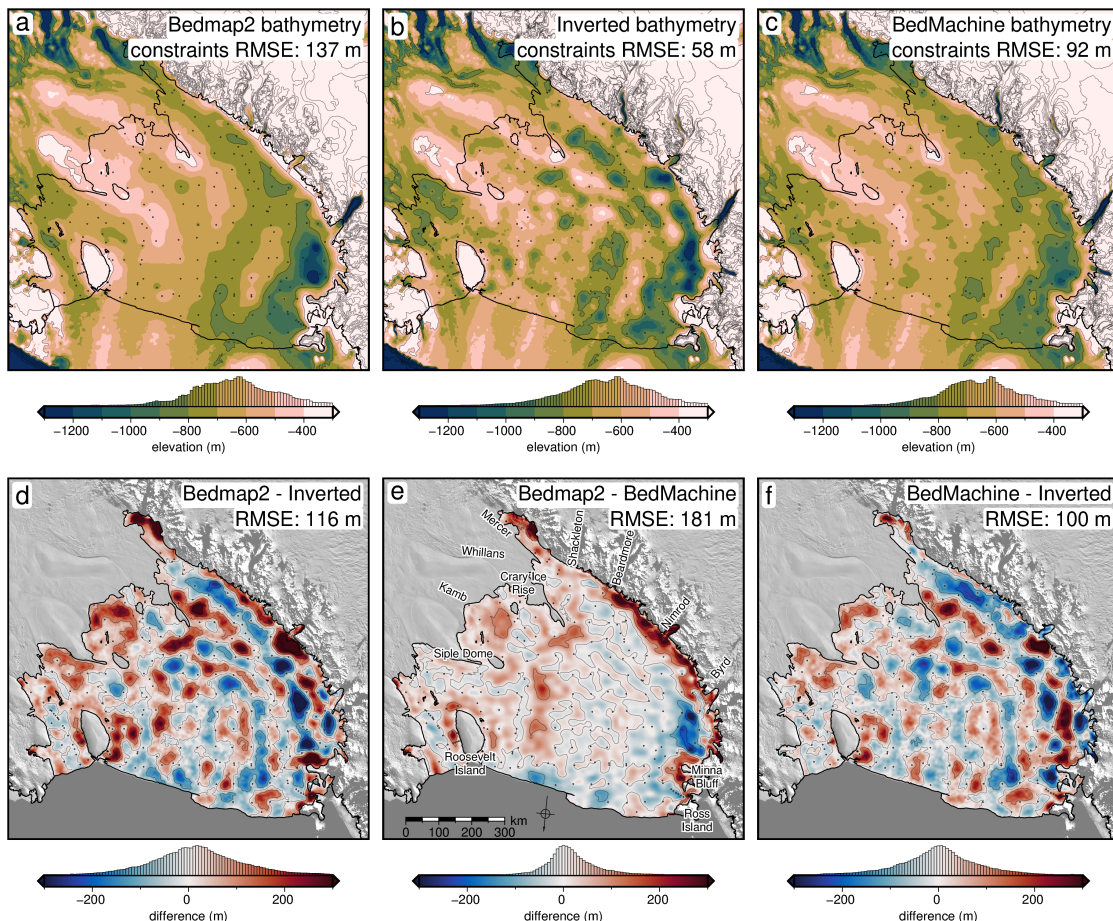


**Figure 4.17:** Comparison of our inverted bathymetry with past models. **a)** Bedmap2 bathymetry, **b)** our inversion results, from the weighted mean of the full Monte Carlo simulation, and **c)** BedMachine bathymetry. All three share the same colour scale and are contoured at 400 m intervals. RMS difference with the constraint points for each model is stated on the maps. **d)** Difference between our model and Bedmap2, **e)** difference between Bedmap2 and BedMachine v3, and **f)** difference between our model and BedMachine v3. Grids share a colour scale and are contoured at 100 m intervals. Blue regions in **d** and **f** indicate where our results are shallower, while red regions indicate where our results are deeper than the past models. Blue regions in **e** indicate where BedMachine is shallow, while red regions indicate where BedMachine is deeper than Bedmap2. RMS differences are stated on the maps. Grounding line and coastline are shown in black (Morlighem, 2022). Background imagery is from Scambos et al. (2007). Elevations are referenced to the WGS-84 ellipsoid.

### 3617 Bedmap2 comparison

3618 Figure 4.17 compares our final bathymetry results with the models of Bedmap2 and  
 3619 BedMachine v3. Additionally, several profiles across different regions are shown in

3620 Figure 4.18, comparing the various models. Interestingly, the inversion has raised  
3621 the RMS difference with Bedmap2, compared to the starting model. But due to the  
3622 issues with the Bedmap2 grid along the mountain front, this increased difference is  
3623 expected. The differences between our inverted bed and Bedmap2 have a normal  
3624 distribution (Figure 4.17d). Our results introduce many small-scale features, as ex-  
3625 pected since Bedmap2 is an inherently smooth product. However, there are several  
3626 noticeable large-scale differences with Bedmap2. Proximal to the grounding line,  
3627 our results are generally deeper, as seen with the starting model comparison (Figure  
3628 4.18g). Many of the regions where our results are deeper are related to the issue of  
3629 over-shallow interpolation of Bedmap2. Portions of the grounding zone along the  
3630 Siple Coast are over 200 m deeper, including the Kamb (Figure 4.18c) and Mercer  
3631 ice stream grounding zones.

3632  
3633 Another notable difference is an NW-SE oriented trough which appears in our  
3634 results but is essentially absent in Bedmap2. This feature begins at the southern  
3635 end of the Crary Ice Rise grounding zone and continues  $\sim$  300 km, paralleling the  
3636 mountain front (Figure 4.18c). This feature is the southwestern-most of a series of  
3637 2 or 3 parallel troughs and ridges, as shown in Figure 4.18d. These features are  
3638 oriented at a high angle to both E-W and N-S flight lines, increasing their likelihood  
3639 as true features of the bathymetry and not flight line levelling artifacts. While they  
3640 are subtle, their presence alters the general *texture* in the region from a primary  
3641 N-S / NNE-SSW to an NW-SW orientation. This switches the general trend of  
3642 bathymetry features in the region to be aligned with Siple Coast ice flow, rather  
3643 than the Transantarctic outlet glacier ice flow. Whether these bedforms are tectonic  
3644 in nature, revealing the tectonic fabric, or are erosion/depositional, and thus reveal-  
3645 ing the past flow directions of the previously grounded ice sheet is unknown. The  
3646 last major difference with Bedmap2 is a significantly deeper bathymetry along the  
3647 western edge of Roosevelt Island (Figure 4.18a).

3648

### 3649 **Bedmachine comparison**

3650 Comparing our results to Bedmachine v3 provides a unique opportunity to evaluate  
3651 the differences resulting from different gravity inversion algorithms. The gravity  
3652 inversion results of Tinto et al. (2019), which comprise the Bedmachine v3 data be-  
3653 neath the ice shelf, used similar input datasets (gravity data and constraint points),  
3654 suggesting that differing inversion algorithms and workflows are likely responsible  
3655 for the majority of the differences shown in Figure 4.17f. However, some of the  
3656 differences may arise from re-processing the gravity data, and a different method of  
3657 gravity reduction applied here, as compared in Section 4.3.

3658

3659 To remove the regional component of gravity, Tinto et al. (2019) used a smoothly  
3660 varying density model in their inversion. To create this density model, they created  
3661 an initial prism layer with prisms extending from their starting bathymetry to a  
3662 depth of 60 km. With the gravity disturbance, they performed a density inversion  
3663 to recover the density of each prism. This spatially variable density was then low-  
3664 pass filtered, with a 50 km cutoff. Incorporating this remaining long-wavelength  
3665 gravity signal within the density model removed the regional component from the  
3666 gravity input to the inversion. This technique is conceptually similar to high-pass  
3667 filtering the gravity data to remove the long-wavelength component. For the in-

3668 version, Tinto et al. (2019) used the commercial software Geosoft Oasis Montaj.  
3669 Limited information is available from Geosoft as to the specifics of this inversion  
3670 procedure.

3671

3672 Comparing our bathymetry (Figure 4.17f), there is a normal distribution of dif-  
3673 ferences, centred on zero. The RMS difference between the two grids is  $\sim$ 100 m.  
3674 Comparing each grid to the constraint point depths, the BedMachine grid has an  
3675 RMS difference of 92 m, compared to our RMS of 44 m. Generally, our results  
3676 are approximately 50-100 m deeper proximal to most of the Siple Coast ground-  
3677 ing line. Conversely, our results are approximately 50-100 m shallower along the  
3678 Transantarctic Mountain front. This could be due to our inability to fully fix the  
3679 issue of overly-shallow interpolation of data along the mountain front in the creation  
3680 of our starting model, as discussed.

3681

3682 Alternatively, the differences could be a result of the different gravity reduction  
3683 steps. Figure 4.12b and e show that correcting the gravity disturbance for the terrain  
3684 mass effect results in a large negative topo-free disturbance along the Transantarc-  
3685 tic Mountain front (dark blues in b). During the regional field estimation, fitting  
3686 a spline to these large negative values would bring down the nearby regional field,  
3687 resulting in an underestimation of the regional (more negative), and thus an over-  
3688 estimation of the residual (positive values). This is shown by the profile of Figure  
3689 4.12e. On the right side, along the mountain front, in an attempt to fit the negative  
3690 values of the topo-free disturbance (red dashed line), the regional field (blue) has  
3691 been underestimated, leaving a large positive residual anomaly (pink dashed). This  
3692 positive residual results in a shallowing of the inverted bathymetry.

3693

3694 These shallower depths along the mountain front, instead, could be revealing a  
3695 flaw in the constraint point minimization assumption of the residual being 0 at con-  
3696 straint points. While the constraint point itself doesn't contribute to the residual  
3697 signal, since the actual bed is equal to the starting bed at those points, deviations  
3698 between the actual bed and the starting bed in the vicinity of the constraints may  
3699 lead to a non-zero residual at the constraint. In this case, the interpolation of the  
3700 regional field attempts to smoothly connect extremely negative values at the moun-  
3701 tain front, and high values at the nearby constraint points. This high gradient leads  
3702 to poor interpolation. This can be seen in 4.12e where the regional (blue line) is  
3703 forced exactly equal to the topo-free disturbance (red dashed line) at the constraint  
3704 point at 700 km along the profile. In reality, the residual gravity at that constraint  
3705 is likely non-zero. A non-zero value may allow the regional field to more closely  
3706 match the large positive topo-free disturbance located at 720 km.

3707

3708 The remaining major differences between our results and BedMachine v3 in-  
3709 clude the same series of alternating NW-SE troughs and ridges as discussed above,  
3710 an  $\sim$ 100 m deeper region on the west side of Roosevelt Island, and a significantly  
3711 deeper ( $\sim$ 250 m) trough spanning from the south side of Minna Bluff to the outlet of  
3712 the Byrd Glacier. The greatest depths we model in this trough are  $\sim 1350 \pm 100$  m,  
3713 located offshore of the Byrd Glacier Outlet. Preliminary results of a seismic survey at  
3714 Discovery Deep, just south of Minna Bluff (cyan line Figure 4.15), in the 2021/2022  
3715 field season report depths up to 1450 m (pers. comm. Prof. A. Gorman). These  
3716 findings confirm the presence of depths of this magnitude. However, our deepest

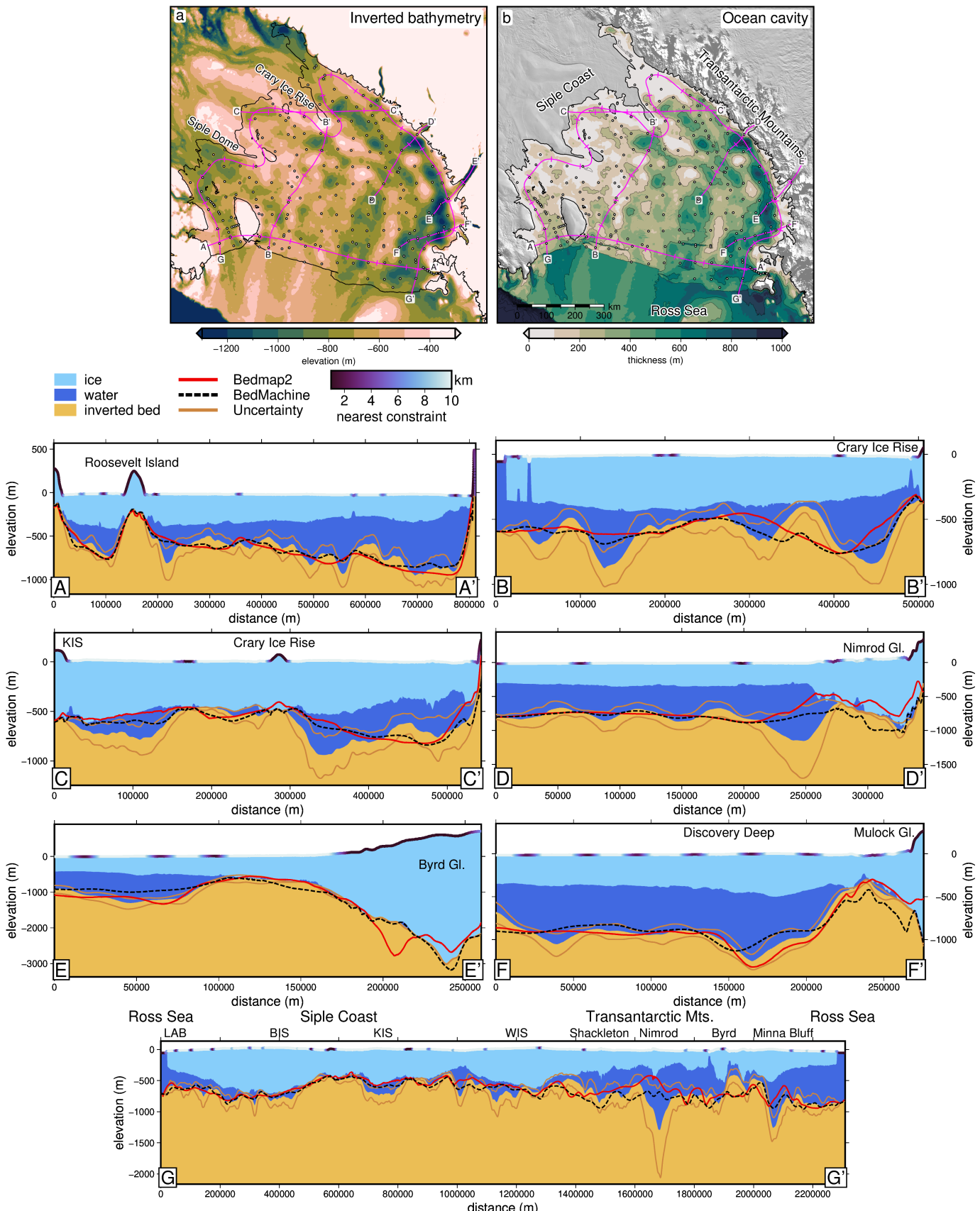


**Figure 4.18: Upper panel)** Ross Ice Shelf inverted bathymetry (left) and water column thickness (bed to ice base) relative to BedMachine v3 ice base (Morlighem, 2022). Pink lines show profile locations with ticks every ~100 km. Grounding line and coastline in black (Mouginot et al., 2017). Constraint points shown as dots. **Profiles A-G)** Various cross-sections showing the ice layer (light blue), water layer (darker blue), and bathymetry (yellow), with uncertainties (brown). Red and black lines show Bedmap2 and BedMachine v3 bathymetry, respectively. The colour of the ice surface indicates the distance to the nearest constraint. Legend and colourmap shown above profile A.

location is approximately 100 km south of the Discovery Deep survey. These seismic data were not included in this inversion. An additional comparison to a seismic survey can be made proximal to the Kamb Ice Stream grounding zone (cyan line Figure 4.15). Horgan et al. (2017) image bathymetry depths along a  $\sim$  20 km seismic survey with a mean depth of  $\sim$  605 m. Sampling our bathymetry and uncertainty along this profile yields a mean depth of  $\sim$  608  $\pm$  45 m, while sampling BedMachine v3 bathymetry and uncertainty yields a mean depth of  $\sim$  572  $\pm$  79 m.

3724

Comparing the various difference maps of Figure 4.17 shows that our inversion has resulted in more varied topography across the ice shelf compared to Tinto et al. (2019). This increased amplitude is likely due to the differences in densities used between the inversions. Tinto et al. (2019) used a spatially variable density model, which ranged from  $\sim$ 2600 - 2800 kg m $^{-3}$ , with a mean of  $\sim$ 2700 kg m $^{-3}$ . While we used a spatially-constant density value, in the Monte Carlo analysis the density was varied between  $\sim$ 1800 - 3000 kg m $^{-3}$ , with a mean of  $\sim$ 2400 kg m $^{-3}$ . This  $\sim$ 300 kg m $^{-3}$  difference between the mean density values would result in a more subdued inverted bathymetry from the (Tinto et al., 2019) model. While the Tinto et al. (2019) density model does a good job of removing the regional field prior to the inversion, whether or not the density values used are representative of the seafloor is questionable. The lowest values in their model of approximately 2600 kg m $^{-3}$  represent the upper end of sedimentary rock densities (Schön, 2015), and are significantly greater than expected densities of unconsolidated sediments. For a region with an expected continuous drape of seafloor sediments (Chapter 2, Tankersley et al., 2022), we expect the densities used in (Tinto et al., 2019) were too high. This explanation for the differences between the inversion results is supported by the strong correlation between our bathymetry uncertainty resulting from the choice in density (Figure 4.16c) and the difference between the inversion results (Figure 4.17f). This shows the importance of picking a plausible density value, and the added benefit of testing many values to estimate the uncertainty related to the chosen density value.

3746

#### 4.5.2.3 Ocean cavity comparison

Due to the smoothness of the base of an ice shelf, relative to bathymetry, the water column thickness beneath many ice shelves is predominately determined by the bathymetry. We use BedMachine v3 ice base elevations and our updated bathymetry to calculate the water column thickness beneath the Ross Ice Shelf and compare the results to the water column thicknesses of Bedmap2 and BedMachine (Figure 4.19). These differences are very similar to those described above, due to the smooth nature of the ice base. Notable areas where our results show a thicker ocean cavity (within uncertainty ranges) compared to past models include;

1. Nearby the Kamb grounding zone ( $\sim$  100  $\pm$  50 m thicker, Figure 4.18c near km 100).
2. The west side of Crary Ice Rise ( $\sim$  300  $\pm$  150 m thicker, Figure 4.18c near km 350).
3. The south side of Minna Bluff ( $\sim$  300  $\pm$  200 m thicker, Figure 4.18g near km 2100).

- 3762 4. The west side of Roosevelt Island ( $\sim 200 \pm 100$  m thicker, Figure 4.18a near  
 3763 km 220)).

3764 Notable areas where our results show a thinner cavity include;

- 3765 1. The mountain front north of Byrd Glacier ( $\sim 300 \pm 50$  m thinner, Figure 4.18g  
 3766 near km 2000)).
- 3767 2. Three 50 km wide regions in the central ice shelf, which are up to  $200 \pm 50$  m  
 3768 thinner.
- 3769 3. Several points approximately 50 km off of the Transantarctic Mountain front  
 3770 which are up to  $400 \pm 50$  m thinner (Figure 4.18c near km 450).

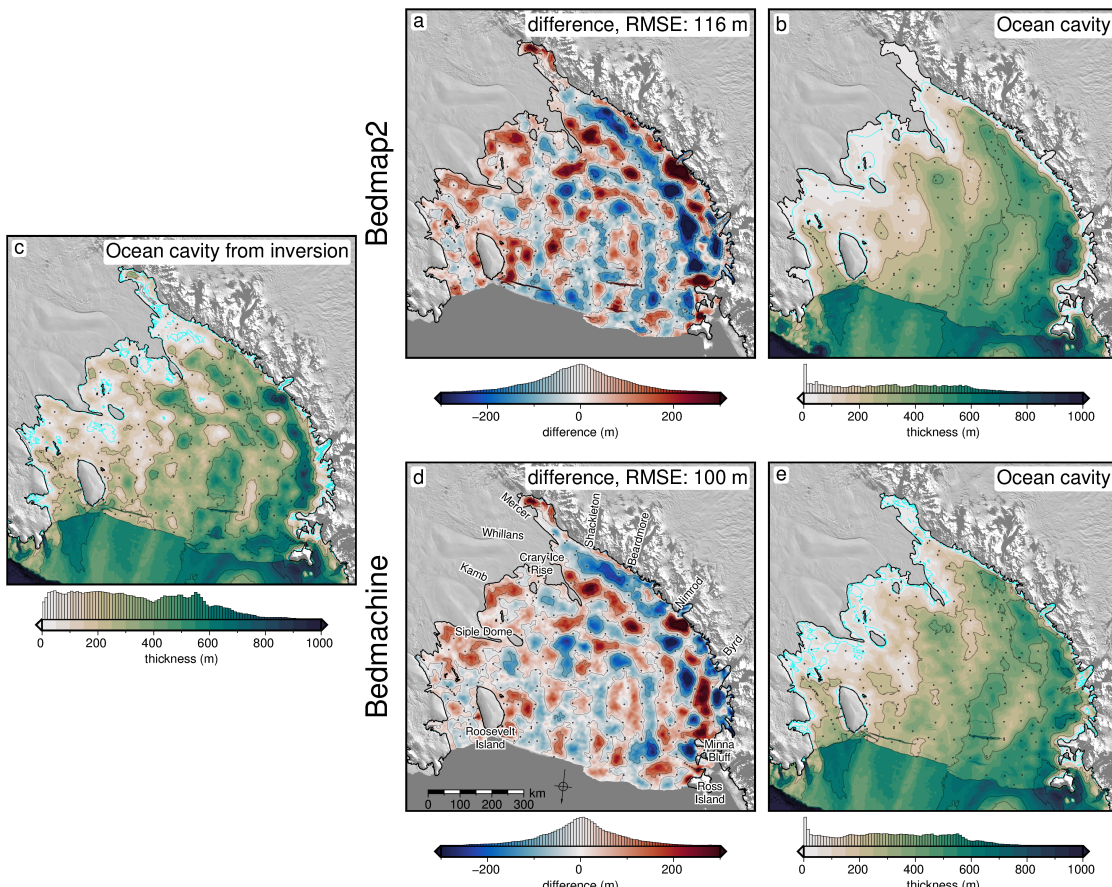


**Figure 4.19:** Comparison of our updated water column thickness with past models. **a)** Difference between our model and the water column thickness from Bedmap2, and **b)** the Bedmap2 water column thickness. **c)** Water column thickness calculated as the difference between BedMachine v3 icebase and our inverted bathymetry. **d)** Difference between our model and the water column thickness from BedMachine v3, and **e)** the BedMachine v3 water column thickness. Blue regions in the difference maps indicate where our results' water column is thinner, while red regions indicate where our results are thicker than the past models. Grounding line and coastline are shown in black (Morlighem, 2022). Background imagery is from Scambos et al. (2007). Water column thickness grids are contoured at 200 m intervals, and the 20 m contour is shown in bright blue. The difference grids are contoured at 100 m intervals. Water column thickness grids and difference grids share common colour scales.

### 3771 4.5.3 Implications

3772 Here, we discuss several of the important implications of our updated sub-RIS  
3773 bathymetry. These implications relate to the stability of the Ross Ice Shelf, ge-  
3774 ology, and tectonics.

#### 3775 4.5.3.1 New potential pinning points

3776 We have identified several areas of thin water column thickness (< 20 m) with our  
3777 updated results beneath the Ross Ice Shelf. These areas are shown by the 20 m  
3778 water column thickness contour, in bright blue in Figure 4.19a. These include a  
3779 ~100x100 km region SW of Roosevelt Island, several ~50x50 km regions on the  
3780 north flank of Crary Ice Rise (Figure 4.18g at km ~ 900), and a widespread region  
3781 south of Crary Ice Rise (Figure 4.18g at km ~ 1350). Thin water depths south of  
3782 Crary Ice Rise have also been modelled by a local gravity survey along the Whillans  
3783 Ice Stream grounding zone (Muto et al., 2013b). Additionally, two smaller regions  
3784 of sub-20 m water column thickness are found nearer the centre of the ice shelf. One  
3785 is approximately 100 km off the point of Crary Ice Rise and is ~ 400 km<sup>2</sup> (Figure  
3786 4.18c at km ~ 200). The second is ~ 200 km north of Crary Ice Rise and is slightly  
3787 smaller (Figure 4.18b at km ~ 350). None of these shallow water column regions are  
3788 present in either of the past models. Interestingly, these regions coincide with some  
3789 of the lowest uncertainties we report ~ 20 m. A portion of this low uncertainty may  
3790 be related to the inversion constraining the bathymetry to the ice base, which in  
3791 regions of thin water column will reduce the variability of the suite of inversions in  
3792 the Monte Carlo simulation which were used to define the uncertainty.

3793  
3794 These newly-identified shallow regions highlight where the Ross Ice Shelf was  
3795 likely grounded in the recent past, or could likely become re-grounded in the future.  
3796 While some of these regions are small, analysis of pinning points on the Ross Ice  
3797 Shelf has shown some of the smallest pinning points can create the largest effective  
3798 resistance on the ice shelf (Still et al., 2019). Additionally, some of these locations  
3799 (north side of Crary Ice Rise) are predicted to have on the order of 1 m/yr of basal  
3800 accretion (Adusumilli et al., 2020). An already thickening shelf within ~20 m of  
3801 the bed will likely affect the ice sheet dynamics as part of future projections of the  
3802 ice shelf. Incorporation of these localities of likely past pinning points may aid in  
3803 resolving the ongoing debate of the style of grounding line retreat and readvance of  
3804 the Ross Ice Shelf throughout the Holocene (Kingslake et al., 2018; Lowry et al.,  
3805 2019; Venturelli et al., 2020).

3806

#### 3807 4.5.3.2 Basal melting

3808 Our updated bathymetry, water column thickness, and uncertainty maps provide  
3809 additional information vital to understanding the distribution of basal melt beneath  
3810 the ice shelf. Melt beneath the Ross Ice Shelf is thought to predominantly occur  
3811 1) along the ice front, where Antarctic Surface Water causes rapid melting in the  
3812 summer (Figure 4.20 Horgan et al., 2011; Moholdt et al., 2014), and along the deep  
3813 grounding zones of the Transantarctic Mountain front, where contact with High  
3814 Salinity Shelf Water induces melting (Figure 4.20b Adusumilli et al., 2020; Tinto  
3815 et al., 2019). Throughout the centre of the ice shelf are zones of refreezing (Figure

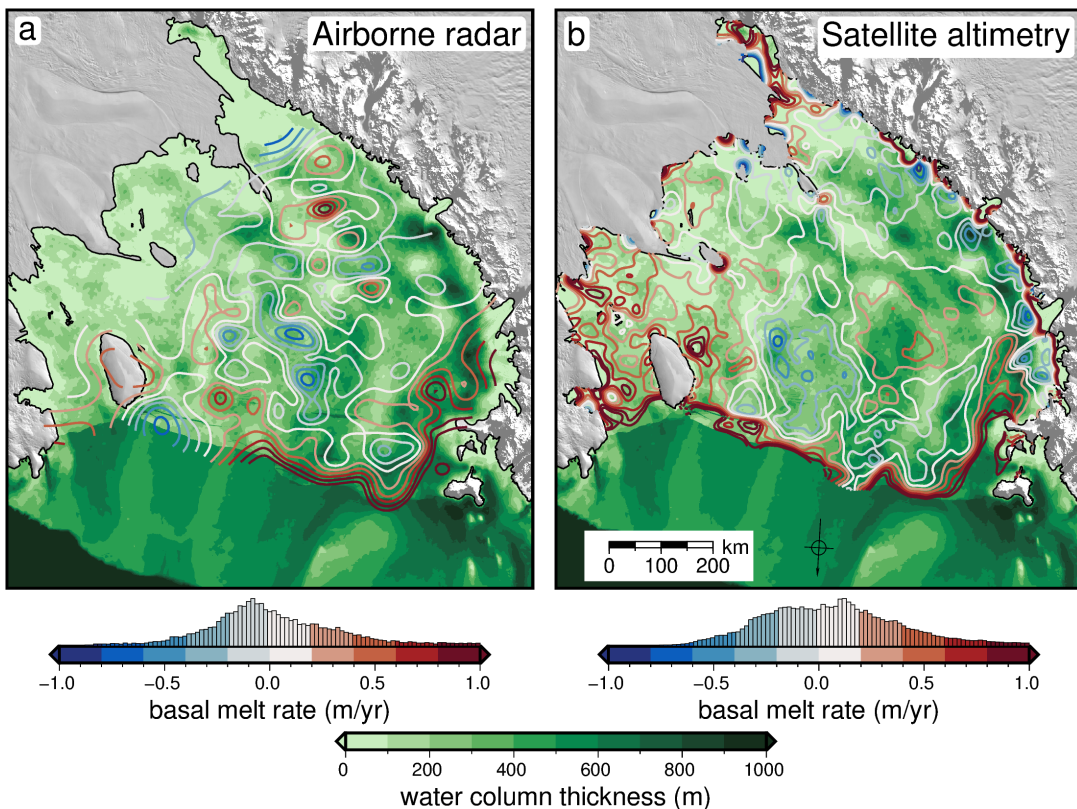


**Figure 4.20:** Basal melt rate and water column thickness compared for the Ross Ice Shelf. **a)** Blue to red contours show interpolated basal melt rate from Das et al. (2020) derived from ROSETTA-ice airborne ice-penetrating radar. Background shows water column thickness from this study. **b)** Same as **a** but with basal melt rate from Adusumilli et al. (2020) derived from satellite altimetry. Black line is the grounding line from Mouginot et al. (2017). Background imagery is from MODIS-MOA (Scambos et al., 2007).

4.20 Adusumilli et al., 2020; Das et al., 2020). Overall basal melting of the Ross Ice  
 3816 Shelf is thought to be low compared to other shelves due to the blocking of warm  
 3817 Circumpolar Deep Water from entering the cavity. This blocking is from a layer of  
 3818 dense High Salinity Shelf Water (Dinniman et al., 2011; Tinto et al., 2019). The  
 3819 Hayes Bank (Figure 4.1b) has been identified as one location where the Circumpolar  
 3820 Deep Water is able to penetrate the ice shelf cavity and induce melting, but this  
 3821 penetration is thought to be limited to the region near Roosevelt Island (Das et al.,  
 3822 2020; Tinto et al., 2019). Our ocean cavity is  $\sim 100$  m thicker than Tinto et al.  
 3823 (2019) immediately to the west of Roosevelt Island (Figures 4.18a and 4.19d). This  
 3824 region should be investigated with sub-shelf circulation models using our updated  
 3825 bathymetry. Our larger cavity allowing the inflow of warm Circumpolar Deep Water  
 3826 beyond Roosevelt Island could help explain the relatively large basal melt rate found  
 3827 in the region as shown by satellite altimetry (Figure 4.20b).

3829

3830 The high melt rates measured along the Transantarctic Mountain front (Adusumilli  
 3831 et al., 2020) are caused by the inflow of High Salinity Shelf Water (Tinto et al.,  
 3832 2019). This water is thought to be guided by bathymetric troughs and is able to  
 3833 induce melting only at large depths, due to the pressure suppression of the melting  
 3834 temperature of ice. Figures 4.20 show a comparison of both airborne radar and  
 3835 satellite altimetry-derived basal melt rates to the updated water column thickness  
 3836 resulting from our bathymetry inversion. The deeper bathymetry proximal to the

3837 Transantarctic Mountain front found in both our inversion and Tinto et al. (2019),  
3838 compared to the depths of Bedmap2, help explain the high melt rates measured  
3839 there. The other locations we report with deeper bathymetry near grounding zones,  
3840 such as the south side of Minna Bluff, and the far southern end of the ice shelf, at the  
3841 Mercer Ice Stream grounding zone, may be potential locations where High Salinity  
3842 Shelf Water is able to induce basal melt. Additionally, some of the very shallow  
3843 water column thicknesses ( $< 20$  m) we find (Figure 4.19c), for instance to the south  
3844 of Crary Ice Rise, correspond with low basal melt rates (Figure 4.20). This may  
3845 be due to the lack of stratification in the water column, which occurs due to tidal  
3846 mixing possible only in thin water columns (Holland, 2008; Muto et al., 2013b).

#### 3847 4.5.3.3 Geologic and tectonic significance

3848 While there are many interesting implications to explore in this new dataset, we  
3849 limit our discussion to several sub-Ross Ice Shelf bathymetric features of possible  
3850 importance to solid-Earth investigations. These features include the bathymetry  
3851 along the Transantarctic Mountain front, a deep feature on the southwest flank of  
3852 Crary Ice Rise, and a newly identified orientation of bathymetry features, aligned  
3853 with the Siple Coast ice streams.

#### 3854 Transantarctic Mountain front

3855 The Transantarctic Mountains (Figure 4.1a) make up the world's largest rift shoul-  
3856 der. Despite their prominence, the uplift mechanisms are still debated (Goodge,  
3857 2020). It is likely that these mechanisms vary along-strike, and consist of some com-  
3858 bination of thermal, flexural, or isostatic support (Goodge, 2020). For the central  
3859 TAM, a mechanism of cantilevered flexure is proposed for the uplift of the moun-  
3860 tains (Wannamaker et al., 2017; Yamasaki et al., 2008). This theoretically should  
3861 be accompanied by a deep trough parallel just offshore the range front, and an  
3862 outer bathymetric high, approximately 200 km from the range front (Stern & ten  
3863 Brink, 1989). These features have not yet been observed (ten Brink et al., 1993;  
3864 Wannamaker et al., 2017). Our results show a deep trough along the range front  
3865 between the Nimrod Glacier and Minna Bluff, with bathymetry highs further off-  
3866 shore. These features may support the theory of flexural uplift along this portion of  
3867 the TAM (Wannamaker et al., 2017). Further south, where the trough disappears,  
3868 the mechanism of flexural uplift is not required, since the mountains have a crustal  
3869 root, which likely provides the uplift mechanism, via Airy isostasy (Block et al.,  
3870 2009; Wannamaker et al., 2017).

#### 3871 Fault bound Crary Ice Rise

3872 Figure 4.18c shows a profile of the updated bathymetry model across the Crary Ice  
3873 Rise. Our results show a steep drop off the south flank of the ice rise (at km  $\sim 320$ ),  
3874 to depths up to  $\sim 1000 \pm 200$  m. This steep drop-off is aligned with an NW-SE fault  
3875 proposed by Muto et al. (2013b) from a local gravity survey along the Whillan Ice  
3876 Stream grounding zone. Depth to basement analysis from magnetic data (Chapter  
3877 2, Tankersley et al., 2022) also highlights this north flank of Crary Ice Rise as a  
3878 likely location for faults. We believe this steep bathymetry feature adds evidence to  
3879 the proposition of the Crary Ice Rise as a fault-bound horst (Muto et al., 2013b).  
3880 This would imply the current grounding of the Ross Ice Shelf along the Crary Ice  
3881 Rise is in part controlled by regional tectonics.

**3882 New bathymetric trend**

3883 From the gridding of point data, the bathymetry of the central Ross Ice Shelf is  
3884 dominated by an N-S - NNE-SSW trend, aligned with the flow directions of the outlet  
3885 glaciers of the Transantarctic Mountains (Figure 4.1). Our updated bathymetry  
3886 model (Figure 4.15a) adds an overprinted NW-SE trend to the bathymetry features  
3887 of the central portion of the ice shelf. This trend is prevalent, but subtle, in the  
3888 inversion of Tinto et al. (2019). The features comprising this trend are a series of  
3889 2-3 ridges and troughs of  $\sim 100$  m amplitudes and  $\sim 50$  km wavelengths, as shown  
3890 in Figure 4.18d. These features are oblique to flight lines, adding to their validity,  
3891 and are well-aligned with the Crary Ice Rise and the general ice flow direction of the  
3892 Siple Coast ice streams. This trend could signify several things; 1) the most recently  
3893 grounded ice in this region had a flow direction aligned with the Siple Coast ice  
3894 streams, leaving behind erosional or depositional features with these orientations, 2)  
3895 these features are tectonic in origin, and are the surface expressions of rift structures.  
3896 These structures overprint the large bathymetric depression which runs from the  
3897 Nimrod glacier to the calving front. If these are features left behind from the most  
3898 recent grounding line retreat, they might inform the style of retreat. As seen in the  
3899 Ross Sea, physiography of the sea floor exerts the primary control on ice stream flow  
3900 and the patterns of retreat (Halberstadt et al., 2016).

**3901 4.6 Conclusion**

3902 Here we present an updated model of bathymetry depths beneath Antarctica's Ross  
3903 Ice Shelf, as modelled from airborne gravity data. Our inversion algorithm provides  
3904 a comprehensive spatial uncertainty analysis and parameter sensitivity estimation.  
3905 This uncertainty highlights regions of high uncertainty that would benefit from additional  
3906 seismic constraints. These regions include the entire Transantarctic Mountain  
3907 front and two points near the centre of the shelf which are up to 40 km from the  
3908 nearest constraints. We summarize some key findings from the research below;

- 3909 1. Monte Carlo sampling is a robust method of uncertainty quantification and  
3910 parameter sensitivity analysis for bathymetric gravity inversions.
- 3911 2. Sensitivity analysis shows that gravity data are the largest contributor to  
3912 bathymetry uncertainty, followed by assumptions of the geology of the region.
- 3913 3. Our updated bathymetry model better matches *a priori* sub-ice shelf measurements  
3914 compared to past models.
- 3915 4. Compared to Bedmap2, our results are deeper proximal to the grounding line  
3916 and shallower along the ice front.
- 3917 5. Differences with the inversion of Tinto et al. (2019) (BedMachine v3) are  
3918 mostly due to different chosen density contrasts.
- 3919 6. Newly identified potential past pinning points are found along the Siple Coast  
3920 and in the central Ross Ice Shelf.
- 3921 7. Thick ocean cavity is found along the west flank of Roosevelt Island, where  
3922 Circumpolar Deep Water flows under the shelf and may highlight a region of  
3923 importance for ocean circulation modelling.

- 3924     8. Possible tectonic implications including a fault-bound Crary Ice Rise and a  
3925       flexural trough associated with Transantarctic Mountain uplift.

3926     Our results provide the datasets necessary to begin answering key questions re-  
3927       garding the role of the Ross Ice Shelf in various components of the Earth system.  
3928     These questions include: 1) where are melt-inducing bodies of water guided beneath  
3929       the ice shelf? 2) where was the ice shelf grounded in the recent past, and what was  
3930       the geometry of Holocene grounding line retreat and re-advance? Are the modern  
3931       bathymetry features remnants of the last grounding line retreat, or are they tec-  
3932       tonic in origin? While we don't provide direct answers to these questions, without  
3933       adequate knowledge of the sea floor morphology and the associated uncertainties, in-  
3934       vestigators won't have the relevant boundary conditions to answer these questions.  
3935     All of the research conducted here is published as open-source Python code (see  
3936       Chapter 1 Section 1.6), with hopes that the methods presented here can be used by  
3937       researchers to better model the bathymetry and uncertainty of other Antarctic ice  
3938       shelves.



<sup>3939</sup> Chapter 5

<sup>3940</sup> Synthesis

<sup>3941</sup> Improving decadal to centennial projections of global sea level rise is of utmost im-  
<sup>3942</sup> portance for mitigating future environment and socio-economic impacts (Durand  
<sup>3943</sup> et al., 2022). Antarctica's projected contributions to global sea level rise by the  
<sup>3944</sup> end of the century under a high-emission scenario is between 0.03 and 0.28 m (RCP  
<sup>3945</sup> 8.5, Intergovernmental Panel on Climate Change (IPCC), 2022). This wide range  
<sup>3946</sup> of possible values expresses the uncertainty of the Antarctic Ice Sheet's response to  
<sup>3947</sup> a warming world. Over 80% of ice loss from Antarctica occurs through ice shelves  
<sup>3948</sup> (Rignot et al., 2013), highlighting their importance in reducing the uncertainty in  
<sup>3949</sup> sea level rise projections. Antarctica's largest ice shelf, the Ross Ice Shelf, is fed  
<sup>3950</sup> from both the East and West Antarctic Ice Sheets. Its catchment contains a total  
<sup>3951</sup> volume of ice equivalent to 11.6 m of global sea level rise (Fretwell et al., 2013;  
<sup>3952</sup> Rignot et al., 2011; Tinto et al., 2019). While the Ross Ice Shelf is relatively stable  
<sup>3953</sup> currently (Moholdt et al., 2014; Rignot et al., 2013), geologic evidence shows the  
<sup>3954</sup> rapid destabilization of the ice shelf within the past ~7,000 years (e.g., Naish et al.,  
<sup>3955</sup> 2009; Venturelli et al., 2020).

<sup>3956</sup>  
<sup>3957</sup> The destabilization of the ice shelf is thought to have been primarily caused  
<sup>3958</sup> by ocean forcings (Lowry et al., 2019), as bathymetric troughs guide the inflow of  
<sup>3959</sup> melt-inducing ocean circulations (Tinto et al., 2019). The subsequent grounding  
<sup>3960</sup> line retreat however is predominantly controlled by the physiography, geology, and  
<sup>3961</sup> glaciological feedbacks (Halberstadt et al., 2016). This highlights the solid earth,  
<sup>3962</sup> through its bathymetric control on basal melt and its effects on grounding line re-  
<sup>3963</sup> treat dynamics, as an important component of the dynamics of the Ross Ice Shelf.  
<sup>3964</sup> To reliably understand the contribution of the Ross Ice Shelf to future sea level rise,  
<sup>3965</sup> we must provide ocean and ice modellers with the necessary geologic boundary con-  
<sup>3966</sup> ditions. This thesis aimed to provide both these boundary conditions and estimates  
<sup>3967</sup> of their uncertainties to the modelling community. A series of research questions  
<sup>3968</sup> were proposed, as restated below.

- <sup>3969</sup> 1. What is the geologic structure of the upper crust beneath the Ross Ice Shelf?  
<sup>3970</sup> If there are sediments, what is their thickness and distribution? Where are  
<sup>3971</sup> the major faults likely located?
- <sup>3972</sup> 2. How can bathymetry beneath an ice shelf best be modelled? Are there further  
<sup>3973</sup> improvements that can be made to the gravity-inversion process? What are  
<sup>3974</sup> the predominant sources of uncertainty, and how can these be limited?

- 3975     3. How deep is the bathymetry beneath the Ross Ice Shelf and where are we most  
3976       and least certain about it?

3977     4. What are the geologic controls on the Ross Ice Shelf's stability?

3978 Here we draw from the various research chapters to provide answers to these  
3979 questions.

## 3980 5.1 Investigating geologic structures

### **3981 Research question 1**

To address research question 1 we sought to model the depth of the crystalline basement rock beneath the ice shelf. We accomplished this with a depth-to-magnetic source technique, which used airborne magnetic data and was calibrated to seismically imaged basement depths of the Ross Sea. Our resulting basement topography revealed large-scale, fault-controlled extensional basins throughout the sub-Ross Ice Shelf crust (Figure 5.1f). Above this basement sits various sediments, likely ranging from coherent sedimentary rock to unconsolidated recent glacial and marine deposits. While there is a continuous drape of sediments across the entire ice shelf, we also image several distinct depocenters; the Western Ross Basin, covering the East Antarctic half of the ice shelf, and several basins on the West Antarctic side, including the Siple Dome Basin and the Crary Trough (Figure 5.1f). These results were incorporated into an Antarctic-wide review of sedimentary basins (Figure 5.1a Aitken et al., 2023b), showing the widespread distribution of similar basins across much of Antarctica. From our findings, we were able to draw a wide range of implications, ranging from tectonic influence on ice dynamics along the Siple Coast to the buried and subsided remnants of an above-sea-level Oligocene mountain range, which likely accommodated alpine glaciers. These results provided the first view of the upper crust beneath the entirety of the Ross Ice Shelf.

## 5.2 Developing a gravity inversion

#### 4002 Research question 2

4003 To provide modellers with accurate bathymetry depths beneath the Ross Ice Shelf,  
4004 we utilized a gravity inversion technique. While there is an existing gravity-inverted  
4005 bathymetry model for the Ross Ice Shelf (Tinto et al., 2019), the reported uncertain-  
4006 ties were spatially uniform. To provide spatial uncertainties, we chose to develop  
4007 a new gravity inversion algorithm. In addition, since the majority of gravity inves-  
4008 tions use proprietary and expensive software, in an effort towards open-source and  
4009 reproducible science, we chose to develop our gravity inversion using Python and  
4010 release the code in an online repository.

Chapter 3 described this algorithm in detail. Extensive testing of various synthetic and semi-realistic datasets revealed several intricacies of performing a gravity inversion to attain a bathymetry model. The estimation and removal of the regional component of gravity, which occurs in the data reduction steps before the inversion, accounts for the majority of the error in the model. There are various techniques to

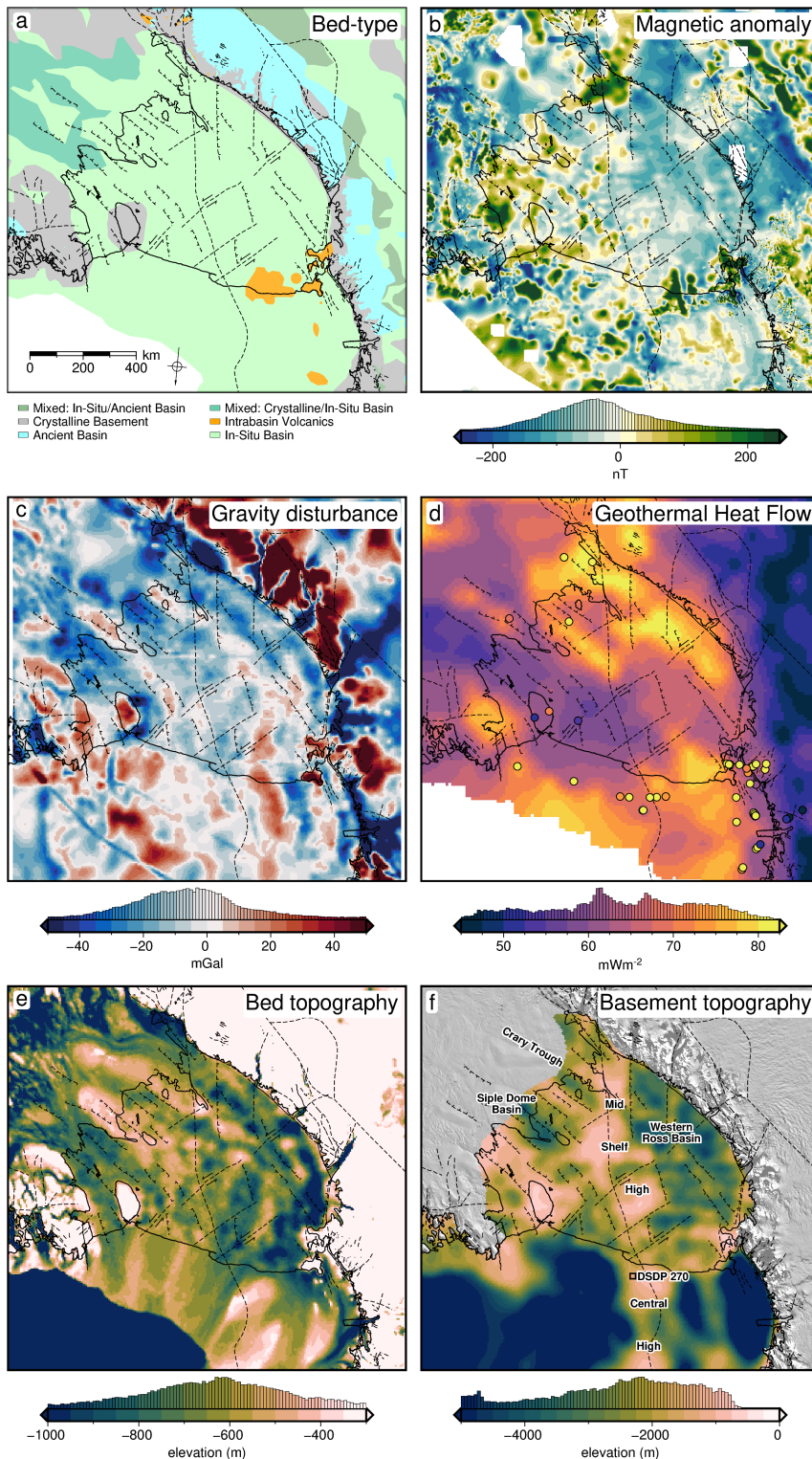


**Figure 5.1:** Summary of southern Ross Embayment geophysical and geologic information. **a)** Generalized geologic classification of the bed from Aitken et al. (2023a), **b)** ROSETTA-Ice airborne magnetic anomalies (Tinto et al., 2019) merged with ADMAP2 magnetic anomaly compilation (Golynsky et al., 2018), **c)** Gravity disturbance compilation from Forsberg (2020), include ROSETTA-Ice data. **d)** Geothermal heat flux from a seismically-derived model (Shen et al., 2020), and point measurements compiled from Burton-Johnson et al. (2020). **e)** Inverted bathymetry from Chapter 4, **f)** Basement topography from Chapter 2. Solid black line shows the grounding line and ice front from Mouginot et al. (2017). Fainter black lines show inferred (dashed) and exposed (solid) faults from a combination of Chapter 2 and Cox et al. (2023). Background imagery in **f** from MODIS-MOA (Scambos et al., 2007).

remove the regional field. We explore several of these methods and provide recommendations to best reduce the errors. Our uncertainty analysis highlighted regions of either steep topography or high gradient gravity anomalies as key regions where additional bathymetry measurements will make a significant contribution to reducing uncertainties. These suggestions of where to collect additional data should be considered alongside key regions of investigation identified through ocean modelling. Our findings suggest the quantity of bathymetry measurements is more important for reducing inversion uncertainty than the quality of these measurements. Conversely, we show larger sensitivity of the inversion results to the noise in the gravity data, relative to the density of gravity data collected. This suggests optimizing quantity over quality for bathymetry constraints while optimizing quality over quantity for gravity observation data. We hope these suggestions are able to better inform future Antarctic data collection for the goal of improving sub-ice shelf bathymetry models.

4030

As part of Chapter 4, we compared our methods, of both the gravity reduction process and the inversion procedure, to all past bathymetry models conducted in Antarctica, as well as several from Greenland. Several other inversions have used a regional separation method similar to ours; however, none of these have provided an assessment of the associated uncertainties related to this method, which we found to be significant. We also found that all other inversions utilized a non-rigorous method of correcting the gravity data for the effects of ice, water, and topography. While the error introduced is likely small, with modern computing, applying this correction correctly is trivial.

4040

From the other studies, excluding those with undocumented inversion algorithms, we found only one study which used a conventional regularized least-squares approach, similar to ours. Comparing our uncertainty analysis to past inversions revealed only two studies that report spatially variable uncertainties of their bathymetry model. It is our hope that the improvements made for the gravity inversion process are incorporated in future inversions in order to attain better estimates of uncertainties.

4048

## 5.3 Modelling Ross Ice Shelf Bathymetry

### Research question 3

With the gravity inversion methodology laid out in Chapter 3, we created a new model of sub-Ross Ice Shelf bathymetry (Figure 5.1e). This model highlighted some important differences from past bathymetry models. In general, our model has more varied topography, compared to the smooth Bedmap2 model, and the intermediate BedMachine model. Compared to Bedmap2, we report significantly deeper bathymetry proximal to the entire grounding zone, including notably deeper areas near the Kamb Ice Stream, along the west side of Roosevelt Island, and south of Minna Bluff. Compared to the past inverted bathymetry (Tinto et al., 2019), our results are deeper along the Siple Coast but vary between deeper and shallower along the Transantarctic Mountain front. Our uncertainty analysis identified gravity data quality as the largest component of the overall uncertainty, while the distance from the nearest constraint and interpolation parameter values contributed significantly

4063 to the spatial variability of the uncertainty. From this, the largest uncertainties were  
4064 found either far from constraints, or along the steep topography of the Transantarctic  
4065 Mountains. This highlighted several locations where future seismic surveys would  
4066 be able to effectively reduce uncertainties.

## 4067 5.4 Geologic controls on Ross Ice Shelf Stability

### 4068 Research question 4

4069 Next, we synthesize our findings which relate to the geologic influence on the Ross  
4070 Ice Shelf, in an attempt to answer research question 4. We start with the controls  
4071 on the ice shelf as it is today, before speculating on what these geologic controls  
4072 were in the past or will be in the future.

#### 4073 5.4.1 Present controls

##### 4074 5.4.1.1 Basal melt

4075 Basal mass loss of the Ross Ice Shelf is dominated at the deep grounding zones,  
4076 where relatively cool High Salinity Shelf Water is able to induce melting due to the  
4077 high pressure at depth (Adusumilli et al., 2020; Tinto et al., 2019). These inflows of  
4078 cold and dense water occur along the seafloor and are guided south beneath the ice  
4079 shelf by bathymetric features (Holland, 2008). Tinto et al. (2019) model the domi-  
4080 nant inflow of High Salinity Shelf Water starting near Ross Island, flowing south  
4081 along the mountain front, where at the southern flank of Crary Ice Rise the flow  
4082 turns north and flows back to the ice front through the centre of the ice shelf. This  
4083 inflow is responsible for much of the basal melting of the Ross Ice Shelf (Adusumilli  
4084 et al., 2020; Tinto et al., 2019). Our bathymetry model (Figure 5.1e) confirms the  
4085 presence of a deep trough ranging from the western ice front along the Transantarctic  
4086 Mountain front which accommodates this High Salinity Shelf Water inflow. Our  
4087 mountain front trough, however, is both narrower and deeper than past models. At  
4088 the Nimrod Glacier outlet our trough steps to the east by ~ 100 km, and eventually  
4089 ends along the south flank of Crary Ice Rise.

4090  
4091 This eastward step is likely important for two reasons. 1) South of Nimrod  
4092 Glacier, we model a shallow bathymetric shelf proximal to the grounding line. This  
4093 likely blocks grounding line access to southward flowing High Salinity Shelf Water,  
4094 limiting basal melt for the southernmost outlet glaciers. 2) The eastward step likely  
4095 re-directs southward flowing High Salinity Shelf Water closer to the Siple Coast  
4096 grounding zone, particularly the south flank of Crary Ice Rise. In this region, past  
4097 bathymetry models show a continuous bathymetric ridge for ~ 300 km off the edge  
4098 of Crary Ice Rise which blocks the inflow of High Salinity Shelf Water to the Siple  
4099 Coast north of Crary Ice Rise (Tinto et al., 2019). Our results however show this  
4100 ridge being dissected by two low saddles. If included in ocean circulation models,  
4101 the lack of a continuous ridge and the presence of these low saddles may allow the  
4102 inflow of circulations to the Siple Coast; a scenario which should be further explored.

4103  
4104 The Hayes Bank, to the west of Roosevelt Island, has been identified as the  
4105 primary location of inflow of warm Circumpolar Deep Water (Das et al., 2020;

4106 Tinto et al., 2019). We model a region of deeper-than-previously seen bathymetry  
 4107 along the west edge of Roosevelt Island and propose this as a location that may  
 4108 allow the incursion of this ocean water with a high potential for melt. Additionally,  
 4109 along the Shirase Coast, south of Roosevelt Island, we model a thicker ocean cavity  
 4110 than past estimates. This may allow further penetration of water which enters the  
 4111 shelf near Hayes Bank. To address these highlighted regions of importance for basal  
 4112 melt, future ocean circulation models should incorporate our bathymetry model.  
 4113 Further, to test the sensitivity of sub-shelf circulations to bathymetry, the upper  
 4114 and lower bounds of uncertainty should be used in separate circulation models to  
 4115 test the range of possible sub-shelf circulations.

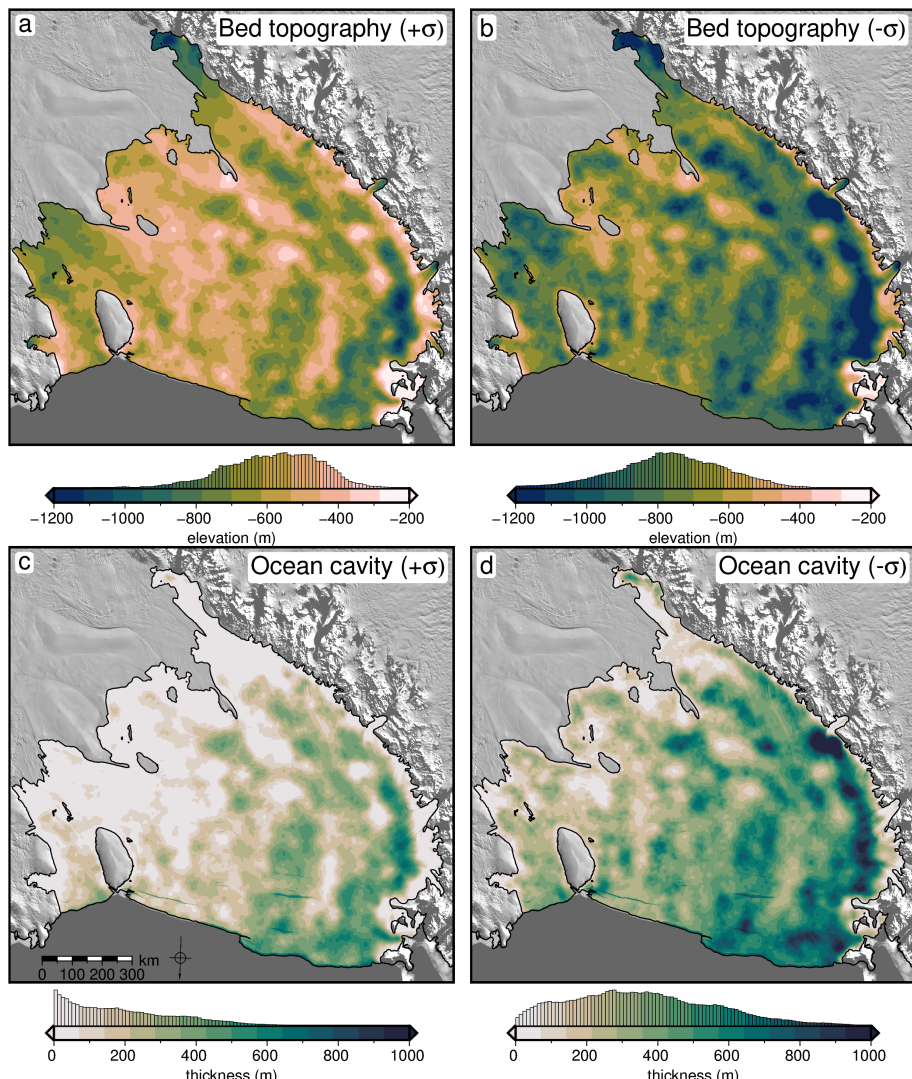


**Figure 5.2:** Lower and upper uncertainty bounds of Ross Ice Shelf bathymetry and ocean cavity thickness. **a)** Upper bathymetry uncertainty bound, **b)** lower bathymetry uncertainty bound, **c)** upper ocean cavity uncertainty bound, **d)** lower ocean cavity uncertainty bound.

#### 4116 5.4.1.2 Modern pinning points

4117 Analysis of Ross Ice Shelf's pinning points has shown that the effective resistance as  
 4118 well as the temporal persistence of pinning points are not tied solely to their size, but  
 4119 are strongly influenced by the competency of the bedrock (Still et al., 2019; Still &  
 4120 Hulbe, 2021). A really small pinning points which exert large effective resistance are

assumed to be grounded on bed with a high friction coefficient, while large pinning points which exert only minor resistance are assumed to be grounded on an easily deformable substrate. Based on the ratio of area to effective resistance, Still et al. (2019) suggested the bed beneath the Shirase Coast Ice Rumples, to the south-east of Roosevelt Island (Figure 5.3), is likely composed of competent bedrock with a high friction coefficient. Conversely, they suggest pinning point #14, just north of Crary Ice Rise, to be grounded on easily deformable till. The downstream extent of streaklines from pinning points provides an estimate of the temporal persistence of these features. Based on these streaklines, the Shirase Coast Ice Rumples and the Crary Ice Rise have likely been grounded for hundreds of years, while the large Steershead Ice Rise, just west of Siple Dome, only became grounded within the last 400 years (Fahnstock et al., 2000; Still et al., 2019).

4133

#### 4134 Persistent pinning points

4135 Our basement and sediment thickness results provide support for many of these  
4136 observations of ice dynamics. The Shirase Coast Ice Rumples, predicted to have  
4137 been long-lasting and grounded on competent bedrock, are shown in our basement  
4138 results to sit upon a large basement high, with thin sedimentary cover. This implies  
4139 both that the bedrock beneath the pinning point is either crystalline basement, or  
4140 very coarse sediment from minimally re-worked basement material, and that the  
4141 elevation of the bed is stable. This stability is likely due to both the tectonic nature  
4142 of the bed as a fault-bounded horst, and the higher strength of the bedrock, able to  
4143 resist erosion by the overriding ice. Similarly, the persistence of Crary Ice Rise in  
4144 the glaciologic record may be owed to its location above a basement ridge. Of the  
4145 areas of possible recent grounding we identified, the region to the south of Crary Ice  
4146 Rise, and the smaller area  $\sim$  200 km north of Crary Ice Rise, both are located on  
4147 similar large basement highs with thin sedimentary cover. When grounded, these  
4148 past pinning points likely imparted a large effective resistance on the overriding ice.

4149

#### 4150 Recent pinning points

4151 The predicted deformable substrate of both Steershead Ice Rise and pinning point  
4152 #14 (Still et al., 2019), as well as the recent grounding of Steershead Ice Rise  
4153 (Fahnstock et al., 2000), are supported by our findings of these features being  
4154 located over thick fault-bound sedimentary basins. These thick sediments provide  
4155 material that is easily weathered into glacial till by the overriding ice, which lowers  
4156 the effective resistance of the pinning point. If the basin bounding faults we predicted  
4157 in Chapter 2 are truly active, they could accommodate local vertical bed movements  
4158 associated with glacial isostatic adjustment following changing ice loads (Peltier et  
4159 al., 2022; Steffen et al., 2021). For the very low-viscosity upper mantle and thin  
4160 lithosphere beneath West Antarctica (Chen et al., 2018; Pappa et al., 2019), these  
4161 solid earth responses to changing ice thickness may occur on decadal timescales  
4162 (Barletta et al., 2018). This may help explain the short-lived history of these pinning  
4163 points. One of the possible recent pinning points we identified is within the same  
4164 sedimentary basin as Steershead Ice Rise (between Steershead Ice Rise and Roosevelt  
4165 Island), and when grounded, likely shared these qualities. With these observations,  
4166 we support the notion of a strong geologic control on the buttressing ability and  
4167 persistence of pinning points throughout the Ross Ice Shelf. As the West Antarctic

4168 Ice Sheet thins, swift glacial isostatic rebound may lead to re-grounding; a response  
4169 which may promote stability of the ice sheet (Barletta et al., 2018; Coulon et al.,  
4170 2021; Kachuck et al., 2020). Accurate bathymetry beneath the Ross Ice Shelf is  
4171 vital for knowing where this re-grounding may occur, and thus where new pinning  
4172 points will develop.

4173 **5.4.1.3 Sediment distribution**

4174 The dynamics of Siple Coast ice streams are intrinsically tied to the bed which  
4175 they flow over. The presence of sediments and sedimentary basins allows for several  
4176 mechanisms to achieve the fast flow seen in these ice streams. 1) The sediments are  
4177 able to deform in response to the shear stress of the overriding ice, allowing faster  
4178 flow (Alley et al., 1986), 2) groundwater stored within the sedimentary basins both  
4179 lubricates the ice base, reducing basal friction and increases till deformation, through  
4180 increased pore-fluid pressure (Tulaczyk et al., 2000). Our results of Chapter 2 show  
4181 a continuous drape of sediments across the ice shelf including along the Siple Coast  
4182 grounding zone. The presence of these sediments helps explain the fast-flowing ice  
4183 along this region. Additionally, we image several large sediment basins beneath the  
4184 Siple Coast (Figure 5.1f). The groundwater storage capabilities of such basins could  
4185 provide up to half of the groundwater in the subglacial system of West Antarctica  
4186 (Christoffersen et al., 2014). The southernmost of these sedimentary basins has been  
4187 confirmed by a recent magnetotelluric survey, which identified > 1 km of sediments  
4188 with extensive groundwater storage (Gustafson et al., 2022). The other two basins  
4189 we imaged, the Siple Dome Basin, and the Crary Trough (Figure 5.3), could be key  
4190 drivers on subglacial hydrology beneath the Siple Coast.

4191 **5.4.1.4 Geothermal heat flux at Siple Coast**

4192 **Spatial control on geothermal heat**

4193 The last main geologic control on Ross Ice Shelf stability we propose is the distribu-  
4194 tion of geothermal heat along the Siple Coast (Figure 5.1d). Geothermal heat flux  
4195 is one of the least constrained boundary conditions for Antarctica (Larour et al.,  
4196 2012; Pollard et al., 2005; Seroussi et al., 2017). High geothermal heat supplied to  
4197 the ice base can accelerate flow by 1) increasing englacial temperatures, reducing ice  
4198 viscosity, 2) increasing basal lubrication through meltwater production and 3) in-  
4199 creasing the ability of subglacial tills to deform, through water-saturation (Golledge  
4200 et al., 2014; Pollard et al., 2005). While we don't provide any direct measurements  
4201 of geothermal heat flux, our fault-bound sedimentary basins along the Siple Coast  
4202 provide important insights into the temporal and spatial variability expected for  
4203 geothermal heat flux along the Siple Coast.

4204  
4205 Measurements and predictions of geothermal heat flux along the Siple Coast are  
4206 shown to vary significantly, even between nearby (within ~ 100 km) measurements  
4207 (Figure 5.1d, Begeman et al., 2017; Fox Maule et al., 2005). This high spatial  
4208 variability is attributed to the localization of heat due to upper crustal structures  
4209 (Begeman et al., 2017). Faults and basement margins act as efficient fluid conduits,  
4210 which can localize the already regionally elevated heat (e.g., Burton-Johnson et al.,  
4211 2020; Fox Maule et al., 2005), resulting in vastly enhanced heat flow to the ice  
4212 base (Gooch et al., 2016), which is likely the cause of the anomalously high heat

4213 flow measured at Subglacial Lake Whillans ( $285 \text{ mWm}^{-2}$ , Fisher et al., 2015). We  
4214 hypothesized in Chapter 2 that these faults not only provide a spatial control on  
4215 geothermal heat flux, but a temporal control as well.

4216

#### 4217 Temporal control on geothermal heat

4218 As ice thickness has varied throughout the Holocene, the changing ice overburden  
4219 pressure on the subglacial sediments drives the discharge and recharge of these sedi-  
4220 mentary aquifers (Gooch et al., 2016; Li et al., 2022). This fluid movement is  
4221 accommodated along fault-damage zones and impermeable basement margins (Fig-  
4222 ure 5.1 Jolie et al., 2021). This may present a positive feedback, where thickening  
4223 ice drives groundwater into the aquifers, advecting heat away from the ice base,  
4224 which slows the flow of ice, leading to increased thickness. Similarly, as ice thins,  
4225 the reduced overburden on the aquifers results in water discharge to the ice base and  
4226 an associated localization of heat. The resulting increased flow speed and thinning  
4227 of the ice further reduces the overburden pressure. These mechanisms express how  
4228 crustal structures often thought of as static on a millennial timescale from the view-  
4229 point of ice dynamics may enable rapid changes in ice dynamics. The co-location of  
4230 highly dynamic ice streams (Bougamont et al., 2015; Catania et al., 2012), extensive  
4231 groundwater reservoirs (Christoffersen et al., 2014; Gustafson et al., 2022), elevated  
4232 geothermal heat flux (Burton-Johnson et al., 2020; Shen et al., 2020), and fluid  
4233 pathways (Chapter 2), highlight the Siple Coast as an ideal study site to investigate  
4234 these possible relations between changes in ice thickness, groundwater discharge,  
4235 and the advection of geothermal heat. We now discuss various implications of our  
4236 geologic findings for understanding past and future ice dynamics of the Ross Ice  
4237 Shelf region.

4238

#### 4239 5.4.2 Constraining past and future ice sheet behaviour

4240 While the above geologic controls on the ice sheet likely existed in the past and will  
4241 continue into the future, our study has implications that are exclusive to past or  
4242 future ice sheet configurations. The pinning points we discussed, and the regions of  
4243 thin draft, were all likely pinning points during periods of thicker ice. Since the Last  
4244 Glacial Maximum ( $\sim 22 \text{ ka}$ ) retreat of the grounding line from the outer shelf edge  
4245 has been primarily controlled by the physiography of the bed, as well as its geologic  
4246 composition (Anderson et al., 2019; Halberstadt et al., 2016). While the retreat  
4247 dynamics have been well studied in the Ross Sea, where the open ocean conditions  
4248 allow seismic and high-resolution multi-beam sonar surveying (Anderson et al., 2019;  
4249 Halberstadt et al., 2016), and drill cores provide sedimentary records (McKay et al.,  
4250 2016), under the Ross Ice Shelf there has been very little investigation on retreat  
4251 dynamics, apart from modelling studies (Kingslake et al., 2018; Lowry et al., 2020).  
4252 Here we have provided the physiography of the region, through the sub-Ross Ice  
4253 Shelf bathymetry model, enabling insight into the retreat dynamics throughout the  
4254 Holocene.

4255

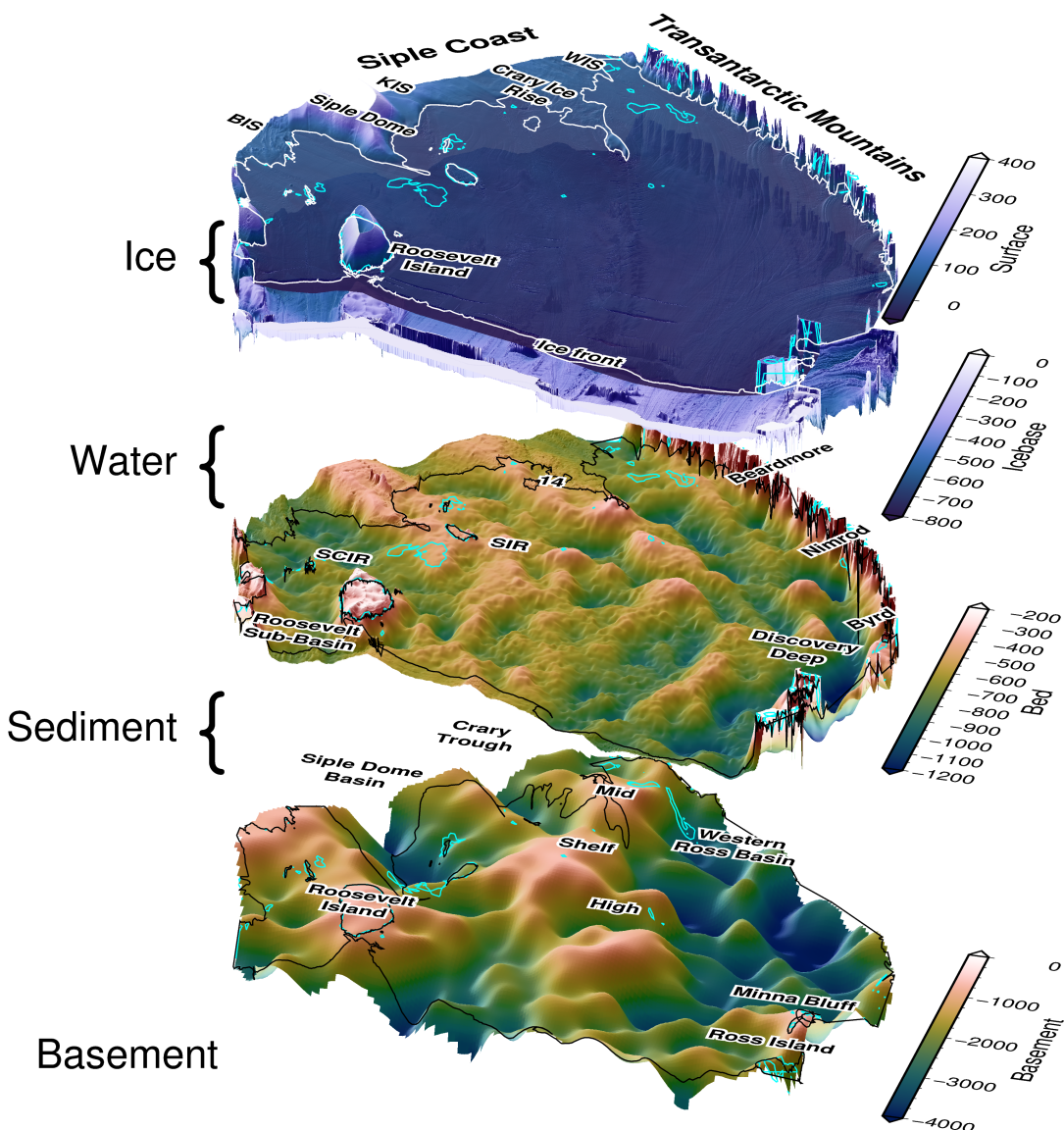


**Figure 5.3:** A 3D perspective view of the structure of the Ross Ice Shelf. Starting at the top, ice surface, and ice base from BedMachine v3 (Morlighem, 2022; Morlighem et al., 2020), inverted bathymetry results from Chapter 4, and basement topography from Chapter 2. Grounding line shown in all layers if from Morlighem (2022). Bright blue contour shows 20 m water column thickness. Note each layer has an independent vertical exaggeration to aid in visualization. Acronyms: BIS: Bindschadler Ice Stream, KIS: Kamb Ice Stream, WIS: Whillans Ice Stream, SCIR: Shirase Coast Ice Rumples, SIR: Steershead Ice Rise.

#### 4256 5.4.2.1 Retreat dynamics

4257 While we don't constrain the age of the sea floor sediments, the general physiography  
 4258 of the sea floor can provide some insights. The eastern side of the ice shelf, apart  
 4259 from Roosevelt Island, shows similar physiography to the eastern Ross Sea, with  
 4260 relatively flat bathymetry without major banks or troughs (Figure 5.1e). There,  
 4261 the subdued bathymetry likely resulted in a stepwise style of grounding line retreat  
 4262 throughout the Miocene, with the stabilizing build-up of grounding zone wedges, fol-  
 4263 lowed by decoupling and rapid retreat of 10's of kilometres (Anderson et al., 2019;  
 4264 Bart et al., 2017). The bathymetry of the western Ross Ice Shelf, characterized by

depth troughs and shallow banks, is similar to that of the western Ross Sea (Figure 5.1e). There, the retreat style, also controlled by the bathymetry, was continuous and complex, as ice streams followed the bathymetry in a continuous retreat back to the outlet valleys in the Transantarctic Mountains (Anderson et al., 2019; Halberstadt et al., 2016). In the western Ross Sea, repeated cycles of advance and retreat within these confined bathymetry troughs led to the scouring of sediments from the inner shelf, and an over-deepened, landward sloping inner shelf (Anderson et al., 2019). These contrasting styles of retreat proposed for the eastern and western Ross Ice Shelf may be in part responsible for the varied bathymetry found on either side of the ice shelf. The above section discussed our bathymetry results in relation to past and future ice dynamics. Next, we discuss the implication of our basement topography on the glacial history of the region.

4277

#### 4278 5.4.2.2 Glacial initialization

4279 During the Oligocene, the Ross Embayment contained a long and broad mountain range emergent above sea level, trending N-S from the Ross Sea through the ice shelf. This feature was first recognized from the drill cores of DSDP (Deep Sea Drilling Project) site 270 in the Ross Sea (Figure 5.1f, Leckie, 1983), where a 400 m sedimentary sequence with depositional environments ranging from above sea level to  $\sim$  500 m below sea level was found, dating from late Oligocene to early Miocene (Kulhanek et al., 2019). Beneath this sequence was crystalline basement. The broad dome-like shape of this basement high was revealed by shipborne seismic surveys (Brancolini et al., 1995), which imaged a similar basement high further north. These basement features were termed the Northern and Southern Central High. Seismic data also revealed small U-shaped channels within the acoustic basement, which were attributed to alpine glaciation (De Santis et al., 1995). Off the flanks of these fault-bound basement highs, wider troughs in the basement were imaged and attributed to the erosion of ice streams flowing off these basement highs. During the late Oligocene, ice caps nucleated on these subaerial basement features (De Santis et al., 1995; Olivetti et al., 2023). Thermal subsidence following the onset of mid-Cretaceous West Antarctic Rift System extension (Karner et al., 2005; Wilson & Luyendyk, 2009) gradually submerged these basement highs (De Santis, 1999; Olivetti et al., 2023). In addition to the North and South Central High features in the Ross Sea, paleotopographic reconstructions of the Oligocene (Paxman et al., 2019; Wilson et al., 2012) have predicted the continuation of this broad subaerial mountain range under the Ross Ice Shelf. Our depth to magnetic basement (Chapter 2) provided the first observations of the feature, which we termed the Mid Shelf High, beneath the Ross Ice Shelf (Figure 5.1f).

4303

4304 The strong continuity of the Mid Shelf High with the Ross Sea's Central High suggests that these features have similar histories. We propose the three blocks of the 4305 Mid Shelf High were emergent and hosted ice caps in the Oligocene. Following their 4306 submersion, likely in the latest Oligocene (Olivetti et al., 2023) these features would 4307 have acted as major bathymetry pinning points, similar to the modern Roosevelt 4308 Island. We suggest this chain of shallow basement blocks formed a long-lasting 4309 catchment divide of both sediment transport and ice flow between East and West 4310 Antarctica. This divide has been predicted as far back as the Paleogene, from 4311 distinct microfossil assemblages on either side of the Ross Embayment (Coenen et 4312

al., 2019). Since the Last Glacial Maximum, the Central High has been thought to be an ice flow divide, separating ice originating from the East and West Antarctic Ice Sheets (Li et al., 2020; Licht et al., 2014; Licht et al., 2005). The prominent Mid Shelf High / Central High appears to have played a central role in the history of the Ross Embayment since the Oligocene.

## 5.5 Future work

Here we provide several suggestions for future research and fieldwork related to this thesis. A primary piece of future work resulting from this thesis should be the incorporation of the updated bathymetry into a sub-ice shelf circulation model. To access the sensitivity of sub-shelf circulations to bathymetry, models should be run for our mean bathymetry model, as well as the upper and lower ranges of our uncertainties, as defined by the mean model plus and minus the spatial uncertainty we present (Figure 5.2). To better improve the bathymetry model and reduce uncertainties, we suggest three alternatives for field seasons on the Ross Ice Shelf.

1. Collect additional seismic depth measurements along the Transantarctic Mountain front. This would serve to lower uncertainties in the bathymetry associated with the nearby steep topography. A traverse-style field season would be best for this to accommodate the linear nature of the grounding zone. Collecting occasional cross lines, running perpendicular to the grounding line, would likely image the range front faults, commonly inferred by only rarely imaged.
2. A seismic survey of the central block of the Mid Shelf High (Figure 5.1f). This survey would accomplish several goals. First, it would fill one of the two major gaps in bathymetry measurements in the central ice shelf, reducing the bathymetry uncertainty. Secondly, it would inform on the nature of the Mid Shelf High as a past pinning point and nucleation site of Oligocene ice caps. Lastly, it would act as a site survey for potential sea-floor drilling. The thin sedimentary cover of the Mid Shelf High may provide a good target for future drilling since a temporally wide-ranging sequence may be concentrated into a thin sedimentary package. Additionally, sampling of the crystalline basement, trace element and provenance analysis will give further insights into 1) the proposed East-West Antarctic geologic boundary along the middle of the Ross Embayment (Tinto et al., 2019), 2) the region's Cretaceous extensional history (Olivetti et al., 2023), and 3) the region's Oligocene to Miocene climatic evolution (Olivetti et al., 2023).
3. Conduct a regional seismic survey across portions of the Siple Coast to better image the sedimentary basins and basin bounding faults, especially where the faults proposed in Chapter 2 may interact with the ice streams.

We make several suggestions for future inversions based on our comprehensive review of past Antarctic bathymetry gravity inversions. To test the inversion method developed here, it would be useful to perform another inversion for an ice shelf that has been previously inverted. The three best options would be the Getz Ice Shelf, the Thwaites Glacier, and the Pine Island Glacier. The bathymetry beneath each of these ice shelves has been inverted three separate times, allowing the comparison of several different methods. The Getz Ice shelf bathymetry has been inverted in 2D

(Cochran et al., 2020; Wei et al., 2020), and with a 3D frequency-based inversion (Millan et al., 2020). The Thwaites cavity has also been inverted in both 2D (Tinto & Bell, 2011) and 3D, with both the "topo-shift method" (Jordan et al., 2020a), and a frequency-based method (Millan et al., 2017). Lastly, the Pine Island Glacier bathymetry has been inversion twice with Simulated Annealing (Muto et al., 2013a; Muto et al., 2016), and once with a frequency-based inversion (Millan et al., 2017). To compare to a wider range of methods, the Thwaites glacier would be optimal. To gain insights into the effectiveness of our uncertainty analysis, Pine Island Glacier should be chosen since spatially variable uncertainty estimates exist from the studies which used Simulated Annealing.

4367

4368 Of the major Antarctic ice shelves, there are four that stand out as prime can-  
4369 didates for a future inversion if the goal is to increase our sub-ice shelf bathymetric  
4370 knowledge. These include the Larsen C Ice Shelf, the Ronne Filchner Ice Shelf, the  
4371 Riiser-Larsen Ice Shelf, and the Shackleton Ice Shelf.

4372

1. Larsen C is the largest ice shelf on the Antarctic Peninsula, yet bathymetry knowledge beneath it is still limited. A bathymetry inversion has been conducted (Cochran & Bell, 2012), but comparison with seismic constraints revealed large uncertainties in the model. A recent constraint compilation and new seismic data (Brisbourne et al., 2020) make this an ideal candidate without needing any field work. Additional gravity data has also been collected over the ice shelf during 2016, 2017, and 2018 Operation Ice Bridge flights ("IceBridge Sander AIRGrav L1B Geolocated Free Air Gravity Anomalies, Version 1", 2020).
2. The Ronne Filchner is the second-largest ice shelf, yet has not been included in a gravity inversion. An extensive array of seismic constraints, similar to the RIGGS survey of the Ross Ice Shelf exists (Fretwell et al., 2013; Rosier et al., 2018), and gravity data from compiled from Russian airborne and ground-based surveys (Aleshkova et al., 2000; Studinger & Miller, 1999) is accessible as part of the continent-wide AntGG gravity compilation (Scheinert et al., 2016).
3. and 4. The Riiser-Larsen and the Shackleton Ice Shelves are the 5th and 7th largest ice shelves, respectively. To our knowledge, there is no bathymetry knowledge beneath the entirety of either shelf. Gravity data exists for both shelves from the AntGG compilation (Scheinert et al., 2016). Performing inversions for these shelves would require extensive seismic data acquisition to be adequately constrained.

4394

Lastly, we highlight a few alternative use cases and limitations for our gravity inversion algorithm. While this has been developed for a regional-scale sub-ice shelf application, at its core the inversion is a standard geometric (sometimes referred to as structural) inversion. Therefore, this code can be used to invert any topographic surface of a user-defined density contrast based on input gravity anomaly data. It is compatible with domains ranging from small-scale, local areas, to large domains such as ours ( $1000 \times 1000$  km). However, domains significantly larger than ours (continental scale) will introduce inaccuracies due to our use of vertical right-rectangular prisms, which makes assumptions of a planar Earth. For these

<sup>4403</sup> continental to global scale inversions, vertical prisms should be replaced with spher-  
<sup>4404</sup> ical prisms (tesseroids), as implemented by (Uieda & Barbosa, 2017). With this, our  
<sup>4405</sup> inversion will work for other applications, such as predicting regional Moho depths,  
<sup>4406</sup> the sediment-basement contact, or determining bed depths beneath grounded ice,  
<sup>4407</sup> under subglacial lakes, or in the open ocean. We hope this code is used by others  
<sup>4408</sup> for these various applications.

<sup>4409</sup> **5.6 Concluding remark**

<sup>4410</sup> The primary aim of this thesis was to use existing airborne geophysical data to better  
<sup>4411</sup> characterize the geology and physiography beneath Antarctica's Ross Ice Shelf. We  
<sup>4412</sup> used and developed several geophysical techniques to accomplish this. We first used  
<sup>4413</sup> variations in Earth's magnetic field measured over the ice shelf to model the spatial  
<sup>4414</sup> distribution and thickness of sediments beneath the ice shelf. We then developed  
<sup>4415</sup> and extensively tested a geophysical inversion, which uses measurements of Earth's  
<sup>4416</sup> gravity field to model the depth to the seafloor. With this, we created an updated  
<sup>4417</sup> model of the bathymetry beneath the ice shelf.

<sup>4418</sup>

<sup>4419</sup> From this geophysically informed knowledge of the upper crust of the sub-Ross  
<sup>4420</sup> Ice Shelf, we were able to draw inferences on the complex interactions between the  
<sup>4421</sup> solid Earth, ocean, and ice for the Ross Embayment. We highlighted the Siple  
<sup>4422</sup> Coast as a location with strong geologic control on ice dynamics, through 1) the  
<sup>4423</sup> distribution of sediments, which control the competency of bedrock material beneath  
<sup>4424</sup> grounded ice, and 2) the location of deep sedimentary basins, which likely supply  
<sup>4425</sup> the ice base with lubricating water and localize the geothermal heat delivered to the  
<sup>4426</sup> ice. Our bathymetry model confirms the findings of past models which show a deep  
<sup>4427</sup> trough spanning from the ice front near Ross Island south along the Transantarctic  
<sup>4428</sup> Mountain Front. This trough likely guides High Salinity Shelf Water from the ice  
<sup>4429</sup> front to the deep grounding zone of the Transantarctic Mountain outlet glaciers,  
<sup>4430</sup> where it induces significant basal melting. Our spatial uncertainty results highlight  
<sup>4431</sup> the Transantarctic Mountain Front as the least-certain portion of the sub-ice shelf  
<sup>4432</sup> bathymetry model. Combined with this region's importance for basal melt, we  
<sup>4433</sup> suggest future seismic surveys target the mountain front. This thesis provides the  
<sup>4434</sup> necessary boundary conditions and estimates of their uncertainties for ice and ocean  
<sup>4435</sup> modellers to better characterize the Ross Ice Shelf's response to past, present, and  
<sup>4436</sup> future changes in the climate.

# <sup>4437</sup> Appendix A

<sup>4438</sup> This appendix section provides supplementary information to Chapter 2, and is  
<sup>4439</sup> taken directly from the published supplementary materials of Tankersley et al.  
<sup>4440</sup> (2022).

## <sup>4441</sup> A.1 Introduction

<sup>4442</sup> This supplement provides additional information on the assumptions behind the  
<sup>4443</sup> process of determining basement depth from magnetic anomalies (Section A.2), the  
<sup>4444</sup> collection and processing of aeromagnetic line data (Section A.3), the methodolo-  
<sup>4445</sup> gy of tying ROSETTA-Ice magnetic basement to ANTOSTRAT acoustic base-  
<sup>4446</sup> ment (Brancolini et al., 1995), through the use of Operation IceBridge (OIB) mag-  
<sup>4447</sup> netic data (Cochran et al., 2014a) (Section A.4 & A.5), the gridding, merging,  
<sup>4448</sup> and filtering of the resulting basement grid (Section A.6), the calculation of sedi-  
<sup>4449</sup> ment thickness and  $\beta$ -factors for the region (Section A.7), and our quantification  
<sup>4450</sup> of uncertainties and comparison with points of previously measured sediment thick-  
<sup>4451</sup> ness (Section A.8). Sediment thickness comparisons with past seismic surveys are  
<sup>4452</sup> included in Table S1. Also included are supplementary figures showing various  
<sup>4453</sup> additional Ross Ice Shelf grids (Figure A.1), the Werner deconvolution solutions  
<sup>4454</sup> of OIB flight 403.3 (A.2), several selected ROSETTA-Ice flight lines with Werner  
<sup>4455</sup> deconvolution solutions (A.3), unfiltered basement solutions with flight line loca-  
<sup>4456</sup> tions and individual Werner deconvolution solutions (A.4), uncertainties applied to  
<sup>4457</sup> basement and sediment thickness results (A.5), and misfit distributions between  
<sup>4458</sup> OIB, ANTOSTRAT, and ROSETTA basement models (A.6). Python code, within  
<sup>4459</sup> a Jupyter notebook, documents our workflow and figure creation and is accessi-  
<sup>4460</sup> ble here: <https://zenodo.org/badge/latestdoi/470814953> or at the GitHub reposi-  
<sup>4461</sup> tory: [https://github.com/mdtanker/RIS\\_basement\\_sediment](https://github.com/mdtanker/RIS_basement_sediment). Results in the form  
<sup>4462</sup> of netCDF's and csv's are available at <https://doi.pangaea.de/10.1594/PANGAEA.941238>, including figures of all ROSETTA-ice flight line basement solutions.

## <sup>4464</sup> A.2 Depth to basement assumptions

<sup>4465</sup> Our resulting basement grid is the depth to the shallowest magnetic signal. It is  
<sup>4466</sup> assumed that the crystalline basement in this region produces significantly larger  
<sup>4467</sup> magnetic anomalies compared to the overlying sediment fill. Note that in some  
<sup>4468</sup> instances, such as igneous bodies intruded into sedimentary basin fill, Werner de-  
<sup>4469</sup> termined solutions fall upon the crest of the intrusion, and the actual top of the  
<sup>4470</sup> crystalline basement could be at a deeper level. Intrusions of small lateral extent

will have small widths, resulting in small values of parameter S (susceptibility  $\times$  width) and therefore will be removed by our filter (Section A.4). For larger intrusions into existing basins, (i.e. Ross Island and Minna Bluff Cox et al., 2023), the modelled magnetic basement surface will be shallower than the bottom of the sedimentary basin. While this underestimates sediment volume, it better characterizes the competency of the substrate from an ice dynamics perspective. This is similar to how extensive intrusions into basins would be imaged by seismic surveys as shallow basement. However, these extensive regions of late-Cretaceous-Cenozoic magmatism are not expected to be prevalent under the RIS (Andrews & LeMasurier, 2021).

## 4480 A.3 Magnetic data collection, processing, and Werner 4481 deconvolution

Both ROSETTA-Ice and OIB data sets were collected with a Scintrex CS3 Cesium magnetometer. Average flight speeds were 123 m/s and 93 m/s for OIB and ROSETTA-Ice respectively. Altitudes for the sections of OIB flight 403 used here average around 400 m above sea level, while ROSETTA-Ice altitude averaged at 750 m above the ice sheet surface. OIB data were resampled from 20 Hz to 1 Hz to match the frequency of the ROSETTA-Ice data. Both datasets have been despiked, diurnally corrected, and had the International Geomagnetic Reference Field model removed. See Tinto et al. (2019) for more details of the ROSETTA-Ice survey and flight line locations. Due to variable flight elevations, both between and within the datasets, all magnetic data were upward continued to 1000 m above sea level. To avoid artifacts of downwards continuing, any data with flight elevations above 1000 m were removed ( $\sim 10\%$  of the data).

Here we use 2D Werner deconvolution Werner (1953), applied to aeromagnetic line data, to image the shallowest magnetic signals in the crust. Assuming that the overlying sediments produce smaller magnetic anomalies than the crystalline basement, we treat the resulting solutions as a depth to the magnetic basement. During Werner deconvolution, moving and expanding windows are passed over the magnetic anomaly line data. Within each window, after linearly detrending the data, the source parameters of the anomalies are estimated with a least-squares approach, assuming the source bodies are infinite-depth dikes or contacts. The source parameters include position (distance along profile and depth), magnetic susceptibility, and source geometry (contact or dike). Solutions are considered valid between 1200 m and 20 km of upward continued flight elevation (approx. 200 m - 19 km bsl). Windows ranged from 500 m - 50 km, with a window shift increment of 1 km and an expansion of 1 km.

Due to passing over the data many times with varying window widths, Werner deconvolution produces a depth-scatter of solutions, which tend to cluster vertically beneath the true magnetic sources. Each of these solutions consists of location, depth, susceptibility (S), window width (W), and a simplified source geometry (dike or contact). For contact-type solutions, parameter S is the estimated magnetic susceptibility of the body, while for dike-type solutions, S is the product of susceptibility and dike width. During filtering (Sections A.4 & A.5), a cut-off based on parameter S is used to remove shallow solutions. Since the value of parameter S for

4517 contact solutions are typically much smaller than for dike solutions (since they are  
4518 not multiplied by dike width), only dike solutions have been considered here. To  
4519 achieve a basement surface from this resulting depth-scatter of solutions, we have  
4520 utilized parameter-based filtering and clustering, described in Sections A.4 & A.5.  
4521 This Werner deconvolution process was the same for both OIB and ROSETTA-Ice  
4522 magnetics data. Werner deconvolution was performed in Geosoft's Oasis Montaj and  
4523 subsequent processing of these results was performed in Python, and is included in  
4524 a Jupyter notebook; <https://zenodo.org/badge/latestdoi/470814953>.

4525  
4526 This magnetic basement approach has been used to map sedimentary basins  
4527 throughout Antarctica, including the Ross Sea (Karner et al., 2005), western Marie  
4528 Byrd Land (Bell et al., 2006), and Wilkes Subglacial Basin (Frederick et al., 2016;  
4529 Studinger et al., 2004a). Our approach is similar to past studies, but our proximity  
4530 to well-constrained offshore seismic basement depths (Brancolini et al., 1995) allows  
4531 us to develop the method further. Most studies display their results as 2D profiles  
4532 with the depth-scatter of solutions mentioned above, and simply use the tops of the  
4533 clusters as the basement depth. By comparison with seismic basement, we have  
4534 developed a reliable, automated method of 'draping' a surface over these depth-  
4535 scattered solutions to produce a 3D surface. This process is described below.

## 4536 **A.4 Tying magnetic basement to seismic basement**

4537 To validate the method described in Section A.3 and address uncertainty we per-  
4538 form Werner deconvolution for OIB magnetics data (Figure 2.1b, Cochran et al.,  
4539 2014a) over the Ross Sea. Here, ice-free conditions have permitted shipborne seis-  
4540 mic surveys to image basement depths in the region. These have been compiled by  
4541 the Antarctic Offshore Acoustic Stratigraphy project (ANTOSTRAT) (Brancolini  
4542 et al., 1995) (Figure 2.1b). The basement was not imaged for the deepest portions  
4543 of the basins and data coverage of actual basement reflectors, versus interpolation  
4544 between basement reflectors, is not reported. Werner deconvolution (Section A.3)  
4545 produces a series of many solutions (black dots in Figures 2.2 & A.2) at each window  
4546 along the line.

4547  
4548 To achieve a basement surface, instead of a depth-scatter of solutions, solutions  
4549 were filtered based on Werner window width (W) and the product of magnetic sus-  
4550 ceptibility and body width (parameter S). Filtered solutions (black circles, scaled to  
4551 parameter S in Figures 2.2 & A.2) were then horizontally binned with variable bin  
4552 sizes (parameter B) (vertical grey lines in Figures 2.2 & A.2). Bins with a minimum  
4553 count of solutions (parameter C) were retained, and the depth of the bin centre was  
4554 set to the 95th-percentile depth of the solutions in the bin. This removed spurious  
4555 shallow solutions, while effectively retaining the 'top' of the magnetic signal. These  
4556 bin centres (orange crosses in Figures 2.2 & A.2) were then interpolated, producing  
4557 our model of magnetic basement depths (orange line in Figures 2.2 & A.2). The  
4558 above filtering techniques removed the solutions above the basement, and the clus-  
4559 tering technique fitted a surface over the remaining points, which represents the  
4560 top of the basement. This interpolated line allowed a direct comparison between  
4561 ANTOSTRAT seismic basement and OIB magnetic basement.

4562  
4563 We varied each of the four parameters (W, S, B, and C) with 21 different values

and conducted the above procedures for all unique combinations of them on OIB line 403, segments 1 and 3, in the Ross Sea (location in Figure 2.1b). This resulted in 194,481 iterations, for each of which we calculated a mean absolute difference at points every 5 km between ANTOSTRAT seismic basement and the resulting OIB magnetic basement. We found the parameter values which produced the closest match between OIB magnetic basement and ANTOSTRAT seismic basement, as shown in Figures 2.2 & A.2. These resulting values were a maximum Werner deconvolution window width (parameter W) of 10 km, a minimum product of magnetic susceptibility and body width (parameter S) of 1.0, a horizontal bin width (parameter B) of 36 km, and a minimum number of solutions per bin (parameter C) of 6. The median absolute misfit between OIB and ANTOSTRAT basement for the two line-segments was 480 m (260 m for Line 403.1 (Figure 2.2), and 1040 m for Line 403.3 (Figure A.2)). This equates to 11% of average ANTOSTRAT depths for the two lines. The close fit between the OIB magnetic basement and the ANTOSTRAT seismic basement both supports the validity of this method and gives us the parameters necessary to repeat this method for data over the RIS.

## 4580 A.5 Tying Ross Sea magnetic basement to Ross Ice 4581 Shelf magnetic basement

Having optimized our method to match OIB magnetic basement to ANTOSTRAT seismic basement in the Ross Sea (Section A.4, Figures 2.2 & A.2), we now optimize the method to match ROSETTA-Ice magnetic basement to OIB magnetic basement. This additional optimization is necessary due to differences in processing and survey design, including flight elevations, speed, aircraft, mounting equipment used, and frequency of recording. With the optimized parameters for OIB data (Section A.4), we calculate magnetic basement for OIB flight 404 over the ice shelf. We treat this as the 'true' basement and update the filtering and clustering parameters (Section A.3) to minimize the misfit between OIB basement and the resulting ROSETTA-Ice basement. This tuning was performed on ROSETTA-Ice lines 590 and 650, which were coincident with segments from OIB line 404 (location in Figures 2.1b & A.4). Optimal parameters to match ROSETTA-Ice solutions to OIB basement are found to be  $W < 26$  km,  $S > 1.2$ ,  $B = 36$  km, and  $C > 40$ , resulting in a median absolute misfit between OIB basement and ROSETTA-Ice solutions of 400 m (630 m for line 404.590 (Figure A.3e) and 310 m for line 404.590 (Figure A.3f)). This equates to 18% of OIB depths for the two lines. With these parameters which best match ROSETTA magnetic basement to OIB magnetic basement, we performed the same procedure on all the ROSETTA-ice flight lines. A selection of these lines, and the two ties to OIB 404, are shown in Figure A.3. All ROSETTA-ice flight line solutions are available as images at the PANGAEA link.

## 4602 A.6 Gridding, merging, and filtering

The above processes were performed on all ROSETTA-ice flight lines (white lines in Figure A.4), including the N-S tie lines at  $\sim 55$  km spacing. Where the tie lines crossed over the E-W flight lines, some resulting basement solutions (black dots in Figure A.4) are nearby those from the crossing line. Since we are interested in the

shallowest magnetic signals, we have retained only the shallowest solution with 8 km cells across our region. Since bin widths (parameter B) were set to 36 km, the nearest solutions along individual lines were further apart than the 8 km cell. The closest spacing of E-W flight lines was 10 km, so this process only affected solutions at the crossover between N-S and E-W lines. These points were then gridded with a 5 km cell size and a minimum curvature spline with a tension factor of 0.35 Smith and Wessel, 1990 (Figure A.4). This grid was then merged with a Ross Sea seismic basement grid. The Ross Sea grid, while mostly ANTOSTRAT data, was sourced from a regional compilation of sediment thicknesses (Lindeque et al., 2016; Wilson & Luyendyk, 2009) we have subtracted from bathymetry depths (Morlighem et al., 2020) to achieve basement depths. Where the grids overlap near the ice shelf edge, we retain our RIS values. To aid in the merging at the overlaps, and to match RIS basement wavelengths to the characteristic basement wavelengths of ANTOSTRAT, we filtered the merged grid with an 80 km Gaussian filter (Figure 2.3a). This filtering was performed with a variety of wavelengths (20-120 km), where we found filters  $<80$  km didn't significantly alter the regional basement, while filters  $>80$  km excessively smoothed the basement topography. A few locations with anomalously shallow basement were set equal to BedMachine bathymetry.

## 4625 **A.7 Sediment thickness and $\beta$ -factor calculations**

With the regional basement model (Figure 2.3a) including RIS magnetic basement and offshore seismic basement, we calculated sediment thickness (Figure 2.3b) by subtracting the grid from BedMachine bathymetry depths (Figure 2.1a & A.1e, Morlighem et al., 2020). Previous estimates of sediment thickness for the sub-RIS come from the extrapolation of gravity anomalies with bathymetry trends (Wilson & Luyendyk, 2009). These were included in the Lindeque et al. (2016) compilation (Figure A.1d). Eocene Oligocene boundary paleotopographic reconstructions (Paxman et al., 2019; Wilson et al., 2012) assumed this sediment estimate was post-Eocene and used it as their maximum sub-RIS sediment thickness, incorporated into their minimum surface reconstruction. The thickness of sediment affects onshore erosion estimates, surface raising due to deposition, and isostatic surface subsidence due to loading. For their maximum paleotopographic reconstructions, they used a thinner sediment model, with the same general trends (Wilson & Luyendyk, 2009). Figure A.1 (c, d, & f) shows the comparison between the sediment thickness models. Figure A.1f colorbar histogram shows the distribution, with our values having a mean thickness  $\sim 115$  m greater than the past model. Yet, along the Siple Coast, we show much greater discrepancies, up to 2 km thicker.  $\beta$ -factor, the ratio of initial crustal thickness to final crustal thickness, is useful for quantifying the thinning of crust in extensional settings. We calculate a distribution of  $\beta$ -factors beneath the RIS by assuming a uniform initial crustal thickness and dividing it by current crustal thickness. We pick an initial crustal thickness of 38 km, which represents a global average for un-thinned plateau-type crust (Mooney et al., 1998), and has been used for the West Antarctic Rift System  $\beta$ -factor calculations (Müller et al., 2007). For the final (current) crustal thickness, we use a continent-wide Moho model from surface wave observations to define the bottom of the crust (An et al., 2015). For the top of the crust, we use our resulting RIS basement grid.

| Name | Reference                   | Seismic sediment thickness (m) | Magnetic sediment thickness (m) | Absolute difference (m) |
|------|-----------------------------|--------------------------------|---------------------------------|-------------------------|
| CIR  | (Rooney et al., 1987)       | 400                            | 514                             | 114                     |
| I10S | (Robertson & Bentley, 1989) | $750 \pm 100$                  | 1281                            | 818                     |
| J9DC | (Greischar et al., 1992)    | 1350                           | 770                             | 580                     |
| BC   | (Robertson & Bentley, 1989) | $1900 \pm 400$                 | 1082                            | 818                     |
| RI   | (Greischar et al., 1992)    | 850                            | 822                             | 28                      |
| C49  | (Crary, 1961)               | 754                            | 1162                            | 408                     |
| LAS  | (Crary, 1961)               | 1325                           | 1799                            | 474                     |
| Q13  | (Greischar et al., 1992)    | $255 \pm 145$                  | 721                             | 466                     |

**Table A.1:** Previous seismic sediment thickness results for the Ross Ice Shelf. Stations names are labelled in Figure 2.3b. Magnetic sediment thickness column shows our sampled results at the location of each station. Comparing the seismic estimates with our sediment thickness at the eight stations gives a median absolute misfit of 470 m.

## 4652 A.8 Uncertainties

4653 We estimated a representative uncertainty for our basement model by examining  
 4654 the misfit of our modelled basement compared to offshore seismic basement depths  
 4655 (Brancolini et al., 1995). We did this by sampling our OIB magnetic basement  
 4656 estimate and the coincident ANTOSTRAT basement at 1 km intervals along lines  
 4657 403.1 and 403.3 (Figures 2.2 and A.2) and compared the values. The resulting ab-  
 4658 sOLUTE values of the differences don't exhibit a normal distribution (Figure A.6a);  
 4659 therefore, we use the median of the absolute misfit ( $\pm 480$  m) as the basement model  
 4660 uncertainty. This equates to 22% of average basement depths for the sub-RIS. We  
 4661 performed a similar analysis between OIB magnetic basement and ROSETTA-Ice  
 4662 magnetic basement for coincident lines 590 and 650 (Figure A.3 e & f). This resulted  
 4663 in a median absolute misfit of 400 m (Figure A.6b). Tinto et al. (2019) report an un-  
 4664 certainty of 68 m for their bathymetry model. Incorporating this with our basement  
 4665 model gives an uncertainty of 550 m (37% of average thickness) for our sediment  
 4666 thickness results. Comparison with sub-RIS sediment thickness and distribution re-  
 4667 sults from a variety of methods, including active source seismic surveys (Table A.1  
 4668 and references within), seismic radial anisotropy (Zhou et al., 2022), geophysical  
 4669 machine learning (Li et al., 2022), and magnetotelluric surveying (Gustafson et al.,  
 4670 2022), all show general agreement with our results.

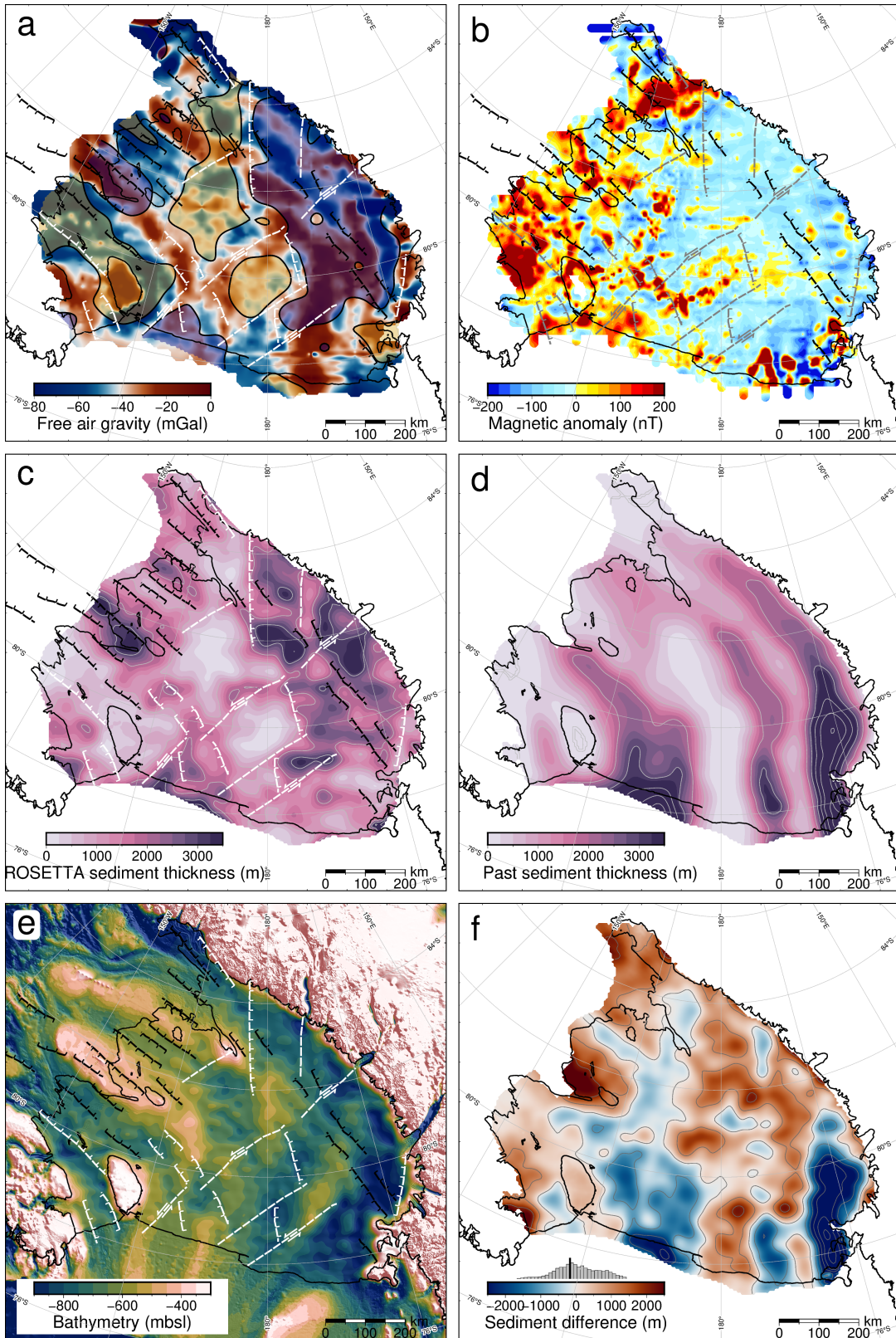


**Figure A.1:** **a)** ROSETTA-Ice free air gravity (Tinto et al., 2019). Shaded yellow regions are shallow basement ( $<\sim 1600$  mbsl), shaded blue regions are deep basement ( $>\sim 2600$  mbsl). **b)** ROSETTA-Ice airborne magnetic anomaly data (Tinto et al., 2019). **c)** Sediment thickness from this study (same as Figure 2.3b), with 1 km contours. **d)** Sediment thickness from a regional compilation (Section A.7, Lindeque et al., 2016; Wilson & Luyendyk, 2009), with 1 km contours. **e)** BedMachine2 bathymetry (Morlighem et al., 2020), from which sediment thickness in c) was calculated. **f)** Difference between c) and d). Red signifies our results have more sediment, while blue signifies our results have less sediment. Histogram shows data distribution, with mean value (black) at 115 m. Inferred faults in a), b), c), and e) same as Figure 2.4a. Grounding line and coastlines in black (Rignot et al., 2013). Projection is Antarctic Polar Stereographic: EPSG 3031.

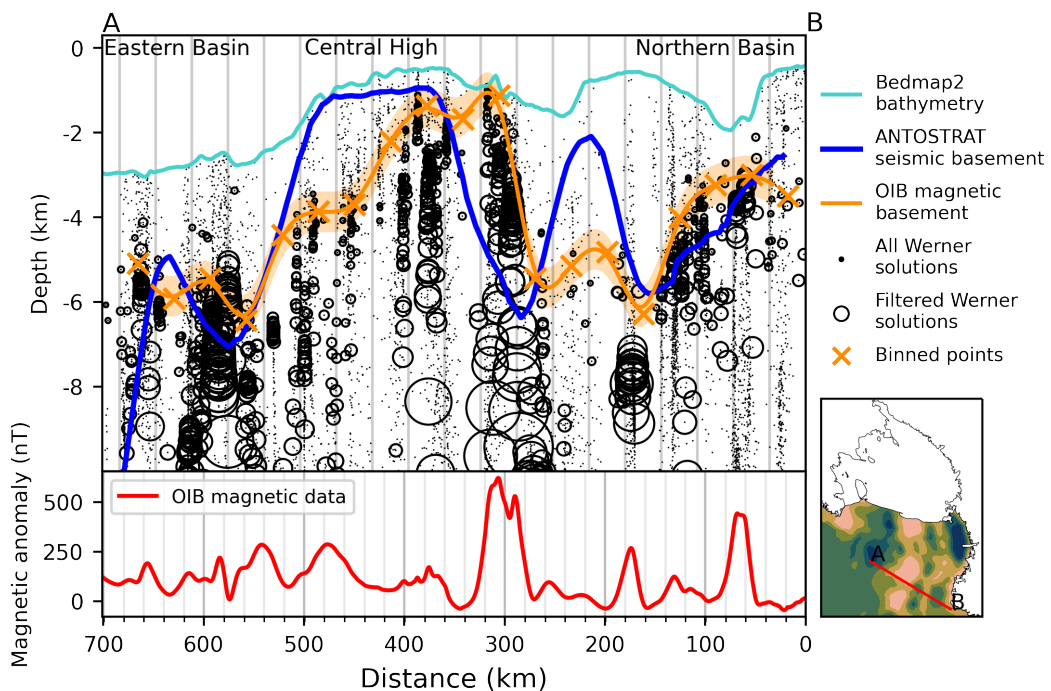


**Figure A.2:** Ross Sea magnetic and seismic basement comparison. Operation IceBridge airborne magnetic data (lower panel) from segment 403.3 (Figure 2.1b). Small dots show Werner deconvolution solutions, which were filtered based on parameters S and W (Section A.3) to produce black circles, which are scaled to parameter S. These circles were binned at a width equal to parameter B, shown by the vertical grey lines in the upper panel. Orange crosses show bin centres, which were fitted to a line to facilitate the comparison between the magnetic basement (orange line) and seismic basement (blue line). Orange band shows  $\pm 480$  m uncertainty for the basement model. Ross Sea basement features are labelled on top.

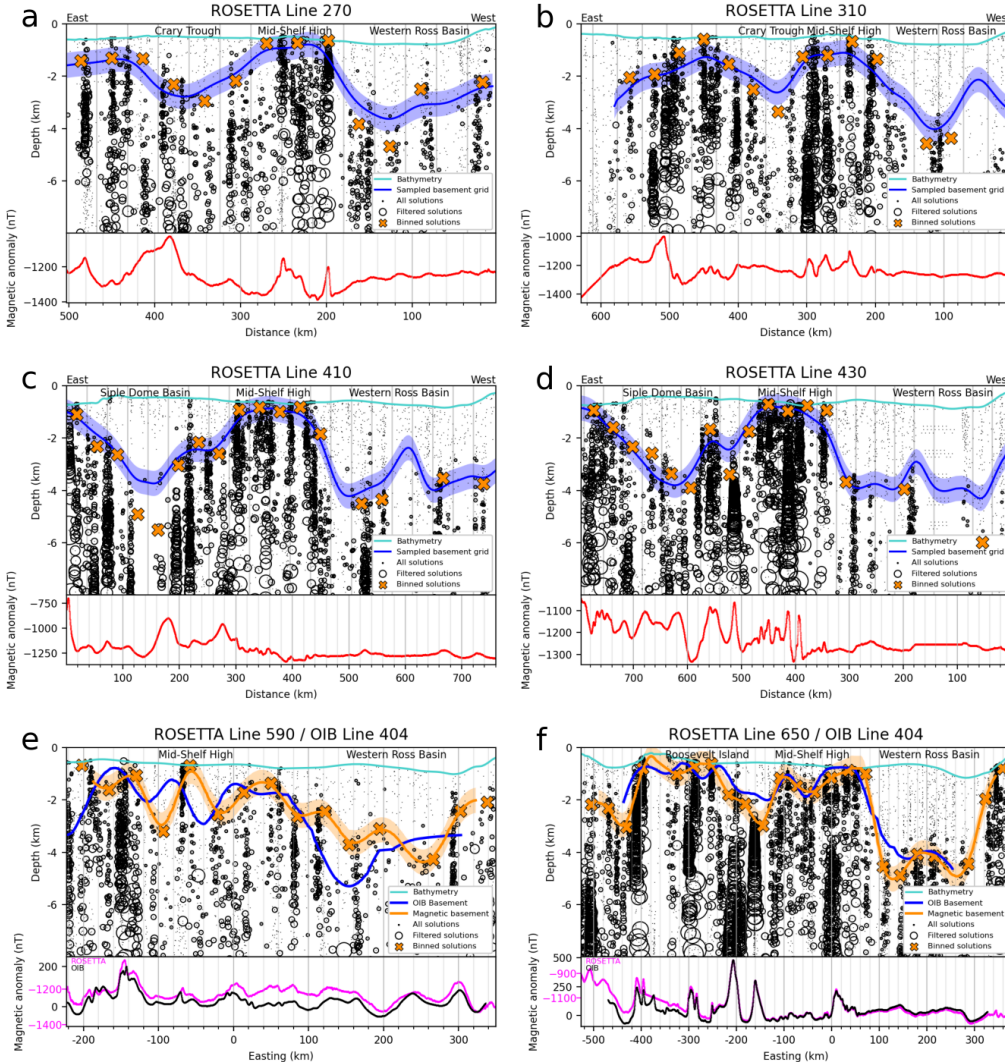


**Figure A.3:** Werner deconvolution solutions for a selection of ROSETTA-Ice lines, locations highlighted in Figure A.4. Bathymetry from Bedmap2 (Fretwell et al., 2013). Dots, circles, and vertical grey lines same as Figure A.2. **a-d)** Comparison between magnetic basement before and after filtering and gridding. Orange crosses are magnetic basement solutions, shown as black dots in Figure A.4, and highlighted for these lines. Blue lines are magnetic basement sampled from the grid of Figure 1a, after gridding and filtering. Red lines show 258 ROSETTA-Ice magnetics data. **e-f)** Comparison between magnetic basement resulting from Werner deconvolution of coincident OIB and ROSETTA-Ice flight lines. Location is shown in Figures 2.1b and A.4. These two lines were used to tie the ROSETTA-Ice survey to the OIB survey (Section A.5). Blue lines are OIB magnetic basement results, orange crosses and fitted orange lines with uncertainty bands are ROSETTA-Ice magnetic basement. ROSETTA-Ice (pink) and OIB (black) magnetics data are shown in lower panels.

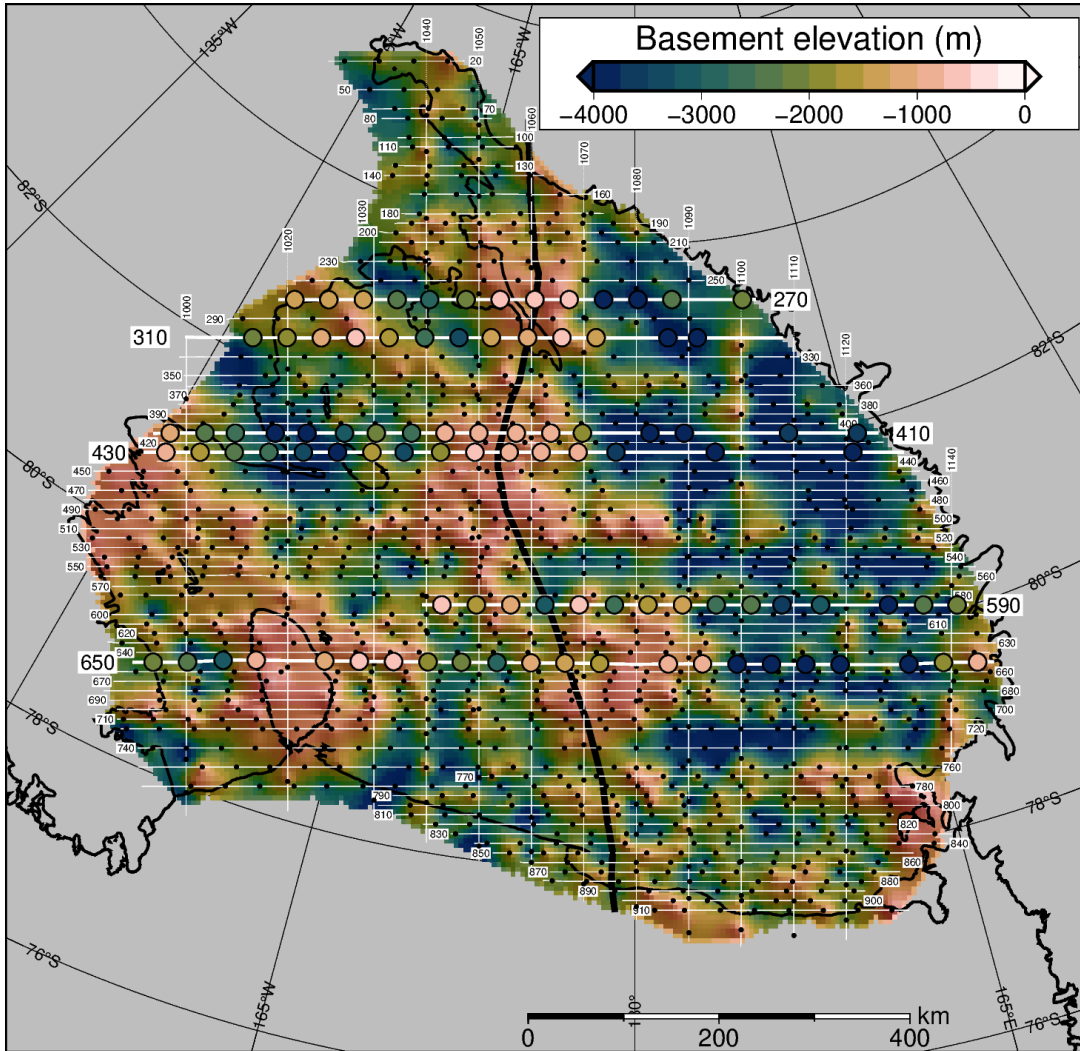


**Figure A.4:** Unfiltered magnetic basement. Point solutions (black dots here, orange crosses in Figure A.3) along ROSETTA-Ice flight lines (labelled) were gridded with a 5 km cell size and a minimum curvature spline with a tension factor of 0.35. Figure A.3 flight lines (bold white) and point solutions (coloured circles) are shown. Black line through the Mid-Shelf High shows the East-West Antarctic divide used in colorbar histograms of Figures 2.3 and 2.4a. Grounding line and coastlines in black (Rignot et al., 2013).

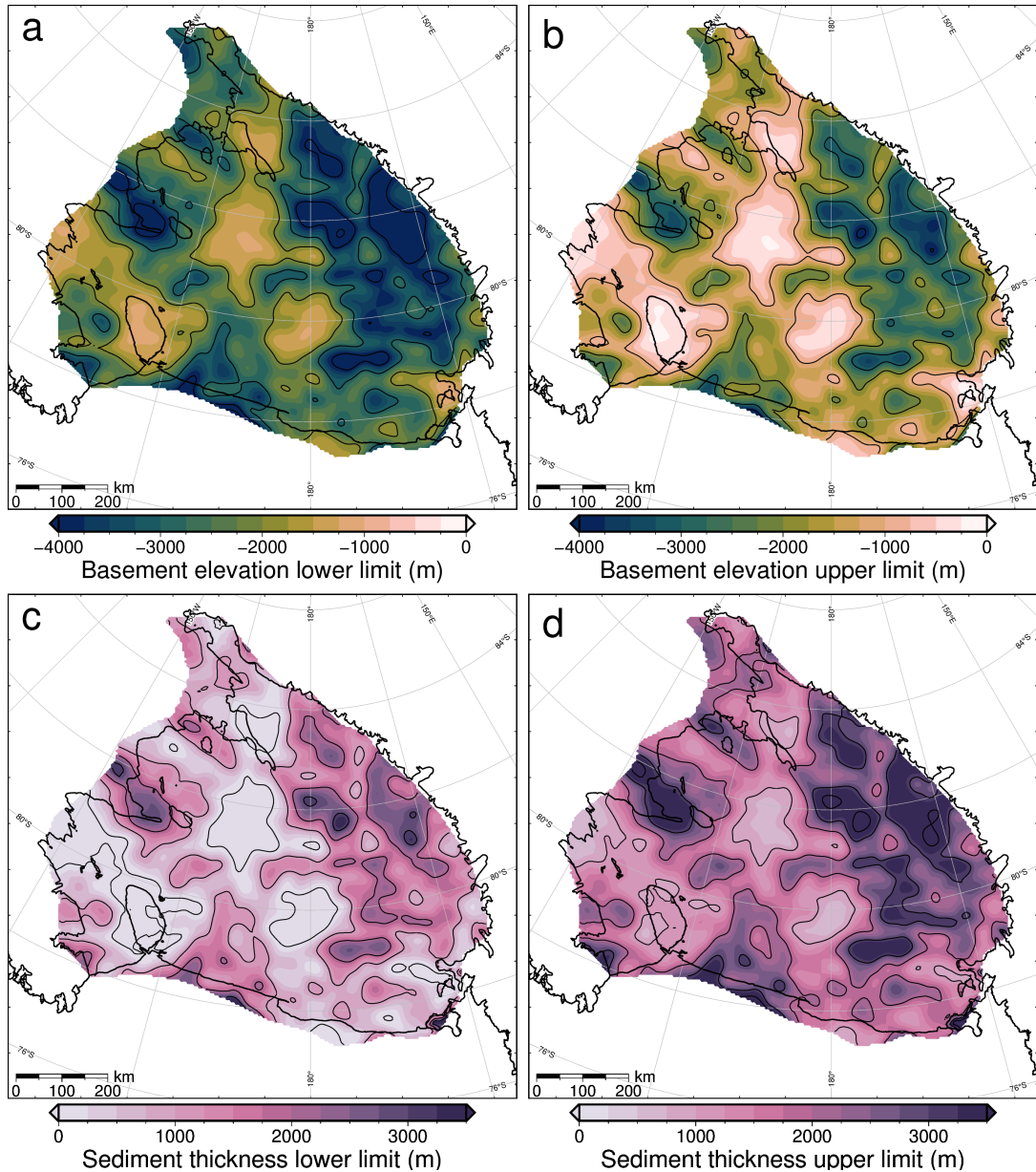


**Figure A.5:** Upper and lower limits of uncertainty applied to a-b) magnetic basement and c-d) sediment thickness. See Section A.8 for how these uncertainties were determined.

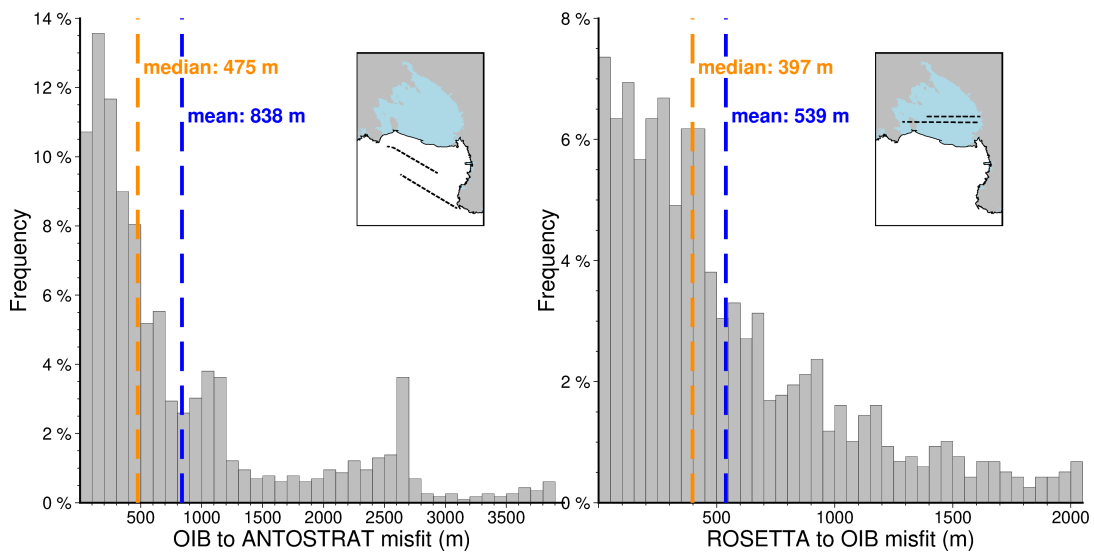


**Figure A.6:** Misfit distributions for comparisons between **a)** OIB magnetic basement and ANTOSTRAT seismic basement and between **b)** ROSETTA magnetic basement and OIB magnetic basement. Inset maps show the locations of flight lines. Basement models were sampled at 1 km intervals for the comparison.

# 4671 Appendix B

4672 This appendix section provides supplementary information to Chapter 3.

## 4673 B.1 Synthetic inversion with a regional field

### 4674 Regional separation techniques

4675 Figure B.1 shows profiles comparing the various regional separation techniques  
4676 shown in Figure 3.19 of Chapter 3.

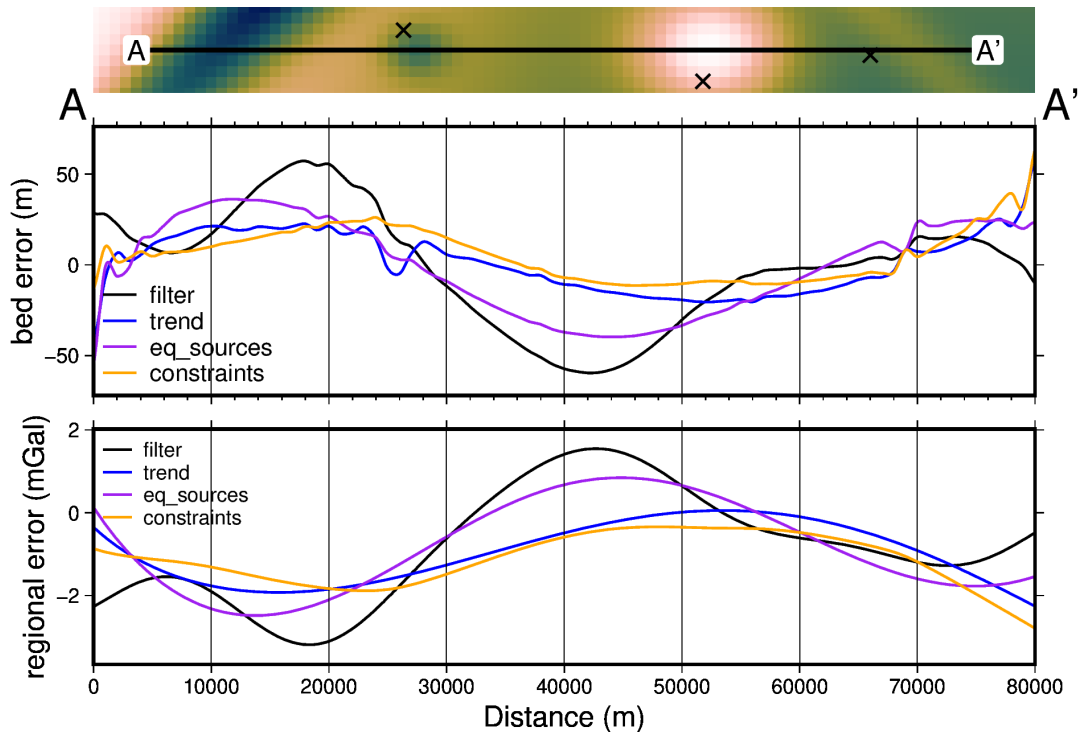


**Figure B.1:** Comparison of four methods of regional separation. **Upper panel** shows the error in the inverted bathymetry models for each method. **Lower panel** shows the errors in the regional field estimation of each method. Profile location shown at the top.

### 4677 Constraint point minimization gridding techniques

4678 Figure B.1 shows profiles comparing the various gridding techniques for the con-  
4679 straint point minimization regional separation method. These various gridding tech-  
4680 niques are shown in map view in Figure 3.20 of Chapter 3.

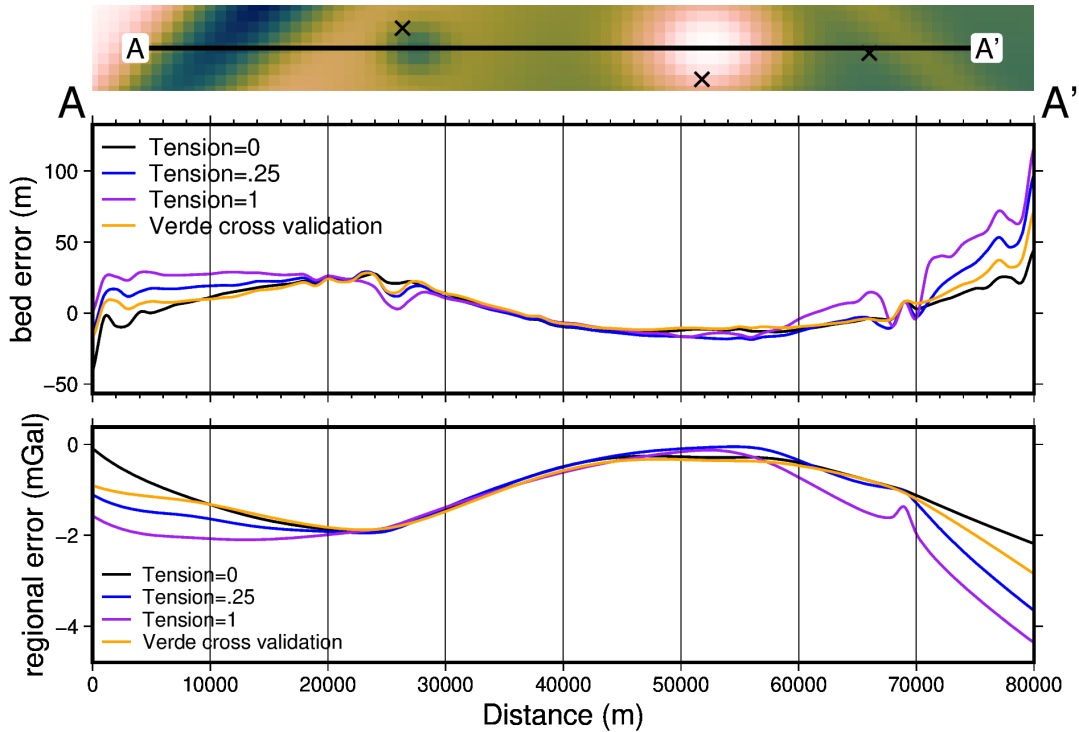


**Figure B.2:** Comparison of gridding techniques for the constraint point minimization method of regional separation. **Upper panel** shows the error in the inverted bathymetry models for each method. **Lower panel** shows the errors in the regional field estimation of each method. Profile location shown at the top.

#### 4681    Added noise

4682    Here, we repeat the inversion from Section 3.4 with noise added to the observed  
 4683    gravity data. Noise was from a Gaussian distribution with a mean of 0 and a stan-  
 4684    dard deviation of 2% of the max absolute values of the data, equating to 0.24 mGal.  
 4685    The cross-validation curve and a profile across the inverted bathymetry as shown in  
 4686    Figure B.3. The inverted bathymetry and difference with the true bathymetry as  
 4687    shown in Figure B.4. The error in the inverted bathymetry is compared to the error  
 4688    in the regional field estimation in Figure B.5.

#### 4689    Lower-resolution gravity survey

4690    This same inversion is now repeated with a lower-resolution gravity survey. Instead  
 4691    of the original 1 km survey grid, a 4 km grid is used.

## 4692    B.2    Ross Sea synthetic model

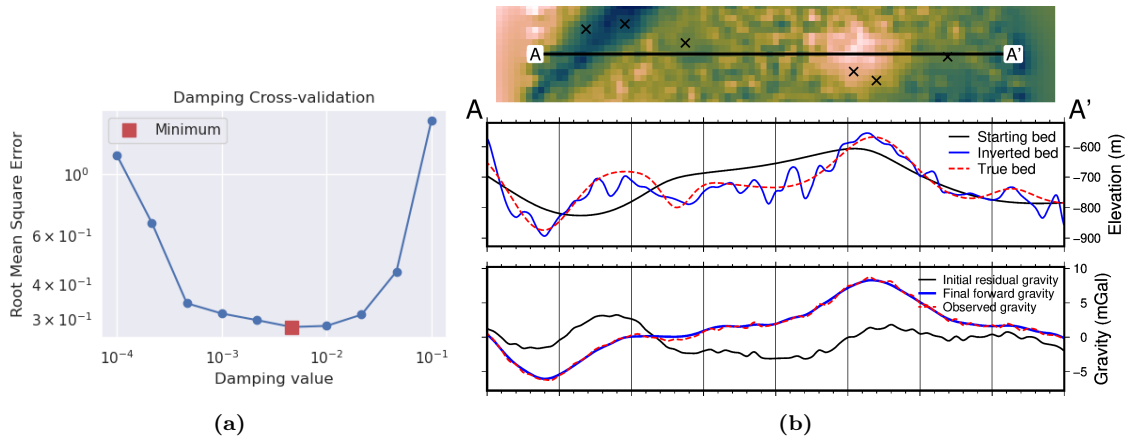


**Figure B.3:** Cross-validation and profiles for the simple synthetic inversion with a regional component removed and 2% noise added to the observed gravity data. a) Cross-validation curve showing the optimal damping parameter (red square). b) 2D profile of the inversion results. The top panel shows profile location and constraint points (black crosses). The middle panel contains topographic profiles of the starting, inverted, and true bathymetries. The bottom panel contains gravity anomaly profiles.

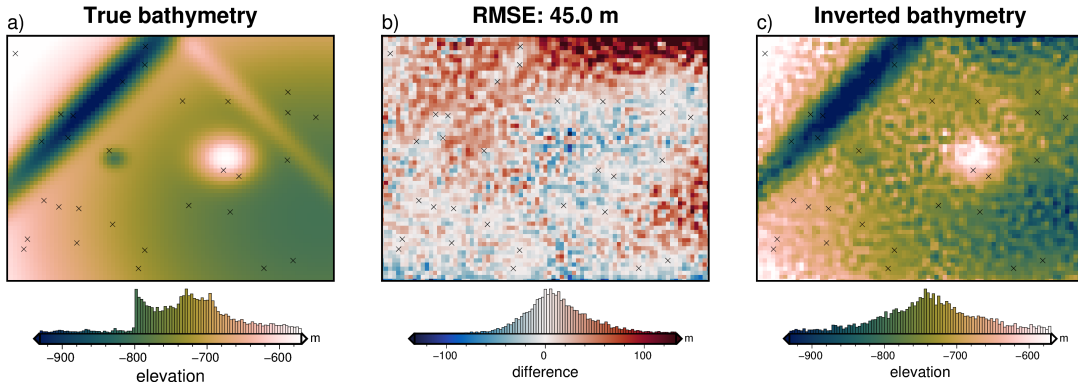


**Figure B.4:** Simple synthetic model inversion with a removed regional component and noise contamination. a) True bathymetry, b) difference between a) and c), c) final inverted bathymetry. Black crosses are constraint points. The RMS difference with the true bathymetry at these constraints is 2 m.

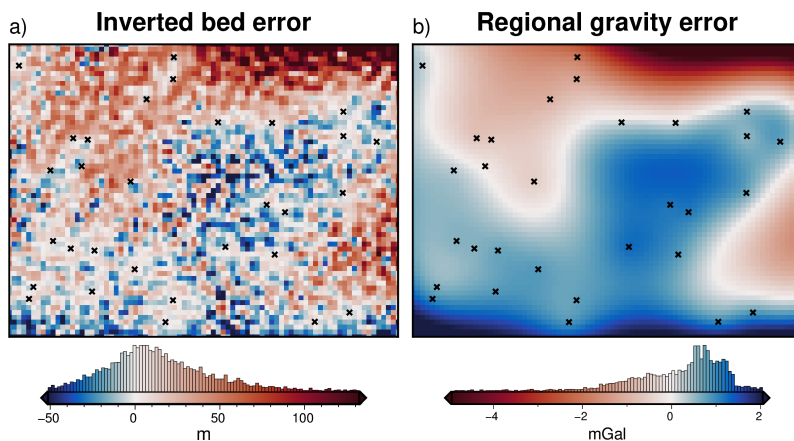


**Figure B.5:** Source of inverted bathymetry error for model with regional field and noise. a) Inverted bathymetry error from Figure 3.22b. b) Error in the estimation of the regional component of gravity from comparison with the true regional component (Figure 3.18b). Black cross show constraint points. Colourmaps are opposed to highlight the similarities and the mean has been removed from the regional error.

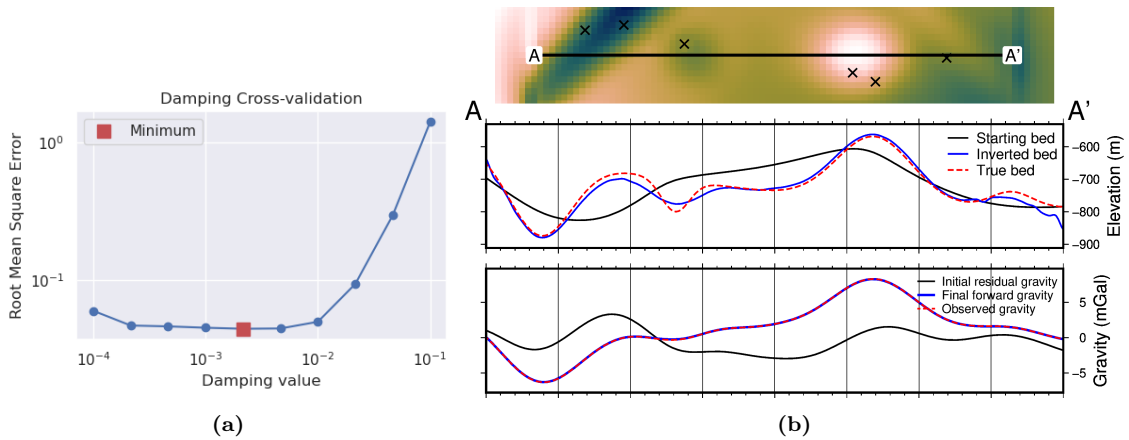


**Figure B.6:** Cross-validation and profiles for the simple synthetic inversion with a regional component removed and low-resolution gravity data. a) Cross-validation curve showing the optimal damping parameter (red square). b) 2D profile of the inversion results. The top panel shows profile location and constraint points (black crosses). The middle panel contains topographic profiles of the starting, inverted, and true bathymetries. The bottom panel contains gravity anomaly profiles.

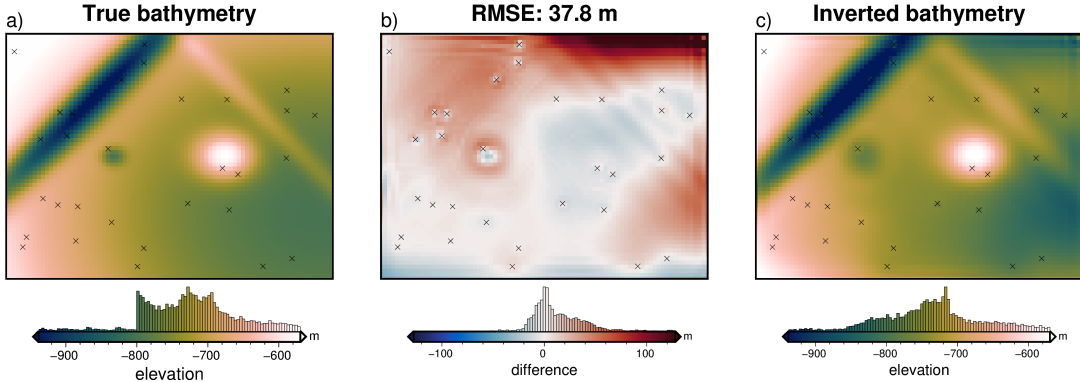


**Figure B.7:** Simple synthetic model inversion with a removed regional component and gravity resampling. a) True bathymetry, b) difference between a) and c), c) final inverted bathymetry. Black crosses are constraint points. The RMS difference with the true bathymetry at these constraints is 2 m.

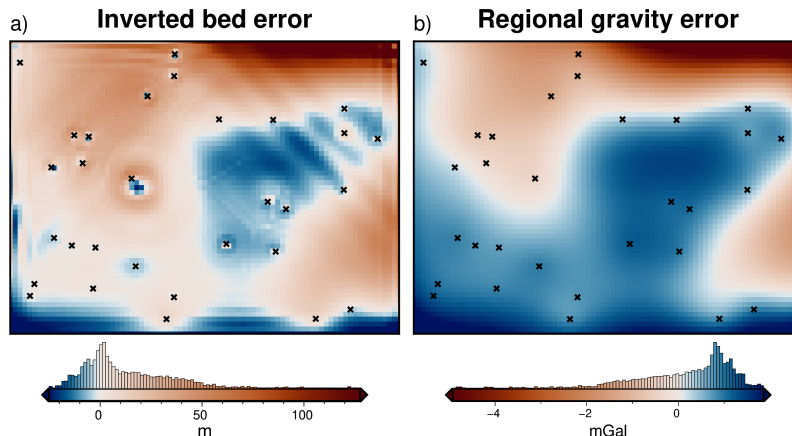


**Figure B.8:** Source of inverted bathymetry error for model with regional field and re-sampled gravity data. a) Inverted bathymetry error from Figure 3.22b. b) Error in the estimation of the regional component of gravity from comparison with the true regional component (Figure 3.18b). Black crosses show constraint points. Colourmaps are opposed to highlight the similarities and the mean has been removed from the regional error.

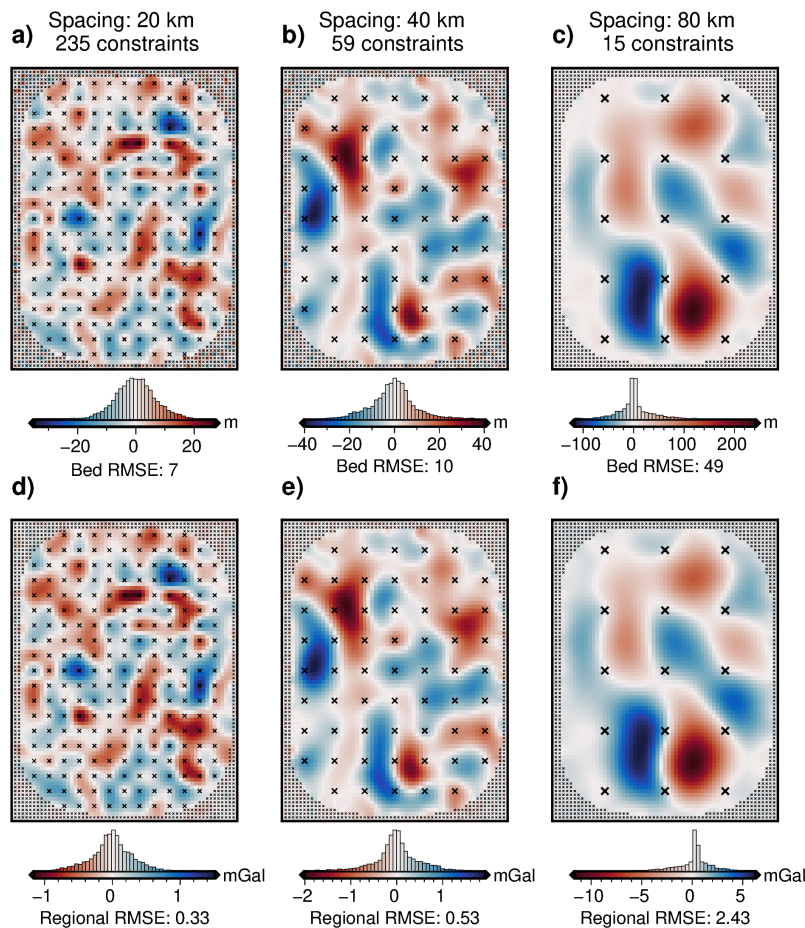


**Figure B.9:** Source of inverted bathymetry error for three inversion with varying constraint spacings. a) Inverted bathymetry error from three of the models in the constraint ensemble of Figure 3.31. b) Error in the estimation of the regional component of gravity from comparison with the true regional component for each model. Black crosses show constraint points. Colormaps are opposed to highlight the similarities and the mean has been removed from the regional error.



4693

# Appendix C

4694 This appendix provides supplemental information to Chapter 4.

4695

## C.1 Gravity disturbance vs anomaly

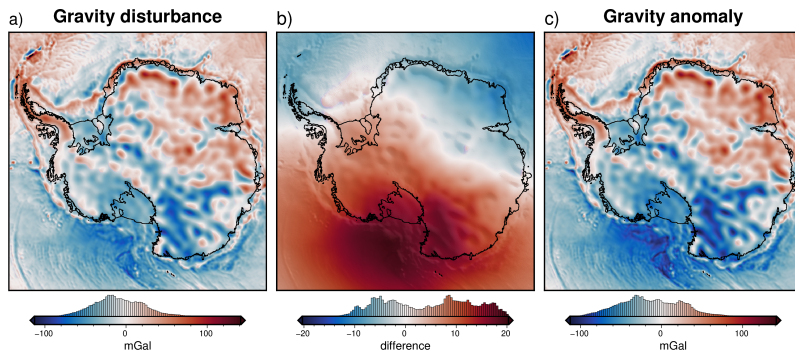


**Figure C.1:** Difference between the gravity disturbance and anomaly for Antarctica. Observed gravity is from Förste et al. (2014) and the normal gravity for each was calculated with the python package Boule (Fatiando a Terra Project et al., 2022). See Section 4.2.1 for further details.



# 4696 Appendix D

## 4697 Antarctic-Plots

4698 This appendix briefly describes the Python package Antarctic-Plots (Tankersley,  
4699 2023) which I developed during this thesis and is used in all of the chapters. The  
4700 documentation of the package is hosted at the following link; <https://antarctic-plots.readthedocs.io/en/latest/index.html> and the code is stored and developed in the fol-  
4701 lowing GitHub repository; [https://github.com/mdtanker/antarctic\\_plots](https://github.com/mdtanker/antarctic_plots).  
4702

4703

4704 The Antarctic-Plots Python package aims to help automate common tasks as-  
4705 sociated with researching Antarctica. There are four main modules of the package;  
4706 **Fetch**, **Map**, **Profile**, and **Regions**.

### 4707 D.1 Fetch

4708 The Fetch module contains functions to download data related to Antarctica. These  
4709 downloads are accomplished with the Python package Pooch Uieda et al. (2020).  
4710 Calls to these functions will download the respective data and store it in a com-  
4711 mon folder in your system. Subsequent calls to the same function will retrieve the  
4712 already downloaded file. There is no need for remembering file paths or having  
4713 multiple copies of the same data throughout your projects. Additionally, some of  
4714 this data is pre-processed. This pre-processing includes re-projecting all data (grid-  
4715 ded or tabular) to a common projection, South Polar Stereographic (EPSG:3031),  
4716 and converting pre-gridded tabular data into more useful formats, such as Xarray  
4717 dataarrays. (Hoyer & Hamman, 2017).

4718 This module currently contains over 40 datasets, which include; topography  
4719 products, imagery, grounding line, coastline, and basin shapefiles, gravity, magnetics,  
4720 geothermal heat flow, ice velocity, sediment thickness, moho depths, basal melt,  
4721 ice mass change, and geologic units and faults. Below is an example that downloads,  
4722 or retrieves if already download, BedMachine v3 surface elevation data, converted  
4723 to be referenced to the WGS-84 ellipsoid (as opposed to the original data which is  
4724 referenced to the geoid), and resampled at a 5 km spacing.

```
4725 from antarctic_plots import fetch
4726
4727 surface_data = fetch.bedmachine(
4728     layer="surface",
4729     reference="ellipsoid",
4730     spacing=5000,
4731 )
4732
```

**4734 D.2 Map**

4735 The Map module provides convenient methods for plotting geospatial data. Most of  
4736 these plotting functions use the Python package PyGMT (Uieda et al., 2021). All  
4737 of the maps in Chapters 3, 4, & 5 were created with the help of these functions. In  
4738 addition to static figures, there are several functions for creating interactive figures,  
4739 which help with data visualization.

**4740 D.3 Profile**

4741 The Profile module is used to sample gridded data along specified profiles, and plot  
4742 cross-sections and profiles of the data. The cross-section plots of Chapters 3 & 4 were  
4743 created using these functions. Profiles can be defined by clicking on an interactive  
4744 map to help with quickly exploring and visualizing datasets.

**4745 D.4 Regions**

4746 The Regions module provides pre-defined variables of region boundaries in EPSG:3031  
4747 for commonly studied Antarctic areas. These region variables are used by the  
4748 other modules to subset the desired region. For example, if you only want to fetch  
4749 BedMap2 surface topography only for the Ross Ice Shelf, instead of the whole continent,  
4750 you can pass the parameter "region = regions.ross\_ice\_shelf".

4751 Additionally, there are geospatial tools provided for re-projecting, masking, and  
4752 gridding data. This package is still early in its development and many more datasets  
4753 and functions will still be added.

# 4754 Bibliography

- 4755 Adusumilli, S., Fricker, H. A., Medley, B., Padman, L., & Siegfried, M. R. (2020). Interannual  
4756 variations in meltwater input to the Southern Ocean from Antarctic ice shelves. *Nature  
4757 Geoscience*, *13*(9), 616–620. <https://doi.org/10.1038/s41561-020-0616-z> (cit. on pp. 16,  
4758 39, 90, 131, 132, 141)
- 4759 Aitken, A., Li, L., Kulessa, B., Schroeder, D., Jordan, T., Whittaker, J., Anandakrishnan, S.,  
4760 Dawson, E., Wiens, D., Eisen, O., & Siegert, M. (2023a). *Antarctic sedimentary basin  
4761 distribution and classification* (Version v1.04). Zenodo. <https://doi.org/10.5281/zenodo.7984586>. (Cit. on p. 139)
- 4763 Aitken, A. R., Li, L., Kulessa, B., Schroeder, D. M., Jordan, T. A., Whittaker, J. M., Anandakr-  
4764 ishnan, S., Dawson, E. J., Wiens, D. A., Eisen, O., & Siegert, M. J. (2023b). *Antarctica's  
4765 sedimentary basins and their influence on ice sheet dynamics* (Preprint). Preprints. <https://doi.org/10.11002/essoar.10510905.2>. (Cit. on pp. 17, 20, 138)
- 4767 Akiba, T., Sano, S., Yanase, T., Ohta, T., & Koyama, M. (2019). Optuna: A Next-generation  
4768 Hyperparameter Optimization Framework. *Proceedings of the 25th ACM SIGKDD Interna-  
4769 tional Conference on Knowledge Discovery & Data Mining*, 2623–2631. <https://doi.org/10.1145/3292500.3330701> (cit. on p. 51)
- 4771 Aleshkova, N. D., Golynsky, A. V., Kurinini, R. G., & Mandrikov, V. S. (2000). Gravity Mapping in  
4772 the Southern Weddell Sea Region. (Explanatory note for free-air and Bouguer anomalies  
4773 maps). *Polarforschung*, 15 pages. <https://doi.org/10.2312/POLARFORSCHUNG.67.3.163>  
4774 (cit. on p. 149)
- 4775 Alley, R. B., Blankenship, D. D., Bentley, C. R., & Rooney, S. T. (1986). Deformation of till  
4776 beneath ice stream B, West Antarctica. *Nature*, *322*(6074), 57–59. <https://doi.org/10.1038/322057a0> (cit. on pp. 20, 144)
- 4778 An, L., Rignot, E., Elieff, S., Morlighem, M., Millan, R., Mouginot, J., Holland, D. M., Holland,  
4779 D., & Paden, J. (2017). Bed elevation of Jakobshavn Isbrae, West Greenland, from high-  
4780 resolution airborne gravity and other data. *Geophysical Research Letters*, *44*(8), 3728–  
4781 3736. <https://doi.org/10.1002/2017GL073245> (cit. on pp. 105, 106, 120)
- 4782 An, L., Rignot, E., Chauche, N., Holland, D. M., Holland, D., Jakobsson, M., Kane, E., Wood,  
4783 M., Klaucke, I., Morlighem, M., Velicogna, I., Weinrebe, W., & Willis, J. K. (2019a).  
4784 Bathymetry of Southeast Greenland From Oceans Melting Greenland (OMG) Data. *Geo-  
4785 physical Research Letters*, *46*(20), 11197–11205. <https://doi.org/10.1029/2019GL083953>  
4786 (cit. on pp. 46, 63, 105–107, 120, 122)
- 4787 An, L., Rignot, E., Millan, R., Tinto, K., & Willis, J. (2019b). Bathymetry of Northwest Greenland  
4788 Using “Ocean Melting Greenland” (OMG) High-Resolution Airborne Gravity and Other  
4789 Data. *Remote Sensing*, *11*(2), 131. <https://doi.org/10.3390/rs11020131> (cit. on pp. 105–  
4790 107)
- 4791 An, M., Wiens, D. A., Zhao, Y., Feng, M., Nyblade, A. A., Kanao, M., Li, Y., Maggi, A., & Lévéque,  
4792 J.-J. (2015). S-velocity model and inferred Moho topography beneath the Antarctic Plate  
4793 from Rayleigh waves: Antarctic S-velocities and Moho. *Journal of Geophysical Research:  
4794 Solid Earth*, *120*(1), 359–383. <https://doi.org/10.1002/2014JB011332> (cit. on pp. 29, 155)
- 4795 Anandakrishnan, S., Blankenship, D. D., Alley, R. B., & Stoffa, P. L. (1998). Influence of subglacial  
4796 geology on the position of a West Antarctic ice stream from seismic observations. *Nature*,  
4797 *394*(6688), 62–65. <https://doi.org/10.1038/27889> (cit. on p. 20)
- 4798 Anderson, J. B., Conway, H., Bart, P. J., Witus, A. E., Greenwood, S. L., McKay, R., Hall, B. H.,  
4799 Ackert, R. P., Licht, K., Jakobsson, M., & Stone, J. O. (2014). Ross Sea paleo-ice drainage  
4800 and deglacial history during and since the LGM. *Quaternary Science Reviews*, *100*, 31–54.  
4801 <https://doi.org/10.1016/j.quascirev.2013.08.020> (cit. on p. 16)

- 4802 Anderson, J. B., Simkins, L. M., Bart, P. J., De Santis, L., Halberstadt, A. R. W., Olivo, E., &  
 4803 Greenwood, S. L. (2019). Seismic and geomorphic records of Antarctic Ice Sheet evolution  
 4804 in the Ross Sea and controlling factors in its behaviour. *Geological Society, London, Special*  
 4805 *Publications*, 475(1), 223–240. <https://doi.org/10.1144/SP475.5> (cit. on pp. 16, 20, 145–  
 4806 147)
- 4807 Andrews, J. T., & LeMasurier, W. (2021). Resolving the argument about volcanic bedrock under  
 4808 the West Antarctic Ice Sheet and implications for ice sheet stability and sea level change.  
 4809 *Earth and Planetary Science Letters*, 568, 117035. [https://doi.org/10.1016/j.epsl.2021.](https://doi.org/10.1016/j.epsl.2021.117035)  
 4810 117035 (cit. on p. 152)
- 4811 Aster, R. C., Borchers, B., & Thurber, C. H. (2018). *Parameter estimation and inverse problems*.  
 4812 Elsevier. (Cit. on pp. 42, 48, 103, 106).
- 4813 Austermann, J., Pollard, D., Mitrovica, J. X., Moucha, R., Forte, A. M., DeConto, R. M., Rowley,  
 4814 D. B., & Raymo, M. E. (2015). The impact of dynamic topography change on Antarctic  
 4815 ice sheet stability during the mid-Pliocene warm period. *Geology*, 43(10), 927–930. <https://doi.org/10.1130/G36988.1> (cit. on p. 26)
- 4816 Bamber, J. L., Oppenheimer, M., Kopp, R. E., Aspinall, W. P., & Cooke, R. M. (2022). Ice  
 4817 Sheet and Climate Processes Driving the Uncertainty in Projections of Future Sea Level  
 4818 Rise: Findings From a Structured Expert Judgement Approach. *Earth's Future*, 10(10).  
 4819 <https://doi.org/10.1029/2022EF002772> (cit. on pp. 15, 16)
- 4820 Bamber, J., & Bentley, C. R. (1994). A comparison of satellite-altimetry and ice-thickness mea-  
 4821 surements of the Ross Ice Shelf, Antarctica. *Annals of Glaciology*, 20, 357–364. <https://doi.org/10.3189/1994AoG20-1-357-364> (cit. on p. 38)
- 4822 Barbosa, V. C., Menezes, P. T., & Silva, J. B. (2007). Gravity data as a tool for detecting faults:  
 4823 In-depth enhancement of subtle Almada's basement faults, Brazil. *GEOPHYSICS*, 72(3),  
 4824 B59–B68. <https://doi.org/10.1190/1.2713226> (cit. on p. 42)
- 4825 Barletta, V. R., Bevis, M., Smith, B. E., Wilson, T., Brown, A., Bordoni, A., Willis, M., Khan,  
 4826 S. A., Rovira-Navarro, M., Dalziel, I., Smalley, R., Kendrick, E., Konfal, S., Caccamise,  
 4827 D. J., Aster, R. C., Nyblade, A., & Wiens, D. A. (2018). Observed rapid bedrock uplift in  
 4828 Amundsen Sea Embayment promotes ice-sheet stability. *Science*, 360(6395), 1335–1339.  
 4829 <https://doi.org/10.1126/science.aa01447> (cit. on pp. 18, 143, 144)
- 4830 Bart, P., & De Santis, L. (2012). Glacial intensification during the Neogene: A review of seismic  
 4831 stratigraphic evidence from the Ross Sea, Antarctica, continental shelf. *Oceanography*,  
 4832 25(3), 166–183. <https://doi.org/10.5670/oceanog.2012.92> (cit. on p. 34)
- 4833 Bart, P. J., Krogmeier, B. J., Bart, M. P., & Tulaczyk, S. (2017). The paradox of a long grounding  
 4834 during West Antarctic Ice Sheet retreat in Ross Sea. *Scientific Reports*, 7(1), 1262. <https://doi.org/10.1038/s41598-017-01329-8> (cit. on p. 146)
- 4835 Beaudoin, B. C., ten Brink, U. S., & Stern, T. A. (1992). Characteristics and processing of seismic  
 4836 data collected on thick, floating ice: Results from the Ross Ice Shelf, Antarctica. *Geo-  
 4837 physics*, 57(10), 1359–1372. <https://doi.org/10.1190/1.1443205> (cit. on p. 31)
- 4838 Begeman, C. B., Tulaczyk, S. M., & Fisher, A. T. (2017). Spatially Variable Geothermal Heat  
 4839 Flux in West Antarctica: Evidence and Implications. *Geophysical Research Letters*, 44(19),  
 4840 9823–9832. <https://doi.org/10.1002/2017GL075579> (cit. on pp. 28, 144)
- 4841 Bell, R. E., Blankenship, D. D., Finn, C. A., Morse, D. L., Scambos, T. A., Brozena, J. M., &  
 4842 Hodge, S. M. (1998). Influence of subglacial geology on the onset of a West Antarctic ice  
 4843 stream from aerogeophysical observations. *Nature*, 394(6688), 58–62. <https://doi.org/10.1038/27883> (cit. on p. 20)
- 4844 Bell, R. E., Studinger, M., Karner, G., Finn, C. A., & Blankenship, D. D. (2006). Identifying  
 4845 major sedimentary basins beneath the West Antarctic Ice Sheet from aeromagnetic data  
 4846 analysis. In D. K. Fütterer, D. Damaske, G. Kleinschmidt, H. Miller, & F. Tessensohn  
 4847 (Eds.), *Antarctica* (pp. 117–121). Springer-Verlag. [https://doi.org/10.1007/3-540-32934-X\\_13](https://doi.org/10.1007/3-540-32934-X_13). (Cit. on pp. 28, 30–32, 153)
- 4848 Bell, R. E., Ferraccioli, F., Creyts, T. T., Braaten, D., Corr, H., Das, I., Damaske, D., Frearson,  
 4849 N., Jordan, T., Rose, K., Studinger, M., & Wolovick, M. (2011). Widespread Persistent  
 4850 Thickening of the East Antarctic Ice Sheet by Freezing from the Base. *Science*, 331(6024),  
 4851 1592–1595. <https://doi.org/10.1126/science.1200109> (cit. on p. 26)
- 4852 Bennett, H. F. (1964). *A gravity and magnetic survey of the Ross Ice Shelf area, Antarctica* (tech.  
 4853 rep. No. 64-3). The University of Wisconsin. Madison. (Cit. on p. 108).
- 4854 Bentley, C. R., Crary, A. P., Ostenso, N. A., & Thiel, E. C. (1960). Structure of West Antarctica.  
 4855 *Science*, 131(3394), 131–136. <https://doi.org/10.1126/science.131.3394.131> (cit. on p. 21)

- 4861 Bentley, C. R. (1984). The Ross Ice Shelf: Glaciology and Geophysics Paper 1: Introduction and  
 4862 summary of measurements performed. In C. R. Bentley & D. E. Hayes (Eds.), *Antarctic*  
 4863 *Research Series* (pp. 1–20). American Geophysical Union. <https://doi.org/10.1029/AR042p0001>. (Cit. on pp. 18, 21, 91, 108, 111)
- 4865 Block, A. E., Bell, R. E., & Studinger, M. (2009). Antarctic crustal thickness from satellite gravity:  
 4866 Implications for the Transantarctic and Gamburtsev Subglacial Mountains. *Earth and*  
 4867 *Planetary Science Letters*, 288(1-2), 194–203. <https://doi.org/10.1016/j.epsl.2009.09.022>  
 4868 (cit. on p. 133)
- 4869 Boghosian, A., Tinto, K., Cochran, J. R., Porter, D., Elieff, S., Burton, B. L., & Bell, R. E. (2015).  
 4870 Resolving bathymetry from airborne gravity along Greenland fjords. *Journal of Geophysical*  
 4871 *Research: Solid Earth*, 120(12), 8516–8533. <https://doi.org/10.1002/2015JB012129>  
 4872 (cit. on pp. 78, 104–107, 120)
- 4873 Borg, S. G., Depaolo, D. J., & Smith, B. M. (1990). Isotopic structure and tectonics of the central  
 4874 Transantarctic mountains. *Journal of Geophysical Research*, 95(B5), 6647. <https://doi.org/10.1029/JB095iB05p06647> (cit. on pp. 32, 34)
- 4875 Borghi, A. (2022). Moho depths for Antarctica Region by the inversion of ground-based gravity  
 4876 data. *Geophysical Journal International*, 231(2), 1404–1420. <https://doi.org/10.1093/gji/ggac249> (cit. on p. 42)
- 4877 Bougamont, M., Christoffersen, P., Price, S. F., Fricker, H. A., Tulaczyk, S., & Carter, S. P. (2015).  
 4878 Reactivation of Kamb Ice Stream tributaries triggers century-scale reorganization of Siple  
 4879 Coast ice flow in West Antarctica: Restructuring of Siple Coast Ice Flow. *Geophysical*  
 4880 *Research Letters*, 42(20), 8471–8480. <https://doi.org/10.1002/2015GL065782> (cit. on  
 4881 p. 145)
- 4882 Bourgeois, B. S., Elmore, P. A., Avera, W. E., & Zambo, S. J. (2016). Achieving comparable uncer-  
 4883 tainty estimates with Kalman filters or linear smoothers for bathymetry data. *Geochemistry,*  
 4884 *Geophysics, Geosystems*, 17(7), 2576–2590. <https://doi.org/10.1002/2015GC006239>  
 4885 (cit. on pp. 84, 85)
- 4886 Brancolini, G., Busetti, M., Marchetti, A., Santis, L. D., Zanolla, C., Cooper, A. K., Cochrane,  
 4887 G. R., Zayatz, I., Belyaev, V., Knyazev, M., Vinnikovskaya, O., Davey, F. J., & Hinze, K.  
 4888 (1995). Descriptive text for the seismic stratigraphic atlas of the Ross Sea, Antarctica. In  
 4889 A. K. Cooper, P. F. Barker, & G. Brancolini (Eds.), *Geology and Seismic Stratigraphy of*  
 4890 *the Antarctic Margin* (A271–A286). American Geophysical Union. <https://doi.org/10.1002/9781118669013.app1>. (Cit. on pp. 26–28, 67, 68, 147, 151, 153, 156)
- 4891 Brisbourne, A. M., Kulessa, B., Hudson, T., Harrison, L., Holland, P., Luckman, A., Bevan, S.,  
 4892 Ashmore, D., Hubbard, B., Pearce, E., White, J., Booth, A., Nicholls, K., & Smith, A.  
 4893 (2020). An updated seabed bathymetry beneath Larsen C Ice Shelf, Antarctic Peninsula.  
 4894 *Earth System Science Data*, 12(2), 887–896. <https://doi.org/10.5194/essd-12-887-2020>  
 4895 (cit. on pp. 70, 124, 149)
- 4896 Brisbourne, A. M., Smith, A. M., King, E. C., Nicholls, K. W., Holland, P. R., & Makinson,  
 4897 K. (2014). Seabed topography beneath Larsen C Ice Shelf from seismic soundings. *The*  
 4898 *Cryosphere*, 8(1), 1–13. <https://doi.org/10.5194/tc-8-1-2014> (cit. on pp. 45, 80, 99, 120)
- 4899 Burton-Johnson, A., Dziadek, R., & Martin, C. (2020). Geothermal heat flow in Antarctica: Current  
 4900 and future directions. *The Cryosphere Discussions*, 1–45. <https://doi.org/10.5194/tc-2020-59> (cit. on pp. 32, 139, 144, 145)
- 4901 Calder, B., & Elmore, P. (2017). Development of an Uncertainty Propagation Equation for Scalar  
 4902 Fields. *Marine Geodesy*, 40(5), 341–360. <https://doi.org/10.1080/01490419.2017.1345811>  
 4903 (cit. on p. 85)
- 4904 Catania, G., Hulbe, C., Conway, H., Scambos, T., & Raymond, C. (2012). Variability in the  
 4905 mass flux of the Ross ice streams, West Antarctica, over the last millennium. *Journal of*  
 4906 *Glaciology*, 58(210), 741–752. <https://doi.org/10.3189/2012JoG11J219> (cit. on p. 145)
- 4907 Chen, B., Haeger, C., Kaban, M. K., & Petrunin, A. G. (2018). Variations of the effective elastic  
 4908 thickness reveal tectonic fragmentation of the Antarctic lithosphere. *Tectonophysics*, 746,  
 4909 412–424. <https://doi.org/10.1016/j.tecto.2017.06.012> (cit. on p. 143)
- 4910 Cheng, W., Hu, X. G., & Liu, L. T. (2021). Anisotropy Gradients in the Middle of the Ross Sea  
 4911 Embayment, West Antarctica: Evidence From QL Scattered Surface Waves. *Geophysical*  
 4912 *Research Letters*, 48(6). <https://doi.org/10.1029/2020GL091232> (cit. on p. 34)
- 4913 Chiappini, M., Ferraccioli, F., Bozzo, E., & Damaske, D. (2002). Regional compilation and analysis  
 4914 of aeromagnetic anomalies for the Transantarctic Mountains–Ross Sea sector of the Antarc-

- tic. *Tectonophysics*, 347(1-3), 121–137. [https://doi.org/10.1016/S0040-1951\(01\)00241-4](https://doi.org/10.1016/S0040-1951(01)00241-4) (cit. on p. 30)
- Christoffersen, P., Bougamont, M., Carter, S. P., Fricker, H. A., & Tulaczyk, S. (2014). Significant groundwater contribution to Antarctic ice streams hydrologic budget. *Geophysical Research Letters*, 41(6), 2003–2010. <https://doi.org/10.1002/2014GL059250> (cit. on pp. 19, 26, 144, 145)
- Clough, J. W., & Hansen, B. L. (1979). The Ross Ice Shelf Project. *Science*, 203(4379), 433–434. <https://doi.org/10.1126/science.203.4379.433> (cit. on pp. 18, 91)
- Cochran, J. R., Burton, B., Frearson, N., & Tinto, K. (2014a). IceBridge Scintrex CS-3 Cesium magnetometer L1B geolocated magnetic anomalies, version 2. [Line 403, 404]. *Boulder, Colorado USA. NASA National Snow and Ice Data Center Distributed Active Archive Center*. <https://doi.org/10.5067/OY7C2Y61YSYW> (cit. on pp. 28, 151, 153)
- Cochran, J. R., Jacobs, S. S., Tinto, K. J., & Bell, R. E. (2014b). Bathymetric and oceanic controls on Abbot Ice Shelf thickness and stability. *The Cryosphere*, 8(3), 877–889. <https://doi.org/10.5194/tc-8-877-2014> (cit. on pp. 105, 106)
- Cochran, J. R., & Bell, R. E. (2012). Inversion of IceBridge gravity data for continental shelf bathymetry beneath the Larsen Ice Shelf, Antarctica. *Journal of Glaciology*, 58(209), 540–552. <https://doi.org/10.3189/2012JoG11J033> (cit. on pp. 104–106, 149)
- Cochran, J. R., Tinto, K. J., & Bell, R. E. (2020). Detailed Bathymetry of the Continental Shelf Beneath the Getz Ice Shelf, West Antarctica. *Journal of Geophysical Research: Earth Surface*, 125(10). <https://doi.org/10.1029/2019JF005493> (cit. on pp. 46, 104–106, 149)
- Coenen, J. J., Scherer, R. P., Baudoin, P., Warny, S., Castañeda, I. S., & Askin, R. (2019). Paleogene marine and terrestrial development of the West Antarctic Rift System. *Geophysical Research Letters*, 47(3). <https://doi.org/10.1029/2019GL085281> (cit. on pp. 26, 33, 147)
- Colleoni, F., De Santis, L., Montoli, E., Olivo, E., Sorlien, C. C., Bart, P. J., Gasson, E. G. W., Bergamasco, A., Sauli, C., Wardell, N., & Prato, S. (2018). Past continental shelf evolution increased Antarctic ice sheet sensitivity to climatic conditions. *Scientific Reports*, 8(1), 11323. <https://doi.org/10.1038/s41598-018-29718-7> (cit. on p. 26)
- Constantino, R. R., & Tinto, K. J. (2023). Cook Ice Shelf and Ninnis Glacier Tongue Bathymetry From Inversion of Operation Ice Bridge Airborne Gravity Data. *Geophysical Research Letters*, 50(11), e2023GL103815. <https://doi.org/10.1029/2023GL103815> (cit. on pp. 106, 120)
- Constantino, R. R., Tinto, K. J., Bell, R. E., Porter, D. F., & Jordan, T. A. (2020). Seafloor Depth of George VI Sound, Antarctic Peninsula, From Inversion of Aerogravity Data. *Geophysical Research Letters*, 47(21). <https://doi.org/10.1029/2020GL088654> (cit. on pp. 104, 105, 107, 120, 122)
- Cooper, A. K., Barker, P. F., & Brancolini, G. (Eds.). (1995). *Geology and seismic stratigraphy of the Antarctic margin*. AGU. <https://doi.org/10.1029/AR068>. (Cit. on p. 31)
- Coulon, V., Bulthuis, K., Whitehouse, P. L., Sun, S., Haubner, K., Zipf, L., & Pattyn, F. (2021). Contrasting response of West and East Antarctic Ice Sheets to glacial isostatic adjustment. *Journal of Geophysical Research: Earth Surface*, 126(7). <https://doi.org/10.1029/2020JF006003> (cit. on pp. 18, 33, 144)
- Cox, S. C., Smith Lyttle, B., Elkind, S., Smith Siddoway, C., Morin, P., Capponi, G., Abu-Alam, T., Ballinger, M., Bamber, L., Kitchener, B., Lelli, L., Mawson, J., Millikin, A., Dal Seno, N., Whitburn, L., White, T., Burton-Johnson, A., Crispini, L., Elliot, D., ... Wilson, G. (2023). A continent-wide detailed geological map dataset of Antarctica. *Scientific Data*, 10(1), 250. <https://doi.org/10.1038/s41597-023-02152-9> (cit. on pp. 139, 152)
- Crary, A. P. (1961). Marine-sediment thickness in the eastern Ross Sea area, Antarctica. *Geological Society of America Bulletin*, 72(5), 787. [https://doi.org/10.1130/0016-7606\(1961\)72\[787:MTITER\]2.0.CO;2](https://doi.org/10.1130/0016-7606(1961)72[787:MTITER]2.0.CO;2) (cit. on p. 156)
- Crary, A. P., Robinson, E. S., Bennett, H. F., & Boyd, W. (1962). *Glaciological studies on the Ross Ice Shelf, Antarctica; 1957-1960* (tech. rep. No. 6). American Geographical Society. New York, NY, USA. (Cit. on pp. 91, 108).
- Crary, A. (1959). Oversnow Traverses from IGY Little American Station. *Transactions, American Geophysical Union*, 40(3), 311–315. <https://doi.org/10.1029/TR040i003p00269> (cit. on pp. 21, 91, 108)
- Crary, A., & Robinson, E. (1962). Oversnow Traverse from McMurdo to the South Pole. *Science*, 135(3500), 291–295. <https://doi.org/10.1126/science.135.3500.291> (cit. on pp. 91, 108)

- 4977 Dampney, C. N. G. (1969). The equivalent source technique, 15. <https://doi.org/10.1190/1.1439996>  
 4978 (cit. on pp. 57, 112)
- 4979 Das, I., Padman, L., Bell, R. E., Fricker, H. A., Tinto, K. J., Hulbe, C. L., Siddoway, C. S.,  
 4980 Dhakal, T., Frearson, N. P., Mosbeux, C., Cordero, S. I., & Siegfried, M. R. (2020). Multi-  
 4981 decadal basal melt rates and structure of the Ross Ice Shelf, Antarctica using airborne ice  
 4982 penetrating radar. *Journal of Geophysical Research: Earth Surface*, 1–20. <https://doi.org/10.1029/2019JF005241> (cit. on pp. 21, 38, 132, 141)
- 4984 De Rydt, J., Holland, P. R., Dutrieux, P., & Jenkins, A. (2014). Geometric and oceanographic  
 4985 controls on melting beneath Pine Island Glacier. *Journal of Geophysical Research: Oceans*,  
 4986 119(4), 2420–2438. <https://doi.org/10.1002/2013JC009513> (cit. on pp. 16, 90, 91)
- 4987 De Santis, L. (1999). The Eastern Ross Sea continental shelf during the Cenozoic: Implications for  
 4988 the West Antarctic ice sheet development. *Global and Planetary Change*, 23(1-4), 173–196.  
 4989 [https://doi.org/10.1016/S0921-8181\(99\)00056-9](https://doi.org/10.1016/S0921-8181(99)00056-9) (cit. on p. 147)
- 4990 De Santis, L., Anderson, J. B., Brancolini, G., & Zayatz, I. (1995). Seismic record of late Oligocene  
 4991 through Miocene glaciation on the central and eastern continental shelf of the Ross Sea. In  
 4992 A. K. Cooper, P. F. Barker, & G. Brancolini (Eds.), *Antarctic Research Series* (pp. 235–  
 4993 260). American Geophysical Union. <https://doi.org/10.1029/AR068p0235>. (Cit. on pp. 34,  
 4994 147)
- 4995 DeConto, R. M., & Pollard, D. (2003). A coupled climate–ice sheet modeling approach to the  
 4996 Early Cenozoic history of the Antarctic ice sheet. *Palaeogeography, Palaeoclimatology,*  
 4997 *Palaeoecology*, 198(1-2), 39–52. [https://doi.org/10.1016/S0031-0182\(03\)00393-6](https://doi.org/10.1016/S0031-0182(03)00393-6) (cit. on  
 4998 p. 26)
- 4999 Deng, X., & Tang, Z.-a. (2011). Moving Surface Spline Interpolation Based on Green’s Function.  
 5000 *Mathematical Geosciences*, 43(6), 663–680. <https://doi.org/10.1007/s11004-011-9346-5>  
 5001 (cit. on p. 63)
- 5002 Dinniman, M. S., Klinck, J. M., & Smith, W. O. (2011). A model study of Circumpolar Deep Water  
 5003 on the West Antarctic Peninsula and Ross Sea continental shelves. *Deep Sea Research Part*  
 5004 *II: Topical Studies in Oceanography*, 58(13–16), 1508–1523. <https://doi.org/10.1016/j.dsr2.2010.11.013> (cit. on pp. 90, 132)
- 5006 Dorschel, B., Hehemann, L., Viquerat, S., Warnke, F., Dreutter, S., Tenberge, Y. S., Accettella, D.,  
 5007 An, L., Barrios, F., Bazhenova, E., Black, J., Bohoyo, F., Davey, C., De Santis, L., Dotti,  
 5008 C. E., Fremand, A. C., Fretwell, P. T., Gales, J. A., Gao, J., ... Arndt, J. E. (2022). The  
 5009 International Bathymetric Chart of the Southern Ocean Version 2. *Scientific Data*, 9(1),  
 5010 275. <https://doi.org/10.1038/s41597-022-01366-7> (cit. on pp. 67, 68, 70)  
 5011 IBCSO
- 5012 Dowdeswell, J., Evans, J., Mugford, R., Griffiths, G., McPhail, S., Millard, N., Stevenson, P., Brandon,  
 5013 M., Banks, C., Heywood, K., Price, M., Dodd, P., Jenkins, A., Nicholls, K., Hayes,  
 5014 D., Abrahamsen, E., Tyler, P., Bett, B., Jones, D., ... Ackley, S. (2008). Autonomous  
 5015 underwater vehicles (AUVs) and investigations of the ice–ocean interface in Antarctic  
 5016 and Arctic waters. *Journal of Glaciology*, 54(187), 661–672. <https://doi.org/10.3189/002214308786570773> (cit. on p. 18)
- 5018 Drenth, B. J., Grauch, V., Turner, K. J., Rodriguez, B. D., Thompson, R. A., & Bauer, P. W.  
 5019 (2019). A shallow rift basin segmented in space and time: The southern San Luis Basin,  
 5020 Rio Grande rift, northern New Mexico, U.S.A. *Rocky Mountain Geology*, 54(2), 97–131.  
 5021 <https://doi.org/10.24872/rmgjournal.54.2.97> (cit. on p. 29)
- 5022 Dupont, T. K., & Alley, R. B. (2005). Assessment of the importance of ice-shelf buttressing to  
 5023 ice-sheet flow. *Geophysical Research Letters*, 32, 1–4. <https://doi.org/10.1029/2004GL022024> (cit. on pp. 17, 38, 90)
- 5025 Durand, G., van den Broeke, M. R., Le Cozannet, G., Edwards, T. L., Holland, P. R., Jourdain,  
 5026 N. C., Marzeion, B., Mottram, R., Nicholls, R. J., Pattyn, F., Paul, F., Slangen, A. B. A.,  
 5027 Winkelmann, R., Burgard, C., van Calcar, C. J., Barré, J.-B., Bataille, A., & Chapuis, A.  
 5028 (2022). Sea-Level Rise: From Global Perspectives to Local Services. *Frontiers in Marine*  
 5029 *Science*, 8, 709595. <https://doi.org/10.3389/fmars.2021.709595> (cit. on pp. 15, 137)
- 5030 Dutrieux, P., De Rydt, J., Jenkins, A., Holland, P. R., Ha, H. K., Lee, S. H., Steig, E. J., Ding,  
 5031 Q., Abrahamsen, E. P., & Schröder, M. (2014). Strong Sensitivity of Pine Island Ice-Shelf  
 5032 Melting to Climatic Variability. *Science*, 343(6167), 174–178. <https://doi.org/10.1126/science.1244341> (cit. on p. 90)
- 5034 Edwards, T. L., Nowicki, S., Marzeion, B., Hock, R., Goelzer, H., Seroussi, H., Jourdain, N. C.,  
 5035 Slater, D. A., Turner, F. E., Smith, C. J., McKenna, C. M., Simon, E., Abe-Ouchi, A.,

- 5036 Gregory, J. M., Larour, E., Lipscomb, W. H., Payne, A. J., Shepherd, A., Agosta, C., ...  
 5037 Zwinger, T. (2021). Projected land ice contributions to twenty-first-century sea level rise.  
 5038 *Nature*, 593(7857), 74–82. <https://doi.org/10.1038/s41586-021-03302-y> (cit. on p. 15)
- 5039 Eisermann, H., Eagles, G., Ruppel, A., Smith, E. C., & Jokat, W. (2020). Bathymetry Beneath Ice  
 5040 Shelves of Western Dronning Maud Land, East Antarctica, and Implications on Ice Shelf  
 5041 Stability. *Geophysical Research Letters*, 47(12). <https://doi.org/10.1029/2019GL086724>  
 5042 (cit. on pp. 45, 104–106, 120)
- 5043 Eisermann, H., Eagles, G., Ruppel, A. S., Läufer, A., & Jokat, W. (2021). Bathymetric Control  
 5044 on Borchgrevink and Roi Baudouin Ice Shelves in East Antarctica. *Journal of Geophysical*  
 5045 *Research: Earth Surface*, 126(10). <https://doi.org/10.1029/2021JF006342> (cit. on pp. 105,  
 5046 106, 120)
- 5047 Fahnestock, M. A., Scambos, T. A., Bindschadler, R. A., & Kvaran, G. (2000). A millennium of  
 5048 variable ice flow recorded by the Ross Ice Shelf, Antarctica. *Journal of Glaciology*, 13.  
 5049 <https://doi.org/10.3189/172756500781832693> (cit. on p. 143)
- 5050 Fatiando a Terra Project, Dinneen, C., Gomez, M., Li, L., Pesce, A., Soler, S. R., & Uieda, L.  
 5051 (2022). Boule v0.4.1: Reference ellipsoids for geodesy and geophysics. <https://doi.org/10.5281/zenodo.7258175>. (Cit. on p. 169)
- 5052 Fatiando a Terra Project, Esteban, F. D., Li, L., Oliveira, V. C., Pesce, A., Shea, N., Soler, S. R.,  
 5053 Tankersley, M., & Uieda, L. (2023). Harmonica v0.6.0: Forward modeling, inversion, and  
 5054 processing gravity and magnetic data. <https://doi.org/10.5281/zenodo.7690145>. (Cit. on  
 5055 pp. 43, 48, 51, 95)
- 5056 Ferraccioli, F., Bozzo, E., & Damaske, D. (2002). Aeromagnetic signatures over western Marie Byrd  
 5057 Land provide insight into magmatic arc basement, mafic magmatism and structure of the  
 5058 Eastern Ross Sea Rift flank. *Tectonophysics*, 347, 139–165. [https://doi.org/10.1016/S0040-1951\(01\)00242-6](https://doi.org/10.1016/S0040-1951(01)00242-6) (cit. on p. 30)
- 5059 Filina, I. Y., Blankenship, D. D., Thoma, M., Lukin, V. V., Masolov, V. N., & Sen, M. K. (2008).  
 5060 New 3D bathymetry and sediment distribution in Lake Vostok: Implication for pre-glacial  
 5061 origin and numerical modeling of the internal processes within the lake. *Earth and Planetary*  
 5062 *Science Letters*, 276(1-2), 106–114. <https://doi.org/10.1016/j.epsl.2008.09.012>  
 5063 (cit. on pp. 106, 120)
- 5064 Finn, C. (2002). *Examples of the utility of magnetic anomaly data for geologic mapping* (Open-File  
 5065 Report No. 02-400). USGS. Denver, Colorado. (Cit. on p. 29).
- 5066 Fisher, A. T., Mankoff, K. D., Tulaczyk, S. M., Tyler, S. W., Foley, N., & and the WISSARD  
 5067 Science Team. (2015). High geothermal heat flux measured below the West Antarctic Ice  
 5068 Sheet. *Science Advances*, 1, 1–9. <https://doi.org/10.1126/sciadv.1500093> (cit. on pp. 33,  
 5069 145)
- 5070 Ford, A., & Barrett, P. J. (1975). *Basement rocks of the south-central Ross Sea, site 270, DSDP*  
 5071 *leg 28* (tech. rep.). Texas A & M University, Ocean Drilling Program. College Station, TX,  
 5072 United States. <https://doi.org/10.2973/dsdp.proc.28.130.1975>. (Cit. on p. 26)
- 5073 Forsberg, R. (2020). Preliminary compilation of Antarctica gravity and gravity gradient data (cit.  
 5074 on p. 139).
- 5075 Förste, C., Bruinsma, S., Abrikosov, O., Lemoine, J.-M., Marty, J. C., Flechtner, F., Balmino, G.,  
 5076 Barthelmes, F., & Biancale, R. (2014). EIGEN-6C4 The latest combined global gravity  
 5077 field model including GOCE data up to degree and order 2190 of GFZ Potsdam and GRGS  
 5078 Toulouse. <https://doi.org/10.5880/ICGEM.2015.1>. (Cit. on pp. 95, 169)
- 5079 Fox Maule, C., Purucker, M. E., Olsen, N., & Mosegaard, K. (2005). Heat Flux Anomalies in  
 5080 Antarctica Revealed by Satellite Magnetic Data. *Science*, 309(5733), 464–467. <https://doi.org/10.1126/science.1106888> (cit. on p. 144)
- 5081 Frederick, B. C., Young, D. A., Blankenship, D. D., Richter, T. G., Kempf, S. D., Ferraccioli, F.,  
 5082 & Siegert, M. J. (2016). Distribution of subglacial sediments across the Wilkes Subglacial  
 5083 Basin, East Antarctica. *Journal of Geophysical Research: Earth Surface*, 121(4), 790–813.  
 5084 <https://doi.org/10.1002/2015JF003760> (cit. on pp. 28, 153)
- 5085 Frémard, A. C., Fretwell, P., Bodart, J., Pritchard, H. D., Aitken, A., Bamber, J. L., Bell, R.,  
 5086 Bianchi, C., Bingham, R. G., Blankenship, D. D., Casassa, G., Catania, G., Christianson,  
 5087 K., Conway, H., Corr, H. F. J., Cui, X., Damaske, D., Damm, V., Drews, R., ... Zirizzotti,  
 5088 A. (2022). Antarctic Bedmap data: FAIR sharing of 60 years of ice bed, surface and  
 5089 thickness data. *Earth System Science Data Discussions*, 1–25. <https://doi.org/10.5194/essd-2022-355> (cit. on p. 17)

- 5094 Fretwell, P., Pritchard, H. D., Vaughan, D. G., Bamber, J. L., Barrand, N. E., Bell, R. E., Bianchi,  
 5095 C., Bingham, R. G., Blankenship, D. D., Casassa, G., Catania, G., Callens, D., Conway,  
 5096 H., Cook, A. J., Corr, H. F. J., Damaske, D., Damm, V., Ferraccioli, F., Forsberg, R.,  
 5097 ... Zirizzotti, A. (2013). Bedmap2: Improved ice bed, surface and thickness datasets for  
 5098 Antarctica. *The Cryosphere*, 7(1), 375–393. <https://doi.org/10.5194/tc-7-375-2013> (cit.  
 5099 on pp. 15, 18, 20, 77, 90, 91, 97, 98, 108, 124, 137, 149, 159)
- 5100 Fricker, H. A., Popov, S., Allison, I., & Young, N. (2001). Distribution of marine ice beneath the  
 5101 Amery Ice Shelf. *Geophysical Research Letters*, 28(11), 2241–2244. <https://doi.org/10.1029/2000GL012461> (cit. on p. 121)
- 5102 Fürst, J. J., Durand, G., Gillet-Chaulet, F., Tavard, L., Rankl, M., Braun, M., & Gagliardini, O.  
 5103 (2016). The safety band of Antarctic ice shelves. *Nature Climate Change*, 6(5), 479–482.  
 5104 <https://doi.org/10.1038/nclimate2912> (cit. on p. 90)
- 5105 Gladish, C. V., Holland, D. M., Rosing-Asvid, A., Behrens, J. W., & Boje, J. (2015). Oceanic  
 5106 Boundary Conditions for Jakobshavn Glacier. Part I: Variability and Renewal of Ilulissat  
 5107 Icefjord Waters, 2001–14. *Journal of Physical Oceanography*, 45(1), 3–32. <https://doi.org/10.1175/JPO-D-14-0044.1> (cit. on p. 90)
- 5108 Goldberg, D. N., Gourmelen, N., Kimura, S., Millan, R., & Snow, K. (2019). How Accurately  
 5109 Should We Model Ice Shelf Melt Rates? *Geophysical Research Letters*, 46(1), 189–199.  
 5110 <https://doi.org/10.1029/2018GL080383> (cit. on p. 91)
- 5111 Goldberg, D. N., Smith, T. A., Narayanan, S. H. K., Heimbach, P., & Morlighem, M. (2020).  
 5112 Bathymetric Influences on Antarctic Ice-Shelf Melt Rates. *Journal of Geophysical Research: Oceans*, 125(11). <https://doi.org/10.1029/2020JC016370> (cit. on pp. 16, 91,  
 5113 92)
- 5114 Golledge, N. R., Marsh, O. J., Rack, W., Braaten, D., & Jones, R. S. (2014). Basal conditions of two  
 5115 Transantarctic Mountains outlet glaciers from observation-constrained diagnostic mod-  
 5116elling. *Journal of Glaciology*, 60(223), 855–866. <https://doi.org/10.3189/2014JoG13J131>  
 5117 (cit. on p. 144)
- 5118 Golynsky, A. V., Ferraccioli, F., Hong, J. K., Golynsky, D. A., von Frese, R. R. B., Young, D. A.,  
 5119 Blankenship, D. D., Holt, J. W., Ivanov, S. V., Kiselev, A. V., Masolov, V. N., Eagles, G.,  
 5120 Gohl, K., Jokat, W., Damaske, D., Finn, C., Aitken, A., Bell, R. E., Armadillo, E., ...  
 5121 Roberts, J. L. (2018). New Magnetic Anomaly Map of the Antarctic: ADMAP2. *Geophys-  
 5122 ical Research Letters*, 45(13), 6437–6449. <https://doi.org/10.1029/2018GL078153> (cit. on  
 5123 p. 139)
- 5124 Gooch, B. T., Young, D. A., & Blankenship, D. D. (2016). Potential groundwater and heteroge-  
 5125 neous heat source contributions to ice sheet dynamics in critical submarine basins of East  
 5126 Antarctica. *Geochemistry, Geophysics, Geosystems*, 17(2), 395–409. <https://doi.org/10.1002/2015GC006117> (cit. on pp. 19, 28, 33, 144, 145)
- 5127 Goodge, J. W. (2020). Geological and tectonic evolution of the Transantarctic Mountains, from  
 5128 ancient craton to recent enigma. *Gondwana Research*, 80, 50–122. <https://doi.org/10.1016/j.gr.2019.11.001> (cit. on pp. 26, 30, 133)
- 5129 Granot, R., & Dyment, J. (2018). Late Cenozoic unification of East and West Antarctica. *Nature  
 5130 Communications*, 9(1), 3189. <https://doi.org/10.1038/s41467-018-05270-w> (cit. on pp. 26,  
 5131 32)
- 5132 Greenbaum, J. S., Blankenship, D. D., Young, D. A., Richter, T. G., Roberts, J. L., Aitken, A. R. A.,  
 5133 Legresy, B., Schroeder, D. M., Warner, R. C., van Ommen, T. D., & Siegert, M. J. (2015).  
 5134 Ocean access to a cavity beneath Totten Glacier in East Antarctica. *Nature Geoscience*,  
 5135 8(4), 294–298. <https://doi.org/10.1038/ngeo2388> (cit. on pp. 104–106, 120)
- 5136 Greene, C. A., Gardner, A. S., Schlegel, N.-J., & Fraser, A. D. (2022). Antarctic calving loss rivals  
 5137 ice-shelf thinning. *Nature*, 609(7929), 948–953. <https://doi.org/10.1038/s41586-022-05037-w> (cit. on p. 16)
- 5138 Greischar, L. L., Bentley, C. R., & Whiting, L. R. (1992). An analysis of gravity measurements on  
 5139 the Ross Ice Shelf, Antarctica. In *Contributions to Antarctic Research III* (pp. 105–155).  
 5140 American Geophysical Union (AGU). <https://doi.org/10.1029/AR057p0105>. (Cit. on  
 5141 pp. 21, 32, 156)
- 5142 Griggs, J. A., & Bamber, J. L. (2011). Antarctic ice-shelf thickness from satellite radar altimetry.  
 5143 *Journal of Glaciology*, 57(203), 485–498. <https://doi.org/10.3189/002214311796905659>  
 5144 (cit. on pp. 38, 112)
- 5145 Gustafson, C. D., Key, K., Siegfried, M. R., Winberry, J. P., Fricker, H. A., Venturelli, R. A.,  
 5146 & Michaud, A. B. (2022). A dynamic saline groundwater system mapped beneath an

- 5153        Antarctic ice stream. *Science*, 376(6593), 640–644. <https://doi.org/10.1126/science.abm3301> (cit. on pp. 19, 26, 32, 33, 144, 145, 156)
- 5154        Halberstadt, A. R. W., Simkins, L. M., Greenwood, S. L., & Anderson, J. B. (2016). Past ice-  
5155        sheet behaviour: Retreat scenarios and changing controls in the Ross Sea, Antarctica. *The  
5156        Cryosphere*, 10(3), 1003–1020. <https://doi.org/10.5194/tc-10-1003-2016> (cit. on pp. 16,  
5157        20, 34, 134, 137, 145, 147)
- 5158        Hammer, S. (1939). Terrain corrections for gravimeter stations. *GEOPHYSICS*, 4(3), 184–194.  
5159        <https://doi.org/10.1190/1.1440495> (cit. on p. 47)
- 5160        Harlan, R. B. (1968). Eotvos corrections for airborne gravimetry. *Journal of Geophysical Research*,  
5161        73(14), 4675–4679. <https://doi.org/10.1029/JB073i014p04675> (cit. on p. 111)
- 5162        Helton, J., Johnson, J., Sallaberry, C., & Storlie, C. (2006). Survey of sampling-based methods for  
5163        uncertainty and sensitivity analysis. *Reliability Engineering & System Safety*, 91(10-11),  
5164        1175–1209. <https://doi.org/10.1016/j.ress.2005.11.017> (cit. on pp. 73, 100–102, 116)
- 5165        Hinze, W. J., Aiken, C., Brozena, J., Coakley, B., Dater, D., Flanagan, G., Forsberg, R., Hilden-  
5166        brand, T., Keller, G. R., Kellogg, J., Kucks, R., Li, X., Mainville, A., Morin, R., Pilk-  
5167        ington, M., Plouff, D., Ravat, D., Roman, D., Urrutia-Fucugauchi, J., ... Winester, D.  
5168        (2005). New standards for reducing gravity data: The North American gravity database.  
5169        *GEOPHYSICS*, 70(4), J25–J32. <https://doi.org/10.1190/1.1988183> (cit. on pp. 92, 93)
- 5170        Hinze, W. J., Von Frese, R., & Saad, A. H. (2013). *Gravity and magnetic exploration: Principles,  
5171        practices, and applications*. Cambridge University Press. (Cit. on p. 92).
- 5172        Hodgson, D. A., Jordan, T. A., De Rydt, J., Fretwell, P. T., Seddon, S. A., Becker, D., Hogan,  
5173        K. A., Smith, A. M., & Vaughan, D. G. (2019). Past and future dynamics of the Brunt Ice  
5174        Shelf from seabed bathymetry and ice shelf geometry. *The Cryosphere*, 13(2), 545–556.  
5175        <https://doi.org/10.5194/tc-13-545-2019> (cit. on pp. 46, 105, 106, 120)
- 5176        Hofmann-Wellenhof, B., & Moritz, H. (2006). *Physical geodesy* (2nd, corrected ed). SpringerWien-  
5177        NewYork. (Cit. on pp. 92, 94).
- 5178        Hofstede, C., Beyer, S., Corr, H., Eisen, O., Hattermann, T., Helm, V., Neckel, N., Smith, E. C.,  
5179        Steinhage, D., Zeising, O., & Humbert, A. (2021). Evidence for a grounding line fan at the  
5180        onset of a basal channel under the ice shelf of Support Force Glacier, Antarctica, revealed  
5181        by reflection seismics. *The Cryosphere*, 15(3), 1517–1535. <https://doi.org/10.5194/tc-15-1517-2021> (cit. on p. 121)
- 5182        Holland, P. R. (2008). A model of tidally dominated ocean processes near ice shelf grounding  
5183        lines. *Journal of Geophysical Research*, 113(C11), C11002. <https://doi.org/10.1029/2007JC004576> (cit. on pp. 16, 133, 141)
- 5184        Horgan, H. J., Hulbe, C., Alley, R. B., Anandakrishnan, S., Goodsell, B., Taylor-Offord, S., &  
5185        Vaughan, M. J. (2017). Poststagnation Retreat of Kamb Ice Stream's Grounding Zone.  
5186        *Geophysical Research Letters*, 44(19), 9815–9822. <https://doi.org/10.1002/2017GL074986>  
5187        (cit. on pp. 21, 129)
- 5188        Horgan, H. J., Walker, R. T., Anandakrishnan, S., & Alley, R. B. (2011). Surface elevation changes  
5189        at the front of the Ross Ice Shelf: Implications for basal melting. *Journal of Geophysical  
5190        Research*, 116(C2), C02005. <https://doi.org/10.1029/2010JC006192> (cit. on p. 131)
- 5191        Horgan, H. J., Christianson, K., Jacobel, R. W., Anandakrishnan, S., & Alley, R. B. (2013). Sediment  
5192        deposition at the modern grounding zone of Whillans Ice Stream, West Antarctica.  
5193        *Geophysical Research Letters*, 40(15), 3934–3939. <https://doi.org/10.1002/grl.50712> (cit.  
5194        on p. 121)
- 5195        Hoyer, S., & Hamman, J. (2017). Xarray: N-D labeled Arrays and Datasets in Python. *Journal of  
5196        Open Research Software*, 5(1), 10. <https://doi.org/10.5334/jors.148> (cit. on p. 171)
- 5197        IceBridge Sander AIRGrav L1B Geolocated Free Air Gravity Anomalies, Version 1. (2020). (Cit.  
5198        on p. 149).
- 5199        Intergovernmental Panel on Climate Change (IPCC). (2022). *The Ocean and Cryosphere in a  
5200        Changing Climate: Special Report of the Intergovernmental Panel on Climate Change* (First). Cambridge University Press. <https://doi.org/10.1017/9781009157964>. (Cit. on  
5201        pp. 15, 137)
- 5202        Jacobs, S., Helmer, H., Doake, C. S. M., Jenkins, A., & Frolich, R. M. (1992). Melting of ice  
5203        shelves and the mass balance of Antarctica. *Journal of Glaciology*, 38(130), 375–387. <https://doi.org/10.3189/S0022143000002252> (cit. on p. 90)
- 5204        Jacoby, W., & Smilde, P. L. (2009). *Gravity interpretation: Fundamentals and application of gravity  
5205        inversion and geological interpretation ; with CD-ROM*. Springer. (Cit. on pp. 42, 93)  
5206        OCLC: 845389531.

- 5212 Jansen, M. J. W., Rossing, W. A. H., & Daamen, R. A. (1994). Monte Carlo Estimation of Un-  
 5213 certainty Contributions from Several Independent Multivariate Sources. In J. Grasman  
 5214 & G. van Straten (Eds.), *Predictability and Nonlinear Modelling in Natural Sciences and*  
 5215 *Economics* (pp. 334–343). Springer Netherlands. [https://doi.org/10.1007/978-94-011-0962-8\\_28](https://doi.org/10.1007/978-94-011-0962-8_28). (Cit. on pp. 73, 100, 101)
- 5216 Jenkins, A., Dutrieux, P., Jacobs, S. S., McPhail, S. D., Perrett, J. R., Webb, A. T., & White, D.  
 5217 (2010). Observations beneath Pine Island Glacier in West Antarctica and implications for  
 5218 its retreat. *Nature Geoscience*, 3(7), 468–472. <https://doi.org/10.1038/ngeo890> (cit. on  
 5219 p. 38)
- 5220 Jolie, E., Scott, S., Faulds, J., Chambefort, I., Axelsson, G., Gutiérrez-Negrín, L. C., Regenspurg,  
 5221 S., Ziegler, M., Ayling, B., Richter, A., & Zemedkun, M. T. (2021). Geological controls on  
 5222 geothermal resources for power generation. *Nature Reviews Earth & Environment*, 2(5),  
 5223 324–339. <https://doi.org/10.1038/s43017-021-00154-y> (cit. on pp. 19, 26, 145)
- 5224 Jordan, T. A., Ferraccioli, F., Vaughan, D. G., Holt, J. W., Corr, H., Blankenship, D. D., &  
 5225 Diehl, T. M. (2010). Aerogravity evidence for major crustal thinning under the Pine Island  
 5226 Glacier region (West Antarctica). *Geological Society of America Bulletin*, 122(5-6), 714–  
 5227 726. <https://doi.org/10.1130/B26417.1> (cit. on pp. 78, 85)
- 5228 Jordan, T. A., Riley, T. R., & Siddoway, C. S. (2020a). The geological history and evolution of  
 5229 West Antarctica. *Nature Reviews Earth & Environment*, 1, 117–133. <https://doi.org/10.1038/s43017-019-0013-6> (cit. on pp. 31, 149)
- 5230 Jordan, T. A., Porter, D., Tinto, K., Millan, R., Muto, A., Hogan, K., Larter, R. D., Graham,  
 5231 A. G. C., & Paden, J. D. (2020b). New gravity-derived bathymetry for the Thwaites,  
 5232 Crosson, and Dotson ice shelves revealing two ice shelf populations. *The Cryosphere*, 14(9),  
 5233 2869–2882. <https://doi.org/10.5194/tc-14-2869-2020> (cit. on pp. 104–106, 120)
- 5234 Kachuck, S. B., Martin, D. F., Bassis, J. N., & Price, S. F. (2020). Rapid Viscoelastic Deformation  
 5235 Slows Marine Ice Sheet Instability at Pine Island Glacier. *Geophysical Research Letters*,  
 5236 47(10). <https://doi.org/10.1029/2019GL086446> (cit. on pp. 18, 144)
- 5237 Karner, G. D., Studinger, M., & Bell, R. E. (2005). Gravity anomalies of sedimentary basins and  
 5238 their mechanical implications: Application to the Ross Sea basins, West Antarctica. *Earth  
 5239 and Planetary Science Letters*, 235, 577–596. <https://doi.org/10.1016/j.epsl.2005.04.016>  
 5240 (cit. on pp. 26, 28, 147, 153)
- 5241 Kingslake, J., Scherer, R. P., Albrecht, T., Coenen, J., Powell, R. D., Reese, R., Stansell, N. D.,  
 5242 Tulaczyk, S., Wearing, M. G., & Whitehouse, P. L. (2018). Extensive retreat and re-  
 5243 advance of the West Antarctic Ice Sheet during the Holocene. *Nature*, 558(7710), 430–  
 5244 434. <https://doi.org/10.1038/s41586-018-0208-x> (cit. on pp. 33, 131, 145)
- 5245 Kirkpatrick, S., Gelatt, C. D., & Vecchi, M. P. (1983). Optimization by Simulated Annealing.  
 5246 *Science*, 220(4598), 671–680. <https://doi.org/10.1126/science.220.4598.671> (cit. on  
 5247 p. 106)
- 5248 Koch, P., Wujek, B., Golovidov, O., & Gardner, S. (2017). Automated Hyperparameter Tuning for  
 5249 Effective Machine Learning. *SAS Institute Inc.* (cit. on p. 103).
- 5250 Kulhanek, D. K., Levy, R. H., Clowes, C. D., Prebble, J. G., Rodelli, D., Jovane, L., Morgans,  
 5251 H. E., Kraus, C., Zwingmann, H., Griffith, E. M., Scher, H. D., McKay, R. M., & Naish,  
 5252 T. R. (2019). Revised chronostratigraphy of DSDP Site 270 and late Oligocene to early  
 5253 Miocene paleoecology of the Ross Sea sector of Antarctica. *Global and Planetary Change*,  
 5254 178, 46–64. <https://doi.org/10.1016/j.gloplacha.2019.04.002> (cit. on pp. 34, 147)
- 5255 Larour, E., Morlighem, M., Seroussi, H., Schiermeier, J., & Rignot, E. (2012). Ice flow sensitivity to  
 5256 geothermal heat flux of Pine Island Glacier, Antarctica. *Journal of Geophysical Research:  
 5257 Earth Surface*, 117(F04023), 1–12. <https://doi.org/10.1029/2012JF002371> (cit. on p. 144)
- 5258 Le Brocq, A. M., Payne, A. J., & Vieli, A. (2010). An improved Antarctic dataset for high resolution  
 5259 numerical ice sheet models (ALBMAP v1). *Earth System Science Data*, 2(2), 247–260.  
 5260 <https://doi.org/10.5194/essd-2-247-2010> (cit. on pp. 91, 124)
- 5261 Leckie, F. M. (1983). Late Oligocene-early Miocene glacial record of the Ross Sea, Antarctica:  
 5262 Evidence from DSDP Site 270. *Geology*, 11, 578–582. [https://doi.org/10.1130/0091-7613\(1983\)11<578:LOMGRO>2.0.CO;2](https://doi.org/10.1130/0091-<br/>
  5263 7613(1983)11<578:LOMGRO>2.0.CO;2) (cit. on pp. 34, 147)
- 5264 Li, L., Aitken, A. R. A., Lindsay, M. D., & Kulessa, B. (2022). Sedimentary basins reduce stability  
 5265 of Antarctic ice streams through groundwater feedbacks. *Nature Geoscience*. <https://doi.org/10.1038/s41561-022-00992-5> (cit. on pp. 19, 31, 145, 156)

- 5269 Li, X., Zattin, M., & Olivetti, V. (2020). Apatite fission track signatures of the Ross Sea ice flows  
 5270 during the Last Glacial Maximum. *Geochemistry, Geophysics, Geosystems*, 21(10), 1–21.  
 5271 <https://doi.org/10.1029/2019GC008749> (cit. on pp. 33, 148)
- 5272 Li, X., & Götze, H.-J. (2001). Ellipsoid, geoid, gravity, geodesy, and geophysics. *Geophysics*, 66(6),  
 5273 1660–1668. <https://doi.org/10.1190/1.1487109> (cit. on pp. 93, 95)
- 5274 Licht, K. J., Hennessy, A. J., & Welke, B. M. (2014). The U-Pb detrital zircon signature of  
 5275 West Antarctic ice stream tills in the Ross embayment, with implications for Last Glacial  
 5276 Maximum ice flow reconstructions. *Antarctic Science*, 26(6), 687–697. <https://doi.org/10.1017/S0954102014000315> (cit. on pp. 33, 148)
- 5277 Licht, K. J., Lederer, J. R., & Jeffrey Swope, R. (2005). Provenance of LGM glacial till (sand  
 5278 fraction) across the Ross embayment, Antarctica. *Quaternary Science Reviews*, 24(12-13),  
 5279 1499–1520. <https://doi.org/10.1016/j.quascirev.2004.10.017> (cit. on p. 148)
- 5280 Lindeque, A., Gohl, K., Wobbe, F., & Uenzelmann-Neben, G. (2016). Preglacial to glacial sediment  
 5281 thickness grids for the Southern Pacific Margin of West Antarctica: Preglacial, transitional  
 5282 and full glacial isopach maps, West Antarctica. *Geochemistry, Geophysics, Geosystems*,  
 5283 17(10), 4276–4285. <https://doi.org/10.1002/2016GC006401> (cit. on pp. 155, 157)
- 5284 Lloyd, A. J., Wiens, D. A., Nyblade, A. A., Anandakrishnan, S., Aster, R. C., Huerta, A. D.,  
 5285 Wilson, T. J., Dalziel, I. W. D., Shore, P. J., & Zhao, D. (2015). A seismic transect across  
 5286 West Antarctica: Evidence for mantle thermal anomalies beneath the Bentley Subglacial  
 5287 Trench and the Marie Byrd Land Dome. *Journal of Geophysical Research: Solid Earth*,  
 5288 120(12), 8439–8460. <https://doi.org/10.1002/2015JB012455> (cit. on p. 33)
- 5289 Llubes, M., Lanseau, C., & Rémy, F. (2006). Relations between basal condition, subglacial hydro-  
 5290 logical networks and geothermal flux in Antarctica. *Earth and Planetary Science Letters*,  
 5291 241(3-4), 655–662. <https://doi.org/10.1016/j.epsl.2005.10.040> (cit. on p. 18)
- 5292 Lowry, D. P., Golledge, N. R., Bertler, N. A. N., Jones, R. S., & McKay, R. (2019). Deglacial  
 5293 grounding-line retreat in the Ross Embayment, Antarctica, controlled by ocean and atmo-  
 5294 sphere forcing. *Science Advances*, 5, 1–12. <https://doi.org/10.1126/sciadv.aav8754> (cit. on  
 5295 pp. 20, 33, 90, 131, 137)
- 5296 Lowry, D. P., Golledge, N. R., Bertler, N. A., Jones, R. S., McKay, R., & Stutz, J. (2020). Geo-  
 5297 logic controls on ice sheet sensitivity to deglacial climate forcing in the Ross Embayment,  
 5298 Antarctica. *Quaternary Science Advances*, 1, 1–17. <https://doi.org/10.1016/j.qsa.2020.100002> (cit. on pp. 33, 145)
- 5299 Luyendyk, B., Sorlien, C. C., Wilson, D. S., Bartek, L. R., & Siddoway, C. S. (2001). Structural  
 5300 and tectonic evolution of the Ross Sea rift in the Cape Colbeck region, Eastern Ross Sea,  
 5301 Antarctica. *Tectonics*, 20(6), 933–958. <https://doi.org/10.1029/2000TC001260> (cit. on  
 5302 p. 30)
- 5303 Luyendyk, B., Wilson, D. S., & Siddoway, C. S. (2003). Eastern margin of the Ross Sea Rift in  
 5304 western Marie Byrd Land, Antarctica: Crustal structure and tectonic development. *Geo-  
 5305 chemistry, Geophysics, Geosystems*, 4(10), 1–25. <https://doi.org/10.1029/2002GC000462>  
 5306 (cit. on p. 26)
- 5307 Martins, C. M., Barbosa, V. C., & Silva, J. B. (2010). Simultaneous 3D depth-to-basement and  
 5308 density-contrast estimates using gravity data and depth control at few points. *GEO-  
 5309 PHYSICS*, 75(3), I21–I28. <https://doi.org/10.1190/1.3380225> (cit. on p. 106)
- 5310 Matsuoka, K., Hindmarsh, R. C., Moholdt, G., Bentley, M. J., Pritchard, H. D., Brown, J., Con-  
 5311 way, H., Drews, R., Durand, G., Goldberg, D., Hattermann, T., Kingslake, J., Lenaerts,  
 5312 J. T., Martín, C., Mulvaney, R., Nicholls, K. W., Pattyn, F., Ross, N., Scambos, T., &  
 5313 Whitehouse, P. L. (2015). Antarctic ice rises and ripples: Their properties and signifi-  
 5314 cance for ice-sheet dynamics and evolution. *Earth-Science Reviews*, 150, 724–745. <https://doi.org/10.1016/j.earscirev.2015.09.004> (cit. on pp. 16, 90)
- 5315 McCubbine, J. (2016). *Airborne Gravity Across New Zealand - For An Improved Vertical Datum*  
 5316 (Doctoral dissertation). Victoria University of Wellington. (Cit. on p. 47).
- 5317 McKay, R., Golledge, N., Maas, S., Naish, T., Levy, R., Dunbar, G., & Kuhn, G. (2016). Antarctic  
 5318 marine ice-sheet retreat in the Ross Sea during the early Holocene. *Geology*, 44(1), 7–10.  
 5319 <https://doi.org/10.1130/G37315.1> (cit. on p. 145)
- 5320 Menke, W. (2012). *Geophysical data analysis: Discrete inverse theory* (Matlab ed., 3rd ed). Academic Press. (Cit. on p. 39).
- 5321 Millan, R., Rignot, E., Mouginot, J., Wood, M., Bjørk, A. A., & Morlighem, M. (2018). Vulner-  
 5322 ability of Southeast Greenland Glaciers to Warm Atlantic Water From Operation Ice-

- 5327 Bridge and Ocean Melting Greenland Data. *Geophysical Research Letters*, 45(6), 2688–  
 5328 2696. <https://doi.org/10.1002/2017GL076561> (cit. on pp. 105, 106, 120)
- 5329 Millan, R., Rignot, E., Bernier, V., Morlighem, M., & Dutrieux, P. (2017). Bathymetry of the  
 5330 Amundsen Sea Embayment sector of West Antarctica from Operation IceBridge gravity  
 5331 and other data. *Geophysical Research Letters*, 44(3), 1360–1368. <https://doi.org/10.1002/2016GL072071> (cit. on pp. 104–106, 120, 149)
- 5333 Millan, R., St-Laurent, P., Rignot, E., Morlighem, M., Mouginot, J., & Scheuchl, B. (2020). Con-  
 5334 straining an Ocean Model Under Getz Ice Shelf, Antarctica, Using A Gravity-Derived  
 5335 Bathymetry. *Geophysical Research Letters*, 47(13). <https://doi.org/10.1029/2019GL086522>  
 5336 (cit. on pp. 46, 63, 104–106, 120, 122, 149)
- 5337 Moholdt, G., Padman, L., & Fricker, H. A. (2014). Basal mass budget of Ross and Filchner-Ronne  
 5338 ice shelves, Antarctica, derived from Lagrangian analysis of ICESat altimetry: Ice shelf  
 5339 basal melting from altimetry. *Journal of Geophysical Research: Earth Surface*, 119(11),  
 5340 2361–2380. <https://doi.org/10.1002/2014JF003171> (cit. on pp. 20, 90, 131, 137)
- 5341 Mooney, W. D., Laske, G., & Masters, T. G. (1998). CRUST 5.1: A global crustal model at 5° ×  
 5342 5°. *Journal of Geophysical Research: Solid Earth*, 103(B1), 727–747. <https://doi.org/10.1029/97JB02122> (cit. on p. 155)
- 5344 Morlighem, M. (2022). MEaSUREs BedMachine Antarctica, Version 3. (Cit. on pp. 39, 92, 108,  
 5345 109, 112, 113, 115, 117, 118, 124, 125, 128, 130, 146)  
 5346 <https://doi.org/10.5067/FPSU0V1MWUB6>.
- 5347 Morlighem, M., Rignot, E., Binder, T., Blankenship, D., Drews, R., Eagles, G., Eisen, O., Ferraci-  
 5348 cioli, F., Forsberg, R., Fretwell, P., Goel, V., Greenbaum, J. S., Gudmundsson, H., Guo, J., Helm, V., Hofstede, C., Howat, I., Humbert, A., Jokat, W., ... Young, D. A. (2020). Deep glacial troughs and stabilizing ridges unveiled beneath the margins of the Antarctic  
 5350 ice sheet. *Nature Geoscience*, 13(2), 132–137. <https://doi.org/10.1038/s41561-019-0510-8>  
 5352 (cit. on pp. 18, 27, 28, 32, 39, 69, 92, 108, 109, 112, 113, 115, 117, 118, 124, 146, 155, 157)  
 5353 BedMachine
- 5354 Mouginot, J., Rignot, E., & Scheuchl, B. (2019). Continent-wide, interferometric SAR phase, map-  
 5355 ping of Antarctic ice velocity. *Geophysical Research Letters*, 46(16), 9710–9718. <https://doi.org/10.1029/2019GL083826> (cit. on p. 32)
- 5357 Mouginot, J., Scheuchl, B., & Rignot, E. (2017). MEaSUREs Antarctic Boundaries for IPY 2007–  
 5358 2009 from Satellite Radar, Version 2. (Cit. on pp. 91, 108–110, 128, 132, 139)  
 5359 <https://doi.org/10.5067/AXE4121732AD>.
- 5360 Müller, R. D., Gohl, K., Cande, S. C., Goncharov, A., & Golynsky, A. V. (2007). Eocene to Miocene  
 5361 geometry of the West Antarctic Rift System. *Australian Journal of Earth Sciences*, 54(8),  
 5362 1033–1045. <https://doi.org/10.1080/08120090701615691> (cit. on pp. 29, 155)
- 5363 Muto, A., Anandakrishnan, S., & Alley, R. B. (2013a). Subglacial bathymetry and sediment layer  
 5364 distribution beneath the Pine Island Glacier ice shelf, West Antarctica, modeled using  
 5365 aerogravity and autonomous underwater vehicle data. *Annals of Glaciology*, 54(64), 27–  
 5366 32. <https://doi.org/10.3189/2013AoG64A110> (cit. on pp. 104, 106, 149)
- 5367 Muto, A., Christianson, K., Horgan, H. J., Anandakrishnan, S., & Alley, R. B. (2013b). Bathymetry  
 5368 and geological structures beneath the Ross Ice Shelf at the mouth of Whillans Ice Stream,  
 5369 West Antarctica, modeled from ground-based gravity measurements. *Journal of Geophys-  
 5370 ical Research: Solid Earth*, 118(8), 4535–4546. <https://doi.org/10.1002/jgrb.50315> (cit. on  
 5371 pp. 21, 32, 105, 131, 133)
- 5372 Muto, A., Peters, L. E., Gohl, K., Sasgen, I., Alley, R. B., Anandakrishnan, S., & Riverman, K. L.  
 5373 (2016). Subglacial bathymetry and sediment distribution beneath Pine Island Glacier ice  
 5374 shelf modeled using aerogravity and in situ geophysical data: New results. *Earth and  
 5375 Planetary Science Letters*, 433, 63–75. <https://doi.org/10.1016/j.epsl.2015.10.037> (cit. on  
 5376 pp. 46, 105–107, 149)
- 5377 Nagy, D., Papp, G., & Benedek, J. (2000). The gravitational potential and its derivatives for the  
 5378 prism. *Journal of Geodesy*, 74(7–8), 552–560. <https://doi.org/10.1007/s001900000116>  
 5379 (cit. on pp. 43, 46, 48, 97)
- 5380 Naish, T., Powell, R., Levy, R., Wilson, G., Scherer, R., Talarico, F., Krissek, L., Niessen, F.,  
 5381 Pompilio, M., Wilson, T., Carter, L., DeConto, R., Huybers, P., McKay, R., Pollard, D., Ross, J., Winter, D., Barrett, P., Browne, G., ... Williams, T. (2009). Obliquity-  
 5382 paced Pliocene West Antarctic ice sheet oscillations. *Nature*, 458(7236), 322–328. <https://doi.org/10.1038/nature07867> (cit. on pp. 20, 90, 137)

- 5385 Nerem, R. S., Beckley, B. D., Fasullo, J. T., Hamilton, B. D., Masters, D., & Mitchum, G. T. (2018).  
 5386 Climate-change-driven accelerated sea-level rise detected in the altimeter era. *Proceedings*  
 5387 *of the National Academy of Sciences*, 115(9), 2022–2025. <https://doi.org/10.1073/pnas.1717312115> (cit. on p. 15)
- 5388 Neuhaus, S. U., Tulaczyk, S. M., Stansell, N. D., Coenen, J. J., Scherer, R. P., Mikucki, J. A., &  
 5389 Powell, R. D. (2021). Did Holocene climate changes drive West Antarctic grounding line  
 5390 retreat and readvance? *The Cryosphere*, 15(10), 4655–4673. <https://doi.org/10.5194/tc-15-4655-2021> (cit. on p. 33)
- 5390 Nicholls, K. W., Abrahamsen, E. P., Buck, J. J. H., Dodd, P. A., Goldblatt, C., Griffiths, G.,  
 5391 Heywood, K. J., Hughes, N. E., Kaletzky, A., Lane-Serff, G. F., McPhail, S. D., Millard,  
 5392 N. W., Oliver, K. I. C., Perrett, J., Price, M. R., Pudsey, C. J., Saw, K., Stansfield, K.,  
 5393 Stott, M. J., ... Wilkinson, J. P. (2006). Measurements beneath an Antarctic ice shelf  
 5394 using an autonomous underwater vehicle. *Geophysical Research Letters*, 33(8), L08612.  
 5395 <https://doi.org/10.1029/2006GL025998> (cit. on p. 18)
- 5396 Oldenburg, D. W. (1974). The inversion and interpretation of gravity anomalies. *Geophysics*, 39(4),  
 5397 526–536 (cit. on p. 106).
- 5398 Oldenburg, D. W., & Li, Y. (2005). Inversion for applied geophysics: A tutorial. In D. K. Butler  
 5399 (Ed.), *Near-Surface Geophysics*. Society of Exploration Geophysicists. <https://doi.org/10.1190/1.9781560801719>. (Cit. on pp. 39, 40, 103)
- 5400 Oldenburg, D. W., & Pratt, D. (2007). Geophysical inversion for mineral exploration: A decade  
 5401 of progress in theory and practice. In B. Milkereit (Ed.), *Proceedings of Exploration 07*  
 5402 (pp. 61–95). (Cit. on p. 42).
- 5403 Oliveira, V. C., & Uieda, L. (2014). Tópicos de inversão em geofísica. *figshare*. <https://doi.org/http://dx.doi.org/10.6084/m9.figshare.1192984> (cit. on p. 40)
- 5404 Oliveira, V. C., Uieda, L., & Hallam, K. A. T. (2018). Should geophysicists use the gravity disturbance or the anomaly?, 11. <https://doi.org/10.5281/zenodo.1255305> (cit. on p. 94)
- 5405 Olivetti, V., Balestrieri, M. L., Chew, D., Zurli, L., Zattin, M., Pace, D., Drakou, F., Cornamusini,  
 5406 G., & Perotti, M. (2023). Ice volume variations and provenance trends in the Oligocene-  
 5407 early Miocene glaciomarine sediments of the Central Ross Sea, Antarctica (DSDP Site 270).  
 5408 *Global and Planetary Change*, 104042. <https://doi.org/10.1016/j.gloplacha.2023.104042>  
 5409 (cit. on pp. 147, 148)
- 5410 Otosaka, I. N., Shepherd, A., Ivins, E. R., Schlegel, N.-J., Amory, C., van den Broeke, M. R.,  
 5411 Horwath, M., Joughin, I., King, M. D., Krinner, G., Nowicki, S., Payne, A. J., Rignot, E.,  
 5412 Scambos, T., Simon, K. M., Smith, B. E., Sørensen, L. S., Velicogna, I., Whitehouse, P. L.,  
 5413 ... Wouters, B. (2023). Mass balance of the Greenland and Antarctic ice sheets from 1992  
 5414 to 2020. *Earth System Science Data*, 15(4), 1597–1616. <https://doi.org/10.5194/essd-15-1597-2023> (cit. on pp. 15, 16)
- 5415 Paige, C. C., & Saunders, M. A. (1982). LSQR: An Algorithm for Sparse Linear Equations and  
 5416 Sparse Least Squares. *ACM Transactions on Mathematical Software*, 8(1), 43–71. <https://doi.org/10.1145/355984.355989> (cit. on p. 48)
- 5417 Pappa, F., Ebbing, J., & Ferraccioli, F. (2019). Moho Depths of Antarctica: Comparison of Seismic,  
 5418 Gravity, and Isostatic Results. *Geochemistry, Geophysics, Geosystems*, 20(3), 1629–1645.  
 5419 <https://doi.org/10.1029/2018GC008111> (cit. on pp. 106, 143)
- 5420 Parker, R. L. (1972). The Rapid Calculation of Potential Anomalies. *Geophysical Journal International*, 31(4), 447–455. <https://doi.org/10.1111/j.1365-246X.1973.tb06513.x> (cit. on  
 5421 p. 106)
- 5422 Pašteka, R., Mikuška, J., & Meurers, B. (2017). *Understanding the Bouguer Anomaly*. Elsevier.  
 5423 <https://doi.org/10.1016/B978-0-12-812913-5.00008-7>. (Cit. on p. 94)
- 5424 Patterson, M. O., Levy, R. H., Kulhanek, D. K., van de Flierdt, T., Horgan, H., Dunbar, G. B.,  
 5425 Naish, T. R., Ash, J., Pyne, A., Mandeno, D., Winberry, P., Harwood, D. M., Florindo,  
 5426 F., Jimenez-Espejo, F. J., Läufer, A., Yoo, K.-C., Seki, O., Stocchi, P., Klages, J. P., ...  
 5427 the SWAIS 2C Science Team. (2022). Sensitivity of the West Antarctic Ice Sheet to +2  
 5428 °C (SWAIS 2C). *Scientific Drilling*, 30, 101–112. <https://doi.org/10.5194/sd-30-101-2022>  
 5429 (cit. on pp. 18, 21)
- 5430 Paulsen, T., Encarnación, J., & Grunow, A. (2004). Structure and timing of transpressional deformation  
 5431 in the Shackleton Glacier area, Ross orogen, Antarctica. *Journal of the Geological Society*, 161(6), 1027–1038. <https://doi.org/10.1144/0016-764903-040> (cit. on p. 34)
- 5432 Paxman, G. J. G., Jamieson, S. S., Hochmuth, K., Gohl, K., Bentley, M. J., Leitchenkov, G., &  
 5433 Ferraccioli, F. (2019). Reconstructions of Antarctic topography since the Eocene–Oligocene

- boundary. *Palaeogeography, Palaeoclimatology, Palaeoecology*, 535, 109346. <https://doi.org/10.1016/j.palaeo.2019.109346> (cit. on pp. 26, 34, 147, 155)
- Pekar, S. F., DeConto, R. M., & Harwood, D. M. (2006). Resolving a late Oligocene conundrum: Deep-sea warming and Antarctic glaciation. *Palaeogeography, Palaeoclimatology, Palaeoecology*, 231, 29–40. <https://doi.org/10.1016/j.palaeo.2005.07.024> (cit. on p. 34)
- Peltier, W. R., Wu, P. P.-C., Argus, D. F., Li, T., & Velay-Vitow, J. (2022). Glacial isostatic adjustment: Physical models and observational constraints. *Reports on Progress in Physics*, 85(9), 096801. <https://doi.org/10.1088/1361-6633/ac805b> (cit. on pp. 19, 143)
- Pérez, F., & Granger, B. E. (2007). IPython: A system for interactive scientific computing. *Computing in Science and Engineering*, 9(3), 21–29. <https://doi.org/10.1109/MCSE.2007.53> (cit. on p. 51)
- Pérez, L. F., De Santis, L., McKay, R. M., Larter, R. D., Ash, J., Bart, P. J., Böhm, G., Brancatelli, G., Browne, I., Colleoni, F., Dodd, J. P., Geletti, R., Harwood, D. M., Kuhn, G., Sverre Laberg, J., Leckie, R. M., Levy, R. H., Marschalek, J., Mateo, Z., ... 374 Scientists, I. O. D. P. E. (2021). Early and middle Miocene ice sheet dynamics in the Ross Sea: Results from integrated core-log-seismic interpretation. *GSA Bulletin*. <https://doi.org/10.1130/B35814.1> (cit. on p. 26)
- Perozzi, L., Guglielmetti, L., & Moscariello, A. (2021). Quantitative uncertainty analysis of gravity disturbance. The case of the Geneva Basin (Switzerland). *Journal of Applied Geophysics*, 193, 104431. <https://doi.org/10.1016/j.jappgeo.2021.104431> (cit. on p. 85)
- Phillips, G., & Läufer, A. (2009). Brittle deformation relating to the Carboniferous–Cretaceous evolution of the Lambert Graben, East Antarctica: A precursor for Cenozoic relief development in an intraplate and glaciated region. *Tectonophysics*, 471(3-4), 216–224. <https://doi.org/10.1016/j.tecto.2009.02.012> (cit. on p. 33)
- Pollard, D., DeConto, R. M., & Nyblade, A. A. (2005). Sensitivity of Cenozoic Antarctic ice sheet variations to geothermal heat flux. *Global and Planetary Change*, 49(1-2), 63–74. <https://doi.org/10.1016/j.gloplacha.2005.05.003> (cit. on pp. 18, 144)
- Pritchard, H. D., Ligtenberg, S. R. M., Fricker, H. A., Vaughan, D. G., van den Broeke, M. R., & Padman, L. (2012). Antarctic ice-sheet loss driven by basal melting of ice shelves. *Nature*, 484(7395), 502–505. <https://doi.org/10.1038/nature10968> (cit. on pp. 38, 90)
- Rashidifard, M., Giraud, J., Lindsay, M., Jessell, M., & Ogarko, V. (2021). Constraining 3D geometric gravity inversion with a 2D reflection seismic profile using a generalized level set approach: Application to the eastern Yilgarn Craton. *Solid Earth*, 12(10), 2387–2406. <https://doi.org/10.5194/se-12-2387-2021> (cit. on p. 55)
- Ravier, E., & Buonchristiani, J.-F. (2018). Glaciohydrogeology. In *Past Glacial Environments* (pp. 431–466). Elsevier. <https://doi.org/10.1016/B978-0-08-100524-8.00013-0>. (Cit. on pp. 19, 33)
- Rignot, E., Jacobs, S., Mouginot, J., & Scheuchl, B. (2013). Ice-Shelf Melting Around Antarctica. *Science*, 341(6143), 266–270. <https://doi.org/10.1126/science.1235798> (cit. on pp. 16, 20, 27, 90, 108, 137, 157, 160)
- Rignot, E., Mouginot, J., & Scheuchl, B. (2011). Antarctic grounding line mapping from differential satellite radar interferometry. *Geophysical Research Letters*, 38, 1–6. <https://doi.org/10.1029/2011GL047109> (cit. on pp. 20, 137)
- Rignot, E., Mouginot, J., Scheuchl, B., van den Broeke, M., van Wessem, M. J., & Morlighem, M. (2019). Four decades of Antarctic Ice Sheet mass balance from 1979–2017. *Proceedings of the National Academy of Sciences*, 116(4), 1095–1103. <https://doi.org/10.1073/pnas.1812883116> (cit. on p. 38)
- Robertson, J. D., & Bentley, C. R. (1989). The Ross Ice Shelf: Glaciology and geophysics paper 3: Seismic studies on the grid western half of the Ross Ice Shelf: RIGGS I and RIGGS II. In C. R. Bentley & D. E. Hayes (Eds.), *Antarctic Research Series* (pp. 55–86). American Geophysical Union. <https://doi.org/10.1029/AR042p0055>. (Cit. on p. 156)
- Rooney, S. T., Blankenship, D. D., & Bentley, C. R. (1987). Seismic refraction measurements of crustal structure in West Antarctica. In G. D. McKenzie (Ed.), *Geophysical Monograph Series* (pp. 1–7). American Geophysical Union. <https://doi.org/10.1029/GM040p0001>. (Cit. on p. 156)
- Rosier, S. H. R., Hofstede, C., Brisbourne, A. M., Hattermann, T., Nicholls, K. W., Davis, P. E. D., Anker, P. G. D., Hillenbrand, C.-D., Smith, A. M., & Corr, H. F. J. (2018). A New Bathymetry for the Southeastern Filchner-Ronne Ice Shelf: Implications for Modern Oceanographic Processes and Glacial History. *Journal of Geophysical Research: Oceans*, 123(7), 4610–4623. <https://doi.org/10.1029/2018JC013982> (cit. on p. 149)

- 5503 Roy, L., Sen, M. K., Blankenship, D. D., Stoffa, P. L., & Richter, T. G. (2005). Inversion and  
 5504 uncertainty estimation of gravity data using simulated annealing: An application over Lake  
 5505 Vostok, East Antarctica. *Geophysics*, 70(1), J1–J12. <https://doi.org/10.1190/1.1852777>  
 5506 (cit. on p. 106)
- 5507 Salvini, F., Brancolini, G., Busetti, M., Storti, F., Mazzarini, F., & Coren, F. (1997). Cenozoic  
 5508 geodynamics of the Ross Sea region, Antarctica: Crustal extension, intraplate strike-slip  
 5509 faulting, and tectonic inheritance. *Journal of Geophysical Research: Solid Earth*, 102(B11),  
 5510 24669–24696. <https://doi.org/10.1029/97JB01643> (cit. on pp. 30, 31)
- 5511 Sandwell, D. T. (1987). Biharmonic spline interpolation of GEOS-3 and SEASAT altimeter data.  
 5512 *Geophysical Research Letters*, 14(2), 139–142. <https://doi.org/10.1029/GL014i002p00139>  
 5513 (cit. on pp. 62, 63, 100, 108)
- 5514 Santos, D. F., Silva, J. B. C., Martins, C. M., dos Santos, R. D. C. S., Ramos, L. C., & de  
 5515 Araújo, A. C. M. (2015). Efficient gravity inversion of discontinuous basement relief. *GEO-  
 5516 PHYSICS*, 80(4), G95–G106. <https://doi.org/10.1190/geo2014-0513.1> (cit. on pp. 42,  
 5517 106)
- 5518 Sauli, C., Sorlien, C., Busetti, M., De Santis, L., Geletti, R., Wardell, N., & Luyendyk, B. P. (2021).  
 5519 Neogene development of the Terror Rift, western Ross Sea, Antarctica. *Geochemistry,  
 5520 Geophysics, Geosystems*, 22(3). <https://doi.org/10.1029/2020GC009076> (cit. on pp. 30,  
 5521 32)
- 5522 Scambos, T. A., Bohlander, J., Shuman, C., & Skvarca, P. (2004). Glacier acceleration and thin-  
 5523 ning after ice shelf collapse in the Larsen B embayment, Antarctica. *Geophysical Research  
 5524 Letters*, 31(18), L18402. <https://doi.org/10.1029/2004GL020670> (cit. on p. 90)
- 5525 Scambos, T., Haran, T., Fahnestock, M., Painter, T., & Bohlander, J. (2007). MODIS-based Mosaic  
 5526 of Antarctica (MOA) data sets: Continent-wide surface morphology and snow grain size.  
 5527 *Remote Sensing of Environment*, 111(2-3), 242–257. <https://doi.org/10.1016/j.rse.2006.12.020> (cit. on pp. 27, 91, 113, 117, 118, 125, 130, 132, 139)
- 5529 Scheinert, M., Ferraccioli, F., Schwabe, J., Bell, R., Studinger, M., Damaske, D., Jokat, W.,  
 5530 Aleshkova, N., Jordan, T., Leitchenkov, G., Blankenship, D. D., Damiani, T. M., Young,  
 5531 D., Cochran, J. R., & Richter, T. D. (2016). New Antarctic gravity anomaly grid for  
 5532 enhanced geodetic and geophysical studies in Antarctica. *Geophysical Research Letters*,  
 5533 43(2), 600–610. <https://doi.org/10.1002/2015GL067439> (cit. on p. 149)
- 5534 Schlegel, N.-J., Seroussi, H., Schodlok, M. P., Larour, E. Y., Boening, C., Limonadi, D., Watkins,  
 5535 M. M., Morlighem, M., & van den Broeke, M. R. (2018). Exploration of Antarctic Ice Sheet  
 5536 100-year contribution to sea level rise and associated model uncertainties using the ISSM  
 5537 framework. *The Cryosphere*, 12(11), 3511–3534. <https://doi.org/10.5194/tc-12-3511-2018>  
 5538 (cit. on p. 15)
- 5539 Schnaidt, S., & Heinson, G. (2015). Bootstrap resampling as a tool for uncertainty analysis in 2-D  
 5540 magnetotelluric inversion modelling. *Geophysical Journal International*, 203(1), 92–106.  
 5541 <https://doi.org/10.1093/gji/ggv264> (cit. on pp. 73, 101)
- 5542 Schön, J. H. (2015). Density. In *Developments in Petroleum Science* (pp. 109–118). Elsevier. <https://doi.org/10.1016/B978-0-08-100404-3.00004-4>. (Cit. on pp. 112, 116, 129)
- 5544 Seroussi, H., Ivins, E. R., Wiens, D. A., & Bondzio, J. (2017). Influence of a West Antarctic mantle  
 5545 plume on ice sheet basal conditions. *Journal of Geophysical Research: Solid Earth*, 122(9),  
 5546 7127–7155. <https://doi.org/10.1002/2017JB014423> (cit. on p. 144)
- 5547 Shen, W., Wiens, D. A., Anandakrishnan, S., Aster, R. C., Gerstoft, P., Bromirski, P. D., Hansen,  
 5548 S. E., Dalziel, I. W. D., Heeszel, D. S., Huerta, A. D., Nyblade, A. A., Stephen, R., Wilson,  
 5549 T. J., & Winberry, J. P. (2018a). The crust and upper mantle structure of Central and  
 5550 West Antarctica from bayesian inversion of Rayleigh wave and receiver functions. *Journal  
 5551 of Geophysical Research: Solid Earth*, 123(9), 7824–7849. <https://doi.org/10.1029/2017JB015346> (cit. on pp. 32, 35)
- 5553 Shen, W., Wiens, D. A., Lloyd, A. J., & Nyblade, A. A. (2020). A geothermal heat flux map  
 5554 of Antarctica empirically constrained by seismic structure. *Geophysical Research Letters*,  
 5555 47(14). <https://doi.org/10.1029/2020GL086955> (cit. on pp. 139, 145)
- 5556 Shen, W., Wiens, D. A., Stern, T., Anandakrishnan, S., Aster, R. C., Dalziel, I., Hansen, S., Heeszel,  
 5557 D. S., Huerta, A., Nyblade, A., Wilson, T. J., & Winberry, J. P. (2018b). Seismic evidence  
 5558 for lithospheric foundering beneath the southern Transantarctic Mountains, Antarctica.  
 5559 *Geology*, 46(1), 71–74. <https://doi.org/10.1130/G39555.1> (cit. on p. 33)
- 5560 Shipp, S., Anderson, J., & Domack, E. (1999). Late Pleistocene-Holocene retreat of the West  
 5561 Antarctic Ice-Sheet system in the Ross Sea: Part 1 - Geophysical results. *Geological Society*

- 5562       of America Bulletin, 111(10), 32. <https://doi.org/10.1130/0016-7606%281999%29111%3C1486%3ALPHROT%3E2.3.CO%3B2> (cit. on p. 16)
- 5563       Siddoway, C. S. (2008). Tectonics of the West Antarctic Rift System: New light on the history  
5564       and dynamics of distributed intracontinental extension. In A. K. Cooper, P. J. Barrett, H.  
5565       Stagg, B. C. Storey, W. Stump, W. Wise, & 10th ISAES editorial team (Eds.), *Antarctica: A  
5566       Keystone in a Changing World*. The National Academies Press. <https://doi.org/10.3133/ofr20071047KP09>. (Cit. on p. 30)
- 5567       Siegent, M. J., Kulessa, B., Bougamont, M., Christoffersen, P., Key, K., Andersen, K. R., Booth,  
5568       A. D., & Smith, A. M. (2018). Antarctic subglacial groundwater: A concept paper on  
5569       its measurement and potential influence on ice flow. *Geological Society, London, Special  
5570       Publications*, 461(1), 197–213. <https://doi.org/10.1144/SP461.8> (cit. on p. 26)
- 5571       Siegent, M. J., Taylor, J., Payne, A. J., & Hubbard, B. (2004). Macro-scale bed roughness of the  
5572       simple coast ice streams in West Antarctica. *Earth Surface Processes and Landforms*, 29(13),  
5573       1591–1596. <https://doi.org/10.1002/esp.1100> (cit. on p. 20)
- 5574       Slater, T., & Shepherd, A. (2018). Antarctic ice losses tracking high. *Nature Climate Change*,  
5575       8(12), 1025–1026. <https://doi.org/10.1038/s41558-018-0284-9> (cit. on p. 15)
- 5576       Smith, B., Fricker, H. A., Gardner, A. S., Medley, B., Nilsson, J., Paolo, F. S., Holschuh, N.,  
5577       Adusumilli, S., Brunt, K., Csatho, B., Harbeck, K., Markus, T., Neumann, T., Siegfried,  
5578       M. R., & Zwally, H. J. (2020a). Pervasive ice sheet mass loss reflects competing ocean and  
5579       atmosphere processes. *Science*, eaaz5845. <https://doi.org/10.1126/science.aaz5845> (cit. on  
5580       p. 38)
- 5581       Smith, E. C., Hattermann, T., Kuhn, G., Gaedicke, C., Berger, S., Drews, R., Ehlers, T. A.,  
5582       Franke, D., Gromig, R., Hofstede, C., Lambrecht, A., Läufer, A., Mayer, C., Tiedemann,  
5583       R., Wilhelms, F., & Eisen, O. (2020b). Detailed Seismic Bathymetry Beneath Ekström Ice  
5584       Shelf, Antarctica: Implications for Glacial History and Ice-Ocean Interaction. *Geophysical  
5585       Research Letters*, 47(10). <https://doi.org/10.1029/2019GL086187> (cit. on p. 121)
- 5586       Smith, W. H. F., & Wessel, P. (1990). Gridding with continuous curvature splines in tension.  
5587       *GEOPHYSICS*, 55(3), 293–305. <https://doi.org/10.1190/1.1442837> (cit. on pp. 60, 62,  
5588       63, 99, 100, 108, 122, 155)
- 5589       Soler, S. R., & Uieda, L. (2021). Gradient-boosted equivalent sources. *Geophysical Journal  
5590       International*, 227(3), 1768–1783. <https://doi.org/10.1093/gji/ggab297> (cit. on pp. 51, 57, 60,  
5591       112)
- 5592       Sorlien, C. C., Luyendyk, B., Wilson, D. S., Decesari, R. C., Bartek, L. R., & Diebold, J. B.  
5593       (2007). Oligocene development of the West Antarctic Ice Sheet recorded in eastern Ross  
5594       Sea strata. *Geology*, 35(5), 467. <https://doi.org/10.1130/G23387A.1> (cit. on p. 26)
- 5595       Spector, P., Stone, J., Cowdery, S. G., Hall, B., Conway, H., & Bromley, G. (2017). Rapid early-  
5596       Holocene deglaciation in the Ross Sea, Antarctica. *Geophysical Research Letters*, 44(15),  
5597       7817–7825. <https://doi.org/10.1002/2017GL074216> (cit. on p. 90)
- 5598       Steffen, H., Olesen, O., & Sutinen, R. (2021). Glacially Triggered Faulting: A Historical Overview  
5599       and Recent Developments. In H. Steffen, O. Olesen, & R. Sutinen (Eds.), *Glacially-  
5600       Triggered Faulting* (First, pp. 3–19). Cambridge University Press. <https://doi.org/10.1017/9781108779906.003>. (Cit. on pp. 19, 143)
- 5601       Stern, T. A., Davey, F. J., & Delisle, G. (1991). Lithospheric flexure induced by the load of the  
5602       Ross Archipelago, southern Victoria land, Antarctica. In M. Thomson, A. Crame, & J.  
5603       Thomson (Eds.), *Geological Evolution of Antarctica* (pp. 323–328). Cambridge University  
5604       Press. (Cit. on p. 31).
- 5605       Stern, T. A., Ten Brink, U. S., Beaudoin, B. C., & Bannister, S. (1994). Seismic Reflection Experiments  
5606       on the Ross Ice Shelf: 1985-1991. *Terra Antarctica*, 1(3), 513–516 (cit. on p. 21).
- 5607       Stern, T. A., & ten Brink, U. S. (1989). Flexural uplift of the Transantarctic Mountains. *Journal  
5608       of Geophysical Research: Solid Earth*, 94(B8), 10315–10330. <https://doi.org/10.1029/JB094iB08p10315> (cit. on p. 133)
- 5609       Stevens, C., Hulbe, C., Brewer, M., Stewart, C., Robinson, N., Ohneiser, C., & Jendersie, S. (2020).  
5610       Ocean mixing and heat transport processes observed under the Ross Ice Shelf control its  
5611       basal melting. *Proceedings of the National Academy of Sciences*, 117(29), 16799–16804.  
5612       <https://doi.org/10.1073/pnas.1910760117> (cit. on p. 91)
- 5613       Still, H., Campbell, A., & Hulbe, C. (2019). Mechanical analysis of pinning points in the Ross Ice  
5614       Shelf, Antarctica. *Annals of Glaciology*, 60(78), 32–41. <https://doi.org/10.1017/aog.2018.31> (cit. on pp. 20, 26, 33, 91, 131, 142, 143)

- 5620 Still, H., & Hulbe, C. (2021). Mechanics and dynamics of pinning points on the Shirase Coast,  
 5621 West Antarctica. *The Cryosphere*, 15(6), 19. <https://doi.org/10.5194/tc-15-2647-2021>  
 5622 (cit. on p. 142)
- 5623 St-Laurent, P., Klinck, J. M., & Dinniman, M. S. (2013). On the Role of Coastal Troughs in the  
 5624 Circulation of Warm Circumpolar Deep Water on Antarctic Shelves. *Journal of Physical*  
 5625 *Oceanography*, 43(1), 51–64. <https://doi.org/10.1175/JPO-D-11-0237.1> (cit. on p. 38)
- 5626 Studinger, M., Bell, R., Fitzgerald, P., & Buck, W. (2006). Crustal architecture of the Transantarctic  
 5627 Mountains between the Scott and Reedy Glacier region and South Pole from aerogeophysical data.  
 5628 *Earth and Planetary Science Letters*, 250(1-2), 182–199. [https://doi.org/](https://doi.org/10.1016/j.epsl.2006.07.035)  
 5629 [10.1016/j.epsl.2006.07.035](https://doi.org/10.1016/j.epsl.2006.07.035) (cit. on p. 34)
- 5630 Studinger, M., Bell, R. E., Buck, W., Karner, G. D., & Blankenship, D. D. (2004a). Sub-ice geology  
 5631 inland of the Transantarctic Mountains in light of new aerogeophysical data. *Earth and*  
 5632 *Planetary Science Letters*, 220(3-4), 391–408. [https://doi.org/10.1016/S0012-821X\(04\)](https://doi.org/10.1016/S0012-821X(04)00066-4)  
 5633 00066-4 (cit. on pp. 28, 153)
- 5634 Studinger, M., Bell, R. E., & Tikku, A. A. (2004b). Estimating the depth and shape of subglacial  
 5635 Lake Vostok's water cavity from aerogravity data: ESTIMATING LAKE VOSTOK'S WA-  
 5636 TER DEPTH. *Geophysical Research Letters*, 31(12), n/a–n/a. [https://doi.org/10.1029/](https://doi.org/10.1029/2004GL019801)  
 5637 [2004GL019801](https://doi.org/10.1029/2004GL019801) (cit. on pp. 106, 120)
- 5638 Studinger, M., & Miller, H. (1999). Crustal structure of the Filchner-Ronne Shelf and Coats Land,  
 5639 Antarctica, from gravity and magnetic data: Implications for the breakup of Gondwana.  
 5640 *Journal of Geophysical Research: Solid Earth*, 104(B9), 20379–20394. [https://doi.org/10.](https://doi.org/10.1029/1999JB900117)  
 5641 [10.1029/1999JB900117](https://doi.org/10.1029/1999JB900117) (cit. on p. 149)
- 5642 Talwani, M., Worzel, J. L., & Landisman, M. (1959). Rapid gravity computations for two-dimensional  
 5643 bodies with application to the Mendocino submarine fracture zone. *Journal of Geophysical*  
 5644 *Research*, 64(1), 49–59. <https://doi.org/10.1029/JZ064i001p00049> (cit. on p. 106)
- 5645 Tankersley, M., Horgan, H. J., Siddoway, C. S., Caratori Tontini, F., & Tinto, K. J. (2022). Basement  
 5646 Topography and Sediment Thickness Beneath Antarctica's Ross Ice Shelf. *Geophysical*  
 5647 *Research Letters*, 49(10). <https://doi.org/10.1029/2021GL097371> (cit. on pp. 22, 116,  
 5648 129, 133, 151)
- 5649 Tankersley, M. D. (2023). Antarctic\_plots: V0.0.6. <https://doi.org/10.5281/zenodo.7750998>.  
 5650 (Cit. on pp. 23, 51, 171)
- 5651 Tankersley, M. (2022). Mdtanker/RIS\_basement\_sediment: V2.0. <https://doi.org/10.5281/zenodo.6499863>. (Cit. on p. 23)
- 5652 Tankersley, M., Horgan, H., & Caratori-Tontini, F. (2023). Mdtanker/RIS\_gravity\_inversion:  
 5653 First release associated with PhD thesis. <https://doi.org/10.5281/zenodo.8084469>.  
 5654 (Cit. on p. 23)
- 5655 Tarantola, A. (2005). *Inverse Problem Theory and Methods for Model Parameter Estimation*. Society  
 5656 for Industrial and Applied Mathematics. <https://doi.org/10.1137/1.9780898717921>.  
 5657 (Cit. on p. 39)
- 5658 ten Brink, U. S., Bannister, S., Beaudoin, B. C., & Stern, T. A. (1993). Geophysical investigations  
 5659 of the tectonic boundary between East and West Antarctica. *Science*, 261(5117), 45–50.  
 5660 <https://doi.org/10.1126/science.261.5117.45> (cit. on pp. 21, 31, 133)
- 5661 Thomas, R. H. (1979). Ice Shelves: A Review. *Journal of Glaciology*, 24(90), 273–286. <https://doi.org/10.3189/S002214300014799> (cit. on p. 17)
- 5662 Timmermann, R., Brocq, A. L., Deen, T., Domack, E., Dutrieux, P., Galton-Fenzi, B., Hellmer,  
 5663 H., Humbert, A., Jansen, D., Jenkins, A., Lambrecht, A., Makinson, K., Niederjasper, F.,  
 5664 Nitsche, F., Nøst, O. A., Smedsrød, L. H., & Smith, W. H. F. (2010). A consistent data set  
 5665 of Antarctic ice sheet topography, cavity geometry, and global bathymetry. *Earth System*  
 5666 *Science Data*, 2(2), 13. <https://doi.org/10.5194/essd-2-261-2010> (cit. on pp. 91, 124)
- 5667 Tinto, K. J., & Bell, R. E. (2011). Progressive unpinning of Thwaites Glacier from newly identified  
 5668 offshore ridge: Constraints from aerogravity. *Geophysical Research Letters*, 38, 1–6. <https://doi.org/10.1029/2011GL049026> (cit. on pp. 46, 105, 106, 120, 149)
- 5669 Tinto, K. J., Padman, L., Siddoway, C. S., Springer, S. R., Fricker, H. A., Das, I., Caratori Tontini,  
 5670 F., Porter, D. F., Frearson, N. P., Howard, S. L., Siegfried, M. R., Mosbeux, C., Becker,  
 5671 M. K., Bertinato, C., Boghosian, A., Brady, N., Burton, B. L., Chu, W., Cordero, S. I.,  
 5672 ... Bell, R. E. (2019). Ross Ice Shelf response to climate driven by the tectonic imprint on  
 5673 seafloor bathymetry. *Nature Geoscience*, 12(6), 441–449. <https://doi.org/10.1038/s41561-019-0370-2> (cit. on pp. 20, 21, 26–28, 30, 32, 34, 38, 46, 68, 90–92, 104–108, 111, 120, 122,  
 5674 124, 126, 127, 129, 131–134, 137–141, 148, 152, 156, 157)

- 5679 Tinto, K. J., Bell, R. E., Cochran, J. R., & Münchow, A. (2015). Bathymetry in Petermann fjord  
 5680 from Operation IceBridge aerogravity. *Earth and Planetary Science Letters*, 422, 58–66.  
 5681 <https://doi.org/10.1016/j.epsl.2015.04.009> (cit. on pp. 16, 45, 46, 105, 106, 120)
- 5682 Tulaczyk, S., Kamb, W. B., & Engelhardt, H. F. (2000). Basal mechanics of Ice Stream B, west  
 5683 Antarctica: 2. Undrained plastic bed model. *Journal of Geophysical Research: Solid Earth*,  
 5684 105(B1), 483–494. <https://doi.org/10.1029/1999JB900328> (cit. on pp. 18, 144)
- 5685 Uieda, L. (2018). Verde: Processing and gridding spatial data using Green's functions. *Journal of  
 5686 Open Source Software*, 3(29), 957. <https://doi.org/10.21105/joss.00957> (cit. on pp. 51, 60,  
 5687 61, 63, 70, 99)
- 5688 Uieda, L., & Barbosa, V. C. (2017). Fast nonlinear gravity inversion in spherical coordinates with  
 5689 application to the South American Moho. *Geophysical Journal International*, 208(1), 162–  
 5690 176. <https://doi.org/10.1093/gji/ggw390> (cit. on pp. 42, 48, 49, 53, 55, 85, 100, 106, 150)
- 5691 Uieda, L., Soler, S., Rampin, R., van Kemenade, H., Turk, M., Shapero, D., Banihirwe, A., & Lee-  
 5692 man, J. (2020). Pooch: A friend to fetch your data files. *Journal of Open Source Software*,  
 5693 5(45), 1943. <https://doi.org/10.21105/joss.01943> (cit. on p. 171)
- 5694 Uieda, L., Tian, D., Leong, W. J., Jones, M., Schlitzer, W., Toney, L., Grund, M., Yao, J., Magen,  
 5695 Y., Materna, K., Newton, T., Anant, A., Ziebarth, M., Wessel, P., & Quinn, J. (2021).  
 5696 PyGMT: A Python interface for the Generic Mapping Tools. <https://doi.org/10.5281/zenodo.5607255>. (Cit. on pp. 36, 51, 172)
- 5698 Vajda, P., Ellmann, A., Meurers, B., Vaníček, P., Novák, P., & Tenzer, R. (2008a). Global ellipsoid-  
 5699 referenced topographic, bathymetric and stripping corrections to gravity disturbance. *Stu-  
 5700 dia Geophysica et Geodaetica*, 52(1), 19–34. <https://doi.org/10.1007/s11200-008-0003-5>  
 5701 (cit. on p. 104)
- 5702 Vajda, P., Ellmann, A., Meurers, B., Vaníček, P., Novák, P., & Tenzer, R. (2008b). Gravity dis-  
 5703 turbances in regions of negative heights: A reference quasi-ellipsoid approach. *Stu-  
 5704 dia Geophysica et Geodaetica*, 52(1), 35–52. <https://doi.org/10.1007/s11200-008-0004-4> (cit. on  
 5705 p. 94)
- 5706 Vajda, P., Vaníček, P., & Meurers, B. (2006). A new physical foundation for anomalous gravity.  
 5707 *Stu- dia Geophysica et Geodaetica*, 50(2), 189–216. <https://doi.org/10.1007/s11200-006-0012-1> (cit. on p. 96)
- 5709 Vajda, P., Vaníček, P., Novák, P., Tenzer, R., & Ellmann, A. (2007). Secondary indirect effects  
 5710 in gravity anomaly data inversion or interpretation. *Journal of Geophysical Research*,  
 5711 112(B6), B06411. <https://doi.org/10.1029/2006JB004470> (cit. on pp. 95, 103)
- 5712 Vajda, P., Vaníček, P., & Meurers, B. (2004). On the removal of the effect of topography on gravity  
 5713 disturbance in gravity data inversion or interpretation. *Contributions to Geophysics and  
 5714 Geodesy*, 34 (cit. on p. 94).
- 5715 Vaňková, I., Winberry, J. P., Cook, S., Nicholls, K. W., Greene, C. A., & Galton-Fenzi, B. K. (2023).  
 5716 High Spatial Melt Rate Variability Near the Totten Glacier Grounding Zone Explained by  
 5717 New Bathymetry Inversion. *Geophysical Research Letters*, 50(10), e2023GL102960. <https://doi.org/10.1029/2023GL102960> (cit. on pp. 105, 107)
- 5719 Venturelli, R. A., Siegfried, M. R., Roush, K. A., Li, W., Burnett, J., Zook, R., Fricker, H. A., Priscu,  
 5720 J. C., Leventer, A., & Rosenheim, B. E. (2020). Mid-Holocene grounding line retreat and  
 5721 readvance at Whillans Ice Stream, West Antarctica. *Geophysical Research Letters*, 47(15).  
 5722 <https://doi.org/10.1029/2020GL088476> (cit. on pp. 20, 32, 33, 36, 90, 131, 137)
- 5723 Virtanen, P., Gommers, R., Oliphant, T. E., Haberland, M., Reddy, T., Cournapeau, D., Burovski,  
 5724 E., Peterson, P., Weckesser, W., Bright, J., van der Walt, S. J., Brett, M., Wilson, J.,  
 5725 Millman, K. J., Mayorov, N., Nelson, A. R. J., Jones, E., Kern, R., Larson, E., ... SciPy  
 5726 1.0 Contributors. (2020). SciPy 1.0: Fundamental algorithms for scientific computing in  
 5727 python. *Nature Methods*, 17, 261–272. <https://doi.org/10.1038/s41592-019-0686-2> (cit. on  
 5728 p. 51)
- 5729 Wannamaker, P., Hill, G., Stodt, J., Maris, V., Ogawa, Y., Selway, K., Boren, G., Bertrand,  
 5730 E., Uhlmann, D., Ayling, B., Green, A. M., & Feucht, D. (2017). Uplift of the central  
 5731 transantarctic mountains. *Nature Communications*, 8(1), 1588. <https://doi.org/10.1038/s41467-017-01577-2> (cit. on pp. 21, 133)
- 5733 Wei, W., Blankenship, D. D., Greenbaum, J. S., Gourmelen, N., Dow, C. F., Richter, T. G., Greene,  
 5734 C. A., Young, D. A., Lee, S., Kim, T.-W., Lee, W. S., & Assmann, K. M. (2020). Getz Ice  
 5735 Shelf melt enhanced by freshwater discharge from beneath the West Antarctic Ice Sheet.  
 5736 *The Cryosphere*, 14(4), 1399–1408. <https://doi.org/10.5194/tc-14-1399-2020> (cit. on  
 5737 pp. 105, 106, 120, 149)

- 5738 Werner, S. (1953). Interpretation of magnetic anomalies at sheet-like bodies. In *Sveriges Geologiska  
5739 Undersök* (pp. 413–449). Stockholm Norstedt. (Cit. on pp. 28, 152).
- 5740 Wessel, P., Luis, J. F., Uieda, L., Scharroo, R., Wobbe, F., Smith, W. H. F., & Tian, D. (2019).  
5741 The Generic Mapping Tools version 6. *Geochemistry, Geophysics, Geosystems*, 20(11),  
5742 5556–5564. <https://doi.org/10.1029/2019GC008515> (cit. on pp. 36, 63)
- 5743 Wessel, P., & Bercovici, D. (1998). Interpolation with splines in tension: A Green's function ap-  
5744 proach. *Mathematical Geology*, 30(1), 77–93. <https://doi.org/10.1023/A:1021713421882>  
5745 (cit. on p. 63)
- 5746 White-Gaynor, A. L., Nyblade, A. A., Aster, R. C., Wiens, D. A., Bromirski, P. D., Gerstoft, P.,  
5747 Stephen, R. A., Hansen, S. E., Wilson, T., Dalziel, I. W., Huerta, A. D., Paul Winberry,  
5748 J., & Anandakrishnan, S. (2019). Heterogeneous upper mantle structure beneath the Ross  
5749 Sea Embayment and Marie Byrd Land, West Antarctica, revealed by P-wave tomography.  
5750 *Earth and Planetary Science Letters*, 513, 40–50. <https://doi.org/10.1016/j.epsl.2019.02.013> (cit. on p. 34)
- 5751 Whitehouse, P. L., Gomez, N., King, M. A., & Wiens, D. A. (2019). Solid Earth change and the  
5752 evolution of the Antarctic Ice Sheet. *Nature Communications*, 10(1), 503. <https://doi.org/10.1038/s41467-018-08068-y> (cit. on pp. 19, 33)
- 5753 Wilkinson, M. D., Dumontier, M., Aalbersberg, I. J., Appleton, G., Axton, M., Baak, A., Blomberg,  
5754 N., Boiten, J.-W., da Silva Santos, L. B., Bourne, P. E., Bouwman, J., Brookes, A. J., Clark,  
5755 T., Crosas, M., Dillo, I., Dumon, O., Edmunds, S., Evelo, C. T., Finkers, R., ... Mons,  
5756 B. (2016). The FAIR Guiding Principles for scientific data management and stewardship.  
5757 *Scientific Data*, 3(1), 160018. <https://doi.org/10.1038/sdata.2016.18> (cit. on p. 23)
- 5758 Wilson, D. S., Jamieson, S. S., Barrett, P. J., Leitchenkov, G., Gohl, K., & Larter, R. D. (2012).  
5759 Antarctic topography at the Eocene–Oligocene boundary. *Palaeogeography, Palaeoclima-  
5760 tology, Palaeoecology*, 335–336, 24–34. <https://doi.org/10.1016/j.palaeo.2011.05.028>  
5761 (cit. on pp. 34, 147, 155)
- 5762 Wilson, D. S., & Luyendyk, B. (2009). West Antarctic paleotopography estimated at the Eocene-  
5763 Oligocene climate transition. *Geophysical Research Letters*, 36(16), L16302. <https://doi.org/10.1029/2009GL039297> (cit. on pp. 26, 34, 147, 155, 157)
- 5764 Wilson, D. S., Pollard, D., DeConto, R. M., Jamieson, S. S., & Luyendyk, B. (2013). Initiation of  
5765 the West Antarctic Ice Sheet and estimates of total Antarctic ice volume in the earliest  
5766 Oligocene. *Geophysical Research Letters*, 40(16), 4305–4309. <https://doi.org/10.1002/grl.50797> (cit. on pp. 26, 34)
- 5767 Yamasaki, T., Miura, H., & Nogi, Y. (2008). Numerical modelling study on the flexural uplift of  
5768 the Transantarctic Mountains. *Geophysical Journal International*, 174(1), 377–390. <https://doi.org/10.1111/j.1365-246X.2008.03815.x> (cit. on p. 133)
- 5769 Yang, J., Guo, J., Greenbaum, J. S., Cui, X., Tu, L., Li, L., Jong, L. M., Tang, X., Li, B., Blanken-  
5770 ship, D. D., Roberts, J. L., Ommen, T., & Sun, B. (2021). Bathymetry Beneath the Amery  
5771 Ice Shelf, East Antarctica, Revealed by Airborne Gravity. *Geophysical Research Letters*,  
5772 48(24). <https://doi.org/10.1029/2021GL096215> (cit. on pp. 38, 46, 63, 104–106, 120, 122)
- 5773 Yang, J., Jekeli, C., & Liu, L. (2018). Seafloor Topography Estimation From Gravity Gradients  
5774 Using Simulated Annealing. *Journal of Geophysical Research: Solid Earth*. <https://doi.org/10.1029/2018JB015883> (cit. on p. 106)
- 5775 Yang, J., Luo, Z., & Tu, L. (2020a). Ocean Access to Zachariæ Isstrøm Glacier, Northeast Green-  
5776 land, Revealed by OMG Airborne Gravity. *Journal of Geophysical Research: Solid Earth*,  
5777 125(11). <https://doi.org/10.1029/2020JB020281> (cit. on pp. 78, 105, 106)
- 5778 Yang, J., Luo, Z., Tu, L., Li, S., Guo, J., & Fan, D. (2020b). On the Feasibility of Seafloor To-  
5779 polography Estimation from Airborne Gravity Gradients: Performance Analysis Using Real  
5780 Data. *Remote Sensing*, 12(24), 4092. <https://doi.org/10.3390/rs12244092> (cit. on p. 104)
- 5781 Yokoyama, Y., Anderson, J. B., Yamane, M., Simkins, L. M., Miyairi, Y., Yamazaki, T., Koizumi,  
5782 M., Suga, H., Kusahara, K., Prothro, L., Hasumi, H., Southon, J. R., & Ohkouchi, N.  
5783 (2016). Widespread collapse of the Ross Ice Shelf during the late Holocene. *Proceedings  
5784 of the National Academy of Sciences*, 113(9), 2354–2359. <https://doi.org/10.1073/pnas.1516908113> (cit. on p. 90)
- 5785 Zhao, C., Gladstone, R. M., Warner, R. C., King, M. A., Zwinger, T., & Morlighem, M. (2018).  
5786 Basal friction of Fleming Glacier, Antarctica – Part 1: Sensitivity of inversion to temper-  
5787 ature and bedrock uncertainty. *The Cryosphere*, 12(8), 2637–2652. <https://doi.org/10.5194/tc-12-2637-2018> (cit. on p. 15)

- 5796 Zhao, K. X., Stewart, A. L., & McWilliams, J. C. (2019). Sill-Influenced Exchange Flows in Ice Shelf  
5797 Cavities. *Journal of Physical Oceanography*, 49(1), 163–191. [https://doi.org/10.1175/JPO-](https://doi.org/10.1175/JPO-D-18-0076.1)  
5798 D-18-0076.1 (cit. on pp. 16, 91)
- 5799 Zhou, Z., Wiens, D. A., Shen, W., Aster, R. C., Nyblade, A., & Wilson, T. J. (2022). Radial  
5800 Anisotropy and Sediment Thickness of West and Central Antarctica Estimated From  
5801 Rayleigh and Love Wave Velocities. *Journal of Geophysical Research: Solid Earth*, 127(3).  
5802 <https://doi.org/10.1029/2021JB022857> (cit. on pp. 31, 156)